

---

---

---

---

JSCSEN 79(7)759–909(2014)

---

---

---

ISSN 1820-7421(Online)

---

---

---

---

---

# Journal of the Serbian Chemical Society

---

---

e  
Version  
electronic

---

---

---

VOLUME 79

---

No 7

---

BELGRADE 2014

---

Available on line at



[www.shd.org.rs/JSCS/](http://www.shd.org.rs/JSCS/)

The full search of JSCS

is available through

DOAJ DIRECTORY OF

OPEN ACCESS

JOURNALS

[www.doaj.org](http://www.doaj.org)



# Journal of the Serbian Chemical Society

JSCS-info@shd.org.rs • www.shd.org.rs/JSCS

*J. Serb. Chem. Soc.* Vol. 79, No. 7 (2014)

## CONTENTS

### Organic Chemistry

- A. Marinković, D. Mijin, J. Mirković, V. Maslak and C. O. Kappe: A microwave approach to the synthesis of certain 4-(substituted phenyl)-6-phenyl-3-cyano-2-pyridones ..... 759  
P. Jovanović, J. Ranđelović, B. Ivković, C. Suteu, Z. Tokić Vujošević and V. Savić: Substituted proline derivatives as organocatalysts in the Michael reaction ..... 767

### Biochemistry and Biotechnology

- S. M. Bukhari, A. J. Feuerherm, F. Boufrad, B. Zlatković, B. Johansen and N. Simić: Anti-inflammatory and antioxidant activities of *Sclerochloa dura* (Poaceae) ..... 779

### Inorganic Chemistry

- M. Montazerzohori, S. Yadegari and A. Naghiha: Synthesis, characterization, electrochemical behavior and antibacterial/antifungal activities of [Cd(L)X<sub>2</sub>] complexes with a new Schiff base ligand ..... 793

### Theoretical Chemistry

- B. Furtula, G. Lekishvili and I. Gutman: A graph theoretical approach to *cis/trans* isomerism ..... 805

### Physical Chemistry

- N. I. Ilić, S. S. Lazarević, V. N. Rajaković-Ognjanović, Lj. V. Rajaković, Đ. T. Janačković and R. D. Petrović: The sorption of inorganic arsenic on modified sepiolite: the effect of hydrated iron(III) oxide ..... 815

### Thermodynamics

- N. D. Grozdanić, M. S. Calado, M. Lj. Kijevčanin, S. P. Šerbanović and Z. P. Višak: Aqueous nicotine solutions: pH-measurements and salting-out effects – Analysis of the effective Gibbs energies of hydration and ionic strengths of the solutions ..... 829

### Polymers

- M. V. Pergal, I. S. Stefanović, D. Gođevac, V. V. Antić, V. Milačić, S. Ostojić, J. Rogan and J. Djoniagić: Structural, thermal and surface characterization of thermoplastic polyurethanes based on poly(dimethylsiloxane) ..... 843

### Materials

- R. M. Dukali, I. M. Radović, D. B. Stojanović, D. M. Šević, V. J. Radojević, D. M. Jocić and R. R. Aleksić: Electrospinning of the laser dye rhodamine B-doped poly(methyl methacrylate) nanofibers ..... 867

### Environmental

- X. Bi, M. Xiao, X. Qiao, C.-F. F. Lee and Y. Liu: An experimental and computational investigation of the effects of temperature on soot formation mechanisms ..... 881  
K. Thirugnanasambandham, V. Sivakumar and J. Prakash Maran: Bagasse wastewater treatment using biopolymer – A novel approach ..... 897

Published by the Serbian Chemical Society  
Karnegijeva 4/III, P. O. Box 36, 11120 Belgrade 35, Serbia  
Printed by the Faculty of Technology and Metallurgy  
Karnegijeva 4, P. O. Box 35-03, 11120 Belgrade, Serbia



## A microwave approach to the synthesis of certain 4-(substituted phenyl)-6-phenyl-3-cyano-2-pyridones

ALEKSANDAR MARINKOVIĆ<sup>1#</sup>, DUŠAN MIJIN<sup>1\*#</sup>, JELENA MIRKOVIĆ<sup>1#</sup>,  
VESELIN MASLAK<sup>2</sup> and C. OLIVER KAPPE<sup>3</sup>

<sup>1</sup>Faculty of Technology and Metallurgy, University of Belgrade, Karnegijeva 4, 11120 Belgrade, Serbia, <sup>2</sup>Faculty of Chemistry, University of Belgrade, Studentski trg 12–16, 11000 Belgrade, Serbia and <sup>3</sup>Christian Doppler Laboratory for Microwave Chemistry (CDLMC) and Institute of Chemistry, Karl-Franzens-University Graz, Heinrichstraße 28, A-8010 Graz, Austria

(Received 18 July, accepted 27 November 2013)

**Abstract:** A study of the synthesis of 4-(substituted phenyl)-6-phenyl-3-cyano-2-pyridones from ethyl 2-cyano-3-(substituted phenyl) acrylates and acetophenone is presented. The 2-pyridones were obtained using conventional as well as microwave synthesis under solvent and solvent-free conditions in domestic and laboratory microwave ovens. The structure of the obtained pyridones was confirmed by m.p., FT-IR, NMR and UV data.

**Keywords:** pyridone; acrylate; cyclocondensation reaction; microwave chemistry.

### INTRODUCTION

It is well known that many naturally occurring and synthetic compounds containing a 2-pyridone ring system have a broad spectrum of biological activity.<sup>1–3</sup> Some of them, such as milrinone, amrinone and their analogues are cardiotonic agents for the treatment of heart failure.<sup>4–7</sup> Other 2-pyridones possess antitumor,<sup>8,9</sup> antibacterial<sup>10</sup> and other biological activities.<sup>1,2,11–15</sup> In addition, derivatives of 3-cyano-2-pyridones are used in the manufacture of dyes, pigments, additives for fuels and lubricants, stabilizers for polymers and varnishes, acid–base indicators and other practically important materials.<sup>2</sup>

3-Cyano-2-pyridones can be obtained using different procedures starting from various initial substrates.<sup>1,2,16,17</sup> Microwave-assisted chemistry has also been used for the synthesis of 2-pyridones and their derivatives.<sup>18–23</sup>

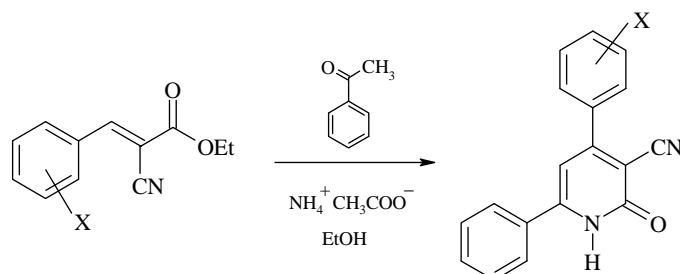
\* Corresponding author. E-mail: kavur@tmf.bg.ac.rs

# Serbian Chemical Society member.

doi: 10.2298/JSC130718145M

4,6-Diphenyl-3-cyano-2-pyridones (4,6-diaryl-2-oxo-1,2-dihydropyridine-3-carbonitriles) can be obtained by cyclization of ethyl cyanoacetate and ketones by ammonium acetate,<sup>24</sup> reaction between 1,3-diaryl-2-propen-1-one and cyanoacetamide using MeONa,<sup>25</sup> piperidine<sup>26</sup> or DMSO-*tert*-BuOK,<sup>27</sup> by the reaction of  $\beta$ -aminoenones with substituted acetonitriles,<sup>28</sup> by the reaction of malononitrile with acetylenic ketones,<sup>29</sup> and by solid-phase<sup>30</sup> and one-pot synthesis *via* three-component cyclocondensation under solvent-free conditions.<sup>31</sup> In addition, 4,6-diphenyl-3-cyano-2-pyridones were prepared by the reaction between 1,3-diaryl-2-propen-1-ones and cyanoacetamide using powdered KOH under microwave irradiation.<sup>32</sup>

One of the less explored synthesis of 4-(substituted phenyl)-6-phenyl-3-cyano-2-pyridones is their synthesis from ethyl 2-cyano-3-(substituted phenyl) acrylates (Scheme 1).<sup>33,34</sup>



Scheme 1. Synthesis of 4-(substituted phenyl)-6-phenyl-3-cyano-2-pyridones from ethyl 2-cyano-3-(substituted phenyl) acrylates (X = H (**1**), 4-CH<sub>3</sub> (**2**), 4-OCH<sub>3</sub> (**3**), 4-Cl (**4**), 4-NO<sub>2</sub> (**5**), 4-Br (**6**), 3-NO<sub>2</sub> (**7**), 3-Cl (**8**), 2-NO<sub>2</sub> (**9**))).

In this work, a microwave approach to the synthesis of known 4-(substituted phenyl)-6-phenyl-3-cyano-2-pyridones from ethyl 2-cyano-3-(substituted phenyl) acrylates and acetophenone was applied. Solvent and solvent-free reactions were performed in a modified domestic microwave oven and laboratory microwave ovens. Low to moderate yields were obtained in relatively short reaction time using optimized procedures.

## RESULTS AND DISCUSSION

In order to study the synthesis of 4-(substituted phenyl)-6-phenyl-3-cyano-2-pyridones by condensation of ethyl 2-cyano-3-(substituted phenyl) acrylates with acetophenone, it was necessary to prepare ethyl 2-cyano-3-(substituted phenyl) acrylates. These compounds can be easily prepared from substituted benzaldehydes and ethyl cyanoacetate, as described elsewhere.<sup>33,34</sup> The reactions proceed relatively smoothly with good to excellent yields.

In the first part of the pyridone synthesis, 4-(substituted phenyl)-6-phenyl-3-cyano-2-pyridones were prepared by conventional methods.<sup>33,34</sup> Ethyl 2-cyano-

-3-(substituted phenyl) acrylates, acetophenone and ammonium acetate were heated in ethanol under reflux for 1 h and the obtained results are given in Table I. The molar ratio of the reactants was ethyl 2-cyano-3-(substituted phenyl) acrylates, acetophenone and ammonium acetate = 1:1:1.5.

TABLE I. Conventional and microwave synthesis of 4-(substituted phenyl)-6-phenyl-3-cyano-2-pyridones

No.	Substituent	Conventional synthesis, %	Microwave synthesis <sup>a</sup>	
			Modified domestic oven, %	Microwave synthesis, %
<b>1</b>	H	35	34	30 <sup>b</sup>
<b>2</b>	4-CH <sub>3</sub>	40	32	14 <sup>c</sup>
<b>3</b>	4-OCH <sub>3</sub>	30	34	9 <sup>c</sup>
<b>4</b>	4-Cl	32	33	32 <sup>c</sup>
<b>5</b>	4-NO <sub>2</sub>	No product	23	20 <sup>c</sup>
<b>6</b>	4-Br	14	20	29 <sup>c</sup>
<b>7</b>	3-NO <sub>2</sub>	35	40	24 <sup>c</sup>
<b>8</b>	3-Cl	26	29	15 <sup>c</sup>
<b>9</b>	2-NO <sub>2</sub>	12	16	12 <sup>c</sup>

<sup>a</sup>Biotage – yield of compound **1** = 29 %; <sup>b</sup>300 W, 5 min; <sup>c</sup>200 W, 2 min

As can be seen from Table I, the pyridones were obtained in low to moderate yields, except for the 4-nitro derivative, which could not be obtained by this procedure. At this moment of the work, it seemed that an improvement in the isolated yield could be achieved if some other approach were used, such as microwave synthesis.

In the early days of microwave-assisted organic synthesis, the only possible way to do the synthesis was to use domestic or modified domestic microwave ovens. In this work, a microwave oven modified in such a manner to provide stirring and refluxing of the reaction mixture as described in literature was used.<sup>35</sup> First, an optimization of the synthesis of 3-cyano-4,6-diphenyl-2-pyridone was performed. The reactant ratio, power of irradiation and reaction time were varied. In addition, several solvents were used (ethanol, ethylene glycol and DMF). The obtained results showed (optimization results not presented) that the optimal reactant ratio was the same as in the conventional synthesis and that the solvent-free reaction gave the best yield. It was established that the optimal reaction time was 2 min (several times shorter than for the conventional method) and using these parameters, the synthesis of the pyridones was performed (Table I). The solvent-free synthesis of 4-(substituted phenyl)-6-phenyl-3-cyano-2-pyridones in the modified domestic microwave oven led to similar or slightly better yields in comparison to conventional procedure. Except for the shorter reaction time, another advantage of the microwave synthesis was the synthesis of the 4-nitro derivative, which could not be obtained by the conventional approach. On the other hand, the disadvantages of such a method are the non-uniform heating,



mixing, and the precise determination of the reaction temperature.<sup>36</sup> In order to overcome the disadvantages of using modified domestic microwave ovens, syntheses in dedicated microwave reactors were performed (MicroSYNTH and Biotage). The reactions were controlled by an IR thermometer. Solvent-free microwave synthesis was used to enable comparison of the results with those obtained using the domestic microwave oven. Optimization of the synthesis of 3-cyano-4,6-diphenyl-2-pyridone synthesis in the MicroSYNTH reactor was performed by varying the irradiation power and reaction time using the previously established ratio of reactants (1:1:1.5). It was found that 5 min and 300 W are optimal for the reaction, since shorter or longer reaction times and lower or higher irradiation power decreased the yield of the pyridone. When these reaction parameters were applied to the synthesis of other pyridones, lower yields were obtained in comparison with those obtained in the modified domestic microwave oven (Table I).

To overcome all the disadvantages of solvent-free reactions, the synthesis of 3-cyano-4,6-diphenyl-2-pyridone in the Biotage reactor using ethanol as a solvent was optimized. The influence of reactant ratio, temperature and reaction time on the pyridone yield (HPLC) was studied. A higher concentration of reactants was also used. Even here, low yields were obtained. The highest yield was obtained at 150 °C after 15 min with the ratio of reactants being 1:1:3. The initial amount of acrylate was 1 mmol and solvent volume was 1 cm<sup>3</sup>. The yield was 29 %.

Moreover, the influence of the structure of the ammonium salt was studied. Ammonium formate, carbonate and hydrogen carbonate were used. While ammonium formate gave a slightly lower yield than ammonium acetate, ammonium carbonate gave no yield at all. Ammonium hydrogen carbonate gave much lower yield than ammonium acetate.

During optimization, it was observed that the starting acrylate was the compound with the highest reactivity present in the reaction mixture. Acetophenone was much less reactive. Since no influence of the initial concentration of acetophenone was observed on the reaction and since no reaction between acetophenone and ammonium acetate was observed, it seems that the reaction proceeds initially by ammonia attack on the acrylate followed by the reaction of the formed amide with acetophenone.<sup>37</sup> The low yields could be explained by a possible parallel reaction of the acrylate molecules that might lead to dimerization.<sup>38</sup>

## EXPERIMENTAL

### Materials

All employed materials were obtained commercially, mostly from Sigma–Aldrich, and were used without further purification.

### Equipment

The IR spectra were recorded on a Bomem MB series FTIR spectrophotometer, in the form of KBr pellets. The <sup>1</sup>H-NMR spectra were recorded as solutions in DMSO-*d*<sub>6</sub> using a



Varian Gemini-200 instrument, with tetramethylsilane as the internal standard. The UV absorption spectra were taken using a Shimadzu 1700 UV–Vis spectrophotometer in 1.00 cm cells at  $25\pm0.1$  °C in ethanol at a concentration of  $5\times10^{-5}$  mol dm<sup>-3</sup>. The spectral data of the synthesized compounds together with their melting points are given in the Supplementary material to this paper.

A Samsung domestic microwave oven was modified as given in the literature<sup>35</sup> in order to provide mixing and refluxing of the reaction mixture. A MicroSYNTH Milestone and a Biotage Initiator 2.5 EXP were used for the microwave experiments. Analytical HPLC analysis (Shimadzu LC20) was performed on a C 18 reversed-phase analytical column (150 mm×4.6 mm, particle size 3 mm) using the mobile phases A (water:acetonitrile 90:10 (V/V) + 0.1 % TFA) and B (acetonitrile + 0.1 % TFA) at a flow rate of 0.5 cm<sup>3</sup> min<sup>-1</sup>. The following gradient was applied: linear increase from 30 to 100 % B in 9 min, hold at 100 % solution B for 5 min.

#### *Conventional synthesis of 4-(substituted phenyl)-6-phenyl-3-cyano-2-pyridones<sup>33,34,37</sup>*

A mixture of ethyl 2-cyano-3-(substituted phenyl) acrylate (0.1 mol), acetophenone (0.1 mol) and ammonium acetate (0.15 mol) in ethanol was heated under reflux for 1 h. After cooling, the obtained crystals were removed by filtration, washed with diethyl ether and purified by recrystallization (DMF/ethanol, 1:1).

#### *Microwave synthesis of 4-(substituted phenyl)-6-phenyl-3-cyano-2-pyridones in a modified domestic oven*

A mixture of ethyl 2-cyano-3-(substituted phenyl) acrylate (0.1 mol), acetophenone (0.1 mol) and ammonium acetate (0.15 mol) was heated in a domestic microwave oven (100 or 200 W) for 2 minutes. Alternatively, a mixture in the chosen solvent was heated in the modified domestic microwave oven. After cooling, the obtained crystals were removed by filtration, washed with diethyl ether and purified by recrystallization (DMF/ethanol, 1:1).

#### *Microwave synthesis of 4-(substituted phenyl)-6-phenyl-3-cyano-2-pyridones in the MicroSYNTH reactor*

A mixture of ethyl 2-cyano-3-(substituted phenyl) acrylate (2 mmol), acetophenone (2 mmol) and ammonium acetate (3 mmol) was heated in a microwave reactor in a glass tube ( $\varnothing$  29 mm) equipped with a condenser for 2 to 5 min. After cooling, the obtained crystals were removed by filtration, washed with diethyl ether and purified by recrystallization (pyridine/ethanol, 1:1).

#### *Microwave synthesis of 4-(substituted phenyl)-6-phenyl-3-cyano-2-pyridones in the Biotage reactor*

A mixture of ethyl 2-cyano-3-(substituted phenyl) acrylate (1 mmol), acetophenone (1 mmol) and ammonium acetate (3 mmol) in ethanol (1 cm<sup>3</sup>) was heated in a Biotage microwave reactor for a period of 15 min at 150 °C. The product yield was established by HPLC analysis at 215 nm.

### CONCLUSIONS

The synthesis of 4-(substituted phenyl)-6-phenyl-3-cyano-2-pyridones from ethyl 2-cyano-3-(substituted phenyl) acrylates and acetophenone using microwave irradiation showed that the reaction time could be shortened from 60 to 2 min while the isolated yields remained constant. The 4-nitro derivative could be



only prepared under microwave irradiation. Solvent-free reactions in comparison to those run in solvents gave better results.

#### SUPPLEMENTARY MATERIAL

Melting points and spectral data of the synthesized pyridones are available electronically from <http://www.shd.org.rs/JSCS/>, or from the corresponding author on request.

*Acknowledgments.* The authors are grateful to the Ministry of Education, Science and Technological Development of the Republic of Serbia for financial support (Project No. 172013). D. M. thanks the Austrian Academic Exchange Service for a scholarship and Prof C. O. Kappe for his support.

#### ИЗВОД

#### МИКРОТАЛСНИ ПРИСТУП СИНТЕЗИ ОДРЕЂЕНИХ 4-(СУПСТИТУИСАНИХ ФЕНИЛ)-6-ФЕНИЛ-3-ЦИЈАНО-2-ПИРИДОНА

АЛЕКСАНДАР МАРИНКОВИЋ<sup>1</sup>, ДУШАН МИЈИН<sup>1</sup>, ЈЕЛЕНА МИРКОВИЋ<sup>1</sup>, ВЕСЕЛИН МАСЛАК<sup>2</sup>  
и С. OLIVER KAPPE<sup>3</sup>

<sup>1</sup>Технолошко-мешавински факултет у Београду, Карнејијева 4, 11120 Београд,

<sup>2</sup>Хемијски факултет у Београду, Студентски јар 3–5, 11000 Београд и <sup>3</sup>Christian Doppler Laboratory for Microwave Chemistry (CDLMC) and Institute of Chemistry, Karl-Franzens-University Graz, Heinrichstraße 28, A-8010 Graz, Austria

У оквиру рада приказана је синтеза 4-(супституисаних фенил)-6-фенил-3-цијано-2-пиридона полазећи од етил-2-цијано-3-(супституисаних фенил) акрилата и ацетофенона. 2-Пиридони су добијени како у присуству тако и у одсуству растварача користећи класичну и микроталасну синтезу, у модификованијој микроталасној пећници за домаћинство као и у лабораторијском микроталасном реактору. Структура добијених пиридона потврђена је температурома топљења, IC, NMR и UV подацима.

(Примљено 18. јула, прихваћено 27 новембра 2013)

#### REFERENCES

1. M. Mišić-Vuković, D. Mijin, M. Radojković-Veličković, N. Valentić, V. Krstić, *J. Serb. Chem. Soc.* **63** (1998) 585
2. V. P. Litvinov, D. Krivokolysko, V. D Dayachenko, *Chem. Heterocycl. Compd.* **35** (1999) 509
3. J. H. Rigby, *Synlett* (2000) 1
4. G. Pastelin, R. Mendez, E. Kabela, A. Farah, *Life Sci.* **33** (1983) 1787
5. E. L. Presti, R. Boggia, A. Feltrin, G. Menozzi, P. Dorigo, L. Mosti, *Farmaco* **54** (1999) 465
6. P. Dorigo, D. Fraccarolo, R. M. Gaion, G. Santostasi, P. A. Borea, M. Floreani, L. Mosti, I. Maragno, *Gen. Pharm.* **28** (1997) 781
7. C. Altomare, S. Cellamare, L. Summo, P. Fossa, L. Mosti, A. Carotti, *Bioorg. Med. Chem.* **8** (2000) 909
8. W. K. Anderson, D. C. Dean, T. Endo, *J. Med. Chem.* **33** (1990) 1667
9. S. B. Margolin, (S. B. Margolin), US 5962478 (1999)
10. Q. Li, L. A. Mitscher, L. L. Shen, *Med. Res. Rev.* **20** (2000) 231
11. P. S. Dragovich, T. J. Prins, R. Zhou, E. L. Brown, F. C. Maldonado, S. A. Fuhrman, L. S. Zalman, T. Tuntland, C. A. Lee, A. K. Patick, D. A. Matthews, T. F. Hendrickson, M.



- B. Kosa, B. Liu, M. R. Batugo, J.-P. R. Gleeson, S. K. Sakata, L. Chen, M. C. Guzman, J. W. III Meador, R. A. Ferre, S. T. J. Worland, *J. Med. Chem.* **45** (2002) 1607
12. P. S. Dragovich, T. J. Prins, R. Zhou, T. O. Johnson, E. L. Brown, F. C. Maldonado, S. A. Fuhrman, L. S. Zalman, A. K. Patick, D. A. Matthews, X. Hou, J. W. Meador, R. A. Ferre, S. T. Worland, *Bioorg. Med. Chem. Lett.* **12** (2002) 733
13. S. J. Patankar, P. C. J. Jurs, *J. Chem. Inf. Comput. Sci.* **42** (2002) 1053
14. E. De Clercq, *Farmaco* **54** (1999) 26
15. R. L. T. Parreira, O. Abrahao, S. E. Galembeck, *Tetrahedron* **57** (2001) 3243
16. F. Brody, P. R. Ruby, in *Pyridine and its Derivatives*, E. Klinsberg, Ed., Interscience, New York, 1960, p. 362
17. M. A. Ciufolini, B. K. Chan, *Heterocycles* **74** (2007) 101
18. N. Y. Gorobets, B. H. Yousefi, F. Belaj, C. O. Kappe, *Tetrahedron* **60** (2004) 8633
19. N. Pemberton, V. Aberg, H. Almstedt, A. Westermark, F. Almqvist, *J. Org. Chem.* **69** (2004) 7830
20. N. Pemberton, E. Chorell, F. Almqvist, *Top. Heterocycl. Chem.* **1** (2006) 1
21. N. Pemberton, L. Jakobsson, F. Almqvist, *Org. Lett.* **8** (2006) 935
22. D. Mijin, A. Marinković, *Synth. Commun.* **36** (2006) 193
23. D. Z. Mijin, M. Baghbanzadeh, C. Reidlinger, C. O. Kappe, *Dyes Pigm.* **85** (2010) 73
24. A. Sakurai, H. Midorikawa, *Bull. Chem. Soc. Jpn.* **40** (1967) 1680
25. Z. Bomika, M. B. Andaburskaya, J. Pelcers, G. Duburs, *Khim. Geterotsikl. Soedin.* (1975) 1108
26. J. L. Soto, C. Seoane, A. M. Mansilla, *Org. Prep. Proced. Int.* **13** (1981) 331
27. R. Jain, F. Roschangar, M. A. Ciufolini, *Tetrahedron Lett.* **36** (1995) 3307
28. A. Alberola, C. Andres, A. Gonzalez Ortega, R. Pedrosa, M. Vincente, *J. Heterocycl. Chem.* **24** (1987) 709
29. K. A. Kandeel, J. M. Vernon, T. A. Dransfield, F. A. Fouli, A. S. A. Youssef, *J. Chem. Res., Synop.* (1990) 276
30. W. Li, Y. Chen, Y. Lam, *Tetrahedron Lett.* **45** (2004) 6545
31. L. Range, H. Han, H. Jong, D. Shi, S. Tu, *Synth. Commun.* **38** (2008) 217
32. C. G. Dave, D. A. Shah, Y. K. Agrawal, *Indian J. Chem., B* **43** (2004) 885
33. S. Kambe, K. Saito, A. Sakurai, T. Hayashi, *Synthesis* (1977) 841
34. K. Saito, S. Kambe, A. Sakurai, H. Midorikawa, *Synthesis* (1981) 211
35. P. Klan, V. Čírkva, in *Microwaves in Organic Synthesis*, A. Loupy, Ed., Wiley–VCH, Weinheim, 2002, pp. 463
36. C. O. Kappe, *Angew. Chem. Int. Ed.* **43** (2004) 6250
37. A. Marinkovic, *Ph.D. Thesis*, University of Belgrade, Belgrade, 2009 (in Serbian)
38. M. Saito, (Nippon Chemical Industries), JP 2012001521 (2012) [C.A.156/2012 122960].







SUPPLEMENTARY MATERIAL TO

**A microwave approach to the synthesis of certain 4-(substituted phenyl)-6-phenyl-3-cyano-2-pyridones**

ALEKSANDAR MARINKOVIĆ<sup>1</sup>, DUŠAN MIJIN<sup>1\*</sup>, JELENA MIRKOVIĆ<sup>1</sup>,  
VESELIN MASLAK<sup>2</sup> and C. OLIVER KAPPE<sup>3</sup>

<sup>1</sup>Faculty of Technology and Metallurgy, University of Belgrade, Karnegijeva 4, 11120 Belgrade, Serbia, <sup>2</sup>Faculty of Chemistry, University of Belgrade, Studentski trg 12–16, 11000 Belgrade, Serbia and <sup>3</sup>Christian Doppler Laboratory for Microwave Chemistry (CDLMC) and Institute of Chemistry, Karl-Franzens-University Graz, Heinrichstraße 28, A-8010 Graz, Austria

J. Serb. Chem. Soc. 79 (7) (2014) 759–765

MELTING POINTS AND SPECTRAL DATA OF THE SYNTHESIZED PYRIDONES

*3-Cyano-4,6-diphenyl-2-pyridone (1).* M.p. 312–314 °C (Lit. 312–314 °C<sup>1</sup>); FTIR (KBr, cm<sup>-1</sup>): 2200 (CN), 1640 (C=O); <sup>1</sup>H-NMR (200 MHz, DMSO-*d*<sub>6</sub>, δ / ppm): 6.84 (1H, *s*, C<sub>5</sub>-H), 7.49–7.62 (6H, *m*, Ar-H), 7.71–7.80 (2H, *m*, Ar-H), 7.88–7.93 (2H, *m*, Ar-H), 12.84 (1H, *s*, NH); UV–Vis (EtOH) (λ<sub>max</sub> / nm): 363.

*3-Cyano-4-(4-methylphenyl)-6-phenyl-2-pyridone (2).* M.p. 302–304 °C (Lit. 302–304 °C<sup>1</sup>); FTIR (KBr, cm<sup>-1</sup>): 2217 (CN), 1642 (C=O); <sup>1</sup>H-NMR (200 MHz, DMSO-*d*<sub>6</sub>, δ / ppm): 2.39 (3H, *s*, CH<sub>3</sub>), 6.78 (1H, *s*, C<sub>5</sub>-H), 7.37 (2H, *d*, *J* = 8.0 Hz, Ar-H), 7.50–7.56 (3H, *m*, Ar-H), 7.65 (2H, *d*, *J* = 8.0 Hz, Ar-H), 7.87–7.92 (2H, *m*, Ar-H), 12.82 (1H, *s*, NH); UV–Vis (EtOH) (λ<sub>max</sub> / nm): 366.

*3-Cyano-4-(4-methoxyphenyl)-6-phenyl-2-pyridone (3).* M.p. 305–306 °C (Lit. 305–306 °C<sup>1</sup>); FTIR (KBr, cm<sup>-1</sup>): 2222 (CN), 1651 (C=O); <sup>1</sup>H-NMR (200 MHz, DMSO-*d*<sub>6</sub>, δ / ppm): 3.85 (3H, *s*, OCH<sub>3</sub>), 6.80 (1H, *s*, C<sub>5</sub>-H), 7.13 (2H, *d*, *J* = 8.6 Hz, Ar-H), 7.45–7.56 (3H, *m*, Ar-H), 7.75 (2H, *d*, *J* = 8.8 Hz, Ar-H), 7.79–7.92 (2H, *m*, Ar-H), 12.73 (1H, *s*, NH); UV–Vis (EtOH) (λ<sub>max</sub> / nm): 343.

*4-(4-Chlorophenyl)-3-cyano-6-phenyl-2-pyridone (4).* M.p. 308–310 °C (Lit. 308–310 °C<sup>1</sup>); FTIR (KBr, cm<sup>-1</sup>): 2218 (CN), 1643 (C=O); <sup>1</sup>H-NMR (200 MHz, DMSO-*d*<sub>6</sub>, δ / ppm): 6.85 (1H, *s*, C<sub>5</sub>-H), 7.49–7.62 (3H, *m*, Ar-H), 7.64 (2H, *d*, *J* = 9.0 Hz, Ar-H), 7.77 (2H, *d*, *J* = 8.8 Hz, Ar-H), 7.82–7.93 (2H, *m*, Ar-H), 12.90 (1H, *s*, NH); UV–Vis (EtOH) (λ<sub>max</sub> / nm): 367.

\*Corresponding author. E-mail: kavur@tmf.bg.ac.rs

*3-Cyano-4-(4-nitrophenyl)-6-phenyl-2-pyridone (5).* M.p. >330 °C (Lit. >330 °C<sup>2</sup>); FTIR (KBr, cm<sup>-1</sup>): 2195 (CN), 1547 (C=O); <sup>1</sup>H-NMR (200 MHz, DMSO-*d*<sub>6</sub>, δ / ppm): 6.95 (1H, *s*, C<sub>5</sub>-H), 7.40–7.48 (3H, *m*, Ar-H), 7.89 (2H, *d*, *J* = 8.8 Hz, Ar-H), 8.03–8.08 (2H, *m*, Ar-H), 8.35 (2H, *d*, *J* = 8.8 Hz, Ar-H), 13.02 (1H, *s*, NH); UV–Vis (EtOH) (λ<sub>max</sub> / nm): 377.

*4-(4-Bromophenyl)-3-cyano-6-phenyl-2-pyridone (6).* M.p. 327–328 °C (Lit. 327–328 °C<sup>2</sup>); FTIR (KBr, cm<sup>-1</sup>): 2218 (CN), 1644 (C=O); <sup>1</sup>H-NMR (200 MHz, DMSO-*d*<sub>6</sub>, δ / ppm): 6.85 (1H, *s*, C<sub>5</sub>-H), 7.49–7.57 (3H, *m*, Ar-H), 7.70 (2H, *d*, *J* = 9.0 Hz, Ar-H), 7.79 (2H, *d*, *J* = 8.8 Hz, Ar-H), 7.88–7.93 (2H, *m*, Ar-H), 12.88 (1H, *s*, NH); UV–Vis (EtOH) (λ<sub>max</sub> / nm): 368.

*3-Cyano-4-(3-nitrophenyl)-6-phenyl-2-pyridone (7).*<sup>3</sup> M.p. >330 °C; FTIR (KBr, cm<sup>-1</sup>): 2221 (CN), 1652 (C=O); <sup>1</sup>H-NMR (200 MHz, DMSO-*d*<sub>6</sub>, δ / ppm): 7.01 (1H, *s*, C<sub>5</sub>-H), 7.50–7.63 (3H, *m*, Ar-H), 7.85–7.96 (3H, *m*, Ar-H), 8.21 (1H, *d*, *J* = 8.2 Hz, Ar-H), 8.42 (1H, *d*, *J* = 8.2 Hz, Ar-H), 8.58 (1H, *s*, Ar-H) 12.99 (1H, *s*, NH); UV–Vis (EtOH) (λ<sub>max</sub> / nm): 371.

*4-(3-Chlorophenyl)-3-cyano-6-phenyl-2-pyridone (8).*<sup>3</sup> M.p. 253–255 °C; FTIR (KBr, cm<sup>-1</sup>): 2221 (CN), 1652 (C=O); <sup>1</sup>H-NMR (200 MHz, DMSO-*d*<sub>6</sub>, δ / ppm): 6.89 (1H, *s*, C<sub>5</sub>-H), 7.49–7.75 (6H, *m*, Ar-H), 7.84 (1H, *s*, Ar-H), 7.91–7.96 (2H, *m*, Ar-H), 12.93 (1H, *s*, NH), UV–Vis (EtOH) (λ<sub>max</sub> / nm): 366.

*3-Cyano-4-(2-Nitrophenyl)-6-phenyl-2-pyridone (9).* M.p. 275–277 °C (Lit. 275–277 °C<sup>2</sup>); FTIR (KBr, cm<sup>-1</sup>): 2217 (CN), 1649 (C=O); <sup>1</sup>H-NMR (200 MHz, DMSO-*d*<sub>6</sub>, δ / ppm): 6.94 (1H, *s*, C<sub>5</sub>-H), 7.49–7.58 (2H, *m*, Ar-H), 7.74 (1H, *d*, *J* = 8.2 Hz, Ar-H), 7.80–8.01 (5H, *m*, Ar-H), 8.32 (1H, *d*, *J* = 8.0 Hz, Ar-H), 13.01 (1H, *s*, NH); UV–Vis (EtOH) (λ<sub>max</sub> / nm): 368.

#### REFERENCES

1. L. Range, H. Han, H. Jong, D. Shi, S. Tu, *Synth. Commun.* **38** (2008) 217
2. A. Marinković, A. Perić-Grujić, B. Jovanović, N. Ilić, M. Neveščanin, *Rapid. Commun. Mass Spectrom.* **20** (2006) 2630
3. A. D. Marinković, B. Ž. Jovanović, N. Todorović, I. O. Juranić, *J. Mol. Struct.* **920** (2009) 90.



## Substituted proline derivatives as organocatalysts in the Michael reaction

PREDRAG JOVANOVIĆ<sup>1</sup>, JELENA RANDELOVIĆ<sup>1</sup>, BRANKA IVKOVIĆ<sup>2</sup>,  
CRISTINA SUTEU<sup>3</sup>, ZORANA TOKIĆ VUJOŠEVIĆ<sup>1</sup> and VLADIMIR SAVIĆ<sup>1\*\*#</sup>

<sup>1</sup>Department of Organic Chemistry, Faculty of Pharmacy, University of Belgrade, Vojvode Stepe 450, 11000 Belgrade, Serbia, <sup>2</sup>Department of Pharmaceutical Chemistry, Faculty of Pharmacy, University of Belgrade, Vojvode Stepe 450, 11000 Belgrade, Serbia and <sup>3</sup>Chiral Technologies Europe, Illkirch, Bd Gonthier d'Andernach, 67400, Illkirch, France

(Received 15 October, accepted 30 December 2013)

**Abstract:** Chiral, polysubstituted proline esters, obtained *via* cycloaddition reactions of azomethine ylides, were studied as organocatalysts in the Michael reaction of aldehydes/ketones and vinylsulphones. Under optimised reaction conditions employing 10 mol % of the catalyst in wet CH<sub>2</sub>Cl<sub>2</sub>, the yields of the products were generally good while the enantioselectivity varied, reaching up to 52 %.

**Keywords:** Michael reaction; organocatalysis; proline derivatives.

### INTRODUCTION

Proline derived compounds have been extensively utilized in organocatalytic processes and have found wide application in many synthetically useful transformations.<sup>1</sup> Various derivatives, exemplified by the structures in Fig. 1, were synthesised and used with high degrees of chemical and stereochemical efficiency.

Proline compounds have most frequently been employed in organocatalytic transformations involving aldehydes and ketones activating them *via* two general modes, enamine or iminium ion formation. While the enamine formation is usually involved in the  $\alpha$ -functionalisation of aldehydes/ketones, the iminium ion is implicated in nucleophilic additions on  $\alpha,\beta$ -unsaturated aldehydes/ketones and related reactions.<sup>2</sup> Even though many organocatalysts of this structure are known, most of them are obtained *via* transformations of the carboxylic group of the parent molecule, while very few examples possess further substituents attached to the ring carbons.

\* Corresponding author. E-mail: vladimir.savic@pharmacy.bg.ac.rs

# Serbian Chemical Society member.

doi: 10.2298/JSC131015002J

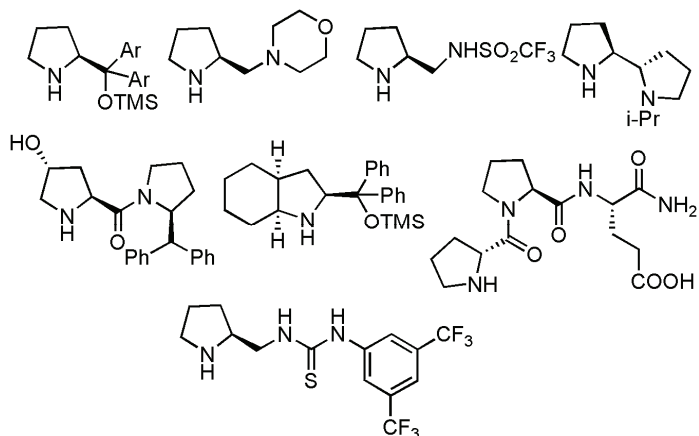


Fig. 1. Proline-derived catalysts.

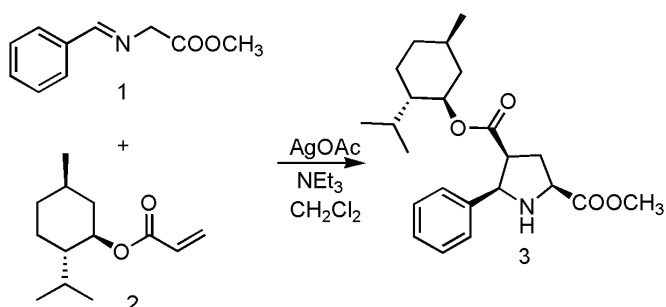
Our work in this area was initiated with the aim of investigating the effect of additional substituents on the organocatalytic efficiency of proline-derived compounds. It was hoped that a range of substituted prolines would be accessible in a straightforward manner *via* highly stereoselective 1,3-dipolar cycloaddition reactions of azomethine ylides.<sup>3</sup> This mild methodology has been extensively investigated in recent decades and a variety of processes employing either chiral auxiliaries or chiral Lewis acids were developed for the stereoselective synthesis of proline derivatives.<sup>4</sup> The substitution pattern of the proline product can be controlled by structural variations of the reacting imine (1,3-dipole) and alkene (dipolarophile).

#### RESULTS AND DISCUSSION

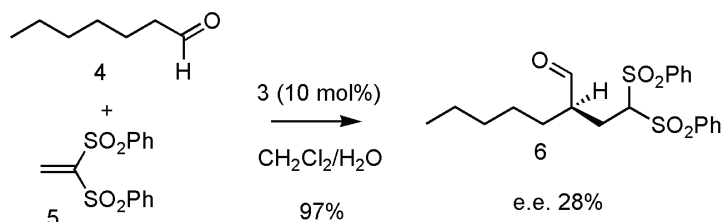
In an initial study and synthesis of substituted proline derivatives, the chiral auxiliary approach using menthyl acrylate was exploited, as outlined in Scheme 1.<sup>5</sup> Thus, the cycloaddition of imine **1** and (–)-menthyl acrylate **2** in the presence of AgOAc afforded the proline derivative **3** as a single diastereomer in 42 % yield. The Ag-catalysed 1,3-dipolar cycloadditions of aminoester derived imines are known to produce all-*cis* prolines and this structural feature was envisaged to be beneficial for organocatalytic processes involving these compounds, due to one face of the pyrrolidine skeleton being better shielded.

Proline ester **3** (10 mol %) was used as a catalyst for the Michael reaction of aldehyde **4** and vinyl sulphone **5**.<sup>6</sup> The reaction was realised in CH<sub>2</sub>Cl<sub>2</sub> saturated with H<sub>2</sub>O at room temperature. The presence of H<sub>2</sub>O proved to be essential and significantly improved the reaction yield (97 *versus* 28 %). Unfortunately, although the product was isolated almost quantitatively, the observed *e.e.* was rather low (28 %), Scheme 2. The absolute stereochemistry of the product was

determined by comparison of the observed and the literature values of  $[\alpha]_D$  for compound **6**.<sup>7</sup>



Scheme 1. Synthesis of catalyst **3**.



Scheme 2. Michael reaction catalysed by proline derivative **3**.

In order to explore the general potential of proline ester **3** as an organocatalyst, a series of reactions were performed using various aldehydes and ketones in place of **4** under the conditions described above, Table I.

The majority of aldehydes (entries a–h, Table I) afforded the products in excellent yields, but with low enantioselectivity. Ketones (entries i–k, Table I) furnished the Michael addition products, generally, in lower yields than the aldehydes but with marginally better stereoselectivity, except in the case of cyclohexanone (entry i, Table I).

With the aim of improving these initial results, the synthesis of a range of related proline catalysts was instigated. The initial focus was on the proline C(5)-substituent originating from the imine, a dipole precursor in the cycloaddition reactions of azomethine ylides. Compounds **17–25** were prepared using  $\text{Ag}^+$ -catalysed, 1,3-dipolar cycloadditions as outlined in Scheme 1 (Fig. 2). While the two esters at C(2) and C(4) were kept constant, the substituent at C(5) was varied, except in the case of the proline derivative **21**, which possessed an additional substituent at C(2).

Replacing catalyst **3** in the reaction outlined in Scheme 2 with the proline derivative **17** (entry a, Table II) resulted in a slight improvement of enantioselectivity. The introduction of an *ortho* substituent on the C(5) phenyl (entries b, c and

TABLE I. Variation of the aldehydes/ketones

Entry	Aldehyde/ketone	Product	Cmpd.	Yield/e.e., % <sup>a,b</sup>
a			<b>6</b>	97/28 ( <i>R</i> ) <sup>c</sup>
b			<b>7</b>	99/28
c			<b>8</b>	70/20
d			<b>9</b>	99/22
e			<b>10</b>	98/24
f			<b>11</b>	99/12
g			<b>12</b>	98/18
h			<b>13</b>	77/32
i			<b>14</b>	42/11( <i>S</i> ) <sup>c</sup>
j			<b>15</b>	56/33
k			<b>16</b>	51/44

<sup>a</sup>Isolated yields after column chromatography; <sup>b</sup>e.e. was determined by chiral HPLC (see experimental); <sup>c</sup>the configuration was determined by comparison of  $[\alpha]_D$  with literature results

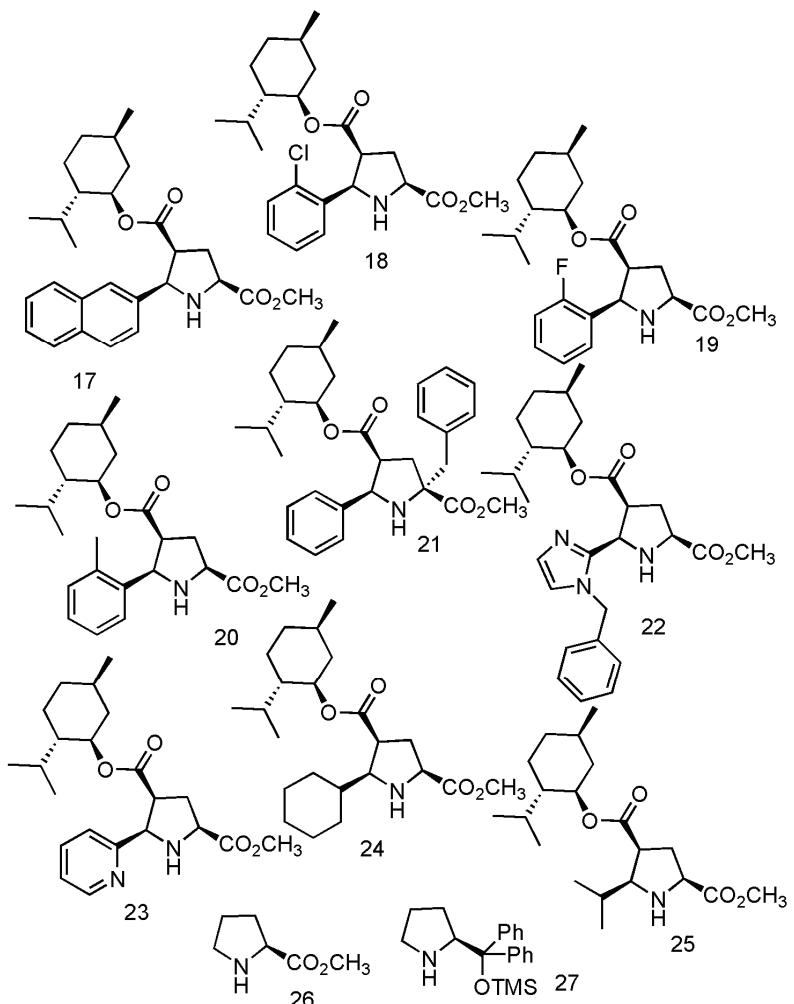


Fig. 2. Variations of the C(5) substituent.

d, Table II) lowered the *e.e.* A similar effect was observed with the catalyst **21** possessing an additional substituent at C(2) (entry e, Table II). An increased steric demand resulted not only in a depleted *e.e.*, but also in a lower chemical yield of the product. The presence of a C(5)-heterocyclic substituent (entries f and g, Table II) did not result in any significant improvement in the enantioselectivity. Compounds possessing an aliphatic substituent at C(5) (entries h and i, Table II) were also briefly tested. They proved to be slightly more efficient, with the isopropyl derived **25** affording the Michael adduct in almost quantitative yield and 42 % *e.e.* Contrary to the other organocatalysts, prolines **24** and **25**, possessing an aliphatic substituent at C(5), afforded product **6** with the *S* con-

figuration.<sup>7</sup> For comparison, the reaction described in Scheme 2 was performed employing proline ester **26** (entry j, Table II) and commercially available **27** (entry k, Table II). While the majority of substituted proline derivatives proved to be more efficient than the parent ester **26**, catalyst **27** showed a significantly better enantioselectivity than the synthesised prolines.

TABLE II. Michael reaction with catalysts **17–27** and product **6**

Entry	Catalyst	Yield, % <sup>a</sup>	e.e., % <sup>b</sup>
a	<b>17</b>	99	38 ( <i>R</i> )
b	<b>18</b>	99	1
c	<b>19</b>	99	10 ( <i>R</i> )
d	<b>20</b>	97	10 ( <i>R</i> )
e	<b>21</b>	24	22 ( <i>R</i> )
f	<b>22</b>	99	10 ( <i>R</i> )
g	<b>23</b>	99	34 ( <i>R</i> )
h	<b>24</b>	70	34 ( <i>S</i> )
i	<b>25</b>	93	42 ( <i>S</i> )
j	<b>26</b>	99	10 ( <i>R</i> )
k	<b>27</b>	77	78 ( <i>R</i> )

<sup>a</sup>Isolated yields after column chromatography; <sup>b</sup>e.e. was determined by chiral HPLC (see experimental)

Further attempts were made to modify the C(2) ester functionality in order to explore the effect of this substituent on the stereoselectivity. Compounds **28–31** (Fig. 3) were synthesised and used as organocatalysts replacing **3** in the reaction outlined in Scheme 2.

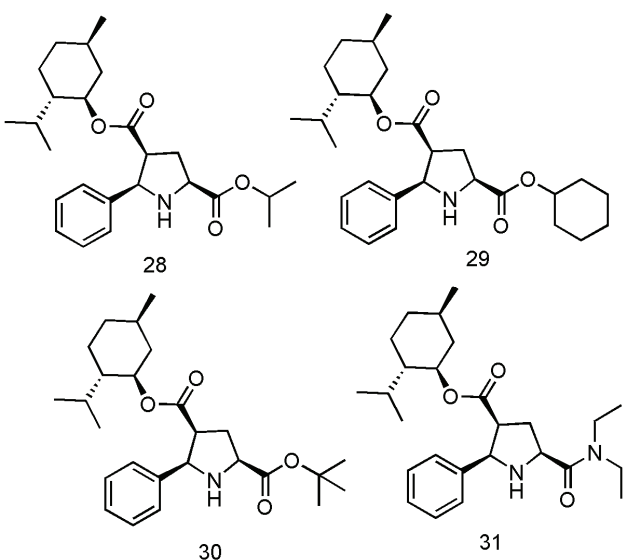


Figure 3. Variations of the C(2) substituent.

Substituting the methyl ester with isopropyl (compound **28**) influenced the stereoselectivity, increasing *e.e.* to 42 % (entry a, Table III). Extension of the ester *via* the introduction of the cyclohexyl moiety (compound **29**) in place of the isopropyl moiety maintained the *e.e.* on the same level (entry b, Table III). This result suggested that substituents at the C-atoms not directly bonded to the ester oxygen would not influence the reaction pathway significantly. Therefore the *t*-butyl derivative **30** was synthesised and employed to furnish product **6** in 52 % *e.e.* (entry c, Table III). Finally, catalyst **31** with a C(2)-amide functionality was briefly studied but the observed *e.e.* (entry d, Table III) was in the range of that obtained with the *t*-butyl compound **30** (entry c, Table III).

TABLE III. Michael reaction with catalysts **28–31** and product **6**

Entry	Catalyst	Yield, % <sup>a</sup>	<i>e.e.</i> , % <sup>b</sup>
a	<b>28</b>	93	42 ( <i>R</i> )
b	<b>29</b>	92	41 ( <i>R</i> )
c	<b>30</b>	97	52 ( <i>R</i> )
d	<b>31</b>	93	47 ( <i>R</i> )

<sup>a</sup>Isolated yields after column chromatography; <sup>b</sup>*e.e.* was determined by chiral HPLC (see experimental)

Although the observed results at this point were not of synthetic significance, attempts were made to rationalise them, in the hope of obtaining some directions for further, rational optimisation of the catalyst properties. In organocatalytic reactions of aldehydes/ketones promoted by secondary amines, such as the one outlined in Scheme 2, the first step is the formation of the enamine. Often, the formed enamino moiety is not planar, with the N-atom being significantly pyramidalized.<sup>8</sup> This places the N-lone pair pseudo-axially, although its localization may depend on steric repulsion between the pseudo-equatorial *N*-substituent and the neighbouring C(2)/C(5) substituents. The intermediate *trans*-**32**, formed in the reaction outlined in Scheme 2, may exist in two forms, **32a** (*s-trans*, related to the C(2)-ester) and **32b** (*s-cis*, related to the C(2)-ester), Fig. 4. Assuming that in both cases the top face of the enamine is better shielded due to the orientation of the pyrrolidine substituents, it is reasonable to expect that the **32a/32b** equilibrium has an influence on the reaction stereoselectivity. The energy difference between the two was calculated using computational methods. Two rotamers, **32a** and **32b**, were optimized using DFT with B3LYP hybrid functional and the def2-SVP basis set, in vacuum and the difference in their stability was calculated.<sup>9</sup> The calculated energy difference between **32a** and **32b** was not significant ( $\Delta E = -0.25$  kJ/mol), favouring slightly rotamer **28b**. For comparison,  $\Delta E$  for the pair **33a/33b**, obtained for the more efficient pyrrolidine catalyst **27**, suggested a noteworthy difference between the two. The slightly better efficiency of the pyrrolidines **28–31** (Table II) that have bulky ester moieties, which are likely to influence the ratio of two rotamers, may suggest that the

equilibrium is, at least, one of the factors contributing to the observed stereo-selectivity. A further study of these polysubstituted prolines is on-going.

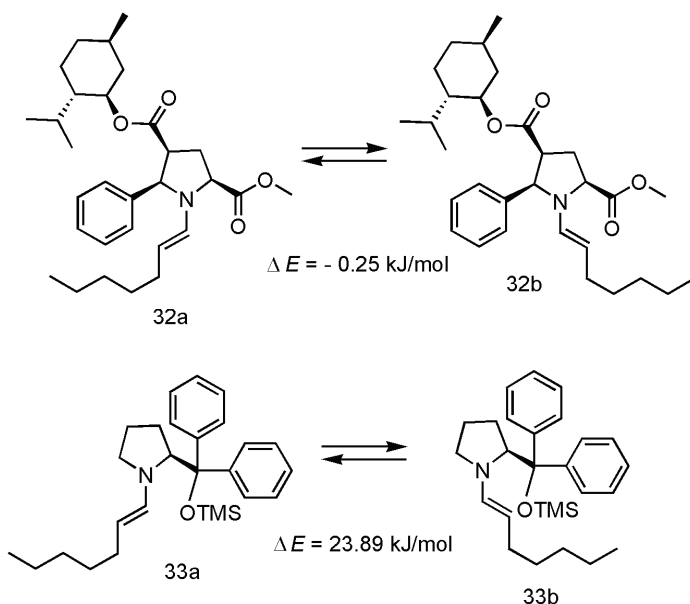


Fig. 4. The enamine equilibrium.

## EXPERIMENTAL

The NMR spectra were recorded on a Bruker Avance III (500 MHz) or a Varian Gemini 2000 (200 MHz) spectrometer. The chemical shifts are given in parts per million ( $\delta$ ) downfield from tetramethylsilane as the internal standard, Deuterochloroform or DMSO- $d_6$  were used as solvents. The mass spectral data were recorded using an Agilent MSD TOF spectrometer coupled with Agilent 1200 HPLC or an Agilent Technologies 5975C MS coupled with Agilent Technologies 6890N GC. The IR spectra were recorded on an IR Thermo Scientific NICOLET iS10 (4950) spectrometer. Silica gel 60 (230–400 mesh was employed for the flash chromatography while thin layer chromatography was realised using alumina plates with 0.25 mm silica layer (Kieselgel 60 F<sub>254</sub>, Merck). The solvents were purified by distillation before use. The enantiomeric excess was determined by HPLC using a CHIRALPAK IA column. Compounds **3**, **17** and **21** were synthesised according to the literature procedures.<sup>10,11</sup>

### *General procedure for the cycloaddition reactions*

A mixture of the imine (1 eq.), triethylamine (0.25 eq.), (−)-menthyl acrylate (1.1 eq.) and AgOAc (0.5 eq.) in dry CH<sub>2</sub>Cl<sub>2</sub> was stirred under nitrogen atmosphere for 48 h at room temperature. After solvent evaporation, the residue was purified by flash column chromatography (SiO<sub>2</sub>). No attempts were made to optimise the reaction conditions.

(2*S*,4*S*,5*R*)-4-[(*1R*,2*S*,5*R*)-2-Isopropyl-5-methylcyclohexyl]-2-methyl 5-(2-chlorophenyl)pyrrolidine-2,4-dicarboxylate (**18**). Flash chromatography (SiO<sub>2</sub>, 1:1 V/V petroleum ether–diethyl ether) afforded the product as a colourless oil in 24 % yield.

(2S,4S,5R)-4-[(1R,2S,5R)-2-*Isopropyl*-5-methylcyclohexyl]-2-methyl 5-(2-fluorophenyl)pyrrolidine-2,4-dicarboxylate (**19**). Flash chromatography (SiO<sub>2</sub>, 1:1V/V petroleum ether–diethyl ether) afforded the product as a white solid (m.p. 82–83 °C) in 32 % yield.

(2S,4S,5R)-4-[(1R,2S,5R)-2-*Isopropyl*-5-methylcyclohexyl]-2-methyl 5-*o*-tolylpyrrolidine-2,4-dicarboxylate (**20**). Flash chromatography (SiO<sub>2</sub>, 1:1V/V petroleum ether–diethyl ether) afforded the product as a white solid (m.p. 66–67 °C) in 31 % yield.

(2S,4S,5R)-4-[(1R,2S,5R)-2-*Isopropyl*-5-methylcyclohexyl]-2-methyl 5-(1-benzyl-1*H*-imidazol-2-yl)pyrrolidine-2,4-dicarboxylate (**22**). Flash chromatography (SiO<sub>2</sub>, EtOAc) afforded the product as a yellow oil in 29 % yield.

(2S,4S,5R)-4-[(1R,2S,5R)-2-*Isopropyl*-5-methylcyclohexyl]-2-methyl 5-(pyridin-2-yl)pyrrolidine-2,4-dicarboxylate (**23**). Flash chromatography (SiO<sub>2</sub>, EtOAc) afforded the product as a white solid (m.p. 104–105 °C) in 38 % yield.

(2S,4S,5S)-4-[(1R,2S,5R)-2-*Isopropyl*-5-methylcyclohexyl]-2-methyl 5-cyclohexylpyrrolidine-2,4-dicarboxylate (**24**). Flash chromatography (SiO<sub>2</sub>, 1:1V/V petroleum ether–diethyl ether) afforded the product as a white solid (m.p. 106–107 °C) in 33 % yield.

(2S,4S,5S)-4-[(1R,2S,5R)-2-*Isopropyl*-5-methylcyclohexyl]-2-methyl 5-*isopropyl*pyrrolidine-2,4-dicarboxylate (**25**). Flash chromatography (SiO<sub>2</sub>, diethyl ether) afforded the product as a white amorphous solid (m.p. 51–53 °C) in 20 % yield.

(2S,4S,5R)-2-*Isopropyl*-4-[(1R,2S,5R)-2-*isopropyl*-5-methylcyclohexyl] 5-phenylpyrrolidine-2,4-dicarboxylate (**28**). Flash chromatography (SiO<sub>2</sub>, 1:1V/V petroleum ether–diethyl ether) afforded the product as a white solid (m.p. 124–126 °C) in 24 % yield.

(2S,4S,5R)-2-Cyclohexyl-4-[(1R,2S,5R)-2-*isopropyl* 5-methylcyclohexyl] 5-phenylpyrrolidine-2,4-dicarboxylate (**29**). Flash chromatography (SiO<sub>2</sub>, 1:1V/V petroleum ether–diethyl ether) afforded the product as a white solid (m.p. 126–127 °C) in 54 % yield.

(2S,4S,5R)-2-tert-Butyl-4-[(1R,2S,5R)-2-*isopropyl* 5-methylcyclohexyl] 5-phenylpyrrolidine-2,4-dicarboxylate (**30**). Flash chromatography (SiO<sub>2</sub>, 1:1V/V petroleum ether–diethyl ether) afforded the product as a white solid (m.p. 134–135 °C) in 24 % yield.

(2R,3S,5S)-[(1R,2S,5R)-2-*Isopropyl*-5-methylcyclohexyl] 5-(N,N-diethylcarbamoyl)-2-phenylpyrrolidine-3-carboxylate (**31**). Flash chromatography (SiO<sub>2</sub>, EtOAc) afforded the product as a yellow amorphous solid (m.p. 103–104 °C) in 29 % yield.

The spectroscopic data for the cycloaddition products **18–31** are given in the Supplementary material to this paper.

*General procedure for catalytic conjugate addition of aldehydes to 1,1-bis(phenylsulphonyl)ethylene*

To a mixture of catalyst (2 mg, 0.005 mmol) and 1,1-bis(phenylsulphonyl)ethylene (15 mg, 0.05 mmol) in 1.0 mL of CH<sub>2</sub>Cl<sub>2</sub> (saturated with H<sub>2</sub>O) was added the corresponding aldehyde (0.15 mmol) and the mixture was stirred for 2 h at room temperature. After solvent evaporation, the residue was purified by flash column chromatography (SiO<sub>2</sub>).

(R)-2-[2,2-Bis(phenylsulphonyl)ethyl]heptanal<sup>7</sup> (**6**). Flash chromatography (SiO<sub>2</sub>, 1:1 V/V petroleum ether–diethyl ether) afforded the product as a white amorphous solid (m.p. 86–87 °C) in 97 % yield. The enantiomeric excess was determined by HPLC with a CHIRALPAK IA column at 210 nm (heptane/i-PrOH in the ratio of 70/30, flow rate = 1.0 mL min<sup>-1</sup>, *t*<sub>r</sub> (minor) = 9.48 min, *t*<sub>r</sub> (major) = 11.28 min), *e.e.* 53 %.

(R)-2-[2,2-Bis(phenylsulphonyl)ethyl]hexanal<sup>7</sup> (**7**). Flash chromatography (SiO<sub>2</sub>, 1:1 V/V petroleum ether–diethyl ether) afforded the product as a white amorphous solid (m.p. 60–62 °C) in 99 % yield. The enantiomeric excess was determined by HPLC with a CHIRALPAK

IA column at 230 nm (heptane/*i*-PrOH in the ratio of 70/30, flow rate = 1.0 mL min<sup>-1</sup>, *t*<sub>r</sub> (minor) = 9.23 min, *t*<sub>r</sub> (major) = 10.55 min), *e.e.* 28 %.

(R)-2-[2,2-Bis(phenylsulphonyl)ethyl]dodecanal (**8**). Flash chromatography (SiO<sub>2</sub>, 1:1 V/V petroleum ether–diethyl ether) afforded the product as a colourless oil in 70 % yield. The enantiomeric excess was determined by HPLC with a CHIRALPAK IA column at 230 nm (heptane/*i*-PrOH in the ratio of 70/30, flow rate = 1.0 mL min<sup>-1</sup>, *t*<sub>r</sub> (minor) = 7.43 min, *t*<sub>r</sub> (major) = 8.68 min), *e.e.* 20 %.

(R)-2-Benzyl-4,4-bis(phenylsulphonyl)butanal<sup>7</sup> (**9**). Flash chromatography (SiO<sub>2</sub>, 1:1 V/V petroleum ether–diethyl ether) afforded the product as a white amorphous solid (m.p. 80–81 °C) in 99 % yield. The enantiomeric excess was determined by HPLC with a CHIRALPAK IA column at 230 nm (heptane/*i*-PrOH in the ratio of 70/30, flow rate = 1.0 mL min<sup>-1</sup>, *t*<sub>r</sub> (minor) = 14.07 min, *t*<sub>r</sub> (major) = 15.87 min), *e.e.* 22 %.

(R)-2-(4-Methoxybenzyl)-4,4-bis(phenylsulphonyl)butanal (**10**). Flash chromatography (SiO<sub>2</sub>, 4:6 V/V petroleum ether–diethyl ether) afforded the product as a white amorphous solid (m.p. 95–96 °C) in 98 % yield. The enantiomeric excess was determined by HPLC with a CHIRALPAK IA column at 230 nm (heptane/*i*-PrOH in the ratio of 70/30, flow rate = 1.0 mL min<sup>-1</sup>, *t*<sub>r</sub> (minor) = 15.08 min, *t*<sub>r</sub> (major) = 17.85 min), *e.e.* 24 %.

(R)-2-[(Naphthalen-1-yl)methyl]-4,4-bis(phenylsulphonyl)butanal (**11**). Flash chromatography (SiO<sub>2</sub>, 4:6 V/V petroleum ether–diethyl ether) afforded the product as a yellow amorphous solid (m.p. 120–121 °C) in 99 % yield. The enantiomeric excess was determined by HPLC with a CHIRALPAK IA column at 230 nm (heptane/*i*-PrOH in the ratio of 70/30, flow rate = 1.0 mL min<sup>-1</sup>, *t*<sub>r</sub> (minor) = 15.95 min, *t*<sub>r</sub> (major) = 20.21 min), *e.e.* 12 %.

(R)-2-(3,4-Dichlorobenzyl)-4,4-bis(phenylsulphonyl)butanal (**12**). Flash chromatography (SiO<sub>2</sub>, 4:6 V/V petroleum ether–diethyl ether) afforded the product as a colourless oil in 98 % yield. The enantiomeric excess was determined by HPLC with a CHIRALPAK IA column at 210 nm (heptane/*i*-PrOH in the ratio of 70/30, flow rate = 1.0 mL min<sup>-1</sup>, *t*<sub>r</sub> (minor) = 16.99 min, *t*<sub>r</sub> (major) = 22.095 min), *e.e.* 18 %.

(R)-2-(4-Fluorobenzyl)-4,4-bis(phenylsulphonyl)butanal (**13**). Flash chromatography (SiO<sub>2</sub>, 4:6 V/V petroleum ether–diethyl ether) afforded the product as a colourless oil in 77 % yield. The enantiomeric excess was determined by HPLC with a CHIRALPAK IA column at 210 nm (heptane/*i*-PrOH in the ratio of 70/30, flow rate = 1.0 mL min<sup>-1</sup>, *t*<sub>r</sub> (minor) = 16.10 min, *t*<sub>r</sub> (major) = 17.93 min), *e.e.* 32 %.

The spectral data for the addition products **6–13** of aldehydes to 1,1-bis(phenylsulphonyl)ethylene are given in the Supplementary material to this paper.

#### General procedure for the catalytic conjugate addition of ketones to 1,1-bis(phenylsulphonyl)ethylene

To a mixture of catalyst (4 mg, 0.01 mmol) and 1,1-bis(phenylsulphonyl)ethylene (15 mg, 0.05 mmol) in 1.0 mL of CH<sub>2</sub>Cl<sub>2</sub> (saturated with H<sub>2</sub>O) was added the corresponding ketone (0.15 mmol) and the mixture was stirred for 18 h at room temperature. After solvent evaporation, the residue was purified by flash column chromatography (SiO<sub>2</sub>).

(S)-2-[2,2-Bis(phenylsulphonyl)ethyl]cyclohexanone<sup>12</sup> (**14**). Flash chromatography (SiO<sub>2</sub>, 1:1 V/V petroleum ether–diethyl ether) afforded the product as a white amorphous solid (m.p. 149–151 °C) in 42 % yield. The enantiomeric excess was determined by HPLC with a CHIRALPAK IA column at 210 nm (heptane/EtOH in the ratio of 70/30, flow rate = 1.0 mL min<sup>-1</sup>, *t*<sub>r</sub> (minor) = 24.15 min, *t*<sub>r</sub> (major) = 25.13 min), *e.e.* 11 %.

(S)-2-[2,2-Bis(phenylsulphonyl)ethyl]cyclopentanone (**15**). Flash chromatography (SiO<sub>2</sub>, 1:1 V/V petroleum ether–diethyl ether) afforded the product as a white amorphous solid (m.p.

110–112 °C) in 56 % yield. The enantiomeric excess was determined by HPLC with a CHIRALPAK IA column at 210 nm (heptane/i-PrOH in the ratio of 70/30, flow rate = 1.0 mL min<sup>-1</sup>, *t*<sub>r</sub> (minor) = 13.76 min, *t*<sub>r</sub> (major) = 16.29 min), *e.e.* 33 %.

(S)-4-Methyl-6,6-bis(phenylsulphonyl)hexan-3-one (**16**). Flash chromatography (SiO<sub>2</sub>, 1:1 V/V petroleum ether–diethyl ether) afforded the product as a colourless oil in 51 % yield. The enantiomeric excess was determined by HPLC with a CHIRALPAK IA column at 230 nm (heptane/i-PrOH in the ratio of 70/30, flow rate = 1.0 mL min<sup>-1</sup>, *t*<sub>r</sub> (minor) = 8.78 min, *t*<sub>r</sub> (major) = 9.36 min), *e.e.* 44%.

#### CONCLUSIONS

This initial study of substituted proline derivatives suggested that these compounds might have potential as organocatalysts but additional investigation is necessary to optimise their catalytic properties. As they are easily accessible *via* highly stereoselective cycloaddition reactions of azomethine ylides and potentially may be used in various organocatalytic transformations requiring secondary amines, they might be attractive molecules for additional investigation.

#### SUPPLEMENTARY MATERIAL

Spectroscopic data for the cycloaddition products **18–31** are available electronically from <http://www.shd.org.rs/JSCS/>, or from the corresponding author on request.

*Acknowledgments.* Financial support from the Ministry of Education, Science and Technological Development of the Republic of Serbia (Grant No. 172009) is greatly appreciated. We thank the Faculty of Pharmacy and Faculty of Chemistry, Belgrade University for their assistance. J. R. would like to thank the Ministry of Education, Science and Technological Development of the Republic of Serbia for a PhD scholarship. We would also like to thank Chiral Technologies Europe for their generous gift of the CHIRALPACK IA 250 HPLC column.

И З В О Д

#### СУПСТИТУИСАНИ ПРОЛИНСКИ ДЕРИВАТИ КАО ОРГАНОКАТАЛИЗATORИ У МАЈКЛОВОЈ РЕАКЦИЈИ

ПРЕДРАГ ЈОВАНОВИЋ<sup>1</sup>, ЈЕЛЕНА РАНЂЕЛОВИЋ<sup>1</sup>, БРАНКА ИВКОВИЋ<sup>2</sup>, CRISTINA SUTEU<sup>3</sup>,  
ЗОРАНА ТОКИЋ ВУЈОШЕВИЋ<sup>1</sup> и ВЛАДИМИР САВИЋ<sup>1</sup>

<sup>1</sup>Каћијера за органску хемију, Фармацеутски факултет, Универзитет у Београду, Војводе Степе 450,  
11000 Београд, <sup>2</sup>Каћијера за фармацеутску хемију, Фармацеутски факултет, Универзитет у  
Београду, Војводе Степе 450, 11000 Београд и <sup>3</sup>Chiral Technologies Europe, Illkirch, Bd Gonthier  
d'Andernach, 67400, Illkirch, France

Хирални, полисупституисани естри пролина, добијени циклоадиционим реакцијама азометинских илида, проучавани су као органокатализатори у Мајкловој реакцији алдехида/кетона и винил-сулфона. Под оптималним реакцијоним условима, у којима се користило 10 mol % катализатора у влажном метилен-хлориду приноси реакција су генерално били добри док је енантиоселективност варијала достижући 52 %.

(Примљено 15. октобра, прихваћено 30. децембра 2013)

## REFERENCES

- For recent reviews related to proline and proline derived organocatalysts, see: C. Bhanja, S. Jena, S. Nayak, S. Mohapatra, *Beilstein J. Org. Chem.* **8** (2012) 1668; H. Yang, R. G. Carter, *Synlett* (2010) 2827; M. Gruttaduria, F. Giacalone, R. Noto, *Chem. Soc. Rev.* **37** (2008) 1666; R. B. Sunoj, *Comp. Mol. Sci.* **1** (2011) 920; H. Kotsuki, H. Ikushima, A. Okuyama, *Heterocycles* **75** (2008) 757; M. J. Gaunt, C. C. C. Johansson, A. McNally, N. T. Vo, *Drug Discov. Today*, **12** (2007) 8; S. Mukherjee, J. W. Yang, S. Hoffmann, B. List, *Chem. Rev.* **107** (2007) 5471; H. Pellissier, *Tetrahedron* **63** (2007) 9267; W. Notze, F. Tanaka, C. F. Barbas, *Acc. Chem. Res.* **37** (2004) 580; C. Allemann, R. Gordillo, F. R. Clemente, P. H. Cheong, K. N. Houk, *Acc. Chem. Res.* **37** (2004) 558; B. List *Tetrahedron* **58** (2002) 5573
- S. Bertelsen, K. A. Jorgensen, *Chem. Soc. Rev.* **38** (2009) 2178
- For recent reviews on azomethine ylides, see: C. Najera, J. M. Sansano, *Monatsh. Chem.* **142** (2011) 659; J. Adrio, J. C. Carretero, *Chem. Commun.* **47** (2011) 6784; A. de Cozar, F. P. Cossio, *Phys. Chem. Chem. Phys.* **13** (2011) 10858; C. Najera, J. M. Sansano, *Org. Biomol. Chem.* **7** (2009) 4567; M. Alvarez-Corral, M. Munoz-Dorado, I. Rodriguez-Garcia, *Chem. Rev.* **108** (2008) 3174; H. Pellissier, *Tetrahedron* **63** (2007) 3235; V. Nair, T. D. Suja, *Tetrahedron* **63** (2007) 12247; G. Pandey, P. Banerjee, S. R. Gadre, *Chem. Rev.* **106** (2006) 4484; I. Coldham, R. Hufton, *Chem. Rev.* **105** (2005) 2765
- For recent work on stereoselective cycloadditions of azomethine ylides, see: F. Shi, G. Xing, W. Tan, R. Zhu, S. Tu, *Org. Biomol. Chem.* **11** (2013) 1482; Z. He, T. Liu, H. Tao, C. Wang, *Org. Lett.* **14** (2012) 6230; J. Hernandez-Toribio, S. Padilla, J. Adrio, J. C. Carretero, *Angew. Chem. Int. Ed.* **51** (2012) 8854; Q. Li, Z. Xue, H. Tao, C. Wang, *Tetrahedron Lett.* **53** (2012) 3650; K. Imae, T. Konno, K. Ogata, S. Fukuzawa, *Org. Lett.* **14** (2012) 4410; N. Fernandez, L. Carrillo, J. L. Vicario, D. Badia, E. Reyes, *Chem. Commun.* **47** (2011) 12313; J. Bai, L. Wang, L. Peng, Y. Guo, J. Ming, F. Wang, X. Xu, L. Wang, *Eur. J. Org. Chem.* (2011) 4472; T. Liu, Z. Xue, H. Tao, C. Wang, *Org. Biomol. Chem.* **9** (2011) 1980; M. Cheng, H. Wang, L. Gong, *Org. Lett.* **13** (2011) 2418; C. Zhang, S. Yu, X. Hu, D. Wang, Z. Zheng, *Org. Lett.* **12** (2010) 5542; T. Arai, N. Yokoyama, A. Mishiro, H. Sato, *Angew. Chem. Int. Ed.* **49** (2010) 7895; I. Oura, K. Shimizu, K. Ogata, S. Fukuzawa, *Org. Lett.* **12** (2010) 1752
- M. I. Calaza, C. Cativiela, *Eur. J. Org. Chem.* (2008) 3427; K. V. Gothelf, K. A. Jorgensen, *Chem. Rev.* **98** (1998) 863
- A. Quintard, A. Alexakis, *Org. Biomol. Chem.* **9** (2011) 1407; Q. Zhu, L. Cheng, Y. Lu, *Chem. Commun.* (2008) 6315; Q. Zhu, Y. Lu, *Org. Lett.* **11** (2009) 1721; S. Sulzer-Moss, A. Alexakis, J. Mareda, G. Bollot, G. Bernardinelli, Y. Filinchuk, *Chem. Eur. J.* **15** (2009) 3204
- Q. Zhu, Y. Lu, *Org. Lett.* **10** (2008) 4803
- D. Seebach, A. K. Beck, D. M. Badine, Michael Limbach, A. Eschenmoser, A. M. Treasurywala, R. Hobi, *Helv. Chim. Acta* **90** (2007) 425
- A. D. Becke, *J. Chem. Phys.* **98** (1993) 5648; C. Lee, W. Yang, R. G. Parr, *Phys. Rev. B* **37** (1988) 785; S. H. Vosko, L. Wilk, M. Nusair, *Can. J. Phys.* **58** (1980) 1200; F. Weigend, R. Alhrichs, *Phys. Chem. Chem. Phys.* **7** (2005) 3297
- D. A. Barr, M. J. Dorrrity, R. Grigg, *Tetrahedron* **51** (1995) 273
- L. N. Goswami, S. Srivastava, S. K. Panday, *Tetrahedron Lett.* **42** (2001) 7891
- Q. Zhu, L. Cheng, Y. Lu, *Chem. Commun.* **47** (2008) 6315.



SUPPLEMENTARY MATERIAL TO  
**Substituted proline derivatives as organocatalysts  
in the Michael reaction**

PREDRAG JOVANOVIĆ<sup>1</sup>, JELENA RANDELOVIĆ<sup>1</sup>, BRANKA IVKOVIĆ<sup>2</sup>,  
CRISTINA SUTEU<sup>3</sup>, ZORANA TOKIĆ VUJOŠEVIĆ<sup>1</sup> and VLADIMIR SAVIĆ<sup>1\*</sup>

<sup>1</sup>Department of Organic Chemistry, Faculty of Pharmacy, University of Belgrade, Vojvode Stepe 450, 11000 Belgrade, Serbia, <sup>2</sup>Department of Pharmaceutical Chemistry, Faculty of Pharmacy, University of Belgrade, Vojvode Stepe 450, 11000 Belgrade, Serbia and <sup>3</sup>Chiral Technologies Europe, Illkirch, Bd Gonthier d'Andernach, 67400, Illkirch, France

J. Serb. Chem. Soc. 79 (7) (2014) 767–778

SPECTROSCOPIC DATA FOR THE CYCLOADDITION PRODUCTS **18–31**

(2S,4S,5R)-4-[(1R,2S,5R)-2-Isopropyl-5-methylcyclohexyl]-2-methyl 5-(2-chlorophenyl)pyrrolidine-2,4-dicarboxylate (**18**). Yield: 24 %; Colourless oil; IR (KBr, cm<sup>-1</sup>): 2953, 1739, 1198, 1169; <sup>1</sup>H-NMR (500 MHz, CDCl<sub>3</sub>, δ / ppm) 7.52 (1H, *m*, phenyl-H), 7.33 (1H, *m*, phenyl-H), 7.25–7.17 (2H, *m*, phenyl-H), 4.74 (1H, *d*, *J* = 7.5 Hz, 5-H), 4.31–4.26 (1H, *m*, OCH), 3.95 (1H, *t*, *J* = 8.5 Hz, 2-H), 3.82 (3H, *s*, OCH<sub>3</sub>), 3.55 (1H, *m*, 4-H), 2.85 (1H, *bs*, NH), 2.52–2.40 (2H, *m*, 3-H), 1.70 (1H, *m*, menthyl-H), 1.53 (2H, *m*, menthyl-H), 1.14 (3H, *m*, menthyl-H), 0.91 (2H, *m*, menthyl-H), 0.82 (3H, *d*, *J* = 7 Hz, CH<sub>3</sub>), 0.68 and 0.65 (2×3H, 2×*d*, *J* = 6.5 Hz, CH(CH<sub>3</sub>)<sub>2</sub>), 0.03 (1H, *m*, menthyl-H); <sup>13</sup>C-NMR (125 MHz, CDCl<sub>3</sub>, δ / ppm) 173.39, 172.72, 136.20, 133.69, 129.18, 128.53, 127.77, 126.80, 74.09, 62.78, 59.34, 52.21, 46.47, 46.32, 39.31, 33.94, 33.89, 30.91, 26.15, 23.29, 21.70, 20.65, 16.32; HRMS (ESI, *m/z*): Calcd. for C<sub>23</sub>H<sub>32</sub>ClNO<sub>4</sub> (M+H)<sup>+</sup>: 422.20926. Found: 422.20957; specific rotation [α]<sub>D</sub> (CHCl<sub>3</sub>, *c* = 5.0 mg/mL): +39.

(2S,4S,5R)-4-[(1R,2S,5R)-2-Isopropyl-5-methylcyclohexyl]-2-methyl 5-(2-fluorophenyl)pyrrolidine-2,4-dicarboxylate (**19**). Yield 32 %; White solid; m.p.: 82–83 °C; IR (KBr, cm<sup>-1</sup>): 2954, 1740, 1199, 1169; <sup>1</sup>H-NMR (500 MHz, CDCl<sub>3</sub>, δ / ppm) 7.43 (1H, *m*, phenyl-H), 7.23 (1H, *m*, phenyl-H), 7.10 (1H, *m*, phenyl-H), 7.00 (1H, *m*, phenyl-H), 4.65 (1H, *d*, *J* = 7.5 Hz, 5-H), 4.35–4.29 (1H, *m*, OCH), 3.96 (1H, *t*, *J* = 8.5 Hz, 2-H), 3.82 (3H, *s*, OCH<sub>3</sub>), 3.40 (1H, *m*, 4-H), 2.83 (1H, *bs*, NH), 2.49 (1H, *m*, 3-H), 2.39 (1H, *m*, 3-H), 1.67 (1H, *m*, menthyl-H),

\*Corresponding author. E-mail: vladimir.savic@pharmacy.bg.ac.rs

1.54 (2H, *m*, menthyl-H), 1.16 (3H, *m*, menthyl-H), 0.88 (2H, *m*, menthyl-H), 0.82 (3H, *d*, *J* = 7 Hz, CH<sub>3</sub>), 0.69 and 0.63 (2×3H, 2×*d*, *J* = 6.5 Hz, CH(CH<sub>3</sub>)<sub>2</sub>), 0.08 (1H, *q*, *J* = 11.5 Hz, menthyl-H); <sup>13</sup>C-NMR (125 MHz, CDCl<sub>3</sub>, δ / ppm): 173.40, 172.76, 161.47, 159.51, 128.90, 127.54, 125.82, 124.07, 74.13, 59.79, 59.76, 52.23, 47.65, 46.44, 39.41, 34.24, 33.95, 30.93, 26.07, 23.22, 21.69, 20.66, 16.21. HRMS (ESI, *m/z*): Calcd. for C<sub>23</sub>H<sub>32</sub>FNO<sub>4</sub> (M+H)<sup>+</sup>: 406.23881. Found: 406.24055; specific rotation [α]<sub>D</sub> (CHCl<sub>3</sub>, *c* = 8.8 mg/mL): -1.8.

(2S,4S,5R)-4-[(1*R*,2*S*,5*R*)-2-Isopropyl-5-methylcyclohexyl]-2-methyl 5-o-tolylpyrrolidine-2,4-dicarboxylate (**20**). Yield: 31 %; White solid; m.p.: 66–67 °C; IR (KBr, cm<sup>-1</sup>): 2953, 1739, 1199, 1167; <sup>1</sup>H-NMR (500 MHz, CDCl<sub>3</sub>, δ / ppm): 7.40 (1H, *m*, phenyl-H), 7.16–7.08 (3H, *m*, phenyl-H), 4.57 (1H, *d*, *J* = 7.5 Hz, 5-H), 4.28–4.23 (1H, *m*, OCH), 3.91 (1H, *t*, *J* = 8.5 Hz, 2-H), 3.81 (3H, *s*, OCH<sub>3</sub>), 3.35 (1H, *m*, 4-H), 2.86 (1H, *bs*, NH), 2.46–2.42 (2H, *m*, 3-H), 2.36 (3H, *s*, Phe-CH<sub>3</sub>), 1.67 (1H, *m*, menthyl-H), 1.52 (2H, *m*, menthyl-H), 1.09 (3H, *m*, menthyl-H), 0.88 (2H, *m*, menthyl-H), 0.82 (3H, *d*, *J* = 7.5 Hz, CH<sub>3</sub>), 0.67 and 0.63 (2×3H, 2×*d*, *J* = 6.5 Hz, CH(CH<sub>3</sub>)<sub>2</sub>), 0.07 (1H, *q*, *J* = 11.0 Hz, menthyl-H); <sup>13</sup>C-NMR (125 MHz, CDCl<sub>3</sub>, δ / ppm): 173.34, 172.53, 136.48, 135.84, 129.98, 127.18, 125.93, 125.58, 73.97, 62.66, 59.49, 52.06, 46.76, 46.51, 38.98, 34.16, 33.89, 30.80, 26.08, 23.24, 21.57, 20.57, 19.60, 16.26; HRMS (ESI, *m/z*): Calcd. for C<sub>24</sub>H<sub>35</sub>NO<sub>4</sub> (M+H)<sup>+</sup>: 402.26389. Found: 402.26458; specific rotation [α]<sub>D</sub> (CHCl<sub>3</sub>, *c* = 1.0 mg/mL): +22.

(2S,4S,5R)-4-[(1*R*,2*S*,5*R*)-2-Isopropyl-5-methylcyclohexyl]-2-methyl 5-(1-benzyl-1*H*-imidazol-2-yl)pyrrolidine-2,4-dicarboxylate (**22**). Yield: 29 %; Yellow oil; IR (KBr, cm<sup>-1</sup>): 2952, 1723, 1203, 1168; <sup>1</sup>H-NMR (500 MHz, CDCl<sub>3</sub>, δ / ppm): 7.35–7.30 (3H, *m*), 7.15 (2H, *m*), 6.96 (1H, *m*), 6.79 (1H, *m*), 5.19 (2H, *s*), 4.51 (1H, *m*, OCH), 4.43 (1H, *d*, *J* = 7.5 Hz, 5-H), 3.87 (1H, *m*, 2-H), 3.75 (3H, *s*, OCH<sub>3</sub>), 3.19 (1H, *m*, 4-H), 2.63 (1H, *m*, 3-H), 2.41 (1H, *m*, 3-H), 1.73–1.59 (4H, *m*, menthyl-H), 1.38–1.17 (2H, *m*, menthyl-H), 0.97 (1H, *m*, menthyl-H), 0.86 and 0.82 (2×3H, 2×*d*, *J* = 6.5 Hz, CH(CH<sub>3</sub>)<sub>2</sub>), 0.76 (1H, *m*, menthyl-H), 0.67 (3H, *d*, *J* = 7 Hz, CH<sub>3</sub>), 0.43 (1H, *q*, *J* = 11.0 Hz, menthyl-H); <sup>13</sup>C-NMR (125 MHz, CDCl<sub>3</sub>, δ / ppm): 173.29, 171.42, 145.52, 136.23, 128.90, 127.97, 127.77, 126.91, 120.29, 74.27, 59.58, 57.26, 52.19, 49.56, 48.26, 46.81, 40.29, 34.13, 33.19, 31.07, 25.98, 23.27, 21.85, 20.74, 16.24; HRMS (ESI, *m/z*): Calcd. for C<sub>27</sub>H<sub>37</sub>N<sub>3</sub>O<sub>4</sub> (M+H)<sup>+</sup>: 468.28568. Found: 468.28442; specific rotation [α]<sub>D</sub> (CHCl<sub>3</sub>, *c* = 4.0 mg/mL): -18.

(2S,4S,5R)-4-[(1*R*,2*S*,5*R*)-2-Isopropyl-5-methylcyclohexyl]-2-methyl 5-(pyridin-2-yl)pyrrolidine-2,4-dicarboxylate (**23**). Yield: 38 %; White solid; m.p.: 104–105 °C; IR (KBr, cm<sup>-1</sup>): 2955, 1727, 1707, 1195, 1168; <sup>1</sup>H-NMR (500 MHz, CDCl<sub>3</sub>, δ / ppm) 8.59 (1H, *m*, Py-H), 8.49 (1H, *m*, Py-H), 7.75 (1H, *m*, Py-H), 7.25 (1H, *m*, Py-H), 4.54 (1H, *d*, *J* = 8.0 Hz, 5-H), 4.37–4.32 (1H, *m*, OCH), 3.99 (1H, *t*, *J* = 8.5 Hz, 2-H), 3.82 (3H, *s*, OCH<sub>3</sub>), 3.37 (1H, *m*, 4-H), 2.52–2.38 (2H,

*m*, 3-H), 1.56 (3H, *m*, menthyl-H), 1.20 (2H, *m*, menthyl-H), 1.01 (1H, *m*, menthyl-H), 0.89 (2H, *m*, menthyl-H), 0.81 (3H, *d*, *J* = 7 Hz, CH<sub>3</sub>) 0.74 and 0.59 (2×3H, 2×*d*, *J* = 6.5 Hz, CH(CH<sub>3</sub>)<sub>2</sub>), 0.25 (1H, *q*, *J* = 11.0 Hz, menthyl-H); <sup>13</sup>C-NMR (125 MHz, CDCl<sub>3</sub>, δ / ppm): 173.38, 171.92, 149.21, 148.72, 134.93, 134.50, 123.22, 74.53, 63.05, 59.69, 52.28, 48.93, 46.43, 39.76, 33.85, 33.78, 30.98, 26.03, 23.14, 21.69, 20.63, 16.07; HRMS (ESI, *m/z*): Calcd. for C<sub>22</sub>H<sub>32</sub>N<sub>2</sub>O<sub>4</sub> (M+H)<sup>+</sup>: 389.24348. Found: 389.24347; specific rotation [α]<sub>D</sub> (CHCl<sub>3</sub>, *c* = 1.2 mg/mL): -16.

(2S,4S,5S)-4-[(1R,2S,5R)-2-Isopropyl-5-methylcyclohexyl]-2-methyl 5-cyclohexylpyrrolidine-2,4-dicarboxylate (**24**). Yield: 33 %; White solid; m.p.: 106–107 °C; IR (KBr, cm<sup>-1</sup>): 2917, 1737, 1719, 1158; <sup>1</sup>H-NMR (500 MHz, CDCl<sub>3</sub>, δ / ppm) 4.68 (1H, *m*, OCH), 3.84 (1H, *m*, 2-H), 3.76 (3H, *s*, OCH<sub>3</sub>), 2.90 (1H, *m*, 4-H), 2.79 (1H, *m*, 5-H), 2.37–2.30 (2H, *m*, 3-H), 2.17 (1H, *m*), 2.09 (1H, *m*), 1.95–1.83 (3H, *m*), 1.75–1.65 (5H, *m*), 1.46 (1H, *m*), 1.37 (2H, *m*), 1.23–1.16 (4H, *m*), 1.07–0.96 (3H, *m*), 0.91 and 0.89 (2×3H, 2×*d*, *J* = 3.5 Hz, CH(CH<sub>3</sub>)<sub>2</sub>), 0.75 (3H, *d*, *J* = 7 Hz, CH<sub>3</sub>); <sup>13</sup>C-NMR (125 MHz, CDCl<sub>3</sub>, δ / ppm): 174.20, 173.63, 74.22, 70.16, 59.72, 52.07, 46.72, 45.79, 40.95, 39.48, 35.11, 34.15, 31.72, 31.29, 30.98, 26.31, 26.26, 25.89, 25.67, 23.26, 21.96, 20.72, 16.17; HRMS (ESI, *m/z*): Calcd. for C<sub>23</sub>H<sub>39</sub>NO<sub>4</sub> (M+H)<sup>+</sup>: 394.29519. Found: 394.29437; specific rotation [α]<sub>D</sub> (CHCl<sub>3</sub>, *c* = 3.5 mg/mL): -4.5.

(2S,4S,5S)-4-[(1R,2S,5R)-2-Isopropyl-5-methylcyclohexyl]-2-methyl 5-*iso*-propylpyrrolidine-2,4-dicarboxylate (**25**). Yield: 20 %; White amorphous solid; m.p.: 51–53 °C; IR (KBr, cm<sup>-1</sup>): 2955, 2928, 1738, 1205, 1167; <sup>1</sup>H-NMR (500 MHz, CDCl<sub>3</sub>, δ / ppm): 4.68 (1H, *m*, OCH), 3.89 (1H, *m*, 2-H), 3.77 (3H, *s*, OCH<sub>3</sub>), 3.00 (1H, *bs*, NH), 2.90 (1H, *m*, 4-H), 2.77 (1H, *m*, 5-H), 2.37 (1H, *m*, 3-H), 2.20 (1H, *m*, 3-H), 1.96 (1H, *m*), 1.85 (1H, *m*), 1.67 (3H, *m*), 1.49–1.34 (3H, *m*), 1.10 and 1.02 (2×3H, 2×*d*, *J* = 6.5 Hz, CH(CH<sub>3</sub>)<sub>2</sub>), 0.99–0.92 (2H, *m*), 0.90 and 0.89 (2×3H, 2×*d*, *J* = 2 Hz, CH(CH<sub>3</sub>)<sub>2</sub>-menthyl), 0.73 (3H, *d*, *J* = 7 Hz, CH<sub>3</sub>); <sup>13</sup>C-NMR (125 MHz, CDCl<sub>3</sub>, δ / ppm) 174.09, 173.54, 74.48, 71.42, 59.66, 52.17, 46.80, 45.97, 40.70, 35.17, 34.18, 31.35, 30.09, 26.32, 23.31, 21.99, 21.60, 21.01, 20.71, 16.13; HRMS (ESI, *m/z*): Calcd. for C<sub>20</sub>H<sub>35</sub>NO<sub>4</sub> (M+H)<sup>+</sup>: 354.26389. Found: 354.26240; specific rotation [α]<sub>D</sub> (CHCl<sub>3</sub>, *c* = 2.0 mg/mL): -44.

(2S,4S,5R)-2-Isopropyl-4-[(1R,2S,5R)-2-isopropyl-5-methylcyclohexyl] 5-phenylpyrrolidine-2,4-dicarboxylate (**28**). Yield: 24 %; White solid; m.p.: 124–126 °C; IR (KBr, cm<sup>-1</sup>): 2951, 2929, 1725, 1211, 1167; <sup>1</sup>H-NMR (500 MHz, CDCl<sub>3</sub>, δ / ppm): 7.35 (2H, *m*, phenyl-H), 7.29 (2H, *m*, phenyl-H), 7.22 (1H, *m*, phenyl-H), 5.15 (1H, *m*, OCH(CH<sub>3</sub>)<sub>2</sub>), 4.49 (1H, *d*, *J* = 7.5 Hz, 5-H), 4.36 (1H, *m*, OCH), 3.92 (1H, *t*, *J* = 8.5 Hz, 2-H), 3.27 (1H, *m*, 4-H), 2.95 (1H, *bs*, NH), 2.47 (1H, *m*, 3-H), 2.32 (1H, *m*, 3-H), 1.55–1.46 (3H, *m*, menthyl-H), 1.30 and 1.29 (2×3H, 2×*d*, *J* = 2.5 Hz, OCH(CH<sub>3</sub>)<sub>2</sub>), 1.22–1.07 (3H, *m*, menthyl-H), 0.86

(1H, *m*, menthyl-H), 0.78 and 0.73 (2×3H, 2×*d*, *J* = 6.5 Hz, CH(CH<sub>3</sub>)<sub>2</sub>), 0.68 (1H, *m*, menthyl-H), 0.55 (3H, *d*, *J* = 7.0 Hz, CH<sub>3</sub>), 0.29 (1H, *q*, *J* = 11.0 Hz, menthyl-H); <sup>13</sup>C-NMR (125 MHz, CDCl<sub>3</sub>, δ / ppm): 172.70, 172.47, 139.13, 128.24, 127.38, 127.10, 74.05, 68.59, 65.83, 60.16, 49.32, 46.54, 39.75, 34.53, 33.99, 31.02, 25.87, 23.11, 21.77, 21.74, 20.72, 16.00; HRMS (ESI, *m/z*): Calcd. for C<sub>25</sub>H<sub>37</sub>NO<sub>4</sub> (M+H)<sup>+</sup>: 416.27954. Found 416.27938; specific rotation [α]<sub>D</sub> (CHCl<sub>3</sub>, *c* = 1.5 mg/mL) = -26.

**(2S,4S,5R)-2-Cyclohexyl-4-[(1R,2S,5R)-2-isopropyl-5-methylcyclohexyl] 5-phenylpyrrolidine-2,4-dicarboxylate (29).** Yield: 54 %; White solid; m.p.: 126–127 °C; IR (KBr, cm<sup>-1</sup>): 2940, 2864, 1735, 1711, 1199, 1168; <sup>1</sup>H-NMR (500 MHz, CDCl<sub>3</sub>, δ / ppm) 7.35 (2H, *m*, phenyl-H), 7.30 (2H, *m*, phenyl-H), 7.23 (1H, *m*, phenyl-H), 4.91 (1H, *m*, OCH), 4.50 (1H, *d*, *J* = 7.5 Hz, 5-H), 4.36 (1H, *m*, OCH), 3.94 (1H, *t*, *J* = 8.5 Hz, 2-H), 3.33 (1H, *m*, 4-H), 2.92 (1H, *bs*, NH), 2.49 (1H, *m*, 3-H), 2.32 (1H, *m*, 3-H), 1.93–1.86 (2H, *m*), 1.78–1.69 (3H, *m*), 1.55–1.05 (12H, *m*), 0.86 (1H, *m*), 0.78 and 0.73 (2×3H, 2×*d*, *J* = 6.5 Hz CH(CH<sub>3</sub>)<sub>2</sub>, 0.55 (3H, *d*, *J* = 7.0 Hz, CH<sub>3</sub>), 0.29 (1H, *q*, *J* = 11.0 Hz, menthyl-H); <sup>13</sup>C-NMR (125 MHz, CDCl<sub>3</sub>, δ / ppm): 172.70, 172.47, 139.21, 128.27, 127.41, 127.13, 74.07, 73.41, 65.85, 60.23, 49.38, 46.56, 39.78, 34.63, 34.01, 31.51, 31.04, 25.89, 25.34, 23.62, 23.13, 21.77, 20.75, 16.02; HRMS (ESI, *m/z*): Calcd. for C<sub>28</sub>H<sub>41</sub>NO<sub>4</sub> (M+H)<sup>+</sup>: 456.31084. Found: 456.31067; specific rotation [α]<sub>D</sub> (CHCl<sub>3</sub>, *c* = 1.6 mg/mL): -26.

**(2S,4S,5R)-2-tert-Butyl-4-[(1R,2S,5R)-2-isopropyl-5-methylcyclohexyl] 5-phenylpyrrolidine-2,4-dicarboxylate (30).** Yield: 24 %; White solid; m.p.: 134–135 °C; IR (KBr, cm<sup>-1</sup>): 2961, 2929, 1732, 1190, 1156; <sup>1</sup>H-NMR (500 MHz, CDCl<sub>3</sub>, δ / ppm) 7.35 (2H, *m*, phenyl-H), 7.28 (2H, *m*, phenyl-H), 7.22 (1H, *m*, phenyl-H), 4.48 (1H, *d*, *J* = 7.5 Hz, 5-H), 4.36 (1H, *m*, OCH), 3.86 (1H, *t*, *J* = 8.5 Hz, 2-H), 3.32 (1H, *m*, 4-H), 2.46 (1H, *m*, 3-H), 2.26 (1H, *m*, 3-H), 1.51 (3×3H, s, C(CH<sub>3</sub>)<sub>3</sub>), 1.45 (3H, *m*, menthyl-H), 1.26–1.08 (3H, *m*, menthyl-H), 0.86 (1H, *m*, menthyl-H), 0.78 and 0.73 (2×3H, 2×*d*, *J* = 6.5 Hz CH(CH<sub>3</sub>)<sub>2</sub>), 0.68 (1H, *m*, menthyl-H), 0.55 (3H, *d*, *J* = 7.0 Hz, CH<sub>3</sub>), 0.32 (1H, *q*, *J* = 11.0 Hz, menthyl-H); <sup>13</sup>C-NMR (125 MHz, CDCl<sub>3</sub>, δ / ppm): 172.49, 172.31, 139.30, 128.25, 127.35, 127.11, 81.44, 74.02, 65.73, 60.65, 49.39, 46.57, 39.80, 34.75, 34.02, 31.05, 28.09, 25.85, 23.11, 21.77, 20.76, 16.00; HRMS (ESI, *m/z*): Calcd. for C<sub>26</sub>H<sub>39</sub>NO<sub>4</sub> (M+H)<sup>+</sup>: 430.29519. Found 430.29574; specific rotation [α]<sub>D</sub> (CHCl<sub>3</sub>, *c* = 2.0 mg/mL): -29.5.

**(2R,3S,5S)-[(1R,2S,5R)-2-Isopropyl-5-methylcyclohexyl] 5-(N,N-diethylcarbamoyl)-2-phenylpyrrolidine-3-carboxylate (31).** Yield: 29 %; Yellow amorphous solid; m.p.: 103–104 °C; IR (KBr, cm<sup>-1</sup>): 2961, 2933, 1720, 1632, 1418, 1161; <sup>1</sup>H-NMR (500 MHz, CDCl<sub>3</sub>, δ / ppm) 7.39 (2H, *m*, phenyl-H), 7.29 (2H, *m*, phenyl-H), 7.22 (1H, *m*, phenyl-H), 4.55 (1H, *d*, *J* = 8.5 Hz, 5-H), 4.35 (1H, *m*, OCH), 4.06 (1H, *m*, 2-H), 3.51 (1H, *m*, 4-H), 3.46–3.32 (4H, *m*, N(CH<sub>2</sub>)<sub>2</sub>),

2.40 (1H, *m*, 3-H), 2.21 (1H, *m*, 3-H), 1.52 (2H, *m*, menthyl-H), 1.44 (1H, *m*, menthyl-H), 1.23–1.16 (2×3H, 2×*t*, *J* = 7.5 Hz, N(CH<sub>2</sub>CH<sub>3</sub>)<sub>2</sub>), 1.20 (2H, *m*, menthyl-H), 1.05 (1H, *m*, menthyl-H), 0.88 (1H, *m*, menthyl-H), 0.78 and 0.73 (2×3H, 2×*d*, *J* = 6.5 Hz, CH(CH<sub>3</sub>)<sub>2</sub>), 0.68 (1H, *m*, menthyl-H), 0.54 (3H, *d*, *J* = 7.0 Hz, CH<sub>3</sub>), 0.36 (1H, *q*, *J* = 11.0 Hz, menthyl-H); <sup>13</sup>C-NMR (125 MHz, CDCl<sub>3</sub>, δ / ppm) 172.01, 170.72, 139.61, 128.30, 127.46, 127.07, 74.18, 65.07, 58.18, 50.46, 46.43, 41.13, 40.28, 39.67, 34.97, 33.95, 31.01, 25.77, 23.07, 21.74, 20.74, 16.00, 14.45, 12.90; HRMS (ESI, *m/z*): Calcd. for C<sub>26</sub>H<sub>40</sub>N<sub>2</sub>O<sub>3</sub> (M+H)<sup>+</sup>: 429.31117. Found: 429.31006. specific rotation [α]<sub>D</sub> (CHCl<sub>3</sub>, *c* = 1.2 mg/mL): -38.3.

#### SPECTRAL DATA FOR THE ADDITION PRODUCTS 6–13

(R)-2-[2,2-Bis(phenylsulphonyl)ethyl]heptanal<sup>1</sup> (**6**). Yield: 97 %; White amorphous solid; m.p.: 86–87 °C; IR (KBr, cm<sup>-1</sup>): 2925, 1728, 1449, 1312, 1152; <sup>1</sup>H-NMR (200 MHz, CDCl<sub>3</sub>, δ / ppm): 9.53 (1H, *s*), 7.96–7.87 (4H, *m*), 7.74–7.66 (2H, *m*), 7.60–7.52 (4H, *m*), 4.76–4.70 (1H, *m*), 3.00–2.89 (1H, *m*), 2.56–2.42 (1H, *m*), 2.24–2.10 (1H, *m*), 1.73–1.39 (2H, *m*), 1.34–1.14 (6H, *m*), 0.88 (3H, *t*, *J* = 6.4 Hz); <sup>13</sup>C-NMR (50 MHz, CDCl<sub>3</sub>, δ / ppm): 203.48, 137.70, 134.72, 134.57, 129.64, 129.35, 129.15, 80.53, 48.85, 31.59, 29.26, 26.06, 24.31, 22.25, 13.84; HRMS (ESI, *m/z*): Calcd. for C<sub>21</sub>H<sub>26</sub>O<sub>5</sub>S<sub>2</sub> (M+H)<sup>+</sup>: 423.12944. Found: 423.13019; specific rotation [α]<sub>D</sub> (CHCl<sub>3</sub>, *c* = 1.5 mg/mL): +16.

(R)-2-[2,2-Bis(phenylsulphonyl)ethyl]hexanal<sup>1</sup> (**7**). Yield: 99 %; White amorphous solid; m.p.: 60–62 °C; IR (KBr, cm<sup>-1</sup>): 2924, 1723, 1447, 1332, 1308, 1163; <sup>1</sup>H-NMR (200 MHz, CDCl<sub>3</sub>, δ / ppm): 9.53 (1H, *s*), 7.96–7.87 (4H, *m*), 7.73–7.66 (2H, *m*), 7.60–7.52 (4H, *m*), 4.76–4.70 (1H, *m*), 2.99–2.89 (1H, *m*), 2.56–2.42 (1H, *m*), 2.24–2.10 (1H, *m*), 1.73–1.43 (2H, *m*), 1.33–1.19 (4H, *m*), 0.88 (3H, *t*, *J* = 6.8 Hz); <sup>13</sup>C-NMR (50 MHz, CDCl<sub>3</sub>, δ / ppm): 203.46, 137.70, 134.72, 134.57, 129.64, 129.35, 129.15, 80.53, 48.81, 28.99, 28.48, 24.31, 22.52, 13.68; HRMS (ESI, *m/z*): Calcd. for C<sub>20</sub>H<sub>24</sub>O<sub>5</sub>S<sub>2</sub> (M+H)<sup>+</sup>: 409.11379. Found: 409.11308; specific rotation [α]<sub>D</sub> (CHCl<sub>3</sub>, *c* = 4.0 mg/mL): +6.

(R)-2-[2,2-Bis(phenylsulphonyl)ethyl]dodecanal (**8**). Yield: 70 %; Colourless oil; IR (KBr, cm<sup>-1</sup>): 2923, 1723, 1447, 1311, 1150; <sup>1</sup>H-NMR (200 MHz, CDCl<sub>3</sub>, δ / ppm): 9.54 (1H, *s*), 7.96–7.87 (4H, *m*), 7.71–7.65 (2H, *m*), 7.60–7.52 (4H, *m*), 4.76–4.70 (1H, *m*), 3.00–2.89 (1H, *m*), 2.56–2.42 (1H, *m*), 2.24–2.10 (1H, *m*), 1.73–1.40 (2H, *m*), 1.34–1.14 (16H, *m*), 0.88 (3H, *t*, *J* = 6.4 Hz); <sup>13</sup>C-NMR (50 MHz, CDCl<sub>3</sub>, δ / ppm): 203.47, 137.67, 134.70, 134.55, 129.65, 129.36, 129.15, 129.11, 80.53, 48.85, 31.79, 29.46, 29.31, 29.22, 26.40, 24.33, 22.58, 14.02; HRMS (ESI, *m/z*): Calcd. for C<sub>26</sub>H<sub>36</sub>O<sub>5</sub>S<sub>2</sub> (M+NH<sub>4</sub>)<sup>+</sup>: 510.23424. Found: 510.23410; specific rotation [α]<sub>D</sub> (CHCl<sub>3</sub>, *c* = 5.0 mg/mL): +4.8.

(R)-2-Benzyl-4,4-bis(phenylsulphonyl)butanal<sup>1</sup> (**9**). Yield: 99 %; White amorphous solid; m.p.: 80–81 °C; IR (KBr, cm<sup>-1</sup>): 1722, 1327, 1311, 1150; <sup>1</sup>H-NMR

(200 MHz, CDCl<sub>3</sub>, δ / ppm): 9.66 (1H, s), 7.87–7.84 (2H, m), 7.71–7.59 (4H, m), 7.58–7.26 (7H, m), 7.22–7.15 (2H, m), 4.73–4.67 (1H, m), 3.48–3.34 (1H, m), 3.20–3.10 (1H, m), 2.67–2.45 (2H, m), 2.13–1.99 (1H, m); <sup>13</sup>C-NMR (50 MHz, CDCl<sub>3</sub>, δ / ppm): 202.59, 137.94, 137.03, 136.61, 134.57, 134.48, 129.87, 129.22, 129.13, 129.09, 128.94, 127.01, 80.28, 50.27, 35.63, 24.13; HRMS (ESI, m/z): Calcd. for C<sub>23</sub>H<sub>22</sub>O<sub>5</sub>S<sub>2</sub> (M+H)<sup>+</sup>: 443.09814. Found: 443.09792; specific rotation [α]<sub>D</sub> (CHCl<sub>3</sub>, c = 5.0 mg/mL): +5.4.

(R)-2-(4-Methoxybenzyl)-4,4-bis(phenylsulphonyl)butanal (**10**). Yield 98 %; White amorphous solid; m.p.: 95–96 °C; IR (KBr, cm<sup>-1</sup>): 1721, 1511, 1447, 1327, 1311, 1151; <sup>1</sup>H-NMR (200 MHz, CDCl<sub>3</sub>, δ / ppm): 9.65 (1H, s), 7.87–7.83 (2H, m), 7.71–7.65 (4H, m), 7.64–7.40 (4H, m), 7.10 (2H, d, J = 8.5 Hz), 6.90 (2H, d, J = 8.5 Hz), 4.74–4.67 (1H, m), 3.83 (3H, s), 3.44–3.30 (1H, m), 3.14–3.05 (1H, m), 2.63–2.43 (2H, m), 2.13–1.99 (1H, m); <sup>13</sup>C-NMR (50 MHz, CDCl<sub>3</sub>, δ / ppm): 202.79, 158.62, 137.92, 136.65, 134.57, 134.48, 130.15, 129.91, 129.24, 129.09, 128.89, 114.31, 80.29, 55.26, 50.45, 34.74, 24.03; HRMS (ESI, m/z): Calcd. for C<sub>24</sub>H<sub>24</sub>O<sub>6</sub>S<sub>2</sub> (M+H)<sup>+</sup>: 473.10871. Found: 473.10822; specific rotation [α]<sub>D</sub> (CHCl<sub>3</sub>, c = 5.0 mg/mL): +1.2.

(R)-2-*I*(Naphthalen-1-yl)methyl]-4,4-bis(phenylsulphonyl)butanal (**11**). Yield: 99 %; Yellow amorphous solid; m.p.: 120–121 °C; IR (KBr, cm<sup>-1</sup>): 1721, 1447, 1328, 1310, 1150; <sup>1</sup>H-NMR (200 MHz, CDCl<sub>3</sub>, δ / ppm): 9.73 (1H, s), 8.00–7.87 (2H, m), 7.83–7.75 (3H, m), 7.64–7.34 (9H, m), 7.27–7.21 (3H, m), 4.70–4.64 (1H, m), 3.70–3.40 (2H, m), 3.02–2.91 (1H, m), 2.76–2.62 (1H, m), 2.14–2.00 (1H, m); <sup>13</sup>C-NMR (50 MHz, CDCl<sub>3</sub>, δ / ppm): 202.61, 137.99, 136.21, 134.41, 134.02, 132.75, 131.35, 129.56, 129.07, 129.04, 128.73, 127.94, 127.80, 126.67, 126.07, 125.50, 123.15, 80.19, 48.98, 33.07, 24.51; HRMS (ESI, m/z): Calcd. for C<sub>27</sub>H<sub>24</sub>O<sub>5</sub>S<sub>2</sub> (M+NH<sub>4</sub>)<sup>+</sup>: 510.14034. Found: 510.13951. specific rotation [α]<sub>D</sub> (CHCl<sub>3</sub>, c = 6.4 mg/mL): -3.3.

(R)-2-(3,4-Dichlorobenzyl)-4,4-bis(phenylsulphonyl)butanal (**12**). Yield: 98 %; Colourless oil; IR (KBr, cm<sup>-1</sup>): 1723, 1447, 1328, 1311, 1150; <sup>1</sup>H-NMR (200 MHz, CDCl<sub>3</sub>, δ / ppm): 9.64 (1H, s), 7.89–7.83 (2H, m), 7.75–7.64 (4H, m), 7.59–7.48 (4H, m), 7.41 (1H, d, J = 7.8 Hz), 7.25 (1H, d, J = 1.8 Hz), 7.03 (1H, m), 4.73–4.66 (1H, m), 3.43–3.29 (1H, m), 3.14–3.04 (1H, m), 2.67–2.42 (2H, m), 2.09–1.95 (1H, m); <sup>13</sup>C-NMR (50 MHz, CDCl<sub>3</sub>, δ / ppm): 201.81, 137.65, 137.28, 136.65, 134.83, 134.66, 132.86, 131.26, 130.95, 130.84, 129.75, 129.24, 129.20, 129.02, 128.54, 80.17, 49.91, 34.54, 24.05; HRMS (ESI, m/z): Calcd. for C<sub>23</sub>H<sub>20</sub>Cl<sub>2</sub>O<sub>5</sub>S<sub>2</sub> (M+H)<sup>+</sup>: 511.02020. Found 511.01930; specific rotation [α]<sub>D</sub> (CHCl<sub>3</sub>, c = 6.0 mg/mL): -4.

(R)-2-(4-Fluorobenzyl)-4,4-bis(phenylsulphonyl)butanal (**13**). Yield: 77 %; Colourless oil; IR (KBr, cm<sup>-1</sup>): 1722, 1508, 1447, 1327, 1311, 1151; <sup>1</sup>H-NMR (200 MHz, CDCl<sub>3</sub>, δ / ppm): 9.65 (1H, s), 7.87–7.83 (2H, m), 7.71–7.65 (4H, m), 7.62–7.42 (4H, m), 7.17–6.98 (4H, m), 4.74–4.67 (1H, m), 3.47–3.32 (1H, m),

3.16–3.06 (1H, *m*), 2.69–2.42 (2H, *m*), 2.11–1.97 (1H, *m*);  $^{13}\text{C}$ -NMR (50 MHz,  $\text{CDCl}_3$ ,  $\delta$  / ppm): 202.43, 164.30, 159.41, 137.77, 136.65, 134.70, 134.55, 132.68, 132.62, 130.73, 130.57, 129.82, 129.22, 129.13, 128.94, 115.98, 115.54, 80.22, 50.27, 34.74, 24.02; HRMS (ESI, *m/z*): Calcd. for  $\text{C}_{23}\text{H}_{21}\text{FO}_5\text{S}_2$  ( $\text{M}+\text{H}$ ) $^+$ : 461.08872. Found: 461.08804; specific rotation  $[\alpha]_D$  ( $\text{CHCl}_3$ , *c* = 6.3 mg/mL): –1.3.

#### SPECTRAL DATA FOR THE ADDITION PRODUCTS **14–16**

(*S*)-2-[2,2-Bis(phenylsulphonyl)ethyl]cyclohexanone<sup>2</sup> (**14**). Yield: 42 %; White amorphous solid; m.p.: 149–151 °C; IR (KBr,  $\text{cm}^{-1}$ ): 2940, 1702, 1448, 1310, 1144;  $^1\text{H}$ -NMR (200 MHz,  $\text{CDCl}_3$ ,  $\delta$  / ppm): 7.97–7.87 (4H, *m*), 7.74–7.67 (2H, *m*), 7.61–7.56 (4H, *m*), 5.02–4.96 (1H, *q*), 3.16–3.01 (1H, *m*), 2.60–2.45 (1H, *m*), 2.35–2.29 (2H, *m*), 2.16–1.98 (3H, *m*), 1.87–1.56 (2H, *m*), 1.32–1.21 (2H, *m*);  $^{13}\text{C}$ -NMR (50 MHz,  $\text{CDCl}_3$ ,  $\delta$  / ppm): 212.44, 137.92, 134.63, 134.44, 129.73, 129.25, 129.11, 129.04, 80.61, 47.29, 41.99, 34.76, 27.75, 26.44, 24.95; HRMS (ESI, *m/z*): Calcd. for  $\text{C}_{20}\text{H}_{22}\text{O}_5\text{S}_2$  ( $\text{M}+\text{H}$ ) $^+$ : 407.09814. Found: 407.09747; specific rotation  $[\alpha]_D$  ( $\text{CHCl}_3$ , *c* = 1.1 mg/mL): –5.5.

(*S*)-2-[2,2-Bis(phenylsulphonyl)ethyl]cyclopentanone (**15**). Yield: 56 %; White amorphous solid; m.p.: 110–112 °C; IR (KBr,  $\text{cm}^{-1}$ ): 2916, 1731, 1447, 1327, 1310, 1140;  $^1\text{H}$ -NMR (200 MHz,  $\text{CDCl}_3$ ,  $\delta$  / ppm): 7.97–7.90 (4H, *m*), 7.74–7.64 (2H, *m*), 7.61–7.48 (4H, *m*), 5.43–5.38 (1H, *q*), 2.80–2.63 (1H, *m*), 2.44–2.37 (1H, *m*), 2.34–2.21 (2H, *m*), 2.07–1.74 (3H, *m*), 1.58–1.43 (2H, *m*);  $^{13}\text{C}$ -NMR (50 MHz,  $\text{CDCl}_3$ ,  $\delta$  / ppm): 220.04, 137.88, 137.54, 134.59, 134.53, 129.55, 129.11, 125.52, 79.60, 45.25, 38.02, 30.26, 25.96, 20.25; HRMS (ESI, *m/z*): Calcd. for  $\text{C}_{19}\text{H}_{20}\text{O}_5\text{S}_2$  ( $\text{M}+\text{H}$ ) $^+$ : 393.08249. Found: 393.08133; specific rotation  $[\alpha]_D$  ( $\text{CHCl}_3$ , *c* = 1.2 mg/mL): –10.8.

(*S*)-4-Methyl-6,6-bis(phenylsulphonyl)3-hexanone (**16**). Yield: 51 %; Colourless oil; IR (KBr,  $\text{cm}^{-1}$ ): 2935, 1708, 1447, 1327, 1311, 1148;  $^1\text{H}$ -NMR (500 MHz,  $\text{CDCl}_3$ ,  $\delta$  / ppm): 7.98–7.90 (4H, *m*), 7.75–7.65 (2H, *m*), 7.61–7.52 (4H, *m*), 4.67 (1H, *q*), 3.26–3.20 (1H, *m*), 2.58–2.51 (1H, *m*), 2.48–2.40 (2H, *m*), 2.12–2.06 (1H, *m*), 1.10 (3H, *d*, *J* = 7.5 Hz), 1.04 (3H, *t*, *J* = 7 Hz);  $^{13}\text{C}$ -NMR (50 MHz,  $\text{CDCl}_3$ ,  $\delta$  / ppm): 213.57, 137.90, 137.77, 134.65, 134.49, 129.74, 129.29, 129.15, 129.07, 80.79, 42.98, 34.01, 28.19, 17.58, 7.63; HRMS (ESI, *m/z*): Calcd. for  $\text{C}_{19}\text{H}_{22}\text{O}_5\text{S}_2$  ( $\text{M}+\text{H}$ ) $^+$ : 395.09814. Found: 395.09843; specific rotation  $[\alpha]_D$  ( $\text{CHCl}_3$ , *c* = 1.0 mg/mL): –8.0.

#### REFERENCES

1. Q. Zhu, Y. Lu, *Org. Lett.* **10** (2008) 4803
2. Q. Zhu, L. Cheng, Y. Lu, *Chem. Commun.* **47** (2008) 6315.



## Anti-inflammatory and antioxidant activities of *Sclerochloa dura* (Poaceae)

SYED MAJID BUKHARI<sup>1\*</sup>, ASTRID JULLUMSTRØ FEUERHERM<sup>2</sup>, FAYSSAL BOULFRAD<sup>3</sup>, BOJAN ZLATKOVIĆ<sup>4</sup>, BERIT JOHANSEN<sup>2</sup> and NEBOJŠA SIMIĆ<sup>1</sup>

<sup>1</sup>Department of Chemistry, Norwegian University of Science and Technology, 7491 Trondheim, Norway, <sup>2</sup>Department of Biology, Norwegian University of Science and Technology, 7491 Trondheim, Norway, <sup>3</sup>UFR de Pharmacie, Grenoble, France and

<sup>4</sup>Faculty of Sciences, University of Niš, 18000 Niš, Serbia

(Received 2 December 2013, accepted 14 January 2014)

**Abstract:** The plant *Sclerochloa dura* is traditionally used in South-East Serbia to treat menstrual disorders characterized by pain and excessive bleeding. According to statements of subjects, a reduction in bleeding and pain is experienced shortly after oral intake. The focus of this investigation was to determine the inhibitory effects of the plant on the arachidonic acid (AA) cascade along with the spectrophotometric determination of its antioxidant capacity. The AA release assay was performed using the human fibroblast-like synoviocyte cell line SW982 to determine the AA release and hence phospholipase A<sub>2</sub> (PLA<sub>2</sub>) activity. The crude extract and subsequent fractions of *S. dura* inhibit IL-1 induced release of AA in a time- and dose-dependent manner in SW982 cells. The  $IC_{50}$  for the crude extract is 1.5 mg mL<sup>-1</sup> at 4 and 24 h of stimulation. Treating the cells with 0.22, 0.11 and 0.06 mg mL<sup>-1</sup> of a methanolic fraction resulted in 97, 91 and 63 % inhibition of AA-release, respectively. One milligram of the crude extract contained 34.78 µg pyrocatechol equivalent phenolic content, 22.80 µg quercetin equivalent flavonoid content and an antioxidant activity of 70.11 µg α-tocopherol equivalents. The strong inhibitory effects of the *S. dura* extracts on the AA cascade may explain the reported pain- and discomfort-relieving effects.

**Keywords:** arachidonic acid release assay; cytosolic phospholipase A<sub>2</sub> enzyme; flavonoid content; free radical scavenging activity; phenolic content; SW 982 fibroblast-like synoviocytes.

### INTRODUCTION

Eicosanoids, such as prostaglandins and leukotrienes, are derivatives of the ω-6 fatty acid (AA) and act as potent lipid mediators of inflammation.<sup>1</sup> AA is released by the action of phospholipase A<sub>2</sub> (PLA<sub>2</sub>) enzymes by hydrolysis of the

\*Corresponding author. E-mail: majid\_bukhari@hotmail.com  
doi: 10.2298/JSC131202003B

*sn*-2 ester bond of membrane glycerophospholipids. PLA<sub>2</sub> enzymes are primarily sorted into five categories; secretory PLA<sub>2</sub> (sPLA<sub>2</sub>), cytosolic PLA<sub>2</sub> (cPLA<sub>2</sub>), Ca<sup>2+</sup>-independent PLA<sub>2</sub> (iPLA<sub>2</sub>), platelet-activating factor acetyl hydrolases (PAF-AH) and lysosomal PLA<sub>2</sub>s.<sup>2,3</sup> Alongside the ongoing elucidation of the roles of different PLA<sub>2</sub> isotypes in physiology or pathophysiology of different diseases,<sup>4</sup> there is great interest in the development of different PLA<sub>2</sub> subtype-specific inhibitors to treat human diseases.<sup>5</sup>

Pro-inflammatory cytokines, such as TNF and IL-1 $\beta$ , activate PLA<sub>2</sub> enzymes, mainly the arachidonyl specific cPLA<sub>2</sub>-IV $\alpha$  isotype, resulting in the subsequent release of AA and the generation of pro-inflammatory eicosanoids.<sup>6-8</sup> In addition, it was previously shown that activated TNF and IL-1 $\beta$  may lead to increased transcription of the cyclooxygenase 2 (COX2) and cPLA<sub>2</sub>-IV $\alpha$  genes, further propagating inflammation by increased availability and metabolism of AA into pro-inflammatory eicosanoids.<sup>8,9</sup> In addition to their association with inflammation, increased availability of AA has also been connected with heavy menstrual bleeding.<sup>10</sup> Prostaglandins, such as PGE<sub>2</sub> and PGF<sub>2</sub>, levels have been found to be elevated in the endometrium of women with heavy menstrual bleeding compared to women with normal menses.<sup>11,12</sup> Prostaglandins contribute to uterus contractions<sup>13</sup> and are thought to be a major factor in primary dysmenorrhea. By targeting the cyclooxygenases (COX1/2) responsible for the enzymatic conversion of AA to eicosanoids, non-steroidal anti-inflammatory drugs are effective in relieving the pain and discomfort of dysmenorrhea.<sup>11</sup>

A good anti-inflammatory activity often accompanies good antioxidant activity.<sup>14,15</sup> There are two basic types of antioxidants available: synthetic and natural ones. The synthetic antioxidants typically contain phenolic groups as the main functionality. The natural antioxidants are mostly obtained from different parts of plants and their structural diversity is much larger. They can be either nitrogen-containing compounds, such as alkaloids, chlorophyll derivatives, amines and amino acids, or phenolic compounds, such as tocopherols, flavonoids and phenolic acids. These compounds can act as oxygen scavengers, thereby terminating the harmful activity of free radicals.<sup>16,17</sup> Flavonoids are considered to be the most potent antioxidants. They can delay or inhibit the oxidation of lipids or other molecules by inhibiting the propagation of oxidative chain reactions.<sup>18</sup> There has been an increased interest in natural antioxidants from plant materials in the recent years.<sup>19</sup>

*Sclerochloa dura* (Linnaeus) P. Beauvois, also known as common hardgrass, belongs to family Poaceae Barnhart, which involves more than 700 genera and almost 50,000 species. It is an annual plant, with flat leaves and a procumbent or erect stem. The inflorescence is a crowded, one-sided series of flattened spikelets.<sup>20</sup> The plant is a common inhabitant of areas with heavy traffic, *e.g.*, along dirty roads, on play yards and walking pathways. It is widely spread in the mode-

rate climate zone on almost all the continents of the North Hemisphere and was introduced to Australia as well.<sup>21</sup>

There are only a few published papers in which this plant is mentioned. However, none of them deal with its chemical composition or bioactivity. In most of the studies, the plant was used as a specimen for the determination of the efficiency of various herbicides.<sup>22–28</sup> Two papers discuss the phylogeny of certain grasses, among them *S. dura*<sup>29,30</sup> and one paper deals with the identification of prolamines in cereal and grass species, including *S. dura*.<sup>31</sup>

The plant is traditionally used in South-East Serbia for the treatment of menstrual disorders, manifested as excessive bleeding and intense pain. Professor Aleksandar Igić (Medical faculty, University of Niš, Serbia) in personal correspondence reported that in this region tea or decocts of *S. dura* have been used by women having menstrual disorders. According to the statements of subjects, the symptoms were significantly alleviated shortly after intake. The remarkable story about the health improving properties of *S. dura*, together with the lack of published data about its chemical composition and bioactivity, was the reason to start studying this plant. Therefore, in this study, the aim was to determine the chemical composition, including free radical scavenging activity, anti-oxidant activity, the total phenolic and flavonoid contents of *S. dura* extract, and its ability to inhibit the release of AA. In addition, such properties of *S. dura* were compared with those reported for other plants reported to alleviate menstrual disorders, *i.e.*, *Wrightia tomentosa*<sup>32,33</sup> and *Dendrophthoe falcata*.<sup>34</sup> The novel findings presented herein, forward the plant *S. dura* as a promising natural source for alleviating inflammatory disorders, including menstrual discomfort.

## EXPERIMENTAL

### *Plant material*

*Sclerochloa dura* (whole plant) was collected in June–July 2009 from the city of Niš, along the river bank near the Gabrovačka Reka, a creek in Serbia. The plant was identified by Bojan Zlatković from the Department of Biology and Ecology, University of Niš, Serbia. A specimen of the identified plant was deposited in the Herbarium of the Faculty of Science and Mathematics (HMN) of the University of Niš, Serbia (voucher number 6922). Total collected weight of the plant was 250 g. The plant material was dried for 10 days in the dark, with proper ventilation and at room temperature. The dried plant was kept in a closed plastic bag in the dark at room temperature until extraction.

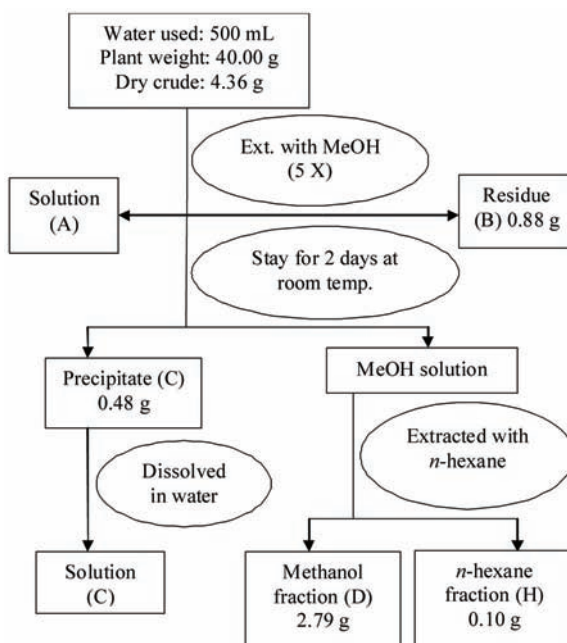
### *Reagents and chemicals*

Water used for extraction was obtained from Millipore Elix 5 water purification system, *n*-hexane was from VWR (USA) and methanol was from Fisher Scientific (UK). Recombinant human IL-1 $\beta$  was from Roche (UK). Phosphate-buffered saline solution (PBS) was from Oxoid (UK). Labelled (5,6,8,9,11,12,14,15- $^3$ H)-arachidonic acid (specific activity 180–240 Ci mmol $^{-1}$ ) and liquid scintillation cocktail Ultima Gold were from NEN Perkin Elmer (USA). Dulbecco's Modified Eagle Medium (DMEM), foetal bovine serum (FBS), fatty acid-free bovine serum albumin (fBSA), gentamicin and L-glutamine were from Sigma-Aldrich (USA).

Potassium acetate, sodium carbonate, 1,1-diphenyl-2-picrylhydrazyl, sodium phosphate,  $\alpha$ -tocopherol, quercetin, ammonium molybdate, Folin-Ciocalteu reagent, pyrocatechol and aluminium nitrate were from Sigma-Aldrich (USA). Sulphuric acid and ascorbic acid were from Merck (Germany).

#### *Extraction procedure*

Aerial parts were crushed into small pieces and extracted by refluxing with water for 20 min. To enhance extraction, the water extract was sonicated for 15 minutes before and after the refluxing (VWR ultrasound cleaner). After 12 h, the extract was filtered (blue ribbon filter paper from Schleicher and Schuell) and the volume reduced on a rotavapor (Büchi rotavapor R-200). Dry plant sample was obtained by freeze drying (Labconco freeze drier model FreeZone 2.5) at  $-70^{\circ}\text{C}$  for 60 h. The crude extract was successively extracted, as shown in Scheme 1.



Scheme 1. Separation of crude extract of *S. dura*.

The crude extracts and the subsequent fractions (C fraction – water soluble, insoluble in methanol, D fraction – methanol extract of crude; water soluble as well) were prepared from *S. dura*. The crude extract was tested for anti-inflammatory and antioxidant activities while the subsequent fractions were tested for anti-inflammatory activity only. The *S. dura* crude extract and related fractions were aliquoted in sterile glass vials and stored protected from light at  $4^{\circ}\text{C}$  prior to use. The *n*-hexane fraction H was not tested for anti-inflammatory activity due to the harmful effect of *n*-hexane on cells.

#### *Culture and treatment of SW982 cells*

The human fibroblast-like synoviocyte cell line SW982 was purchased from ATCC (UK) sub-cultured bi-weekly by routine trypsin detachment and kept in a sub-confluent state. The

cells were maintained in DMEM supplemented with 10 % FBS, 0.1 mg mL<sup>-1</sup> gentamicin and 0.3 mg mL<sup>-1</sup> L-glutamine in a humidified 10 % CO<sub>2</sub> atmosphere at 37 °C. For AA release, 5×10<sup>5</sup> cells were seeded per well in a 48-well per plate format. Cells were cultivated until 2 days post-confluence, serum starved and labelled with <sup>3</sup>H-AA in serum-free DMEM overnight and processed at day 3 post-confluence to ensure differentiation and synchronization of the cells. The experiments were performed in serum-free DMEM in triplicates of the wells and repeated three times. In all experiments, untreated cells without inducing agents or plant extract were included for unstimulated control; distilled water was included for vehicle control. Following the treatments, the cells were routinely microscopically observed to monitor possible effects on cell morphology, integrity and viability.

#### *Arachidonic acid release assay*

The AA release assay determines the amount of AA released from SW982 cells stimulated with IL-1β. AA release corresponds to the activation of PLA<sub>2</sub>-enzymes that cleave off the AA in the *sn*-2 position of the phospholipid. In the presence of inhibiting compound(s), the release of AA is reduced, which is taken as evidence that the compound(s) target some level in the arachidonyl cascade, such as the PLA<sub>2</sub> enzymes.<sup>7-9</sup>

At 2 days post-confluence, the SW982 cells were serum-starved and labelled overnight with <sup>3</sup>H-AA (0.4 µCi mL<sup>-1</sup>) in serum-free DMEM. Prior to the addition of the *S. dura* extract or related fractions, the cells were washed with PBS containing fBSA (2.0 mg mL<sup>-1</sup>) in order to remove unincorporated radioactivity. The cells were pre-treated with various dilutions of the crude extract and subsequent fractions (0–20 % extract in serum-free DMEM, 1 h pre-incubation) followed by the addition of IL-1β (10 ng mL<sup>-1</sup>) to mimic an inflammatory situation. After 4 and 24 h of IL-1β stimulation, the supernatants were cleared of detached cells by centrifugation (13000 rpm, 10 min). The cellular release of <sup>3</sup>H-AA was determined by liquid scintillation counting in an LS 6500 Multi-Purpose Scintillation Counter, Beckman Coulter, Inc. (USA). The adherent cells were dissolved in 1.0 M NaOH in order to determine by liquid scintillation counting the <sup>3</sup>H-AA incorporated in the cells. The results are given as released <sup>3</sup>H-AA in the supernatants relative to total <sup>3</sup>H-AA incorporated in the cells.

#### *Total phenolic content determination*

The total soluble phenolic content of the plant extract was determined with Folin–Ciocalteu reagent using pyrocatechol as a standard.<sup>35,36</sup> An aliquot of 5.0 mg of the dry plant extract was dissolved in 20.0 mL of distilled water in an Erlenmeyer flask. The solution was diluted to 46.0 mL by the addition of distilled water. Folin–Ciocalteu reagent (1 mL) was added to the solution and mixture was shaken vigorously. After 3 min, 3.0 mL of 2 % sodium carbonate solution was added. The flask was covered with aluminium foil to protect the complex from possible effects of light. Flask was shaken occasionally for 2 h at room temperature. The absorbance was measured at 760 nm<sup>37,38</sup> using a UV mini-1240 – Shimadzu (Tokyo, Japan) spectrophotometer. A standard curve was plotted using pyrocatechol as a standard and the total soluble phenolic contents in the extracts were expressed as µg pyrocatechol equivalent, according to the following equation:

$$Y = 0.0533X + 0.0994 \quad (1)$$

where Y is the absorbance and X the concentration.

#### *Total flavonoid content determination*

Dry extract (20.0 mg) was dissolved in 1.0 mL of 80 % ethanol. An aliquot of 0.1 mL was taken and diluted to 1.0 mL, giving a concentration of 2.0 mg mL<sup>-1</sup>. An aliquot of 0.5 mL

(1.0 mg) was taken and added to a test tube containing 4.3 mL of 80 % ethanol, 0.1 mL of 1 M potassium acetate and 0.1 mL of 10 % aluminium nitrate. The mixture was incubated at room temperature for 40 min. The absorbance was measured at 415 nm using a UV mini-1240 – Shimadzu (Tokyo, Japan) spectrophotometer. The total flavonoid content in the plant extract was expressed as µg quercetin equivalents<sup>39–41</sup> using a standard quercetin graph and according to the following equation:

$$Y = 0.0494X - 0.0026 \quad (2)$$

where  $Y$  is the absorbance and  $X$  the concentration.

#### *Antioxidant activity determination*

The antioxidant activity of the extract was determined by the phosphomolybdenum method using  $\alpha$ -tocopherol as a standard.<sup>42,43</sup> One mg of the extract was combined with 2.0 mL of the reagent (0.6 M sulphuric acid, 28.0 mM sodium phosphate and 4.0 mM ammonium molybdate). A blank solution was prepared by mixing 2.0 mL of the reagent solution with the appropriate volume of the same solvent used to dissolve the sample. The tubes were capped and incubated in water bath at 95 °C for 90 min. The sample and blank were left 30 min to cool down to room temperature. The absorbance of the sample was measured against blank solution at 695 nm using a UV mini-1240 – Shimadzu (Tokyo, Japan) spectrophotometer. A tocopherol graph was plotted by using  $\alpha$ -tocopherol as a standard and the total antioxidant activity of the plant extract was expressed as µg  $\alpha$ -tocopherol equivalents according to the following equation:

$$Y = 7.7686X + 1.678 \quad (3)$$

where  $Y$  is the absorbance and  $X$  the concentration.

#### *Free radical scavenging activity*

The ability of the extract to quench the 1,1-diphenyl-2-picrylhydrazyl radical (DPPH) determines the free radical scavenging activity of a plant material.<sup>44–46</sup> It is usually expressed as the  $IC_{50}$  value<sup>37,47,48</sup> (the extract concentration required to inhibit the activity of DPPH<sup>·</sup> by 50 %).

Seven different dilutions of the plant extract were made in 100 % ethanol: 3200, 1600, 800, 400, 200, 100 and 50 µg mL<sup>-1</sup>. A volume of 1.0 mL of 0.3 mM solution of DPPH<sup>·</sup> was mixed with 2.5 mL of each dilution. All the solutions were left at room temperature for 30 min and then the absorption of each was measured at 518 nm using a UV mini-1240 – Shimadzu (Tokyo, Japan) spectrophotometer. A negative control was prepared by mixing 2.5 mL of ethanol with 1.0 mL of DPPH. The percentage inhibition for all dilutions was determined using the following equation:

$$\% \text{ Inhibition} = 100 - 100(A_{\text{sample}} - A_{\text{blank}})/A_{\text{control}} \quad (4)$$

where  $A_{\text{sample}}$  is the absorbance of each dilution;  $A_{\text{blank}}$  is the absorbance of the dilutions without added DPPH<sup>·</sup> and  $A_{\text{control}}$  is the absorbance of the solution of DPPH in ethanol.

The graph between probit of inhibition (a unit of measurement of statistical probability based on deviations from the mean of a normal distribution) vs. the log of concentration was plotted and the  $IC_{50}$  value of the plant extract was calculated from the graph.

#### *Statistical analysis*

All values are expressed as mean  $\pm$  SD. The cellular bioactivity data were analysed by the Student's *t*-test and results were considered significant at  $p < 0.05$ .

## RESULTS AND DISCUSSION

*Physical properties of the crude extract and subsequent fractions*

As the traditional use of *S. dura* is reported to be drinking it as a tea, the dried plant was crushed into small pieces and extracted by refluxing with water. From 40.0 g of the dry aerial plant parts, a yield of 4.36 g (10.9 %) of a dark brown coloured crude extract was obtained, whereas 0.48 g (11.0 % relative to dry crude) of yellow coloured water soluble fraction C, 2.79 g (64.0 % relative to dry crude) of dark brown coloured fraction D soluble in both water and methanol and 0.10 g (2.3 % relative to crude) of a transparent hexane-soluble fraction H. In summary, about 80 % of the dried plant extract was extractable by water, methanol and hexane, whereas 20.2 % of the fraction appeared as a black, insoluble residue. The physical properties of the crude extract and the fractions obtained from it are given in Table I.

TABLE I. Colour, yield and solubility of crude extract and subsequent fractions

Fraction	Colour	Yield, %	Soluble in
Crude	Brown	10.9	Water
C-Fraction	Yellow	11.0 <sup>a</sup>	Water
D-Fraction	Brown	64.0 <sup>a</sup>	Water and methanol
H-Fraction	Transparent	2.3 <sup>a</sup>	Hexane
Residue	Black	20.2 <sup>a</sup>	Insoluble

<sup>a</sup>Relative to dry crude

*The crude extract of *S. dura* inhibits the release of arachidonic acid*

The *S. dura* extract is traditionally used to alleviate menstrual cramping, excessive bleeding and pain, processes known to involve eicosanoids such as PGE<sub>2</sub>,<sup>13</sup> also recognized as a pro-inflammatory mediator.<sup>1</sup> By use of the AA-release assay and the SW982 cell model system, the effect of the extract on the availability of AA, the rate-limiting precursor for PGE<sub>2</sub> synthesis, was investigated. As shown in Fig. 1, the crude extract of *S. dura* inhibits IL-1β induced AA release in a dose-dependent manner, with an observed ≈50 % inhibition at 1.5 mg mL<sup>-1</sup> after both 4 and 24 h of stimulation. Hence, the *S. dura* extract may contain anti-convulsive and/or anti-inflammatory compounds that interfere with the arachidonic acid cascade.

*The methanolic fraction of *S. dura* crude extract efficiently inhibits AA-release*

Having shown that the crude *S. dura* extract inhibited AA-release, the crude extract was further fractionated into a water-soluble fraction C, a hexane-soluble fraction H and a methanol-soluble fraction D (Scheme 1) in an attempt to identify the active compound(s) in *S. dura*. Both the C and D fraction were tested for their bioactivity in the AA-release assay and they inhibited IL-1β induced AA-release in a dose-dependent manner, but with different efficacies. The inhibition ob-

erved for fraction D, when the treatments with 0.22, 0.11 and 0.06 mg mL<sup>-1</sup> resulted in a 97, 91 and 63 % inhibition of AA-release, respectively, was much higher than that observed for fraction C (Fig. 2A and B). Moreover, compared to the inhibition obtained with the crude extract, fraction D was far more efficient as the *IC*<sub>50</sub> value determined for fraction D was in the range of ng mL<sup>-1</sup>, not mg mL<sup>-1</sup> as observed for the crude extract. Fraction H was not tested due to the harmful effect of *n*-hexane to cells. This indicated that most of the bioactive compound(s) responsible for the inhibition of AA-release were located in the methanol-soluble fraction of the crude extract.

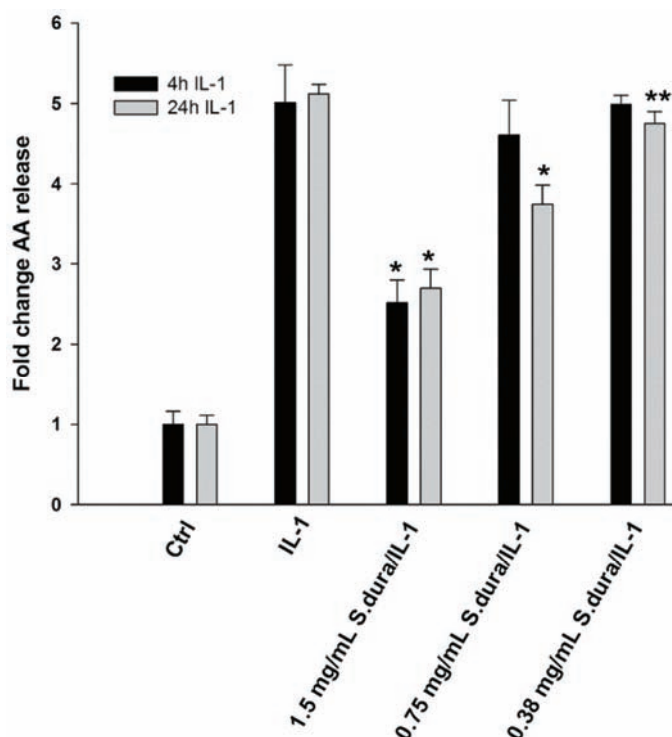


Fig. 1. Crude extract of *S. dura* inhibits IL-1 (10 ng mL<sup>-1</sup>) induced release of arachidonic acid in a time- and dose-dependent manner in SW982 cells. \**p* < 0.001, \*\**p* < 0.02 by Student's *t*-test (means ± SD of three experiments each performed in triplicate).

#### *Antioxidant activity, phenolic content, flavonoid content and free radical scavenging activity of *S. dura* crude extract*

After demonstrating that the crude extract of *S. dura* was effective in inhibiting AA-release, the antioxidant capacity of the crude extract was determined because a good anti-inflammatory activity often accompanies a good antioxidant activity.<sup>14,15</sup> The determination of the antioxidant capacity included the quantifi-

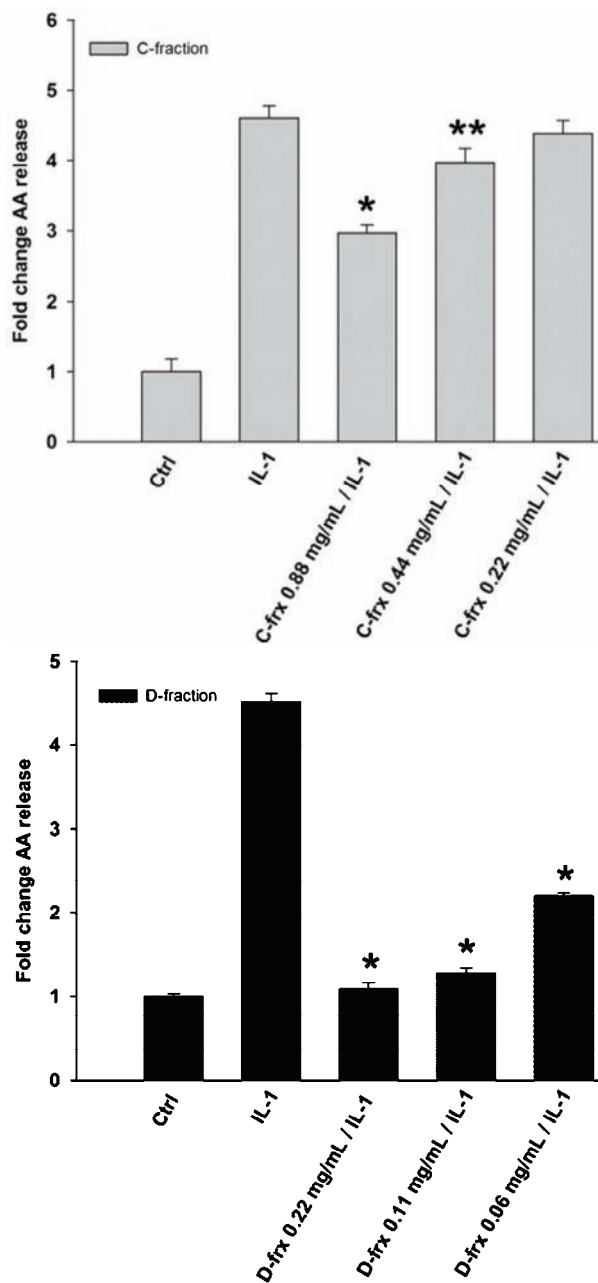


Fig. 2. Different fractions of the *S. dura* crude extract inhibit IL-1 ( $10 \text{ ng mL}^{-1}$ , 24 h) induced AA-release in a dose-dependent manner, but with varying efficacy: a) the water soluble fraction (C) inhibits AA-release at high concentrations and b) the methanol soluble fraction (D) inhibits AA-release more efficiently at lower concentrations. \* $p < 0.001$ , \*\* $p < 0.02$  by the students' *t*-test (means  $\pm SD$  of three experiments each performed in triplicate).

cation of the antioxidant activity, total phenolic content and the total flavonoid content by the linear regression method and an estimation of the free radical scavenging ability by the DPPH method. The antioxidant activity of the crude

extract of *S. dura* was 70.11 µg equivalents of  $\alpha$ -tocopherol, the total soluble phenolic content was 34.78 µg pyrocatechol equivalents and the total soluble flavonoid content was 22.80 µg quercetin equivalents per milligram of the plant extract (Table II). The free radical scavenging activities of several concentrations of *S. dura* extract were determined. The experiment was repeated under same conditions to determine the free radical scavenging activity of ascorbic acid, which was used as a standard. The  $IC_{50}$  values for the plant extract and ascorbic acid were determined by calculating the inhibition values for all used concentrations, taking the probit of all inhibition values and plotting them against the log of the respective concentrations. The  $IC_{50}$  value for the plant extract was 846.64 vs. 11.77 µg mL<sup>-1</sup> for ascorbic acid. The results showed that radical scavenging activities of both ascorbic acid and the plant extract were concentration dependent.

TABLE II. Total antioxidant activity, total soluble phenolic content and total soluble flavonoid content in the extract of *S. dura* compared to *D. falcata* and *W. tomentosa*

Plant	Total content of soluble phenolics, µg pyrocatechol equivalent mg <sup>-1</sup>	Total content of soluble flavonoids, µg quercetin equivalent mg <sup>-1</sup>	Total antioxidant activity, µg $\alpha$ -tocopherol equivalent mg <sup>-1</sup>
<i>S. dura</i>	34.78±0.38	22.80±0.16	70.11±0.66
<i>W. tomentosa</i>	7.20±0.88	16.90±1.00	4.20±0.03
<i>D. falcata</i>	38.66±1.86	21.59±1.09	—

In a quest to determine the antioxidant potency of *S. dura*, the obtained results were compared with the results reported in literature for the aerial parts of *Dendrophthoe falcata* (Loranthaceae) and the leaf extract of *Wrightia tomentosa* (Apocynaceae) (Table II). Both of these plants chosen for comparison have traditional use for the treatment of menstrual disorders,<sup>32–34</sup> *i.e.*, a similar ethnopharmacology to *S. dura*.

The comparison showed that *S. dura* had a 4.8 times higher total soluble phenolic content, a 1.3 times higher quercetin equivalent flavonoid content and a 17 times higher total antioxidant activity than *W. tomentosa*.<sup>42</sup> A comparison of crude extracts of both plants relative to the DPPH scavenging ability of ascorbic acid showed that the extract of *W. tomentosa* was 1.6 times more potent than the extract of *S. dura*.<sup>42</sup> On the other hand, there was not much difference in the total soluble phenolics and flavonoids content of *S. dura* and *D. falcata*.<sup>34</sup> The limitation in comparing the antioxidant activity and free radical scavenging activity of *S. dura* and *D. falcata* was the non-availability of published results of the  $\alpha$ -tocopherol equivalent antioxidant activity and DPPH scavenging ability compared to ascorbic acid of *D. falcata*. In summary, the antioxidant capacity of

*S. dura* is similar to that of *D. falcata* and far better than that of *W. tomentosa* except in terms of its free radical scavenging ability.

#### CONCLUSIONS

The results from the cellular testing of *S. dura* (crude extract and sub-fractions) in the AA-release assay suggested that the reported pain- and discomfort-relieving effects of the plant may be explained by the strong inhibitory effects on the arachidonic acid cascade. By reducing the availability of AA, the synthesis of eicosanoids may be reduced accordingly. Moreover, the total soluble phenolics and flavonoids contents of *S. dura* were similar to those of *D. falcata* but higher than those of *W. tomentosa*. Although *S. dura* is less effective in the DPPH assay, it has higher antioxidant properties compared to *W. tomentosa*.

The presence of flavonoid compounds, known for their various pharmacological activities, a considerably high antioxidant property and the fact that *S. dura* may exert anti-convulsive, anti-inflammatory and pain-relieving properties, gives reasons to believe that the use of the plant in traditional medicine has a solid chemical background. Identification of the active compound(s) is the next step in the study of *S. dura*, which could, potentially, reveal new drug candidates for various indications.

*Acknowledgements.* The funding of this study was provided by HEC Pakistan via SIU Norway. All experimental work was realised at the Department of Chemistry and Department of Biology, NT Faculty, Norwegian University of Science and Technology, Trondheim, Norway.

ИЗВОД  
АНТИИНФЛАМАТОРНА И АНТИОКСИДАТИВНА АКТИВНОСТ БИЉКЕ  
*Sclerochloa dura* (POACEAE)

SYED MAJID BUKHARI<sup>1</sup>, ASTRID JULLUMSTRØ FEUERHERM<sup>2</sup>, FAYSSAL BOULFRAD<sup>3</sup>, БОЈАН ЗЛАТКОВИЋ<sup>4</sup>,  
BERIT JOHANSEN<sup>2</sup> и НЕБОЈША СИМИЋ<sup>1</sup>

<sup>1</sup>Department of Chemistry, Norwegian University of Science and Technology, 7491 Trondheim, Norway,

<sup>2</sup>Department of Biology, Norwegian University of Science and Technology, 7491 Trondheim, Norway,

<sup>3</sup>UFR de Pharmacie, Grenoble, France и <sup>4</sup>Природно-математички факултазет,

Универзитет у Нишу, 18000 Ниш

Биљка *Sclerochloa dura* се традиционално користи у југоисточној Србији за олакшавање менструалних тегоба, као што су бол и претерано крварење. Према искуству корисница, убрзо по узимању биљке, смањује се крварење и бол. Циљ овог испитивања је да се утврди инхибиторни ефекат биљке на активност каскаде коју започиње арахидонска киселина (AA) и да се спектрофотометријски одреди антиоксидативна активност. Тест ослобађања AA изведен је коришћењем хумане ћелијске линије синовиоцита SW982, која је слична фибробластима, а мерена је активност фосфолипазе А2 (PLA<sub>2</sub>). Сирови екстракт и изоловане фракције *S. dura* инхибирају отпуштање AA које иницира интерлеукин 1, на временски и дозно зависан начин.  $IC_{50}$  сировог екстракта је 1,5 mg mL<sup>-1</sup> након 4 h, односно 24 h стимулације. Третирање ћелија метанолним екстрактом концентрација 0,22, 0,11 и 0,06 mg mL<sup>-1</sup> довело је до инхибиције отпуштања AA од 97, 91, односно 63 %. Један милиграм сировог екстракта је садржао фенолна једињења која

би одговарала 34,78 µg пирокатехола и флавоноида који би били еквивалентни 22,80 µg кверцетина. Антиоксидативна активност је била еквивалентна активности 70,11 µg α-токоферола. Јак инхибиторни ефекат екстракта *S. dura* на активацију АА каскаде би могао објаснити смањење бола и других неугодних осећаја.

(Примљено 2. децембра 2013, прихваћено 14. јануара 2014)

#### REFERENCES

1. C. D. Funk, *Science* **294** (2001) 1871
2. B. Johansen, K. Rakkestad, M. A. Balboa, E. A. Dennis, *Prostaglandins Other Lipid Mediator* **60** (2000) 119
3. R. H. Schaloske, E. A. Dennis, *Biochim. Biophys. Acta, Mol. Cell Biol. Lipids* **1761** (2006) 1246
4. J. E. Burke, E. A. Dennis, *J. Lipid Res.* **50** (2009) S237
5. V. Magrioli, G. Kokotos, *Expert Opin. Ther. Pat.* **20** (2010) 1
6. M. W. Anthonsen, S. Andersen, A. Solhaug, B. Johansen, *J. Biol. Chem.* **276** (2001) 35344
7. M. W. Anthonsen, A. Solhaug, B. Johansen, *J. Biol. Chem.* **276** (2001) 30527
8. R. M. Sommerfelt, A. J. Feuerherm, K. Jones, H. M. Tunset, B. Johansen, *PlosOne* (2013), Paper ID: PONE-D-13-31275R1
9. L. Leistad, A. J. Feuerherm, A. Faxvaag, B. Johansen, *Scand. J. Rheumatol.* **40** (2011) 308
10. R. W. Kelly, M. A. Lumsden, M. H. Abel, D. T. Baird, *Prostaglandins, Leukotrienes Med.* **16** (1984) 69
11. A. Lethaby, C. Augood, K. Duckitt, C. Farquhar, *Cochrane Database Syst. Rev.* (2007) CD000400
12. E. A. Willman, W. P. Collins, S. G. Clayton, *Br. J. Obstet. Gynaecol.* **83** (1976) 337
13. H. C. Brummer, *J. Obstet. Gynaecol. Br. Commonw.* **79** (1972) 526
14. C. C. Woo, A. P. Kumar, G. Sethi, K. H. B. Tan, *Biochem. Pharmacol.* **83** (2012) 443
15. D. B. Reddy, T. C. M. Reddy, G. Jyotsna, S. Sharan, N. Priya, V. Lakshmipathi, P. Reddanna, *J. Ethnopharmacol.* **124** (2009) 506
16. I. Gülcin, M. Oktay, Ö. I. Küfrevioğlu, A. Aslan, *J. Ethnopharmacol.* **79** (2002) 325
17. Y. S. Velioglu, S. Mazza, L. Gao, B. D. Oomah, *J. Agric. Food Chem.* **46** (1998) 4113
18. J. Zhishen, T. Mengcheng, W. Jianming, *Food Chem.* **64** (1999) 555
19. A. Barla, M. Öztürk, S. Kültür, S. Öksüz, *Fitoterapia* **78** (2007) 423
20. W. D. Clayton, M. Vorontsova, K. T. Harman, H. Williamson, *Royal Botanic Gardens*, <http://www.kew.org/data/grasses-db/www/imp09285.htm> (accessed 28 July 2014)
21. USDA. *National Genetic Resources Program. Germplasm Resources Information Network – (GRIN, Online Database)*, National Germplasm Resources Laboratory, Beltsville, MD, [http://www.ars-grin.gov/cgi-bin/npgs/html/tax\\_search.pl](http://www.ars-grin.gov/cgi-bin/npgs/html/tax_search.pl) (accessed 6 November 2012)
22. C. Shao, L. Wang, Y. Wang, G. Li, (Zibo Nab Agrochemicals Co., Ltd., China), CN 101438709 A (2009)
23. C. Liu, S. Wang, X. Wu, Y. Yang, T. Pang, Q. Zhai, (Anhui Huaxing Chemical Industry Co., Ltd., China), CN 101313677 A (2008)
24. X. Gao, M. Li, Q. Ge, J. Zhang, Z. Gao, Y. Zhang, *Zhiwu Baohu Xuebao* **38** (2011) 557
25. C. Feng, B. Yu, X. Lu, Y. Ji, A. Meng, (Peop. Rep. China), CN 101485323 A (2009)

26. G. Shen, B. Gu, Y. Zhang, Z. Qian, T. Li, D. Cai, W. Fan, X. Chai, (Shanghai Academy of Agricultural Sciences, Peop. rep. China; Shanghai Pesticide Research Institute), CN 101743964 A (2010)
27. G. Yu, Z. Zhou, Z. Ji, (Jiangsu Changqing Agrochemical Co., Ltd., China), CN 101513186 A (2009)
28. W. Li, S. Wang, G. Wang, Y. Liu, P. Xie, C. Liu, (Anhui Huaxing Chemical Industry Co., Ltd., China), CN 101485315 A (2009)
29. P. Catalán, P. Torrecilla, J. Á. L. Rodríguez, R. G. Olmstead, *Mol. Phylogenet. Evol.* **31** (2004) 517
30. M. K. Choo, R. J. Soreng, J. I. Davis, *Am. J. Bot.* **81** (1994) 119
31. A. V. Konarev, I. O. Vvedenskaya, *Doklady Vsesoyuznoi Akademii Sel'skokhozyaistvennykh Nauk imeni V. I. Lenina*, Issue 11, 1984, p. 16
32. L. J. Lin, G. Topcu, H. Lotter, N. Ruangrungsi, H. Wagner, J. M. Pezzuto, G. A. Cordell, *Phytochemistry* **31** (1992) 4333
33. B. Chakravarti, R. Maurya, J. A. Siddiqui, H. K. Bid, S. M. Rajendran, P. P. Yadav, R. Konwar, *J. Ethnopharmacol.* **142** (2012) 72
34. S. P. Pattanayak, P. M. Mazumder, P. Sunita, *Int. J. PharmTech Res.* **3** (2011) 1392
35. A. Turkoglu, I. Kivrak, N. Mercan, M. Duru, K. Gezer, H. Turkoglu, *Afr. J. Biotechnol.* **5** (2006) 1146
36. M. A. Ashraf, M. J. Maah, I. Yusoff, *Middle East J. Sci. Res.* **6** (2010) 465
37. C. Sarikurkcü, C. F. Eryigit, M. Cengiz, B. Tepe, A. Cakir, E. Mete, *Spectrosc. Lett.* **45** (2012) 352
38. S. M. Bukhari, N. Simic, H. L. Siddiqui, V. U. Ahmad, *World Appl. Sci. J.* **22** (2013) 1561
39. C. Hsu, *Biol. Res. Nurs.* **39** (2006) 281
40. S. Mohammadzadeh, M. Sharriatpanahi, M. Hamed, Y. Amanzadeh, S. E. S. Ebrahimi, S. N. Ostad, *Food Chem.* **103** (2007) 729
41. Y. K. Park, M. H. Koo, M. Ikegaki, J. L. Contado, *Braz. Arch. Biol. Techn.* **40** (1997) 97
42. K. Nagarajan, A. Mazumder, L. K. Ghosh, *Pharmacologyonline* **1** (2008) 196
43. S. Pavagadhi, G. S. Joseph, B. S. Jena, *Int. J. Food Prop.* **15** (2012) 549
44. N. Ara, H. Nur, *Res. J. Med. Med. Sci.* **4** (2009) 107
45. A. Boligon, R. P. Pereira, A. C. Feltrin, M. M. Machado, V. Janovik, J. B. T. Rocha, M. L. Athayde, *Bioresour. Technol.* **100** (2009) 6592
46. L. L. Mensor, F. S. Menezes, G. G. Leitão, A. S. Reis, T. C. Santos, C. S. Coube, S. G. Leitão, *Phytother. Res.* **15** (2001) 127
47. K. Rizwan, M. Zubair, N. Rasool, M. Riaz, M. Zia-ul-Haq, V. de Feo, *Int. J. Mol. Sci.* **13** (2012) 6440
48. D. J. M. Kumar, P. Priya, S. N. Balasundari, G. S. D. N. Devi, A. I. N. Rebecca, P. T. Kalaihelvan, *Middle East J. Sci. Res.* **11** (2012) 900.





## Synthesis, characterization, electrochemical behavior and antibacterial/antifungal activities of $[Cd(L)X_2]$ complexes with a new Schiff base ligand

MORTEZA MONTAZEROZOHORI<sup>1\*</sup>, SAHAR YADEGARI<sup>1</sup> and ASGHAR NAGHIHA<sup>2</sup>

<sup>1</sup>Department of Chemistry, Yasouj University, Yasouj 75918–74831, Iran and <sup>2</sup>Department of Animal Sciences, Faculty of Agriculture, Yasouj University, Yasouj, Iran

(Received 20 May, revised 8 October, accepted 18 October 2013)

**Abstract:** A new symmetrical bidentate Schiff base ligand (L) was applied for the synthesis of some new cadmium coordination compounds having the general formula  $[Cd(L)X_2]$ , in which X is a halide or a pseudo-halide. The ligand and all the cadmium complexes were characterized by elemental analysis, FT-IR, <sup>1</sup>H-NMR, <sup>13</sup>C-NMR and UV–Vis spectroscopy and by molar conductance measurements. Electrochemical behavior of ligand and Cd(II) complexes were investigated by the cyclic voltammetry method. The morphology and shape of the  $[Cd(L)Cl_2]$  particles were depicted by SEM. Antimicrobial properties, such as antibacterial and antifungal activities, of the complexes as compared with ligand were checked against three Gram-negative bacteria: *Escherichia coli* (ATCC 25922), *Pseudomonase aeruginosa* (ATCC 9027) and *Salmonella* Spp. two Gram-positive bacteria: *Staphylococcus aureus* (ATCC 6538) and *Corynebacterium renale* and three fungal strains, including *Aspergillus niger*, *Penicillium chrysogenum* and *Candida albicans*. The results revealed appropriate antibacterial and antifungal activities for all compounds, and it was found that coordination of the ligand to Cd(II) lead to an increase in the antimicrobial activities in most of cases.

**Keywords:** Schiff base; complex; bidentate; voltammetry; antibacterial; anti-fungal.

### INTRODUCTION

Nowadays, facile and simple syntheses of Schiff base ligands and their metal complexes is consequential and comprehensive in coordination chemistry.<sup>1</sup> The Schiff base compounds have a wide range of applications including their usage as dyes and pigments, catalysts, stabilizers of polymers, antibacterial, antifungal, anticancer, antimalarial, antivirus and herbicidal compounds.<sup>2–8</sup> Irregular consumption of clinical drugs has caused a resistance in biological systems against

\*Corresponding author. E-mail: mmzohori@mail.yu.ac.ir  
doi: 10.2298/JSC130520110M

routine antibacterial and antifungal drugs; hence, the synthesis of novel drugs is a necessity.<sup>9–11</sup> Some Schiff base complexes of cadmium containing ligands such as 1,10-phenanthroline-2,9-dicarboxaldehyde-di-2-hydroxybenzoylhydrazone, (*E*)-2-((pyridin-2-yl)methyleneamino) benzoic acid and *N,N'*-(bis(pyridine-2-yl)benzylidene)-1,4-butanediamine possessing various properties, such as structural and chemo-luminescence, have been reported in the literature.<sup>12–15</sup> Some other cadmium Schiff base complexes with the ligands 2-[3-(2-aminophenoxy)naphthalen-2-yloxy]benzenamine and a Schiff base derived from naphthofuran-2-carbohydrazide and cinnamaldehyde were found to show biological properties, such as antibacterial and antifungal activities.<sup>16,17</sup> A literature survey showed that in most of them, the ligand had lower activities in comparison to those of its complexes.<sup>18–21</sup> In the present research, in continuation of previous reports,<sup>22–26</sup> the synthesis, characterization and electrochemical behavior of some Cd(II) complexes of a new bidentate Schiff base are described. The biological activities of these complexes were evaluated and compared with those of the free ligand.

## EXPERIMENTAL

### *Materials and methods*

2,2-Dimethyl-1,3-diaminopropane, 3-(2-nitrophenyl)-1-propenal and the employed Cd(II) salts were provided by Merck, Aldrich or BDH. Cadmium thiocyanate and azide were prepared according to previously reported methods.<sup>22,26</sup> The FTIR spectra were recorded on a JASCO-FT/IR 680 instrument between 4000–400 cm<sup>-1</sup> using the potassium bromide pressed pellets technique. The Ultraviolet-Visible spectra were obtained at room temperature using a JASCO-V570 spectrometer in chloroform and/or dimethylfomamide solution. The <sup>1</sup>H- and <sup>13</sup>C-NMR spectra were recorded using an Avance III 400 MHz NMR spectrometer in (CD<sub>3</sub>)<sub>2</sub>SO and/or CDCl<sub>3</sub>. Microanalysis was realized using a CHN analyzer. Molar conductance of each compound was evaluated by a Metrohm-712 conductometer at a concentration of 10<sup>-3</sup> M solution of the Schiff base ligand and cadmium complexes in chloroform and/or DMF at room temperature. Electrochemical behavior of ligand and its cadmium complexes were studied at room temperature using a SAMA500 Electro-Analyzer at a scan rate of 0.1 V s<sup>-1</sup> in dry acetonitrile (10<sup>-3</sup> mol dm<sup>-3</sup>) under a deoxygenated atmosphere (by blowing argon gas into the solution for about 2 min). The supporting electrolyte was *n*-Bu<sub>4</sub>NPF<sub>6</sub>(TBAHFP). The three electrodes used in this technique were a GC working electrode, Pt-disk supporting electrode and silver wire reference electrode.

### *Synthesis of the ligand (L)*

The bidentate Schiff base ligand was prepared by the gradually addition of 2,2-dimethyl-1,3-diaminopropane (1 mmol) to 3-(2-nitrophenyl)-1-propenal (2 mmol) in ethanol according to a previous report.<sup>27</sup> The resultant honey-colored precipitate was filtered and washed twice with ethanol.

### *Synthesis of [Cd(L)X<sub>2</sub>] type complexes (X = Cl<sup>-</sup>, Br<sup>-</sup>, I<sup>-</sup>, NCS<sup>-</sup> or N<sub>3</sub><sup>-</sup>)*

The cadmium complexes were prepared by the dropwise addition of the ligand (1 mmol in 10 mL) to an ethanolic solution of the required cadmium salt (1 mmol in 10 mL) under vigorous stirring of reaction mixture over 2–3 h at room temperature. Then the cream or milky

precipitate was filtered and washed twice with ethanol. Purification of the metal complexes was realized by recrystallization from dichloromethane/ethanol 1:1 mixture.

#### *Antibacterial activity (in vitro)*

The Schiff base ligand and its cadmium complexes were tested for their antibacterial activities against three Gram-negative bacteria, *i.e.*, *Escherichia coli* (ATCC 25922), *Pseudomonas aeruginosa* (ATCC 9027) and *Salmonella* Spp. and two Gram-positive bacteria, *i.e.*, *Staphylococcus aureus* (ATCC 6538) and *Corynebacterium renale* using the disk diffusion method.<sup>28</sup> Thus, disinfected plates were filled with 12 mL of sterilized Muller–Hinton agar medium (Merck, Germany). Afterwards, 100 µL of particular bacterium which contained of  $0.5 \times 10^6$  CFU mL<sup>-1</sup> (tantamount to 0.5 McFarland standards) was dispersed on the plate surfaces using a sterile swab for about 10 minutes for suitable adsorption.<sup>29,30</sup> Different active disks (6 mm in diameter) of ligand and cadmium complexes (with 2.5, 1.25, 0.5 mg of compound per disk) were constructed and placed on distinctive positions on the agar plates. Prepared plates were incubated at 37 °C for 24 h. The inhibition zone diameter (mm) of each compound was measured using a caliper. DMSO, as the solvent, showed no effect on the biological tests. Disks with the antibacterial drugs amoxicillin, penicillin and cephalexin were applied as positive controls.

#### *Minimum inhibitory concentration (MIC)*

The MIC values were determined as the second applicable test for the investigation of antibacterial properties of ligand and its complexes by serial dilution of each compound (16000 to 3.9 µg mL<sup>-1</sup>).<sup>31</sup> For this means, after preparation of various concentrations of compounds, 650 µL of sterile Muller–Hinton broth medium (Scharlab) and 100 µL of a specific bacterium were added to sterile sample tubes that were then incubated at 37 °C for 24 h. The lowest concentration that inhibited the ocular growth of bacteria (absence of turbidity in the test tubes after incubation for 24 h) was considered as the MIC value.

#### *Minimum bactericidal concentration (MBC)*

The intrinsic turbidity of compounds in solution necessitated the application of the MBC test as the third method for the investigation of antibacterial activities. A loop full of broth of dilution used for the MIC tests in Muller Hinton broth medium was spread on agar plates and then incubated at 37 °C for 24 h.<sup>32</sup> In this method, observation of bacterial growth on the surface of agar medium became possible and therefore recognition of antibacterial activities of compounds was easier with respect to the MIC test.

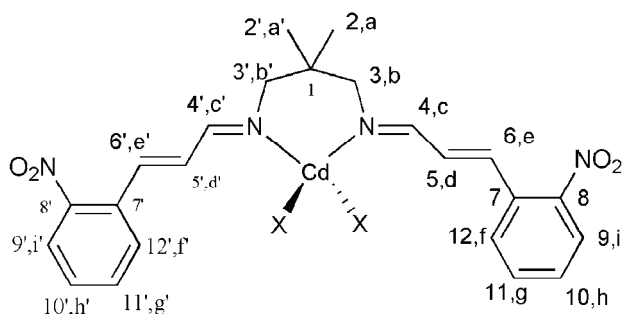
#### *Antifungal activity*

Antifungal activities of cadmium complexes as compared with free ligand were checked against three fungal strains, *i.e.*, *Aspergillus niger*, *Penicillium chrysogenum* and *Candida albicans* (local isolates). For estimation of the antifungal properties of compounds, blank sterile disks (6 mm in diameter) were saturated with the test compounds and then the constructed disks with 5, 2.5, 1.25 mg of active compound per disk were situated on distinctive locations of Petri plates containing Sabouraud dextrose agar (SDA) medium (Oxoid, Basingstoke, UK) and impregnated with 100 µL of fungal spore suspensions (10<sup>5</sup> CFU mL<sup>-1</sup>). The prepared plates were incubated at 32 °C for 7 days for *A. niger* and *P. chrysogenum*, and at 37 °C for 24 h for *C. albicans*.<sup>32</sup>

## RESULTS AND DISCUSSION

*Physical and analytical data*

Some important physical and analytical data attributed to the ligand and the cadmium complexes are given in the Supplementary material to this paper. Low values of the molar conductance ( $0.009\text{--}0.031\text{ S m}^2\text{ mol}^{-1}$  in  $\text{CHCl}_3$  and  $49.20\text{--}74.64\text{ S m}^2\text{ mol}^{-1}$  in DMF) indicate that the cadmium complexes are non-electrolytes.<sup>33,34</sup> The results of microanalysis showed a 1:1 ratio of ligand to metal and thus the general structural formula of the complexes is suggested to be  $[\text{Cd}(\text{L})\text{X}_2]$  ( $\text{X}$  is halide or pseudo-halide, *i.e.*, thiocyanate or azide) (Scheme 1). All the compounds were soluble in DMSO and DMF but insoluble in alcohols. The solid compounds were stable at room temperature. In order to obtain information on the morphology of the solid complexes, an SEM image of the cadmium chloride complex was recorded, as shown in Fig. 1. The microphotograph illustrates a rod-like nano-structure for this complex.



Scheme 1. Structural formula of  $[\text{Cd}(\text{L})\text{X}_2]$  complexes ( $\text{X}$  is  $\text{Cl}^-$ ,  $\text{Br}^-$ ,  $\text{I}^-$ ,  $\text{NCS}^-$  or  $\text{N}_3^-$ ).

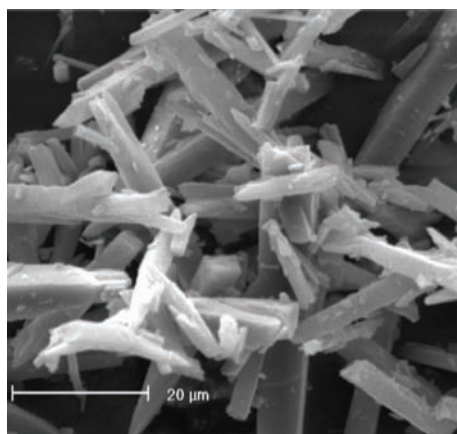


Fig. 1. SEM appearance of the  $[\text{Cd}(\text{L})\text{Cl}_2]$  complex.

### Spectral investigation

*IR and electronic spectra.* Preliminary characterization of the ligand and its cadmium complexes was performed by IR spectroscopy and some characteristic signals are given in the Supplementary material to this paper. The absence of peaks attributed to the parent aldehyde and amine functional groups at 1680 and 3200–3300 cm<sup>-1</sup>, respectively, and the appearance of new strong signals at 1636 and 1614 cm<sup>-1</sup> confirmed azomethine (C=N) formation.<sup>27,32</sup> After coordination of ligand *via* azomethine nitrogens, the C=N signals shifted to lower wavenumbers by 4–6 cm<sup>-1</sup>. The weak signal at 2869 cm<sup>-1</sup> in the ligand spectrum was ascribed to azomethine C–H groups. Two strong signals at 1529 and 1338 cm<sup>-1</sup> were assigned to the asymmetric and symmetric vibrations of the NO<sub>2</sub> groups of the ligand, respectively. These signals shifted to lower and higher wave numbers by 2 to 10 cm<sup>-1</sup> after binding of the ligand to the cadmium center.<sup>33</sup> In the complex spectrum of cadmium thiocyanate, a new sharp signal at 2059 cm<sup>-1</sup> was observed that could be safely assigned to the *N*-coordinated mode of the thiocyanate ion. In addition, a new signal at 2041 cm<sup>-1</sup> in the cadmium azide complex was appointed to coordinated azide ions.<sup>34,35</sup>

As reported in the Supplementary material to this paper, the absorption band at 295 nm and a shoulder band at 328 nm in the electronic spectrum of the ligand may be assigned to internal ligand electronic transitions ( $\pi-\pi^*$ ) of the aromatic, olefinic and azomethine  $\pi$ -systems. In the cadmium complexes, some red or blue shifts by 3–10 nm occurred due to coordination of the ligand to the metal centers *via* azomethine groups.

*<sup>1</sup>H- and <sup>13</sup>C-NMR spectra.* A <sup>1</sup>H- and <sup>13</sup>C-NMR spectral study could be considered as a powerful technique for proving a suggested structure. Accordingly, the <sup>1</sup>H- and <sup>13</sup>C-NMR spectra of the ligand and its Cd(II) complexes were recorded and the data are presented in the Supplementary material to this paper. The detailed assignments of the proton and carbon atoms of the ligand and its cadmium complexes (based on Scheme 1) confirmed the proposed structure. The <sup>1</sup>H-NMR spectra of the ligand and the cadmium iodide complex as typical spectra are illustrated in Figs. 2 and 3. Characteristic signals of the ligand <sup>1</sup>H- and <sup>13</sup>C-NMR spectra attributed to azomethine protons (H<sub>cc</sub>) and carbons (C<sub>4,4'</sub>) atoms appeared at 8.09 ppm (as a doublet with  $J = 8.76$  Hz) and 162.69 ppm respectively.<sup>22–27,36</sup> After coordination of the ligand to cadmium center *via* azomethine nitrogens as suggested in Scheme 1, the above-mentioned signals were found downfield shifted in the range 8.15–8.26 ppm and 162.96–169.75 ppm in the spectra of the cadmium complexes, except for the azomethine carbon signal in the spectrum of the cadmium thiocyanate complex that appeared at upfield chemical shifts. The chemical shifts ( $\delta$ ) assigned to the aromatic hydrogens H<sub>ii'</sub>, H<sub>gg'</sub>, H<sub>hh'</sub> and H<sub>ff'</sub>, the olefin hydrogens H<sub>dd'</sub> and H<sub>ee'</sub> of the ligand were found downfield shifted in the spectra of all complexes except for cadmium chloride,

thiocyanate and azide. The aliphatic hydrogens of the ligand were upfield shifted except for the cadmium bromide and iodide complexes. Similar to the  $^1\text{H}$ -NMR signals, the coordination of the ligand to cadmium ion led to up or downfielded chemical shifts in the  $^{13}\text{C}$ -NMR signals in the spectra of the cadmium complexes. It be noted that in the spectrum of  $[\text{Cd}(\text{L})(\text{NCS})_2]$ , one additional signal appeared at 135.51 ppm that may be ascribed to the carbon of the *N*-coordinated thiocyanate.

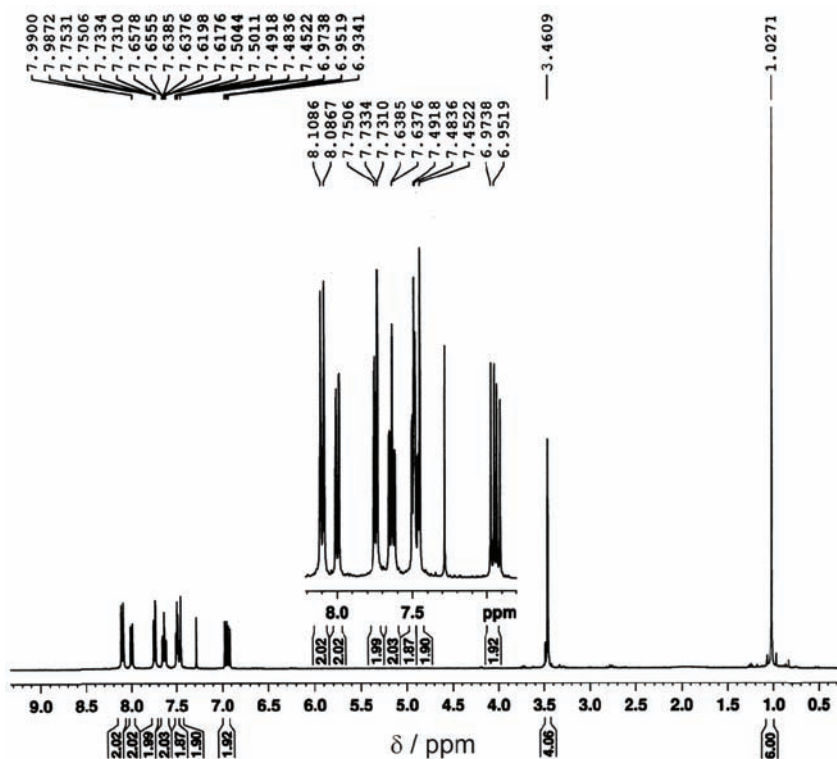


Fig. 2. The  $^1\text{H}$ -NMR spectrum of the ligand.

### *Electrochemical investigation*

Cyclic voltammetry was used as a technique for the study of the redox properties of the ligand and its cadmium complexes, as depicted in Fig. 4. The important electrochemical data are collected in Table I. The cyclic voltammogram of TBAHFP as the supporting electrolyte shows no notable redox activity in acetonitrile under an argon atmosphere at a scan rate of  $0.1 \text{ V s}^{-1}$  in the potential range 0.5 to  $-2.0 \text{ V}$ . The voltammogram of the ligand demonstrated two cathodic waves (at  $-0.87$  and  $-1.40 \text{ V}$ ) and in the contrary potential sweep, it was oxidized reversibly and irreversibly at  $-0.80$  and  $-0.56 \text{ V}$ , respectively. The first

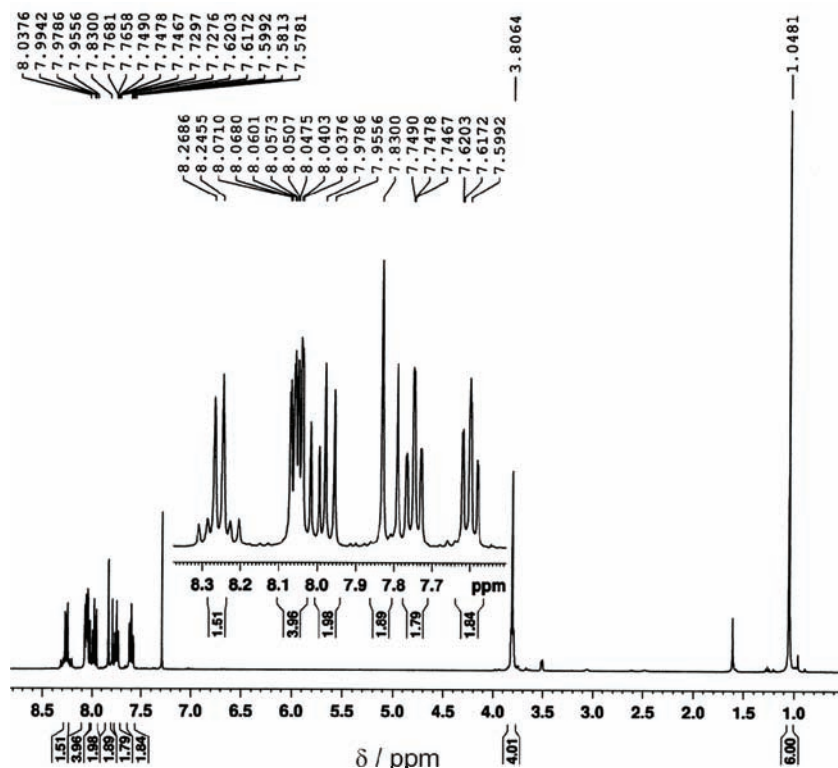


Fig. 3. The  $^1\text{H}$ -NMR spectrum of the cadmium iodide complex.

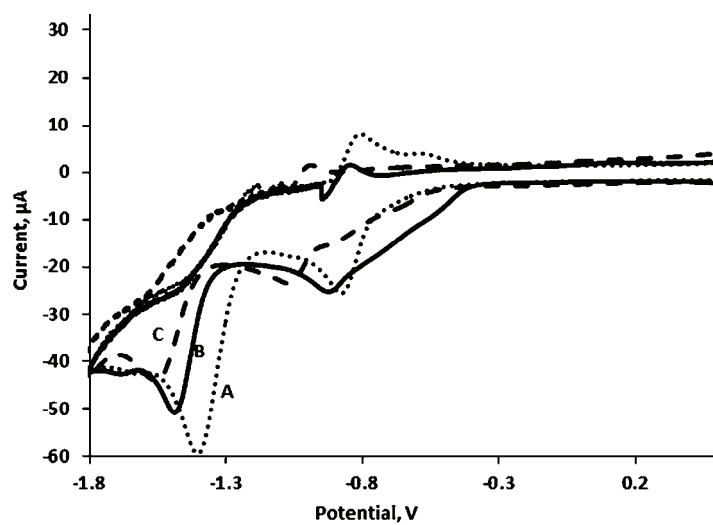


Fig. 4. Cyclic voltammograms of A) the ligand, B) the cadmium iodide complex and C) the cadmium azide complex.

TABLE I. Anodic and cathodic potentials of ligand and its Cd (II) complexes in the voltammograms; Pa and Pc refer to the anodic and cathodic potentials, respectively

Compound	* $E_{Pa1}, E_{Pa2}$ / V	* $E_{Pc1}, E_{Pc2}$ / V
Ligand	-0.80, -0.56	-0.87, -1.40
[Cd(L)Cl <sub>2</sub> ]	-0.97, -0.73	-1.07, -1.64
[Cd(L)Br <sub>2</sub> ]	-0.96	-1.02, -1.57
[Cd(L)I <sub>2</sub> ]	-0.85	-0.92, -1.48
[Cd(L)(NCS) <sub>2</sub> ]	-1.03	-1.09, -1.62,
[Cd(L)(N <sub>3</sub> ) <sub>2</sub> ]	-1.0	-1.06, -1.55

redox pair may be assigned to the reversible one-electron redox of the nitro group, *i.e.*, the nitro/nitro radical anion couple, and the second redox may be assigned to the irreversible three-electron redox *via* the hydroxylamine/nitroso pair.<sup>37</sup> All the complexes were found to be redox active under the same conditions due to the behavior of the ligand. The cathodic and anodic waves of the coordinated ligand in the cadmium complexes were shifted to more negative potentials as compared with the respective waves for the free ligand, which maybe a result of coordination. As compared with the free ligand, the cadmium chloride complex was oxidized and reduced in a similar manner to the ligand but with a negative shift in the potential values. In the other complexes, only one anodic wave with a negative shift in the range -0.85 to 1.03 V was observed, indicating easier oxidation of the coordinated ligand, while they were reduced in a manner similar to that seen for the free ligand but at more negative potentials, suggesting harder reduction of the ligand after coordination. It should be noted that the maximum negative shift of the potential values was related to the cadmium thiocyanate complex, which maybe due to the strongest binding of the ligand to the cadmium ion in this complex.

#### *Antibacterial bioassay (in vitro)*

Regarding the fact that finding an application for each novel compound seemed to be useful, it was decided to explore the biological activity of the ligand and its new cadmium complexes. Fortunately, these compounds showed acceptable results from the antibacterial point of view. The antibacterial activities of these compounds were closely checked against three Gram-negative bacterial strains, *i.e.*, *E. coli* (ATCC 25922), *P. aeruginosa* (ATCC 9027) and *Salmonella* Spp., and two Gram-positive bacterial strains, *i.e.*, *S. aureus* (ATCC 6538) and *C. renale* (Tables II and III). In an overall view, the results revealed the low efficiency for the compounds as compared with standard antibiotics (amoxicillin, penicillin and cephalexin) under the chosen conditions, except against *P. aeruginosa* bacterium, the growth of which was suitably inhibited by all the compounds where as the antibiotics had no effect. The results showed that [CdLCl<sub>2</sub>] was a powerful compound against *E. coli*, *P. aeruginosa* and *Salmonella* Spp.

bacteria.  $[Cd(L)Br_2]$  was an effective compound against *S. aureus* bacterium.  $[Cd(L)I_2]$  exhibited a significant effect (with an inhibition zone of 36.5 mm) against *C. renale*. The ligand showed the minimum effect against some kinds of bacteria in this research, i.e., *E. coli*, *Salmonella* Spp. and *C. renale* and had a medium effect (with an inhibition zone of 16 mm) against *S. aureus* and a poor effect after complexation of  $[Cd(L)(NCS)_2]$  against *P. aeruginosa* bacterium. The *MIC* and *MBC* values revealed that  $CdLBr_2$  ( $3.9 \mu\text{g ml}^{-1}$ ) had the maximum activity against *E. coli*, while the complex  $[Cd(L)(NCS)_2]$ , with the same value, was the effective compound against *P. aeruginosa* bacterium. The  $[Cd(L)Br_2]$  and  $[Cd(L)I_2]$  complexes exhibited maximum antibacterial activities against *C. renale*. In the case of *S. aureus* bacterium, all the compounds had nearly the same effect ( $125 \mu\text{g ml}^{-1}$ ) according to the *MIC* and *MBC* results.

TABLE II. Antibacterial activities of prepared disks saturated at 5, 2.5 and 1.25 mg per disk of ligand or its Cd(II) complexes, established from the diameter of the inhibition zone, mm, against different bacterial strains

Compound	Gram-negative bacteria						Gram-positive bacteria					
	<i>E. coli</i>			<i>P. aeruginosa</i>			<i>Salmonella</i> Spp.			<i>C. renale</i>		
	2.5	1.25	0.5	2.5	1.25	0.5	2.5	1.25	0.5	2.5	1.25	0.5
Ligand	9	7.8	7	17.1	13.7	7.3	9.3	9.0	8.6	14.4	12.0	10.0
$[Cd(L)Cl_2]$	18.7	14.6	12.9	27.2	20.5	12.6	17.5	14.3	12.5	35.7	29.8	24.0
$[Cd(L)Br_2]$	12.5	10.5	7.4	18.8	18.1	17.0	17.0	15.3	12.6	33.2	29.0	24.4
$[Cd(L)I_2]$	15.7	12.7	11.5	24.3	20.2	15.5	15.8	15.2	14.9	36.5	34.5	31.6
$[Cd(L)(NCS)_2]$	11.5	11.1	10	16.9	14.0	10.0	14.8	13.3	12.6	35.0	32.0	30.0
$[Cd(L)(N_3)_2]$	16.0	14.0	10.5	19.5	17.6	16.0	15.3	14.6	12.7	24.5	22.4	20.0

TABLE III. *MIC* and *MBC* ( $\mu\text{g/mL}$ ) inhibitory results of Schiff base ligand and its cadmium complexes; N.D.: not possible to detect

Compound	<i>E. coli</i>		<i>P. aeruginosa</i>		<i>Salmonella</i> Spp.		<i>C. renale</i>		<i>S. aureus</i>	
	<i>MIC</i>	<i>MBC</i>	<i>MIC</i>	<i>MBC</i>	<i>MIC</i>	<i>MBC</i>	<i>MIC</i>	<i>MBC</i>	<i>MIC</i>	<i>MBC</i>
Ligand	N.D.	31.2	N.D.*	1000	N.D.	16000	N.D.	500	N.D.	125
$[Cd(L)Cl_2]$	N.D.	31.2	125	250	N.D.	250	N.D.	15.6	N.D.	125
$[Cd(L)Br_2]$	3.9	3.9	31.2	125	N.D.	1000	N.D.	3.9	N.D.	125
$[Cd(L)I_2]$	N.D.	15.6	62.5	62.5	N.D.	2000	N.D.	3.9	N.D.	125
$[Cd(L)(NCS)_2]$	62.5	125	N.D.	3.9	N.D.	1000	N.D.	15.6	N.D.	125
$[Cd(L)(N_3)_2]$	250	250	N.D.	62.5	N.D.	250	125	125	N.D.	125

#### Antifungal bioassay (in vitro)

The antifungal properties of the compounds were tested against *A. niger*, *P. chrysogenum* and *C. albicans* fungal strains and the diameters of the zone of inhibition (in mm) of the compounds are listed in Table IV. The  $[Cd(L)Br_2]$  complex significantly prevented the growth of *A. niger* (inhibition zone of 29.7

mm) and the  $[Cd(L)(N_3)_2]$  and  $[Cd(L)(NCS)_2]$  complexes showed the same acceptable activities, while the free ligand had the minimum antifungal property. The  $[Cd(L)Br_2]$  and  $[Cd(L)(N_3)_2]$  complexes had similar zones of inhibition of the growth of *P. chrysogenum* (23.9 and 24 mm, respectively). The  $[Cd(L)I_2]$  and  $[Cd(L)(NCS)_2]$  complexes exhibited similar but lower activities than the  $[Cd(L)Br_2]$  and  $[Cd(L)(N_3)_2]$  complexes, while the free ligand showed the minimum effect on *P. chrysogenum*. The  $[Cd(L)I_2]$  complex was found to be the best anti-*C. albicans* agent in this research.  $[Cd(L)(N_3)_2]$  and  $[Cd(L)Br_2]$  complexes exhibited a medium effect against *C. albicans*. The lowest activity against *C. albicans* was evaluated for the  $[Cd(L)(NCS)_2]$  complex.

TABLE IV. Antifungal activities of the prepared disks saturated with 5, 2.5 and 1.25 mg per disk of ligand or its Cd(II) complexes, established from the diameter of the inhibition zone, mm, against different fungi

Compound	<i>A. niger</i>			<i>P. chrysogenum</i>			<i>C. albicans</i>		
	5	2.5	1.25	5	2.5	1.25	5	2.5	1.25
Ligand	0.9	0.8	0.65	16.7	15	14	21	19.2	18.0
$[Cd(L)Cl_2]$	18.6	17.5	17.2	21.3	18	15.3	20.7	20	19.4
$[Cd(L)Br_2]$	26.4	29.7	19.0	25.4	23.9	18.0	24.2	21.6	19.0
$[Cd(L)I_2]$	14.9	12.6	10.4	25.4	20.8	15.4	25.8	23.1	20.7
$[Cd(L)(NCS)_2]$	21.0	19.8	16.3	22.2	20.5	18.0	21.0	17.5	15.3
$[Cd(L)(N_3)_2]$	22.5	19.7	16.0	28.2	24.0	20.0	27.4	22.0	17.0

#### CONCLUSIONS

In this paper, the synthesis method of a new Schiff base ligand is presented and some of its cadmium complexes are introduced. Some spectral specifications, the electrochemical behavior and antibacterial/antifungal activities of the synthesized compounds are described. The results of elemental analysis confirmed a 1:1 ratio of ligand to metal salt perfectly. Based on physical and spectral (IR, UV–Vis and NMR) data, a pseudo-tetrahedral geometry was proposed for the cadmium coordination compounds. The solid compounds were stable for a long duration at room temperature. The redox behavior of the ligand and its complexes were investigated using the cyclic voltammetry technique. The voltammogram of ligand showed two redox steps as reversible and irreversible behavior. The related waves of the coordinated ligand were shifted to negative potentials in the voltammograms of all complexes because of its binding to cadmium ions. Antimicrobial investigations demonstrated that all compounds are antibacterial/antifungal active. In most of cases, complexation increased the ligand activity as compared with the free ligand. Generally, all the compounds showed more activity against *C. renale* than against the other bacteria. The  $[Cd(L)Br_2]$  complex exhibited the best activity against *A. niger*.

## SUPPLEMENTARY MATERIAL

Physical, analytic and spectral data for the ligand and its Cd(II) complexes are available electronically from <http://www.shd.org.rs/JSCS/>, or from the corresponding author on request.

*Acknowledgement.* Partial support of this research by Yasouj University is acknowledged.

## ИЗВОД

СИНТЕЗА, КАРАКТЕРИЗАЦИЈА, ЕЛЕКТРОХЕМИЈСКО ПОНАШАЊЕ И  
АНТИБАКТЕРИЈСКА И АНТИФУНГАЛНА АКТИВНОСТ  $[Cd(L)X_2]$  КОМПЛЕКСА СА  
ШИФОВОМ БАЗОМ КАО ЛИГАНДОМ

MORTEZA MONTAZEROZOHORI<sup>1</sup>, SAHAR YADEGARI<sup>1</sup> и ASGHAR NAGHIHA<sup>2</sup>

<sup>1</sup>Department of Chemistry, Yasouj University, Yasouj 75918–74831, Iran и <sup>2</sup>Department of Animal Sciences, Faculty of Agriculture, Yasouj University, Yasouj, Iran

У овом раду су синтетизовани нови комплекси кадмијума(II) опште формуле  $[Cd(L)X_2]$  ( $X$  је халогенид или псевдохалогенид), полазећи од нове Шифове базе, као симетричног бидентатног лиганда ( $L$ ). Применом елементалне микроанализе, FT-IR,  $^1H$ - и  $^{13}C$ -NMR, UV-Vis методе и мерењем моларне проводљивости окарактерисани су полазни лиганд и сви синтетизовани комплекси кадмијума(II). Применом цикличне волтаметрије испитивано је електрохемијско понашање лиганда и Cd(II) комплекса. Испитивана је антибактеријска активност лиганда и синтетизованих комплекса на три Грам-негативне бактерије, *Escherichia coli* (ATCC 25922), *Pseudomonas aeruginosa* (ATCC 9027) и *Salmonella spp.*, на две Грам-позитивне бактерије, *Staphylococcus aureus* (ATCC 6538) и *Corynebacterium renale*, као и антифунгална активност на три врсте гљива, *Aspergillus niger*, *Penicillium chrysogenum* и *Candida albicans*. Добијени резултати су показали да, у већини случајева, комплекси имају већу антимикробиолашку активност од самог лиганда.

(Примљено 20. маја, ревидирано 8. октобра, прихваћено 18. октобра 2013)

## REFERENCES

1. K. C. Gupta, Alekha Kumar Sutar, *Coord. Chem. Rev.* **252** (2008) 1420
2. D. N. Dhar, C. L. Taploo, *J. Sci. Ind. Res.* **41** (1982) 501
3. P. Przybylski, A. Huczynski, K. Pyta, B. Brzezinski, F. Bartl, *Curr. Org. Chem.* **13** (2009) 124
4. B. S. Holla, B. Veerendra, M. K. Shivananda, B. Poojary, *Eur. J. Med. Chem.* **38** (2003) 759
5. K. Singh, M. S. Barwa, P. Tyagi, *Eur. J. Med. Chem.* **42** (2007) 394
6. N. Raman, S. Ravichandran, C. Thangaraja, *J. Chem. Sci.* **116** (2004) 215
7. R. Nair, A. Shah, S. Baluja, S. Chanda, *J. Serb. Chem. Soc.* **71** (2006) 733
8. J. Lv, T. Liu, S. Cai, X. Wang, L. Liu, Y. Wang, *J. Inorg. Biochem.* **100** (2006) 1888
9. F. Baquero, *J. Antimicrob. Chemother.* **39** (1997) 1 (Suppl. A)
10. M. N. Alekshun, S. B. Levy, *Cell* **128** (2007) 1037
11. L. B. Rice, *Biochem. Pharmacol.* **71** (2006) 991
12. J. Chakraborty, B. Samanta, G. Pilet, S. Mitra, *Inorg. Chem. Commun.* **10** (2007) 40
13. C. Y. Niu, B. L. Wu, X. S. H. Wan, H. Y. Zhang, H. Q. Zhang, *J. Mol. Struct.* **973** (2010) 194
14. S. H. Shit, J. Chakraborty, B. Samanta, G. Pilet, S. Mitra, *J. Mol. Struct.* **919** (2009) 361

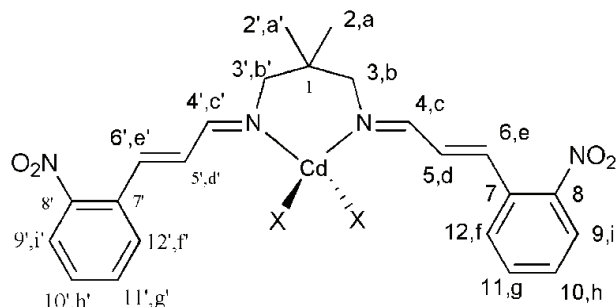
15. S. Das, B. N. Sarkar, K. Bhar, S. Chattopadhyay, H. K. Fun, P. Mitra, B. Kumar Ghosh, *Inorg. Chem. Commun.* **13** (2010) 353
16. M. B. Halli, R. B. Sumathi, *J. Mol. Struct.* **1022** (2012) 130
17. H. Keypour, M. Shayesteh, M. Rezaeivala, F. Chalabian, Y. Elerman, O. Buyukgungor, *J. Mol. Struct.* **1032** (2013) 62
18. S. R. Collinson, D. E. Fenton, *Coord. Chem. Rev.* **148** (1996) 19
19. A. K. Saxena, F. Huber, *Coord. Chem. Rev.* **95** (1989) 109
20. T. Sedaghat, M. Monajemzadeh, H. Motamedi, *J. Coord. Chem.* **64** (2011) 3169
21. T. Sedaghat, M. Naseh, H. R. Khavasi, H. Motamedi, *Polyhedron* **33** (2012) 435
22. M. Montazerohori, S. A. R. Musavi, *J. Coord. Chem.* **61** (2008) 3934
23. M. Montazerohori, *J. Therm. Anal. Calorim.* **111** (2013) 121.
24. M. Montazerohori, S. Khani, H. Tavakol, A. Hojjati, M. Kazemi, *Spectrochim. Acta, A* **81** (2011) 122
25. M. Montazerohori, S. Joohari, S. A. Musavi, , *Spectrochim. Acta, A* **73** (2009) 231
26. M. Montazerohori S. Joohari, S. A. Musavi, *J. Coord. Chem.* **62** (2009) 1285
27. M. Montazerohori, S. Yadegari, A. Naghiha, S. Veyseh, *J. Indust. Eng. Chem.* **20** (2014) 118
28. I. Ahmad, A. J. Beg, *J. Ethnopharmacol.* **74** (2001) 113
29. J. M. Andrews, *J. Antimicrob. Chemother.* **48** (2001) 5
30. M. Shakir, S. Khanam, F. Firdaus, A. Latif, M. Aatif, Saud I. Al-Resayes, *Spectrochim. Acta, A* **93** (2012) 354
31. M. J. Hearn, M. H. Cynamon, *J. Antimicrob. Chemother.* **53** (2004) 185
32. Z. H. Chohan, S. H. Sumrra, M. H. Youssoufi, T. B. Hadda, *Eur. J. Med. Chem.* **45** (2010) 2739
33. M. Grube, O. Muter, S. Strikauska, M. Gavare, B. Limane, *J. Ind. Microbiol. Biotechnol.* **35** (2008) 1545.
34. S. Chattopadhyay, M. G. B. Drew, A. Ghosh, *Inorg. Chim. Acta* **359** (2006) 4519
35. D. Das, B. G. Chand, K. K. Sarker, J. Dinda, C. Sinha, *Polyhedron* **25** (2006) 2333
36. Y. M. S. A. Al-Kahraman, H. M. F. Madkour, D. Ali, M. Yasinzai, *Molecules* **15** (2010) 660
37. S. Bollo, L. J. Nunez-Vergara, M. Bonta, G. Chauviere, J. Perie, J. A. Squella, *J. Electroanal. Chem.* **511** (2011) 46.

SUPPLEMENTARY MATERIAL TO  
**Synthesis, characterization, electrochemical behavior and  
antibacterial/antifungal activities of [Cd(L)X<sub>2</sub>] complexes  
with a new Schiff base ligand**

MORTEZA MONTAZEROZOHORI<sup>1\*</sup>, SAHAR YADEGARI<sup>1</sup> and ASGHAR NAGHIHA<sup>2</sup>

<sup>1</sup>Department of Chemistry, Yasouj University, Yasouj 75918–74831, Iran and <sup>2</sup>Department of Animal Sciences, Faculty of Agriculture, Yasouj University, Yasouj, Iran

*J. Serb. Chem. Soc.* 79 (7) (2014) 793–804



Structural formula of the [Cd(L)X<sub>2</sub>] complexes (X is Cl<sup>-</sup>, Br<sup>-</sup>, I<sup>-</sup>, NCS<sup>-</sup> and N<sub>3</sub><sup>-</sup>) with atomic numbering.

PHYSICAL, ANALYTIC AND SPECTRAL DATA FOR THE LIGAND AND ITS Cd(II)  
COMPLEXES

**Ligand.** Yield: 83 %; m.p.: 85 °C; Anal. Calcd. for C<sub>23</sub>H<sub>24</sub>N<sub>4</sub>O<sub>4</sub>: C, 65.70; H 5.75; N, 13.33 %. Found: C, 65.5, H, 5.6, N, 13.4 %; IR (KBr, cm<sup>-1</sup>): 2869w (iminic –CH stretching), 1636s (C=N– asym. stretching), 1614s (C=N– sym. stretching), 1529vs (–NO<sub>2</sub>, asym. stretching), 1338vs (–NO<sub>2</sub>, sym. stretching); <sup>1</sup>H-NMR (400 MHz, CDCl<sub>3</sub>, δ / ppm): 8.09 (2H, d, J = 8.76 Hz, H<sub>c,c'</sub>), 7.99 (2H, dd, J = 8.20 Hz, J = 1.12 Hz, H<sub>i,i'</sub>), 7.74 (2H, dd, J = 7.86 Hz, J = 1.0 Hz H<sub>f,f'</sub>), 7.64 (2H, dt, J = 7.26 Hz, J = 7.56 Hz, J = 0.92 Hz, H<sub>g,g'</sub>), 7.48 (2H, dt, J = 7.66 Hz, J = 7.44 Hz, J = 1.32 Hz, H<sub>h,h'</sub>), 7.48 (2H, d, J = 15.84 Hz, H<sub>e,e'</sub>), 6.94 (2H, dd, J = 15.86 Hz, J = 8.76 Hz, H<sub>d,d'</sub>), 3.46 (4H, s, H<sub>b,b'</sub>), 1.02 (6H, s, H<sub>a,a'</sub>); <sup>13</sup>C-NMR (100 MHz, CDCl<sub>3</sub>, δ / ppm): 162.69 (C<sub>4,4'</sub>), 147.96 (C<sub>8,8'</sub>), 135.68 (C<sub>6,6'</sub>),

\*Corresponding author. E-mail: mmzohori@mail.yu.ac.ir

133.35 (C<sub>9,9'</sub>), 133.04 (C<sub>7,7'</sub>), 131.49 (C<sub>5,5'</sub>), 129.27 (C<sub>12,12'</sub>), 128.38 (C<sub>11,11'</sub>), 124.87 (C<sub>10,10'</sub>), 70.75 (C<sub>3,3'</sub>), 36.96 (C<sub>1</sub>), 24.59 (C<sub>2,2'</sub>); UV–Vis (CHCl<sub>3</sub>) ( $\lambda_{\text{max}}$  / nm, ( $\varepsilon$  / L mol<sup>-1</sup> cm<sup>-1</sup>)): 295 (19876), 328(sh) (11045); Molar conductance (CHCl<sub>3</sub>) ( $\Lambda_M$  / S m<sup>2</sup> mol<sup>-1</sup>): 0.011.

*Cd(L)Cl<sub>2</sub>*. Yield: 92 %; m.p.(dec.): 243 °C; Anal. Calcd. for C<sub>23</sub>H<sub>24</sub>N<sub>4</sub>O<sub>4</sub>CdCl<sub>2</sub>: C, 45.75; H 4.01; N, 9.28 %. Found: C, 45.6, H, 3.9, N, 9.1 %; IR (KBr, cm<sup>-1</sup>): 2862m (iminic –CH stretching), 1633s (C=N– asym. stretching), 1613s (C=N– sym. stretching), 1519vs (–NO<sub>2</sub>, asym. stretching), 1339vs (–NO<sub>2</sub>, sym. stretching); <sup>1</sup>H-NMR (400 MHz, CDCl<sub>3</sub>,  $\delta$  / ppm): 8.17 (2H, d,  $J$  = 8.68 Hz H<sub>c,c'</sub>), 8.03 (2H, d,  $J$  = 8.16 Hz, H<sub>i,i'</sub>), 7.98 (2H, d,  $J$  = 7.88 Hz, H<sub>f,f'</sub>), 7.78 (2H, t,  $J$  = 7.64 Hz, J = 7.56 Hz, H<sub>g,g'</sub>), 7.62 (2H, t,  $J$  = 7.76 Hz, J = 7.72 Hz, H<sub>h,h'</sub>), 7.43 (2H, d,  $J$  = 15.80 Hz, H<sub>e,e'</sub>), 7.58 (2H, dd,  $J$  = 14.48 Hz, J = 7.44 Hz, H<sub>d,d'</sub>), 3.36 (4H, s, H<sub>b,b'</sub>), 0.91 (6H, s, H<sub>a,a'</sub>); <sup>13</sup>C-NMR (100 MHz, CDCl<sub>3</sub>,  $\delta$  / ppm): 164.30 (C<sub>4,4'</sub>), 148.01 (C<sub>8,8',6,6'</sub>), 136.25 (C<sub>9,9'</sub>), 133.60 (C<sub>7,7'</sub>), 132.11 (C<sub>5,5'</sub>), 130.06 (C<sub>12,12'</sub>), 128.43 (C<sub>11,11'</sub>), 124.56 (C<sub>10,10'</sub>), 69.82(C<sub>3,3'</sub>), 36.42 (C<sub>1</sub>), 24.17 (C<sub>2,2'</sub>); UV–Vis (DMF) ( $\lambda_{\text{max}}$  / nm, ( $\varepsilon$  / L mol<sup>-1</sup> cm<sup>-1</sup>)): 269 (8946), 295 (19641), 327(sh) (10641); Molar conductance (DMF) ( $\Lambda_M$  / S m<sup>2</sup> mol<sup>-1</sup>): 0.031.

[Cd(L)Br<sub>2</sub>]. Yield: 79 %; m.p.(dec.): 235 °C; Anal. Calcd. for C<sub>23</sub>H<sub>24</sub>N<sub>4</sub>O<sub>4</sub>CdBr<sub>2</sub>: C, 39.88; H 3.49; N, 8.09 %. Found: C, 39.7, H, 3.3, N, 8.3 %; IR (KBr, cm<sup>-1</sup>): 2867w (iminic –CH stretching), 1633s (asym. –C=N), 1615s (–C=N sym. stretching), 1524vs (–NO<sub>2</sub>, asym. stretching), 1348vs (–NO<sub>2</sub>, sym. stretching); <sup>1</sup>H-NMR (400 MHz, CDCl<sub>3</sub>,  $\delta$  / ppm): 8.23 (2H, d,  $J$  = 9.2 Hz, H<sub>c,c'</sub>), 8.05 (2H, dd,  $J$  = 8.10 Hz, J = 1.08 Hz, H<sub>i,i'</sub>), 8.04 (2H, d,  $J$  = 7.36 Hz, H<sub>f,f'</sub>), 7.95 (2H, dd,  $J$  = 15.44 Hz, J = 9.2 Hz, H<sub>d,d'</sub>), 7.78 (2H, d,  $J$  = 15.56 Hz, H<sub>e,e'</sub>), 7.74 (2H, t,  $J$  = 10.04 Hz, J = 7.88 Hz, H<sub>g,g'</sub>), 7.59 (2H, dt,  $J$  = 7.72 Hz, J = 1.12 Hz, J = 0.96 Hz H<sub>h,h'</sub>), 3.86(4H, s, H<sub>b,b'</sub>), 1.03 (6H, s, H<sub>a,a'</sub>); <sup>13</sup>C-NMR (100 MHz, CDCl<sub>3</sub>,  $\delta$  / ppm): 169.75 (C<sub>4,4'</sub>), 148.21 (C<sub>8,8'</sub>), 143.32 (C<sub>6,6'</sub>), 133.99 (C<sub>9,9'</sub>), 130.99(C<sub>5,5'</sub>), 129.62(C<sub>7,7'</sub>), 129.32(C<sub>12,12'</sub>), 128.82(C<sub>11,11'</sub>), 125.02 (C<sub>10,10'</sub>), 72.38 (C<sub>3,3'</sub>), 37.74 (C<sub>1</sub>), 24.83 (C<sub>2,2'</sub>); UV–Vis (CHCl<sub>3</sub>) ( $\lambda_{\text{max}}$  / nm, ( $\varepsilon$  / L mol<sup>-1</sup> cm<sup>-1</sup>)): 305 (28273), 325(sh) (22667); Molar conductance (CHCl<sub>3</sub>) ( $\Lambda_M$  / S m<sup>2</sup> mol<sup>-1</sup>): 0.009.

[Cd(L)I<sub>2</sub>]. Yield: 95 %; m.p.(dec.): 237 °C; Anal. Calcd. for C<sub>23</sub>H<sub>24</sub>N<sub>4</sub>O<sub>4</sub>CdI<sub>2</sub>: C, 35.12; H 3.08; N, 7.12 %. Found: C, 34.9, H, 3.2, N, 7.3 %; IR (KBr, cm<sup>-1</sup>): 2861w (iminic –CH stretching), 1635s (–C=N asym. stretching), 1614s (–C=N sym. stretching), 1524vs (–NO<sub>2</sub>, asym. stretching), 1348vs (–NO<sub>2</sub>, sym. stretching); <sup>1</sup>H-NMR (400 MHz, CDCl<sub>3</sub>,  $\delta$  / ppm): 8.26 (2H, d,  $J$  = 9.24 Hz, H<sub>c,c'</sub>), 8.06 (2H, dd,  $J$  = 8.16 Hz, J = 1.28 Hz, H<sub>i,i'</sub>), 8.05 (2H, dd,  $J$  = 7.92 Hz, J = 1.08 Hz, H<sub>f,f'</sub>), 7.99 (2H, dd,  $J$  = 15.44 Hz, J = 9.2 Hz, H<sub>d,d'</sub>), 7.81 (2H, d,  $J$  = 15.52 Hz H<sub>e,e'</sub>), 7.75 (2H, dt,  $J$  = 7.66 Hz, J = 7.64 Hz, J = 0.84 Hz, H<sub>g,g'</sub>), 7.60 (2H, dt,  $J$  = 7.82 Hz, J = 7.58 Hz, J = 1.28Hz, H<sub>h,h'</sub>),

3.81(4H, *s*, H<sub>b,b'</sub>), 1.05 (H6, *s*, H<sub>a,a'</sub>); <sup>13</sup>C-NMR (100 MHz, CDCl<sub>3</sub>, δ / ppm): 169.70 (C<sub>4,4'</sub>), 148.15 (C<sub>8,8'</sub>), 143.41 (C<sub>6,6'</sub>), 133.99 (C<sub>9,9'</sub>), 131.03 (C<sub>5,5'</sub>), 129.71 (C<sub>7,7'</sub>), 129.38 (C<sub>12,12'</sub>), 128.78 (C<sub>11,11'</sub>), 125.05 (C<sub>10,10'</sub>), 71.47 (C<sub>3,3'</sub>), 37.62 (C<sub>1</sub>), 24.90 (C<sub>2,2'</sub>); UV-Vis (CHCl<sub>3</sub>) (λ<sub>max</sub> / nm, (ε / L mol<sup>-1</sup> cm<sup>-1</sup>)): 302 (26263), 326(sh) (19754); Molar conductance (CHCl<sub>3</sub>) (A<sub>M</sub> / S m<sup>2</sup> mol<sup>-1</sup>): 0.011.

[Cd(L)(NCS)<sub>2</sub>]. Yield: 89 %; m.p.(dec.): 210 °C; Anal. Calcd. for C<sub>25</sub>H<sub>24</sub>N<sub>6</sub>O<sub>4</sub>CdS<sub>2</sub>: C, 46.26; H 3.73; N, 12.95 %. Found: C, 45.9, H, 3.6, N, 12.7 %; IR (KBr, cm<sup>-1</sup>): 2860w (iminic -CH stretching), 2059vs (-NCS), 1633s (-C=N asym. stretching), 1610s (-C=N sym. stretching), 1521vs (-NO<sub>2</sub>, asym. stretching), 1340vs (-NO<sub>2</sub> sym. stretching); <sup>1</sup>H-NMR (400 MHz, (CD<sub>3</sub>)<sub>2</sub>SO, δ / ppm): 8.15 (2H, *d*, *J* = 8.68 Hz, H<sub>c,c'</sub>), 8.02 (2H, *d*, *J* = 8.12 Hz, H<sub>i,i'</sub>), 8.00 (2H, *d*, *J* = 7.8 Hz, H<sub>f,f'</sub>), 7.75 (2H, *t*, *J* = 7.56 Hz, *J* = 7.44, H<sub>g,g'</sub>), 7.61 (2H, *t*, *J* = 7.52 Hz, *J* = 7.48 Hz, H<sub>h,h'</sub>), 7.39 (2H, *d*, *J* = 15.76 Hz, H<sub>e,e'</sub>), 7.05 (2H, *dd*, *J* = 14.90 Hz, *J* = 8.92 Hz, *J* = 8.2 Hz, H<sub>d,d'</sub>), 3.35 (4H, *s*, H<sub>b,b'</sub>), 0.93 (6H, *s*, H<sub>a,a'</sub>); <sup>13</sup>C-NMR (100 MHz, (CD<sub>3</sub>)<sub>2</sub>SO, δ / ppm): 160.57 (C<sub>4,4'</sub>), 147.97 (C<sub>8,8'</sub>), 143.18 (C<sub>6,6'</sub>), 135.51 (C<sub>SCN</sub>), 133.57 (C<sub>9,9'</sub>), 132.35 (C<sub>7,7'</sub>), 130.10 (C<sub>5,5'</sub>), 129.89 (C<sub>12,12'</sub>), 128.44 (C<sub>11,11'</sub>), 124.50 (C<sub>10,10'</sub>), 69.68 (C<sub>3,3'</sub>), 36.53 (C<sub>1</sub>), 24.25 (C<sub>2,2'</sub>); UV-Vis (DMF) (λ<sub>max</sub> / nm, (ε / L mol<sup>-1</sup> cm<sup>-1</sup>)): 268 (12934), 297 (22549), 327(sh) (13751); Molar conductance (DMF) (A<sub>M</sub> / S m<sup>2</sup> mol<sup>-1</sup>): 49.20.

[Cd(L)(N<sub>3</sub>)<sub>2</sub>]. Yield: 29 %; m.p.(dec.): 174 °C; Anal. Calcd. for C<sub>23</sub>H<sub>24</sub>N<sub>4</sub>O<sub>4</sub>CdBr<sub>2</sub>: C, 44.78; H, 3.92; N, 22.70 %. Found: C, 44.9, H, 4.1, N, 22.9 %; IR (KBr, cm<sup>-1</sup>): 2865w (iminic -CH stretching), 2041s (-N<sub>3</sub>), 1634s (-C=N asym. stretching), 1613s (-C=N sym. stretching), 1524vs (-NO<sub>2</sub>, asym. stretching), 1345vs (-NO<sub>2</sub> sym. stretching); <sup>1</sup>H-NMR (400 MHz, (CD<sub>3</sub>)<sub>2</sub>SO, δ / ppm): 8.15 (2H, *d*, *J* = 8.68 Hz, H<sub>c,c'</sub>), 8.02 (2H, *dd*, *J* = 8.28 Hz, *J* = 0.92 Hz, H<sub>i,i'</sub>), 7.99 (2H, *d*, *J* = 8.08 Hz, H<sub>f,f'</sub>), 7.75 (2H, *t*, *J* = 7.56 Hz H<sub>g,g'</sub>), 7.61 (2H, *dt*, *J* = 7.84 Hz, *J* = 7.66 Hz, *J* = 1.04 Hz, H<sub>h,h'</sub>), 7.38 (2H, *d*, *J* = 15.84 Hz, H<sub>e,e'</sub>), 7.04 (2H, *dd*, *J* = 15.66 Hz, *J* = 8.68 Hz, H<sub>d,d'</sub>), 3.36 (4H, *s*, H<sub>b,b'</sub>), 0.93 (6H, *s*, H<sub>a,a'</sub>); <sup>13</sup>C-NMR (100 MHz, (CD<sub>3</sub>)<sub>2</sub>SO, δ / ppm): 162.96 (C<sub>4,4'</sub>), 147.97 (C<sub>8,8'</sub>), 135.44 (C<sub>6,6'</sub>), 133.56 (C<sub>9,9'</sub>), 132.37 (C<sub>7,7'</sub>), 130.10 (C<sub>5,5'</sub>), 129.88 (C<sub>12,12'</sub>), 128.42 (C<sub>11,11'</sub>), 124.50 (C<sub>10,10'</sub>), 69.68 (C<sub>3,3'</sub>), 36.52 (C<sub>1</sub>), 24.25 (C<sub>2,2'</sub>); UV-Vis (DMF) (λ<sub>max</sub> / nm, (ε / L mol<sup>-1</sup> cm<sup>-1</sup>)): 268 (8555), 295 (20293), 326(sh) (11212); Molar conductance (DMF) (A<sub>M</sub> / S m<sup>2</sup> mol<sup>-1</sup>): 74.64.



## A graph theoretical approach to *cis/trans* isomerism

BORIS FURTULA<sup>1\*</sup>, GIORGI LEKISHVILI<sup>2</sup> and IVAN GUTMAN<sup>1\*\*\*</sup>

<sup>1</sup>Faculty of Science, University of Kragujevac, P. O. Box 60, 34000 Kragujevac, Serbia and

<sup>2</sup>Department of Medicinal Chemistry, Tbilisi State Medical University, GE-0177,  
31 Vazha-Pshavela Avenue, Tbilisi, Georgia, E-mail: lekishvili@tsmu.edu

(Received 20 January, revised 24 January, accepted 24 January 2014)

**Abstract:** A simple graph-theory-based model is presented, by means of which it is possible to express the energy difference between geometrically non-equivalent forms of a conjugated polyene. This is achieved by modifying the adjacency matrix of the molecular graph, and including into it information on *cis/trans* constellations. The total  $\pi$ -electron energy thus calculated is in excellent agreement with the enthalpies of the underlying isomers and conformers.

**Keywords:** *cis/trans* isomerism; graph theory; molecular graph; total  $\pi$ -electron energy.

### INTRODUCTION

One of the most unpleasant shortcomings of the modeling of molecular properties by means of the graph theory<sup>1–6</sup> is the fact that a molecular graph does not contain information on the actual geometry of the underlying molecule. Consequently, the various graph-based molecular structure descriptors (topological indices) used in contemporary mathematical chemistry<sup>6</sup> cannot distinguish between *cis/trans* isomers. Numerous attempts have been made to overcome this difficulty. Most of these construct 3-dimensional (3D) analogues of topological indices, calculated by using the actual (experimentally or theoretically determined) molecular geometry.<sup>7–10</sup> This approach is often successful, but it abandons the usage of the graph theory.

In order to distinguish between *cis/trans* isomers while remaining within the domain of the chemical graph theory, Pogliani constructed special, *ad hoc* defined, types of molecular graphs.<sup>11,12</sup> A much more direct approach was proposed by one of the present authors,<sup>13</sup> utilizing a complex number-based adjacency matrix  $\mathbf{A}(G)$  of the form:

Corresponding authors. E-mail: (\*boris.furtula@gmail.com, (\*\*gutman@kg.ac.rs

# Serbian Chemical Society member.

doi: 10.2298/JSC140120010F

$$\mathbf{A}(G) = \mathbf{A}_1(G) + i \mathbf{A}_2(G) \quad (1)$$

where  $i = \sqrt{-1}$  is the imaginary unit. In formula (1),  $\mathbf{A}_1(G)$  is the ordinary adjacency matrix defined in the usual manner:<sup>1,3,4</sup> If  $G$  is a (molecular) graph with vertices  $v_1, v_2, \dots, v_n$ , then the  $(i,j)$ -entry of  $\mathbf{A}_1(G)$  is equal to 1 if the vertices  $v_i$  and  $v_j$  are adjacent, and is zero otherwise.

The imaginary part of  $\mathbf{A}_1(G)$  is defined as follows.<sup>13</sup> Let the topological distance (= the number of edges in a shortest path) between the vertices  $v_i$  and  $v_j$  of the graph  $G$  be denoted by  $d(v_i, v_j | G)$ . Then:

$$\begin{aligned} [\mathbf{A}_2(G)]_{ij} &= +1 \quad \text{if } d(v_i, v_j | G) = 3 \quad \& \quad v_i, v_j \text{ are in the } cis \text{ constellation} \\ &= -1 \quad \text{if } d(v_i, v_j | G) = 3 \quad \& \quad v_i, v_j \text{ are in the } trans \text{ constellation} \\ &= 0 \quad \text{otherwise} \end{aligned}$$

The advantage of a topological index,  $TI$ , calculated by means of Eq. (1) is that the contribution coming from the molecular topology (the real part of  $TI$ ) is easily distinguished from the contribution coming from the molecular geometry (the imaginary part of  $TI$ ). It was demonstrated<sup>13</sup> that such an approach worked well in the case of standard graph-based structure descriptors, such as the connectivity index and the Wiener index (see recent reviews<sup>14,15</sup>). However, as shown below, because the matrix  $\mathbf{A}_1(G)$  is not Hermitian and, therefore, its eigenvalues are not real-valued, this approach is not applicable in the case of the total  $\pi$ -electron energy and the thermodynamic properties of polyenes.

In order to be able to check our models, first, data on the energetics of the *cis/trans* isomers of conjugated polyenes had to be acquired.

#### QUANTUM-MECHANICAL CALCULATIONS

In this work, attention was focused on isomers and (planar) conformers of 1,3,5-hexatriene and 2-vinylbutadiene, shown in Fig. 1. The enthalpy of formation of the 9 conjugated triene species of formula  $C_6H_8$  were calculated using Gaussian software.

First, the geometries were optimized, and then – using the B3LYP/6-31G(d, p) basis set – the enthalpies were calculated. The obtained values are given in Table I.

#### RESULTS FOR THE MODEL BASED ON EQ. (1)

The HMO total  $\pi$ -electron energy,  $E_\pi$  is a much studied, graph-based characteristic of unsaturated conjugated molecules, see the books,<sup>2,4,16</sup> surveys,<sup>17,18</sup> recent papers,<sup>19–21</sup> and references cited therein. Detailed examinations<sup>4,22,23</sup> revealed that in the case of strain-free conjugated systems, there is a very good linear correlation between  $E_\pi$  and thermodynamic stability, in particular the enthalpy of formation.

Denote by  $\lambda_1, \lambda_2, \dots, \lambda_n$  the eigenvalues<sup>2,4</sup> of the (ordinary) adjacency matrix  $\mathbf{A}_1(G)$  of the molecular graph  $G$ , and recall that these eigenvalues are always

real-valued. Then for alternant conjugated hydrocarbons, to which the polyenes studied in this work belong, the HMO total  $\pi$ -electron energy is given by:<sup>2,4,16</sup>

$$E_{\pi} = \sum_{k=1}^n |\lambda_k| \quad (2)$$

Recall that  $|x|$  denotes the absolute value of the number  $x$ . If  $x$  is real-valued, then  $|x|=x$  for  $x \geq 0$ , and  $|x|=-x$  for  $x \leq 0$ .

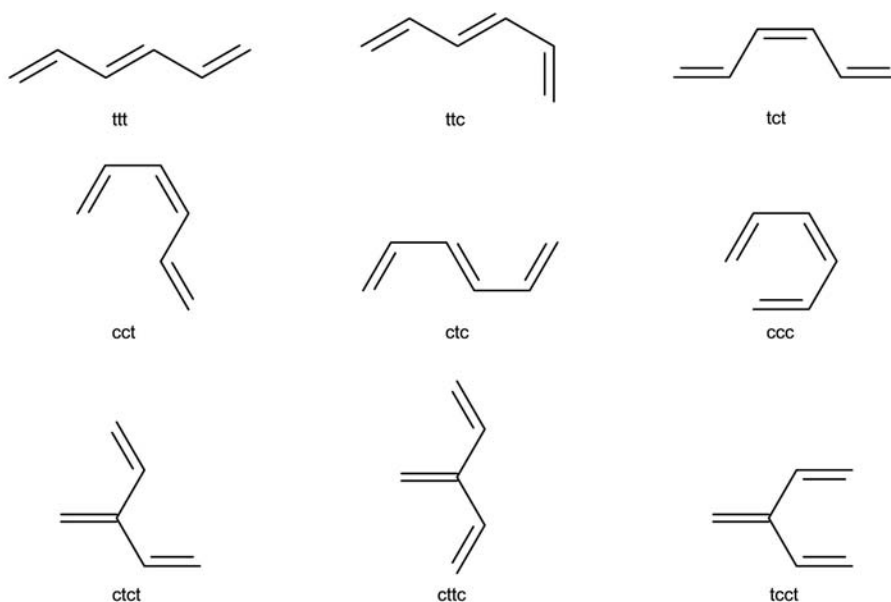


Fig. 1. Isomers and conformers of the conjugated hexatriene and vinylbutadiene,  $C_6H_8$ , examined in this work.

TABLE I. Enthalpies of formation (in  $\text{kJ mol}^{-1}$ ) for the  $C_6H_8$ -species depicted in Fig. 1. The data in the third column were obtained from those in the second column, by subtracting the smallest value (the enthalpy of the *ttt*-species) and by multiplying by 1000

Isomer/conformer	$\Delta_f H$	$\Delta_f H_{\text{nor}}$
<i>ttt</i>	-233.284653	0.000
<i>ttc</i>	-233.279004	5.649
<i>tct</i>	-233.281451	3.202
<i>ctc</i>	-233.272950	11.703
<i>cct</i>	-233.275413	9.240
<i>ccc</i>	-233.265688	18.965
<i>ctct</i>	-233.274059	10.584
<i>cttc</i>	-233.270447	14.206
<i>tcct</i>	-233.272929	11.724

If an analogous expression for the modified adjacency matrix  $\mathbf{A}(G)$ , defined by Eq. (1), is to be applied, then it must be taken into account that its eigenvalues are complex numbers of the form  $\lambda_k = a_k + i b_k$ ;  $k = 1, 2, \dots, n$ . The respective graph energy could then be calculated in two different ways:

*Model 1.* Following an earlier study,<sup>24</sup> the graph energy is obtained by summing the terms  $|a_k|$ ;  $k = 1, 2, \dots, n$ , namely the absolute values of the real parts of the eigenvalues. The results obtained by this model are shown in Fig. 2, from which it could be seen that no correlation exists between  $E_\pi$  and the heats of formation of the examined polyenes. The results were by no means better by employing the alternative model.

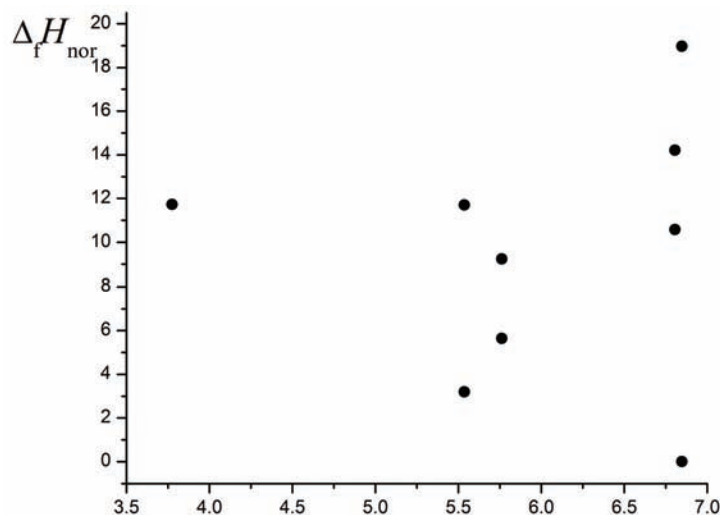


Fig. 2. Correlation between the normalized enthalpies and graph energy according to Model 1; correlation coefficient  $R = 0.054$ .

*Model 2.* The graph energy is obtained by summing the terms:

$$|a_k| + |b_k|; k = 1, 2, \dots, n$$

namely, the absolute values of the real and complex parts of the eigenvalues. The obtained results are shown in Fig. 3, from which it could be seen that within Model 2 also no correlation exists between  $E_\pi$  and the heats of formation of the examined polyenes.

Equally disappointing results were obtained when the graph energy is the sum of terms  $\sqrt{(a_k)^2 + (b_k)^2}$ ;  $k = 1, 2, \dots, n$ .

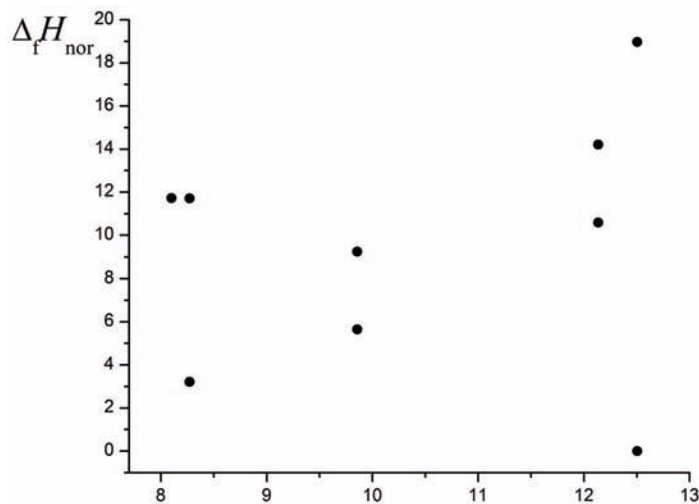


Fig. 3. Correlation between the normalized enthalpies and graph energy according to Model 2; correlation coefficient  $R = 0.177$ .

### A THIRD APPROACH

In view of the findings outlined in the preceding section, it was concluded that in the case of an energy-based approach, Eq. (1) must be abandoned and an attempt made to construct another model, pursuing a more radical generalization.

Consider the graph  $G = (V, E)$  whose vertex set is  $V$  and whose edge set is  $E$ . Suppose that there is a criterion allowing  $E$  to be decomposed into subsets  $E_1$  and  $E_2$ , such that  $E_1 \cup E_2 = E$  and  $E_1 \cap E_2 = \emptyset$ . By this, two subgraphs of  $G$  are defined,  $G_1$  and  $G_2$ , both with vertex sets  $V$ .  $G_1$  will be called the principal subgraph, and  $G_2$  the secondary subgraph. It is plausible to assume that  $G_1$  is the ordinary molecular graph, whereas  $G_2$  may be constructed so as to bear information on geometric (non-topological) features of the underlying molecule. The generalized adjacency matrix may then be defined as:

$$\mathbf{A}_{\text{gen}}(G) = (\mathbf{A}_1 + \mathbf{A}_2) \exp(\mathbf{A}_2) \quad (3)$$

Note that if  $E_2 = \emptyset$ , then  $\mathbf{A}_2 = 0$  and  $\mathbf{A}_{\text{gen}}(G)$  reduces to the ordinary adjacency matrix. Equation (3) can be further modified by using the Taylor series of the matrix exponent:

$$\mathbf{A}_{\text{gen}}^{(0)}(G) = \mathbf{A}_1 + \mathbf{A}_2 \quad (3a)$$

$$\mathbf{A}_{\text{gen}}^{(1)}(G) = (\mathbf{A}_1 + \mathbf{A}_2)(\mathbf{I} + \mathbf{A}_2) \quad (3b)$$

$$\mathbf{A}_{\text{gen}}^{(2)}(G) = (\mathbf{A}_1 + \mathbf{A}_2)(\mathbf{I} + \mathbf{A}_2 + \frac{1}{2}\mathbf{A}_2^2) \quad (3c)$$

and so on. Within all such decompositions, the matrices  $\mathbf{A}_{\text{gen}}^{(k)}(G)$ ,  $k = 0, 1, 2, \dots$ , are symmetric and, thus, all their eigenvalues are real-valued. Unfortunately, computations based on the higher-order members of the Taylor series did not significantly improve the model. Therefore, in the present approach, the simplest version, Eq. (3a), was used and the secondary adjacency matrix was purposefully chosen as:

$$\begin{aligned} [\mathbf{A}_2(G)]_{ij} &= x \quad \text{if } d(v_i, v_j | G) = 3 \quad \& \quad v_i, v_j \text{ are in the } \textit{cis} \text{ constellation} \\ &= 1/x \quad \text{if } d(v_i, v_j | G) = 3 \quad \& \quad v_i, v_j \text{ are in the } \textit{trans} \text{ constellation} \quad (4) \\ &= 0 \quad \text{otherwise} \end{aligned}$$

where  $x$  is a variable parameter. This is referred to as Model 3.

Within Model 3, the energies were first computed for some chosen values of  $x$ , viz.  $x = -3$  and  $x = +2$ . The obtained results were quite good, as can be seen from Figs. 4 and 5.

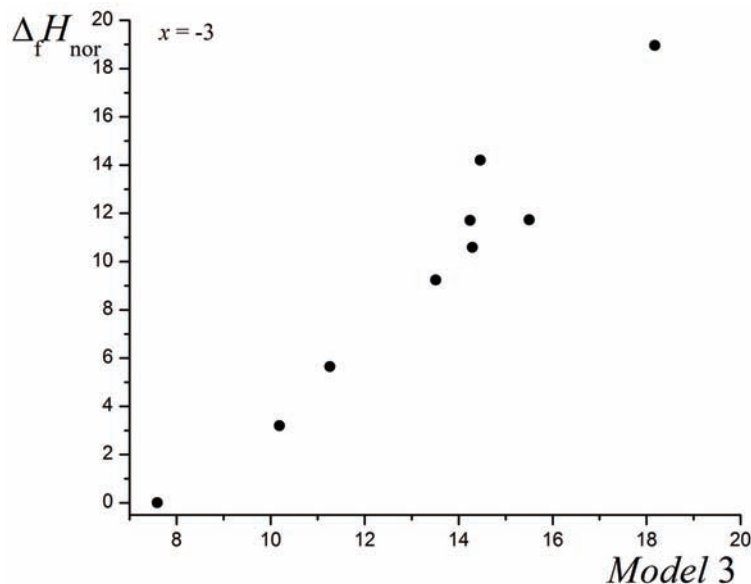


Fig. 4. Correlation between normalized enthalpies and graph energy based on the matrix  $\mathbf{A}_2(G)$  for  $x = -3$ ; correlation coefficient  $R = 0.976$ .

Next,  $x$  was varied in the interval  $\{-10, 10\}$  and the results shown in Fig. 6 were found. These results are surprising: except for the near-zero values of the parameter  $x$  (where instabilities and rapid changes of  $R$  occurred), the quality of the correlations were always almost the same, and were everywhere relatively good. There were insignificant maxima of the correlation coefficient at  $x = -2.569$  (with a correlation coefficient  $R = 0.9804$ ) and at  $x = +2.008$  (with a

correlation coefficient  $R = 0.9592$ ). There was also a third maximum at  $x = 0.814$  (with a correlation coefficient  $R = -0.9658$ ), but for reasons that should be evident from Fig. 6, this value of the parameter  $x$  lies in the domain of instability and is not usable for practical purposes. Thus, Model 3 yields the best results for  $x = -2.569$ , shown in Fig. 7.

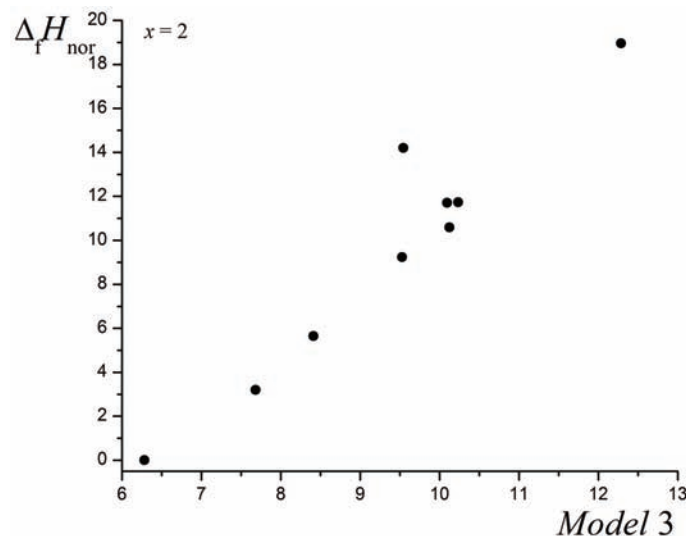


Fig. 5. Correlation between normalized enthalpies and graph energy based on the matrix  $A_2(G)$  for  $x = +2$ ; correlation coefficient  $R = 0.959$ .

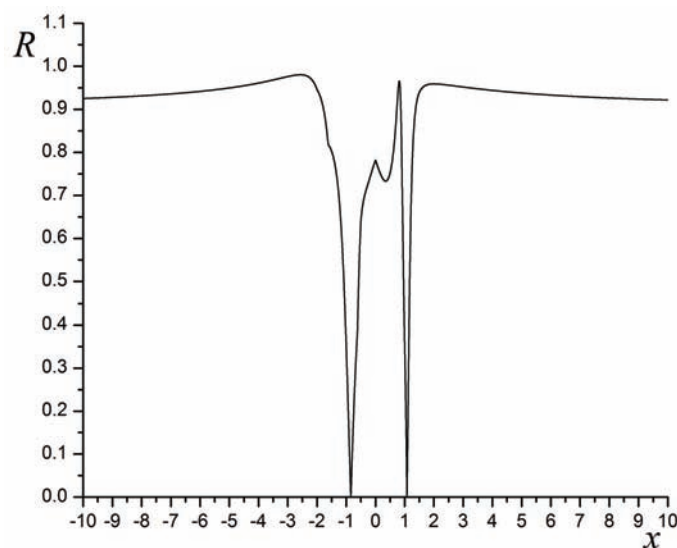


Fig. 6. Absolute value of the correlation coefficient ( $R$ ) of Model 3 for the parameter  $x$  in the interval  $\{-10, 10\}$ .

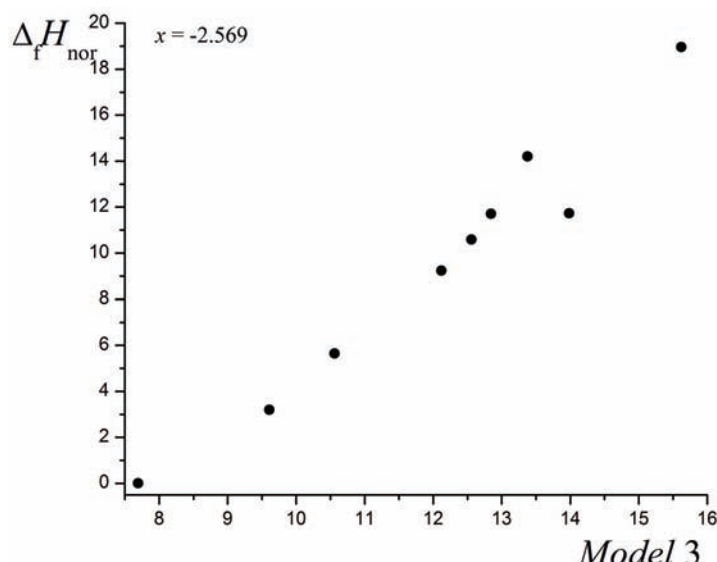


Fig. 7. The best correlation obtained within Model 3, Eqs. (3a) and (4), for  $x = -2.569$ ; correlation coefficient  $R = 0.9804$ .

#### DISCUSSION AND CONCLUDING REMARKS

The main conclusion is that it is possible to construct a graph-based model of the *cis/trans* isomers without using complicated mathematical formalism. In particular, there was no need for complex numbers, and already the simplest modification of the adjacency matrix, namely Eqs. (3a) & (4) (= Model 3) was sufficient for “graph energy” that reasonably well reproduced the differences of thermodynamic properties (expressed *via* enthalpies) of *cis/trans* isomers. The remarkable fact that both large negative and large positive choices of the parameter  $x$  yielded agreeable results (*cf.* Fig. 6), is a further argument corroborating the proposed simple model.

Our attempts in the future will be to explore analogous graph-theoretical models for taking into account the effects of weaker molecular interactions, not necessarily based on covalent bonding. These might include intramolecular hydrogen bonding (with the secondary subgraph possessing directed edges), transition states (where the principal subgraph would consist of edges corresponding to permanent bonds whereas the secondary subgraph would represent the vanishing and emerging bonds), and van der Waals type interactions.

*Acknowledgement.* The first author thanks the Ministry of Education, Science and Technological Development of the Republic of Serbia for support through Grant No. 174033.

И З В О Д  
ГРАНИЦЕ ЗА УКУПНУ  $\pi$ -ЕЛЕКТРОНСКУ ЕНЕРГИЈУ

БОРИС ФУРТУЛА<sup>1</sup>, GIORGI LEKISHVILI<sup>2</sup> И ИВАН ГУТМАН<sup>1</sup>

<sup>1</sup>*Природно-математички факултет Универзитета у Краљеву и <sup>2</sup>Tbilisi State University, Tbilisi, Georgia*

Предложен је једноставни граф-теоријски модел помоћу којег је могуће изразити енергетске разлике између геометријски нееквивалентних форми конјугованих полиена. То је постигнуто модификацијом матрице суседства молекулског графа, тако што је у њу укључена информација о *cis/trans* консталацијама. Укупна  $\pi$ -електронска енергија израчуната на овај начин је у одличној сагласности са енталпијама одговарајућих изомера и конформера.

(Примљено 20. јануара, ревидирано 24. јануара, прихваћено 24. јануара 2014)

REFERENCES

1. A. T. Balaban, *Chemical Applications of Graph Theory*, Academic Press, London, 1976
2. A. Graovac, I. Gutman, N. Trinajstić, *Topological Approach to the Theory of Conjugated Molecules*, Springer, Berlin, 1977
3. N. Trinajstić, *Chemical Graph Theory*, CRC Press, Boca Raton, FL, 1983
4. I. Gutman, O. E. Polansky, *Mathematical Concepts in Organic Chemistry*, Springer, Berlin, 1986
5. J. Devillers, A. T. Balaban, Eds., *Topological Indices and Related Descriptors in QSAR and QSPR*, Gordon & Breach, Amsterdam, 1999
6. R. Todeschini, V. Consonni, *Molecular Descriptors for Chemoinformatics*, Wiley–VCH, Weinheim, Germany, 2009
7. M. Randić, B. Jerman-Blažić, N. Trinajstić, *Comput. Chem.* **14** (1990) 237
8. L. Xu, H. Y. Wang, Q. Su, *Comput. Chem.* **16** (1992) 187
9. A. T. Balaban, Ed., *From Chemical Topology to Three-Dimensional Geometry*, Plenum Press, New York, 1997
10. A. T. Balaban, *J. Chem. Inf. Comput. Sci.* **37** (1997) 645
11. L. Pogliani, *J. Chem. Inf. Comput. Sci.* **34** (1994) 801
12. L. Pogliani, *Novel Molecular Connectivity Indices: Pseudoconnectivity, Dual, cis-trans Indices and Indices Based on a New Valence Delta*, in *Novel Molecular Structure Descriptors – Theory and Applications I*, I. Gutman, B. Furtula, Eds., Univ. Kragujevac, Kragujevac, Serbia, 2010, p. 39
13. G. Lekishvili, *J. Chem. Inf. Comput. Sci.* **37** (1997) 924
14. I. Gutman, *Croat. Chem. Acta* **86** (2013) 351
15. K. Xu, M. Liu, K. C. Das, I. Gutman, B. Furtula, *MATCH Commun. Math. Comput. Chem.* **71** (2014) 461
16. X. Li, Y. Shi, I. Gutman, *Graph Energy*, Springer, New York, 2012
17. I. Gutman, *J. Serb. Chem. Soc.* **70** (2005) 441
18. M. Perić, I. Gutman, J. Radić-Perić, *J. Serb. Chem. Soc.* **71** (2006) 771
19. I. Gutman, K. C. Das, *J. Serb. Chem. Soc.* **78** (2013) 1925
20. M. P. Stanić, I. Gutman, *MATCH Commun. Math. Comput. Chem.* **70** (2013) 681
21. K. C. Das, S. A. Mojallal, *MATCH Commun. Math. Comput. Chem.* **70** (2013) 657
22. L. J. Schaad, B. A. Hess, *J. Am. Chem. Soc.* **94** (1972) 3068
23. I. Gutman, *Topics Curr. Chem.* **162** (1992) 29
24. I. Pena, J. Rada, *Lin. Multilin. Algebra* **56** (2008) 565.





## The sorption of inorganic arsenic on modified sepiolite: the effect of hydrated iron(III) oxide

NIKOLA I. ILIĆ<sup>1\*</sup>, SLAVICA S. LAZAREVIĆ<sup>1#</sup>, VLADANA N.  
RAJAKOVIĆ-OGNJANOVIC<sup>2</sup>, LJUBINKA V. RAJAKOVIĆ<sup>1#</sup>,  
DORDE T. JANAČKOVIĆ<sup>1#</sup> and RADA D. PETROVIĆ<sup>1#</sup>

<sup>1</sup>Faculty of Technology and Metallurgy, University of Belgrade, Kariđelova 4, 11000 Belgrade, Serbia and <sup>2</sup>Faculty of Civil Engineering, University of Belgrade, Bulevar Kralja Aleksandra 73, Belgrade, Serbia

(Received 12 September 2013, revised 13 January, accepted 5 March 2014)

**Abstract:** The sorption of inorganic arsenic species, As(III) and As(V), from water by sepiolite modified with hydrated iron(III) oxide was investigated at 25 °C through batch studies. The influence of the initial pH value, the initial As concentration, the contact time and the type of water on the sorption capacity was investigated. Two types of water were used, deionised and groundwater. The maximal sorption capacity for As(III) dissolved in deionised water was observed at an initial and final pH value 7.0, while the bonding of As(V) was observed to be almost pH independent for pH value in the range from 2.0 to 7.0, while a significant decrease in the sorption capacity was observed at pH values above 7.0. The sorption capacity at initial pH 7.0 was about 10 mg g<sup>-1</sup> for As(III) and 4.2 mg g<sup>-1</sup> for As(V) in deionised water. The capacity in groundwater was decreased by 40 % for As(III) and by 20 % for As(V). The Langmuir model and pseudo-second order kinetic model revealed good agreement with the experimental results. The results showed that Fe(III)-modified sepiolite exhibits significant affinity for arsenic removal and it has the potential for application in water purification processes.

**Keywords:** arsenic(III); arsenic(V); Fe(III)-sepiolite; sorption; pH influence.

### INTRODUCTION

The inorganic arsenic occurs naturally in rocks and soils as a constituent of many minerals (arsenides, sulphides, oxides, arsenates and arsenates).<sup>1</sup> These forms are insoluble, but under certain conditions the minerals might be dissolved, or arsenic could be leached from them, becoming in this way mobile. The mobilization is caused by specific geochemical and hydrogeological triggers.<sup>2</sup> The two

\* Corresponding author. E-mail: niksentije@gmail.com

# Serbian Chemical Society member.

doi: 10.2298/JSC130912017I

main geochemical triggers are: 1) an increase of the pH value to over 8.5, when arsenic releases protons and becomes negatively charged that leads to desorption from minerals; 2) the occurrence of reducing conditions below neutral pH values, when oxides of Fe(III) and Mn(IV) dissolve and become reduced to Fe(II) and Mn(II), which also enables arsenic species from these minerals to dissolve. This is still not sufficient for high levels of arsenic to form in water; the hydrogeological conditions must also be fulfilled: a slow process of ground water exchange in aquifers has to occur or the aquifers have to be very young.<sup>2</sup> Besides all above mentioned, smaller, but still significant amounts of arsenic are released in water from ore smelting.<sup>2,3</sup> Due to all this, arsenic is present in many natural waters, primarily in ground water, in the form of arsenic and arsenous acid and in the form of their anions.<sup>3</sup> These inorganic species could be methylated by bacteria, fungi and yeasts to organic arsenic compounds.<sup>4</sup> All these compounds are highly toxic and carcinogenic.

Arsenic may cause acute and chronic poisoning. Symptoms of chronic poisoning are not specific (weakness, gastritis, colitis, tiredness, hair loss); hence, they are not easily recognizable. Longer exposure to water with arsenic leads to severe health problems: skin lesions, disruptions of cardiovascular, respiratory, digestive, renal and nervous systems, and skin, lung, bladder, liver and kidney cancers.<sup>4,5</sup> There are some indications that inorganic arsenic may also be diabetogenic.<sup>6</sup> Acute poisoning may cause vomiting, dryness of the mouth and throat, muscle cramps, hallucinations, diarrhoea, or even death due to hepatic and renal failure or heart attack.<sup>4</sup> Arsenic compounds accumulate in the body, so even small concentrations in drinking water could be very dangerous. As a result of this, the WHO (World Health Organization) reduced the recommended maximum concentration in drinking water from 50 to 10 µg dm<sup>-3</sup> in 1993.<sup>7-9</sup> At least 60 million people in the world drink water with high levels of arsenic (over 50 µg dm<sup>-3</sup>) every day.<sup>2</sup> The most risky areas are in Bangladesh, India, Argentina and Mexico, but many individual wells can also be polluted, which is the case in the Panonnian Basin region (parts of Serbia, Romania and Hungary).<sup>10,11</sup>

Many techniques have been developed for arsenic removal from water: coagulation by salts of Fe(III) and Al, modified limestone softening, oxidation with filtration, ion exchange, membrane techniques and others.<sup>10,12</sup> This paper investigates sorption, which is still not widely used, although it is a very simple and inexpensive technique. The main issue when sorption is applied is that it is relatively slow process and it lacks in selectivity.

The sorption occurs until dynamic equilibrium is established, when the rates of sorption and desorption become equal. This equilibrium could be presented by sorption isotherms in form of sorption capacity *vs.* concentration diagrams. Several models describe this process mathematically, while the Langmuir and the Freundlich models are the most used ones.<sup>12</sup> The Langmuir model assumes

monolayer sorption onto a homogeneous surface with a finite number of identical active sites. Exchange between sorbed species is negligible, which presumes strong bonds between sorbate species and surface active site, *i.e.*, chemical bonds. The Freundlich isotherm model describes non-ideal and reversible sorption, not restricted to the formation of monolayer.<sup>13</sup> This empirical model can be applied to multilayer sorption, with non-uniform distribution of sorption heat and affinities over a heterogeneous surface. The amount sorbed appears as an overall effect of adsorptions on all sites (each having a particular bond energy), the stronger binding sites are occupied first. The energy of adsorption decreases exponentially upon the completion of the sorption process. That implies that chemisorption (if the active sites are strong enough) is followed by physisorption.

Many materials have been investigated as arsenic sorbents: oxides, salts, activated carbon, biologic materials, organic polymers and waste materials.<sup>10</sup> Moreover, many modifications of these materials are being investigated in order to improve the sorption capacity. It is known that iron oxyhydroxides have good affinities to arsenic, but their flaw is their small specific surface area, which results from agglomeration. A solution could lie in the deposition of Fe(III) oxyhydroxides on porous minerals, such as zeolites, bentonites and sepiolites.<sup>5,7,8,14–17</sup>

Sepiolite is a fibrous hydrated magnesium silicate<sup>18,19</sup> with a unit cell formula  $Mg_8Si_{12}O_{30}(OH)_4(H_2O)_{4-n}H_2O$ ,  $n = 6–8$ . Their structures have blocks and channels running parallel to the fibre axis, which provide excellent potential for the retention of micropollutants from water.<sup>20</sup> Although natural sepiolite has not shown noticeable capacity for inorganic arsenic,<sup>10</sup> because of its large specific surface area, it is a scientific challenge to attempt modification of a sepiolite surface with Fe(III)-oxyhydroxides, which are considered to be the best sorbents for inorganic arsenic species.

The aim of this study was to evaluate the capacity of Fe(III)-modified sepiolite to remove As(III) and As(V) from aqueous media *via* sorption. The influence of the initial pH value, the initial As concentration, the contact time and type of aqueous media were investigated. Two types of aqueous media were used: deionised water and ground water. The Fe(III)-modified sepiolite used in this study was fully characterized in a previous study.<sup>14</sup> The chemical composition, morphology, phase composition, specific surface area and pore volume, qualitative composition and thermal analysis showed that modified sepiolite retained the structure of natural sepiolite with 31.45 wt. % of amorphous  $Fe_2O_3$ . To the best of our knowledge, iron(III)-modified sepiolite has not previously been used for arsenic sorption from aqueous media.

## EXPERIMENTAL

Natural sepiolite from Andrići in Serbia, was dried for 2 h at 150 °C and ground in porcelain mortar. Particles under 250 µm were chosen for the modification. Sepiolite (20 g)

was mixed with 200 cm<sup>3</sup> of 0.5 M FeCl<sub>3</sub> solution and 360 cm<sup>3</sup> of 1.0 M NaOH solution in a polyethylene bottle. The obtained suspension was diluted to 2 dm<sup>3</sup> and then heated to 70 °C for 48 h. The precipitate was washed, dried and used as the sorbent, designated as Fe–SEP.<sup>15</sup> XRD analysis, FTIR spectroscopy and DTA/TGA<sup>15</sup> confirmed that Fe–SEP maintained the basic structure of sepiolite. The presence of new crystalline Fe phases was not observed, indicating that only amorphous Fe species were present. The textural properties of Fe–SEP,<sup>19</sup> determined by nitrogen adsorption and desorption at liquid nitrogen temperature, were similar to the properties of natural sepiolite, meaning high porosity and high specific surface area were maintained.

Stock solutions of As(III) (0.5 g dm<sup>-3</sup>) and As(V) (1.0 g dm<sup>-3</sup>) were prepared by dissolving appropriate quantities of As<sub>2</sub>O<sub>3</sub> (Merck, 99.5 %) with NaOH (Lach-Ner, 98 %) and Na<sub>2</sub>HAsO<sub>4</sub>·7H<sub>2</sub>O (Carlo Erba, 99 %) in deionised water (DW) with a conductivity under 0.2 µS cm<sup>-1</sup> and in ground water (GW). The composition of ground water from a well by the bank of the Sava River was determined by the inductively coupled plasma-optical emission spectrometry (ICP–OES) method (ICP SPECTRO, GENESIS FEE, with the accuracy of 10 µg dm<sup>-3</sup>) and is presented in Table I. As(III) stock solutions were kept in amber bottles.

TABLE I. Ground water composition, determined by the ICP-OES method

Cation	Al	B	Ba	Ca	Fe	K	Mg	Mn	Na	Sr	As, Be, Cd, Co, Cr, Cu, Hg, Li, Mo, Ni, Pb, Sb, Sn, Zn
c / mg dm <sup>-3</sup>	0.08	0.03	0.03	50.8	0.09	3.01	13.3	0.02	14.3	0.25	<0.01

The sorption experiments were performed by batch technique in a thermostated water bath with a shaker (MEMMERT), in which the temperature was maintained at 25±0.1 °C. A mass of 0.02 g of Fe–SEP in 100 cm<sup>3</sup> solutions was used in all sorption experiments. Arsenic concentrations were determined by the ICP-OES method (ICP SPECTRO, GENESIS FEE).

The effect of pH value on As(III) and As(V) sorption from solutions in DW was investigated with arsenic solution of 0.500 mg dm<sup>-3</sup> concentration, by varying the initial solution pH (pH<sub>i</sub>), from 2.0 to 10.0. After 24 h of equilibration, the suspensions were filtered and the final pH (pH<sub>f</sub>) and the As concentration were determined.

The sorption capacity was determined after equilibration of different concentrations (from 0.25 to 7.0 mg dm<sup>-3</sup>) of As(III) or As(V) solutions in DW and GW. The initial pH values were adjusted to 7.0 using 0.01 M KOH or HNO<sub>3</sub> solutions. The equilibrium sorption capacity, *q<sub>e</sub>* (mg g<sup>-1</sup>), was calculated according to the following equation:

$$q_e = (c_o - c_1)V/m \quad (1)$$

where *c<sub>o</sub>* and *c<sub>1</sub>* are the arsenic concentrations before and after sorption (mg dm<sup>-3</sup>), *m* is the mass of sorbent (g), and *V* is a volume of solution (dm<sup>3</sup>).

The kinetic analysis of sorption was realised using As(III) and As(V) solutions in DW of 0.50 and 3.00 mg dm<sup>-3</sup>, at an initial pH value of 7.0±0.1. The suspensions were equilibrated for 1, 2, 4, 8, 16 and 24 h. The amount of As sorbed after time *t*, *q<sub>t</sub>*, were calculated according to Eq. (1), where *c<sub>1</sub>* is As concentration after time *t*.

## RESULTS AND DISCUSSION

### Effect of initial pH

The pH value of the solution is an important controlling parameter in the arsenic sorption process because it has an important effect on the chemistry of

arsenic,<sup>21–23</sup> as demonstrated in Fig. 1, and on the surface properties of the sorbent, and hence on the interactions between arsenic and the sorbent surface.

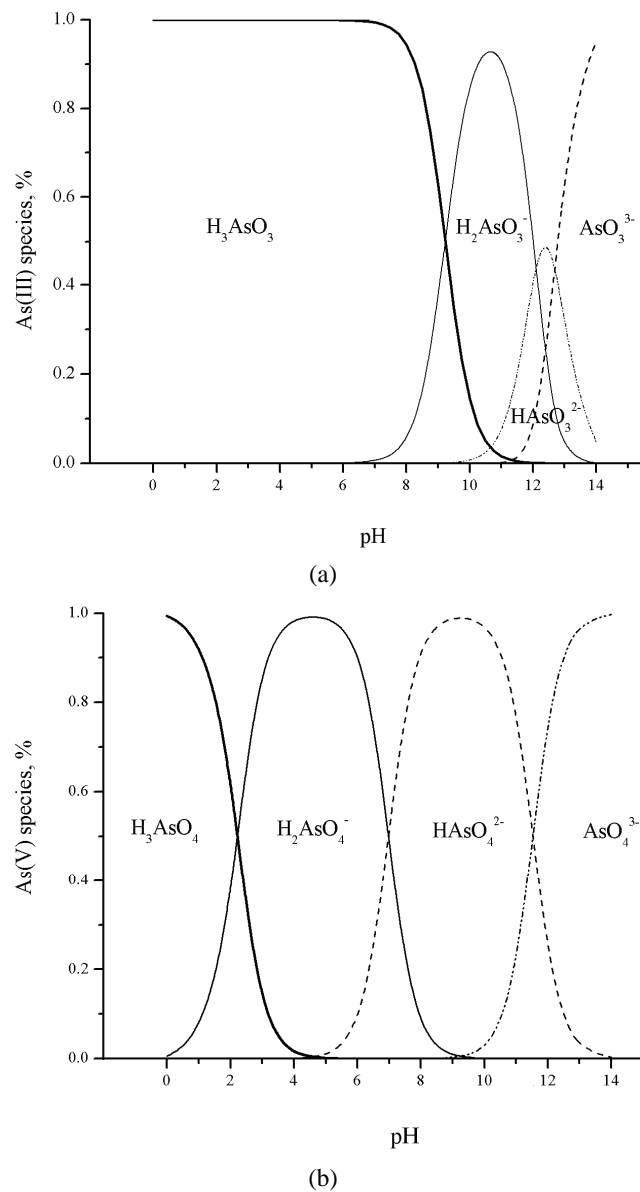


Fig. 1. The distribution of As(V) and As(III) species as a function of the pH value of the water.<sup>12,21–23</sup>

The effect of the initial pH value( $\text{pH}_i$ ) on the equilibrium sorption capacity for  $0.5 \text{ mg dm}^{-3}$  solutions of As(III) and As(V) dissolved in deionised water is

presented in Fig. 2, along with the final pH values ( $\text{pH}_f$ ). According to the position of the plateau on the  $\text{pH}_f$  vs.  $\text{pH}_i$  dependence, a change in surface charge from positive to negative or *vice versa* occurred at a pH value of around 7.0. For  $\text{pH}_i < 7$ , the final pH values were higher than the initial ones, implying protonization of the surface functional groups and thus a sorbent with a positive surface charge. For  $\text{pH}_i > 7$ , the final pH values were lower than the initial ones, indicating deprotonization of the surface functional groups. Accordingly, the adsorbent surface was negatively charged at  $\text{pH}_i > 7$ .

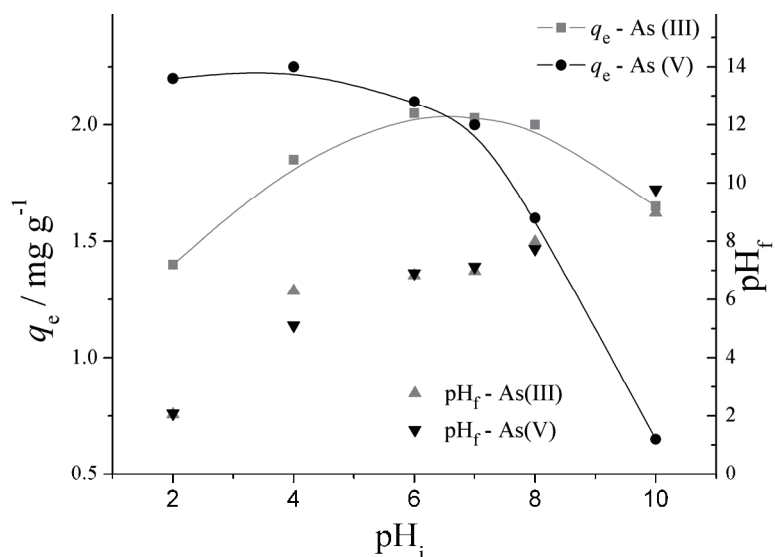


Fig. 2. The influence of the initial pH value on the sorption capacity of Fe–SEP for inorganic arsenic and the dependence of the final pH value of the As(III) and As(V) solutions after the sorption process on the initial pH value of the solutions.

The obtained dependences of the sorption capacity on the  $\text{pH}_i$  value could be explained by the surface charge of the sorbent and the distribution of arsenic species as a function of pH value. Sorption capacity of Fe–SEP for As(V) was almost constant at initial pH values below 7.0 because the positive charge of the sorbent surface decreased with increasing pH and concomitant increase in the content of anionic species (Fig. 1). The sudden reduction of the sorption capacity with increasing  $\text{pH}_i$  value above 7.0 could be explained by the change in the surface charge of the sorbent from positive to negative. In the case of As(III), maximal sorption capacity of the sorbent was reached at  $\text{pH}_i$  values from 6.0 to 7.0, because the sorbent surface was uncharged and arsenic was present mostly in a neutral form of species,  $\text{H}_3\text{AsO}_3$  (Fig. 1). With decreasing  $\text{pH}_i$  value, the sorption capacity decreased because the positive charge of the sorbent surface was increased. When the  $\text{pH}_i$  value increased above 7.0, the sorption capacity for As(III)

decreased because the arsenic was present as anionic species that is weakly sorbed at the negatively charged surface of the sorbent.

Considering the fact that the sorption capacities were the highest at pH<sub>i</sub> values around 7.0 for both As(III) and As(V), that the pH did not change during the sorption for pH<sub>i</sub> 7, and that this pH is close to the pH values of natural waters, pH<sub>i</sub> 7.0 was selected for all subsequent experiments.

#### *Sorption isotherms studies and modelling*

The composition of the aqueous media can have a significant impact on the performance of a sorbent due to the presence of competing ions, complexing anions, dissolved organic matter, *etc.* Therefore, it is important to evaluate potential sorbent materials in aqueous media that represent the conditions under which the adsorbent would most likely be employed. For applications in real water treatment, Fe-SEP was evaluated as a sorbent for As(V) and As(III) in deionised water (DW) and ground water (GW).

The experimental isotherms for the sorption of As(V) and As(III) onto Fe-SEP in DW and GW, as the dependence of  $q_e$  on the equilibrium As concentration  $c_e$ , are presented in Figs. 3 and 4. All isotherm datasets were fitted to the Langmuir and Freundlich isotherm and the model fits are presented with the experimental data in Figs. 3 and 4. The sorption isotherms constants were determined by non-linear regression analysis using OriginPro 8.5 and the results are given in Table II.

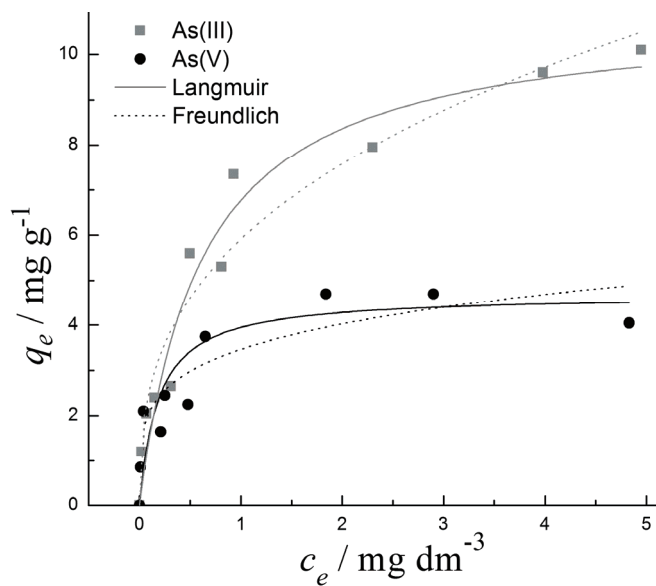


Fig. 3. The sorption isotherms for As(III) and As(V) dissolved in deionised water.

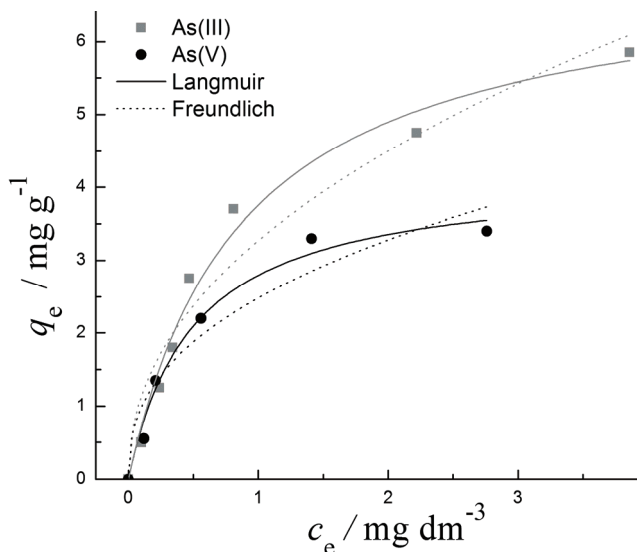


Fig. 4. The sorption isotherms for As(III) and As(V) dissolved in ground water.

Based on the experimental isotherms, Fe–SEP showed capacity of about 10 for As(III) and 4.2 mg g<sup>-1</sup> for As(V) in DW, and 5.8 mg g<sup>-1</sup> for As(III) and 3.4 mg g<sup>-1</sup> for As(V) in GW. As it was expected, the sorption capacities were lower in GW by approximately 20 % for As(V) and 40% for As(III), mainly because the dissolved species present in GW compete with arsenic species for the sorption sites at the surface of the sorbent.

TABLE II. The sorption parameters and correlation coefficients according to the Langmuir and Freundlich model

Mechanism	Langmuir			Freundlich		
Equation	$q_e = \frac{q_m K_L c_e}{1 + K_L c_e}$			$q_e = K_f c_e^{1/n}$		
Type of solution	$K_L / \text{dm}^3 \text{mg}^{-1}$	$q_m / \text{mg g}^{-1}$	$R^2$	$K_f / \text{mg}^{1-1/n} \text{dm}^{3/n} \text{g}^{-1}$	$1/n$	$R^2$
As(III), DW	1.62	10.9	0.952	5.91	0.359	0.948
As(V), DW	3.10	4.95	0.863	3.33	0.247	0.807
As(III), GW	1.14	7.04	0.983	3.27	0.461	0.945
As(V), GW	1.99	4.20	0.982	2.48	0.402	0.921

The values of the correlation coefficients,  $R^2$  (Table II), show that the data fit better to the Langmuir than to the Freundlich model, indicating monolayer adsorption on the homogeneous surface of the adsorbent. The Langmuir sorption model serves to estimate the maximum uptake value or the total capacity of the adsorbent,  $q_m$ , which could not be reached in the experiments. The values of  $q_m$  obtained by the Langmuir model (Table II) were slightly higher than the values

estimated from the experimental isotherms (Fig. 2). The Langmuir constant  $K_L$  represents the strength of adsorption:<sup>13</sup> a higher value of  $K_L$  implies a stronger sorbate–sorbent interaction. As can be seen from Table II, the  $K_L$  values were higher for As(V) than for As(III), indicating that As(V) formed stronger bonds with Fe–SEP than did As(III). As explained in the previous section, at pH<sub>i</sub> 7, As(III) is bonded to the uncharged Fe–SEP surface in the molecular form H<sub>3</sub>AsO<sub>3</sub> and those bonds were weaker than those of the anionic species of As(V) with the positively charged Fe–SEP surface.

#### *Kinetics*

In order to design appropriate sorption units, it is important to predict the rate at which As is removed from contaminated water. The kinetic data for As(III) and As(V) sorption from DW onto Fe–SEP are shown in Fig. 5 ( $c_0 = 0.50 \text{ mg dm}^{-3}$ ) and Fig. 6 ( $c_0 = 3.00 \text{ mg dm}^{-3}$ ). Two stages are noticed for all the curves. The first stage is intensive, and 80 % of the sorption capacity is attained there. The second phase is considerably slower and  $q_t$  value is asymptotically approaching to the equilibrium capacity,  $q_e$ . The first stage was faster for higher concentrations because the driving force for sorption was higher.

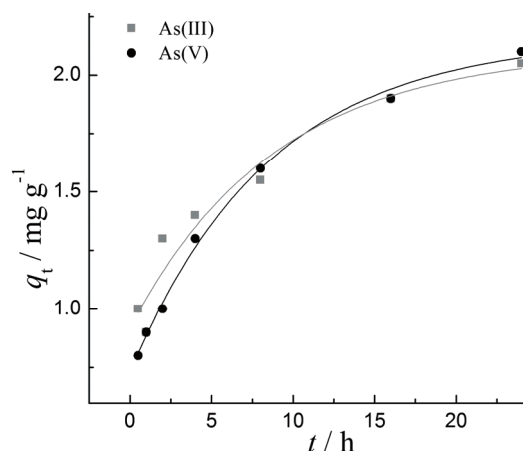


Fig. 5. The sorption kinetics curves for 0.50 mg dm<sup>-3</sup> As(III) and As(V) solutions.

For a lower concentration (0.50 mg dm<sup>-3</sup>), sorption curves for As(III) and As(V) almost overlap, while the curves for concentrations of 3.00 mg dm<sup>-3</sup> have a different shape and plateau position. In this case, Fe–SEP reached considerably higher sorption capacity for As(III) than for As(V), because Fe–SEP has more active sites for As(III) than for As(V) sorption.

The kinetics data were fitted using different models, pseudo-first and pseudo-second order models. Linear forms of these models are presented by Eqs. (2) and (3), respectively.<sup>24–26</sup>

$$\log (q_e - q_t) = \log q_e - k_1 t / 2.303 \quad (2)$$

$$t/q_t = 1/k_2 q_e^2 + t/q_e \quad (3)$$

where  $k_1$  is the rate constant of the pseudo-first order model and  $k_2$  is the rate constant of the pseudo-second order model.

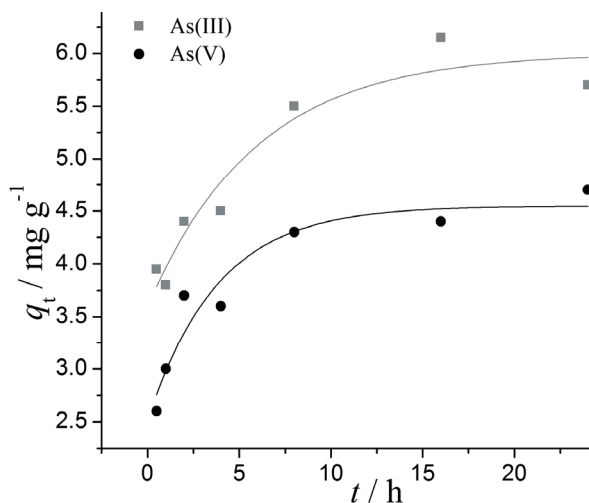


Fig. 6. The sorption kinetics curves for 3.00 mg dm<sup>-3</sup> As(III) and As(V) solutions.

Higher correlation coefficients were obtained for the pseudo-second order model than for the pseudo-first order equation (Fig. 7), and the obtained parameters for this model are given in Table III. Since pseudo-second order implies chemisorption,<sup>25,26</sup> it could be observed that the results of the kinetic analysis are consistent with those of the isothermal studies, *i.e.*, with the applicability of Langmuir model to the isotherm studies. Sorption of As(V) is in better agreement with the pseudo-second order model than As(III) sorption, which is consistent with higher values of Langmuir constant  $K_L$  for As(V) than for As(III) sorption.

#### Comparison of Fe-SEP with other Fe(III)-based sorbents

The sorption capacity of sepiolite toward arsenic was significantly enhanced by the modification, similarly to literature reports for some other natural minerals modified by iron(III) oxyhydroxides. Recently, several Fe(III)-based binary oxide sorbents were synthesized that had surprisingly high sorption capacity for both arsenic(III) and arsenic(V).<sup>33,34</sup> The list of materials and their sorption capacities reported in the literature are summarized in Table IV. The analysis of these values clearly show that sorption capacity of Fe-SEP, being about 10 mg g<sup>-1</sup> for As(III) and 4.2 mg g<sup>-1</sup> for As(V), was comparable with the capacities of some other Fe(III)-based sorbents.

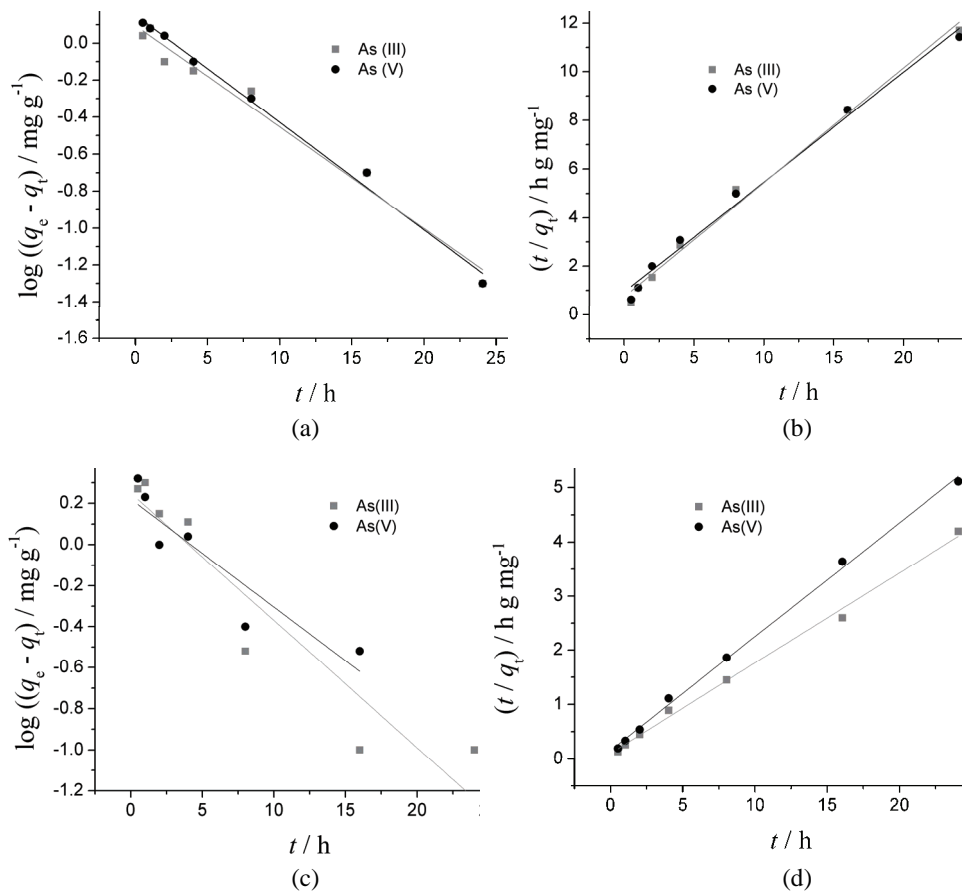


Fig. 7. Experimental data fitting for As(III) and As(V) sorption onto Fe-SEP for  $0.50 \text{ mg dm}^{-3}$  solutions using: a) the pseudo-first and b) the pseudo-second order model, and for  $3.00 \text{ mg dm}^{-3}$  solutions using: c) the pseudo-first and d) the pseudo-second order model.

TABLE III. Kinetic parameters for the pseudo-second order model obtained from Fig. 7

Initial concentration, $\text{mg dm}^{-3}$	Dissolved species	$q_e / \text{mg g}^{-1}$	$k_2 / \text{g mg}^{-1} \text{ h}^{-1}$	$R^2$
0.50	As(III)	2.12	0.302	0.990
	As(V)	2.21	0.218	0.989
3.00	As(III)	6.02	0.271	0.995
	As(V)	4.76	0.279	0.998

TABLE IV. Sorption capacities,  $q_e / \text{mg g}^{-1}$ , of some Fe(III)-based sorbents for As(III) and As(V)

Material	Species		Reference
	As(III)	As(V)	
Zeolite modified with Fe(III)	—	0.68	27
Kaolinite modified with Fe(III)	—	1.74	28
Graphite oxide modified with $\text{Fe}_3\text{O}_4$ and $\text{MnO}_2$	14.04	12.22	9

TABLE IV. Continued

Fe <sub>2</sub> O <sub>3</sub> nanoparticles	20.0	4.90	29
Fe <sub>3</sub> O <sub>4</sub> nanoparticles	5.68	4.78	29
Hematite	—	0.20	30
Mn(II) and Fe(II) in a polymeric matrix	13.5	14.5	31
Fe(III)-Ti(IV) mixed oxide	85.0	14.3	32
Crystalline hydrous ferric oxide	33.3	25.0	32
Fe-Zr mixed oxide	120.0	46.1	33
Fe(III)-Cu(II) binary oxide	122.3	82.7	34
Goethite	22	4	10
Fe-SEP	9.5	4.2	This study

## CONCLUSIONS

Sepiolite modified with hydrated iron(III) oxide was demonstrated to be a very efficient sorbent for the removal of As(III) and As(V) from aqueous solutions. Sorption capacity in deionised water was approximately 10 mg g<sup>-1</sup> for As(III), and 4.2 mg g<sup>-1</sup> for As(V) solutions, at an initial pH value of 7.0. In the case of the sorption from groundwater, the capacity amounts were 5.4 mg g<sup>-1</sup> for As(III), and 3.4 mg g<sup>-1</sup> for As(V).

Sorption isotherm data in all cases showed better fitting to the Langmuir then to the Freundlich model, which indicates single-layer coverage of the sorbent, with a homogeneous distribution of the active sites on the surface. The values of the Langmuir constant showed that As(V) formed stronger bonds with Fe-SEP than As(III). Investigations of kinetics showed that the sorption of inorganic arsenic followed the pseudo-second order model, which is consistent with the applicability of the Langmuir model to the isotherm studies.

The sorption of both As(III) and As(V) species was the best at pH values from 6.0 to 8.0. These are typical pH values of natural waters, so in the case of the application of sepiolite modified with hydrated iron(III) oxide as the sorbent, the water preparation would be easier and less costly.

*Acknowledgements.* The authors would like to acknowledge the financial support of the Ministry of Education, Science and Technological Development of the Republic of Serbia, Project Nos. III 45019, III 43009 and TR 37010.

## ИЗВОД

ПРОУЧАВАЊЕ СОРПЦИЈЕ НЕОРГАНСКОГ АРСЕНА ИЗ ВОДЕНИХ РАСТВОРА НА МОДИФИКОВАНОМ СЕПИОЛИТИУ: УТИЦАЈ ХИДРАТИСАНОГ ГВОЖЂЕ(III)-ОКСИДА

НИКОЛА И. ИЛИЋ<sup>1</sup>, СЛАВИЦА С. ЛАЗАРЕВИЋ<sup>1</sup>, ВЛАДАНА Н. РАЈАКОВИЋ-ОГЊАНОВИЋ<sup>2</sup>,  
ЉУБИНКА В. РАЈАКОВИЋ<sup>1</sup>, ЂОРЂЕ Т. ЈАНАЌКОВИЋ<sup>1</sup> и РАДА Д. ПЕТРОВИЋ<sup>1</sup>

<sup>1</sup>Технолошко-мештаришки факултет, Универзитет у Београду, Карнеијева 4, 11000 Београд и  
<sup>2</sup>Грађевински факултет, Универзитет у Београду, Булевар Краља Александра 83, 11000 Београд

Објект испитивања у овом раду је сепиолит модификовани хидратисаним гвожђе(III)-оксидом и неорганске врсте арсена As(III) и As(V), које представљају најчешће облике арсена у природним водама. Сорпција је изведена у шаржним условима, на 25 °C.

Испитани су утицаји почетне pH вредности раствора, почетних концентрација арсена, времена уравнотежавања и врсте медијума на сорпциони капацитет сорбента. Коришћени су раствори арсена у деминерализованој води и реалној бунарској води. Утврђено је да се максимални сорпциони капацитет за As(III) постиже при константној вредности, pH 7, а за As(V) у ширем интервалу pH вредности од 2 до 7. Сорпциони капацитет при pH 7 је око  $10 \text{ mg g}^{-1}$  за As(III) и  $4,2 \text{ mg g}^{-1}$  за As(V) растворених у деминерализованој води. У бунарској води капацитет је нижи за приближно 40 % у случају As(III) и 20 % за As(V). Експериментални резултати су показали добро слагање са Ленгмировим моделом и кинетичким моделом псеудо-другог реда. Добијени резултати указују на добар потенцијал сепиолита модификованог гвожђе(III)-оксидом за уклањање арсена из природних вода.

(Примљено 12. септембра 2013, ревидирано 13. јануара, прихваћено 5. марта 2014)

#### REFERENCES

1. V. K. Sharma, M. Sohn, *Environ. Int.* **35** (2009) 743
2. P. L. Smedley, D. G. Kinniburgh, *Appl. Geochem.* **17** (2002) 517
3. N. B. Issa, A. D. Marinković, Lj. V. Rajaković, *J. Serb. Chem. Soc.* **77** (2012) 775
4. M. Bissen, F. H. Frimmel, *Acta Hydroch. Hydrob.* **31** (2003) 9
5. M. J. Jiménez-Cedillo, M. T. Olguín, Ch. Fall, A. Colín, *Appl. Clay Sci.* **54** (2011) 206
6. L. M. Camacho, R. R. Parra, S. Deng, *J. Hazard. Mater.* **189** (2011) 286
7. M. B. Baskan, A. Pala, *Desalination* **281** (2011) 396
8. D. L. Guerra, A. C. Batista, P. C. Corrêa da costa, R. R. Viana, C. Airolidi, *J. Colloid Interface Sci.* **346** (2010) 178
9. X. Luo, C. Wang, S. Luo, R. Dong, X. Tu, G. Zeng, *Chem. Eng. J.* **187** (2012) 45
10. B. M. Jovanović, V. L. Vukašinović-Pešić, Đ. N. Veljović, Lj. V. Rajaković, *J. Serb. Chem. Soc.* **76** (2011) 1437
11. Lj. V. Rajaković, Ž. N. Todorović, V. N. Rajaković-Ognjanović, A. Onjia, *J. Serb. Chem. Soc.* **78** (2013) 1461
12. J. C. Crittenden, R. R. Trussell, D. W. Hand, K. J. Howe, G. Tchobanoglous, *Water Treatment, principles and design*, Wiley, Hoboken, NJ, 2005 p. 1245
13. K. Y. Foo, B. H. Hameed, *Chem. Eng. J.* **156** (2010) 2
14. B. M. Jovanović, V. L. Vukašinović-Pešić, Lj. V. Rajaković, *Water Environ. Res.* **83** (2011) 498
15. S. Lazarević, I. Janković-Častvan, V. Đokić, Ž. Radovanović, Đ. Janačković, R. Petrović, *J. Chem. Eng. Data* **55** (2010) 5681
16. Z. Li, J. S. Jean, W. T. Jiang, P. H. Chang, C. J. Chen, L. Liao, *J. Hazard. Mater.* **187** (2011) 318
17. S. Lazarević, I. Janković-Častvan, A. Onjia, J. Krstić, Đ. Janačković, R. Petrović, *Ind. Eng. Chem. Res.* **50** (2011) 11467
18. S. Lazarević, Ž. Radovanović, Đ. Veljović, A. Onjia, Đ. Janačković, R. Petrović, *Appl. Clay Sci.* **43** (2009) 41
19. S. Lazarević, I. Janković-Častvan, B. Potkonjak, Đ. Janačković, R. Petrović, *Chem. Eng. Process.* **55** (2012) 40
20. J. L. Sotelo, G. Ovejero, A. Rodríguez, S. Álvarez, J. García, *Water Air Soil Pollut.* **224** (2013) 1466
21. D. Borat, S. Satokawa, S. Kato, T. Kojima, *J. Hazard. Mater.* **162** (2009) 1269
22. N. B. Issa, V. N. Rajaković-Ognjanović, B. M. Jovanović, Lj. V. Rajaković, *Anal. Chim. Acta* **673** (2010) 185

23. N. B. Issa, V. N. Rajaković-Ognjanović, A. D. Marinković, Lj. V. Rajaković, *Anal. Chim. Acta* **706** (2011) 191
24. S. Lagergren, *Kungliga Svenska Vetensk. Handl.* **24** (1898) 1
25. Y. S. Ho, G. McKay, *Chem. Eng. J.* **70** (1998) 115
26. G. McKay, Y. S. Ho, *Process Biochem.* **34** (1999) 451
27. C. S. Jeon, K. Baek, J. K. Park, Y. K. Oh, S. D. Lee, *J. Hazard. Mater.* **163** (2009) 804
28. L. Dong, P. V. Zinin, J. P. Cowen, L. C. Ming, *J. Hazard. Mater.* **168** (2009) 626
29. S. Luther, N. Borgfeld, J. Kim, J. G. Parsons, *Microchem. J.* **101** (2012) 30
30. U. Shafique, A. Ijaz, M. Salman, W. uz Zaman, N. Jamil, R. Rehman, A. Javaid, *J. Taiwan Inst. Chem. Eng.* **43** (2012) 256
31. I. Jacukowicz-Sobala, D. Ocinski, E. Kocielek-Balawejder, *Ind. Eng. Chem. Res.* **52** (2013) 6453
32. K. Gupta, U. C. Ghosh, *J. Hazard. Mater.* **161** (2009) 884
33. Z. Ren, G. Zhang, J. P. Chen, *J. Colloid Interface Sci.* **358** (2011) 230
34. G. Zhang, Z. Ren, X. Zhang, J. Chen, *Water Res.* **47** (2013) 4022.



## Aqueous nicotine solutions: pH-measurements and salting-out effects – Analysis of the effective Gibbs energies of hydration and ionic strengths of the solutions

NIKOLA D. GROZDANIĆ<sup>1#</sup>, MARTA S. CALADO<sup>2</sup>, MIRJANA LJ. KIJEVČANIN<sup>1#</sup>,  
SLOBODAN P. ŠERBANOVIĆ<sup>1#</sup> and ZORAN P. VIŠAK<sup>2\*</sup>

<sup>1</sup>Faculty of Technology and Metallurgy, University of Belgrade, Karnegijeva 4, 11120 Belgrade, Serbia and <sup>2</sup>Centro de Química Estrutural, Instituto Superior Técnico, Universidade de Lisboa, Av. Rovisco Pais 1, 1049-001 Lisboa, Portugal

(Received 17 August, revised 2 October, accepted 19 October 2013)

**Abstract:** This work is a continuation of previous studies on phase demixing – salting-out effects – in aqueous nicotine solutions. Thus, pH measurements were performed, allowing a brief analysis of the existing hydrogen bond interactions. Salting-out effects – the related experimental cloud point shifts – provoked by the addition of two inorganic salts, potassium nitrate and sodium sulfate, which have not hitherto been studied, were determined. Analysis of the current and previously reported salting-out/or salting-in phenomena in nicotine aqueous solutions was performed. In this respect, five studied salts were included: four inorganic salts (sodium chloride, potassium nitrate, sodium sulfate and trisodium phosphate ( $\text{Na}_3\text{PO}_4$ )), and ionic the liquid 1-ethyl-3-methylimidazolium ethyl sulfate ( $[\text{C}_2\text{mim}][\text{EtSO}_4]$ , commercial name ECOENG212®). Based on pH measurements, the effective Gibbs energies of hydration and the ionic strengths of the respective ternary solutions were calculated and plotted against the related cloud-point shifts caused by the addition of the salts. For the studied salts, the results and diagram obtained within this work may be used to predict the cloud-points shifts, based on the related quantities of the salts added and/or the molar Gibbs energies of hydration and/or ionic strengths requested in each case.

**Keywords:** inorganic salts; ionic liquids; pH measurements of solutions.

### INTRODUCTION

Nicotine is an extremely toxic alkaloid<sup>1</sup> that is completely soluble in water at ambient temperatures.<sup>2,3</sup> It is widely present in tobacco (dust) and the related industrial (aqueous) wastes – thus, nicotine and its aqueous solutions represent a

\* Corresponding author. E-mail: zoran.visak@ist.utl.pt

# Serbian Chemical Society member.

doi: 10.2298/JSC130817109G

dangerous threat to the environment and human health.<sup>1,4–6</sup> On the other hand, nicotine recently started to appear, albeit with concerns, as a potentially useful drug for the treatment of some neurodegenerative diseases.<sup>7–9</sup> Therefore, these issues impose the need not only for nicotine separation/extraction, but also for its purification or recovery. However, common organic (toxic) solvents still play the main role in such applications.<sup>10–14</sup> Thus, it has become an emerging necessity to develop methods that are more environmentally friendly.

In previous studies,<sup>6,15</sup> the potential use of ionic liquids and inorganic salts as the media for eventual sustainable treatment of nicotine and its aqueous solutions were investigated and discussed. In this respect, the salting-out effects, which revealed the very complex nature of the studied aqueous nicotine solutions, were particularly considered.<sup>6</sup>

In this work, the aforementioned studies and the reported salting-out effects – cloud point shifts – provoked by the addition of another two inorganic salts, sodium nitrate and sodium sulfate, were continued. Moreover, both the current and previously reported<sup>6</sup> salting-out and salting-in phenomena were analyzed. Thus, five salting-out media were scrutinized: four inorganic salts (NaCl, KNO<sub>3</sub>, Na<sub>2</sub>SO<sub>4</sub> and Na<sub>3</sub>PO<sub>4</sub>) and the ionic liquid 1-ethyl-3-methylimidazolium ethyl sulfate ([C<sub>2</sub>mim][EtSO<sub>4</sub>], commercial name ECOENG212<sup>®</sup>).

The pH values for the (nicotine+water) binary solutions and for the ((nicotine+water)+salt) systems were measured. Based on these measurements a brief analysis of the hydrogen bond interactions was given. Moreover, the effective Gibbs energy of hydration and ionic strength were calculated for the respective ternary solutions and the diagrams showing their relation to the related cloud-point shifts were constructed. These results enabled the prediction of the cloud-points shifts, for each salt included, based on the related quantities of the salts applied and/or the molar Gibbs energies of hydration or ionic strengths necessary for each shift to be achieved.

## EXPERIMENTAL

### *Chemicals*

Ionic liquid 1-ethyl-3-methyl imidazolium ethyl sulfate, [C<sub>2</sub>mim][EtOSO<sub>3</sub>] (ECOENG 212<sup>®</sup>), was purchased from Solvent Innovation (Merck), with a stated purity > 98 mass % (water and chloride content 153 and 404 ppm, respectively). Nicotine, sodium chloride, potassium nitrate and sodium sulfate were obtained from Sigma–Aldrich, with the stated purities: > 99, 99.5, ≥ 99 and ≥ 99 mass %, respectively. Trisodium phosphate (Na<sub>3</sub>PO<sub>4</sub>) was acquired from Riedel de Haën with a stated purity of 96 mass %.

ECOENG212<sup>®</sup> was subjected to vacuum (0.1 Pa) at moderate temperature (60 °C), several days prior to the experiments. This procedure was primarily applied to reduce significantly the presence of volatile compounds (solvents) in the ionic liquid but also to dry it. The water contents after the drying procedure were very low, below 90 ppm, as determined by coulometric Aquapal Karl–Fischer titration. Thus, the presence of water was not considered in the subsequent preparation of the aqueous solutions. As in previous studies<sup>6,15</sup> and according to

recommendations from literature,<sup>16</sup> the stated chloride contents were taken as acceptable and no further reduction was performed. Considering the possibility of the anion hydrolysis,<sup>6,17</sup> which would lead to acidity increase,<sup>6</sup> the pH of the used ECOENG212<sup>®</sup> was checked and the values were far from acidic (pH 6.50–6.90).

Nicotine was dried using 3 Å molecular sieves for at least 48 h ahead of the experiments and the Karl-Fischer titrations revealed water contents of 100 ppm.

Solutions were prepared gravimetrically using a Mettler AT201 analytical semi-microbalance with a stated accuracy (repeatability) of  $\pm 2 \times 10^{-5}$  in mass fraction. Doubly distilled and deionized Millipore water (Millipore Co. equipment, Bedford, MA) was used to prepare the solutions.

#### *pH Measurements*

Current pH measurements were performed at room temperature, using an InoLab Multi 720 pH meter (WTW GmbH, Germany). The device was calibrated each time prior to the experiments using two different buffers having pH values of 7.00 (Technischen puffer WTW STP 7) and 10.00 (Technischen puffer WTW STP 10). Fresh Millipore water was always used for the measurements.

#### *Liquid–liquid equilibria – cloud-point shift determination*

The liquid–liquid equilibria experiments performed herein were related to the determination of cloud-point shifts due to salt addition (salting-out effects) to the (nicotine+water) solutions initially having a near-critical concentration of nicotine (the mole fraction of nicotine was 0.0708). In this respect, a dynamic, visual method was used – in the studied solutions, the turbidity (cloud-point) that indicates the beginning of phase demixing was observed by eye, while heating a homogeneous solution. The experiments were performed in a Pyrex-glass cell, introduced by Domanska<sup>18</sup> and applied in several studies thereafter.<sup>6,19–25</sup> A description of the cell, its application and the procedure of the cloud-point observation were described in details in earlier contributions.<sup>6,22,23</sup> The uncertainties in the determination of the cloud-point temperatures ( $T_{cp}$ ), estimated from repeated measurements, were  $\pm 0.4$  K. A 2-L glass beaker filled with ethylene glycol, as a thermostatic liquid, was used as a thermostat bath in all the experiments. Temperature was monitored using a Pt100 temperature probe, having an accuracy of  $\pm 0.03$  K.

## RESULTS

The pH values determined for the studied (nicotine+water) solutions, without any added buffer, are presented in Table I. In order to keep the concept of water as a solvent and, thus, its ion product applicable, the measurements were performed in the nicotine concentration range up to 85 % by mass.<sup>26</sup> This table also gives the pH-dependent percentage ( $P$ ) of unprotonated nicotine molecules ( $\text{Nic}^0$  – free base) and protonated nicotine (both  $\text{Nic}^+$  and  $\text{Nic}^{2+}$ ) given as:<sup>27</sup>

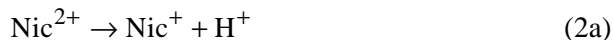
$$P(\text{Nic}^0) = \frac{100}{\frac{[\text{H}^+]^2}{K_{a2}K_{a1}} + \frac{[\text{H}^+]}{K_{a2}} + 1} \quad (1)$$

In Eq. (1),  $[\text{H}^+]$  is the concentration of the protons in the solution, calculated from the related pH values in Table I;  $K_{a1}$  and  $K_{a2}$  are the acid dissociation

equilibrium constants having the values  $10^{-3.41}$  and  $10^{-8.01}$ , respectively, according to the  $pK_a$  values cited in the literature.<sup>28</sup> These constants refer to the following equilibria:

$$K_{a1} = \frac{[\text{Nic}^+][\text{H}^+]}{[\text{Nic}^{2+}]} \quad (2)$$

that is related to the acid dissociation of the nicotine dication:



and to:

$$K_{a2} = \frac{[\text{Nic}^0][\text{H}^+]}{[\text{Nic}^+]} \quad (3)$$

that refers to the acid dissociation of the nicotine monocation:



The percentage of the protonated nicotine is then calculated by the expression:

$$P(\text{Nic}^+ + \text{Nic}^{2+}) = 100 - P(\text{Nic}^0) \quad (4)$$

TABLE I. pH Values of the studied (nicotine+water) solutions, at 298.15 K, and the percentages of nicotine that exists in the solutions as the free base  $P(\text{Nic}^0)$ ;  $w_{\text{Nic}}$  and  $x_{\text{Nic}}$  are the mass and mole fraction of nicotine in the aqueous solutions, respectively;  $\rho$  is density of the studied nicotine aqueous solutions and  $c$  is the related molar concentration of nicotine. The pH of the Millipore water used for the preparation of these solutions was 6.81

$w_{\text{Nic}}$	$x_{\text{Nic}}$	$\rho / \text{kg m}^{-3}$ <sup>a</sup>	$c / \text{mol dm}^{-3}$	pH	$[\text{H}^+] \times 10^{11}$	$P(\text{Nic}^0)$ <sup>b</sup>	$P(\text{Nic}^+ \text{ and } \text{Nic}^{2+})$
0.0002	$2.2 \times 10^{-5}$	997.13	0.0012	9.10	79.4	92.48	7.52
0.0007	$7.6 \times 10^{-5}$	997.13	0.0042	9.55	28.2	97.20	2.80
0.0019	0.0002	997.13	0.0114	9.95	11.2	98.86	1.14
0.0045	0.0005	997.33	0.0277	10.10	7.94	99.19	0.81
0.0103	0.0012	997.61	0.0633	10.25	5.62	99.43	0.57
0.0478	0.0055	999.93	0.2947	10.38	4.17	99.58	0.42
0.1401	0.0178	1006.31	0.8690	10.48	3.31	99.66	0.34
0.2001	0.0270	1010.46	1.2463	10.50	3.16	99.68	0.32
0.4071	0.0708	1024.55	2.5708	10.38	4.17	99.58	0.42
0.6012	0.1433	1034.09	3.8319	10.10	7.94	99.19	0.81
0.7055	0.2100	1035.28	4.5019	9.85	14.1	98.58	1.42
0.8012	0.3074	1031.69	5.0872	9.62	24.0	97.60	2.40
0.8501	0.3860	1027.49	5.3832	9.52	30.2	97.00	3.00

<sup>a</sup>Densities of the (nicotine+water) solutions were calculated using experimental data;<sup>b</sup>nicotine as a free base is an unprotonated form ( $\text{Nic}^0$ ) of this alkaloid represented by its neutral molecule

The experimental cloud-point temperatures, at a pressure of 0.1 MPa, as a function of the salt compositions in the present ternary solutions are given in Table II. Following the previous procedure, the salts were added to the initial

(water+nicotine) solution of a near-critical nicotine concentration ( $(X_S)_T = 0$ ;  $X_{\text{Nic}} = 0.0708$  in mole fractions).<sup>6</sup>

TABLE II. Ternary solutions (nicotine+water+salt) at a pressure of 0.1 MPa: liquid phase demixing temperatures (cloud-points,  $T_{\text{cp}}$ ) and their negative shifts ( $\Delta T_{\text{cp}}$ ) as a function of the salt compositions.  $(x_S)_T$  and  $(x_{\text{Nic}})_T$  are mole fractions of salt and nicotine in the ternary solutions, respectively. The salts were added to the initial (nicotine+water) solution of near-critical nicotine concentration ( $(x_S)_T = 0$ ;  $x_{\text{Nic}} = 0.0708$  in mole fractions). Standard NIST uncertainties were, in mole fraction,  $u(x) = 3 \times 10^{-4}$  and in temperature  $u(T) = \pm 0.4$  K

Salt: $\text{KNO}_3$				Salt: $\text{Na}_2\text{SO}_4$			
$(x_S)_T$	$(x_{\text{Nic}})_T$	$T_{\text{cp}} / \text{K}$	$\Delta T_{\text{cp}} / \text{K}$	$(x_S)_T$	$(x_{\text{Nic}})_T$	$T_{\text{cp}} / \text{K}$	$\Delta T_{\text{cp}} / \text{K}$
0.0000	0.0000	335.0	0.0	0.0000	0.0000	335.0	0.0
0.0087	0.0702	326.3	-8.7	0.0008	0.0707	328.2	-6.8
0.0131	0.0699	322.2	-12.8	0.0013	0.0707	323.1	-11.9
0.0181	0.0695	317.0	-18.1	0.0019	0.0707	318.4	-16.6
0.0247	0.0690	310.6	-24.4	0.0023	0.0706	314.7	-20.4
0.0286	0.0688	306.3	-28.7	0.0027	0.0706	311.3	-23.7

The values of the molar Gibbs energies of hydration of each ion species  $i$  at 298.15 K and 0.1 MPa,  $(G_i)_{\text{hyd}}$ , both for the solutions studied herein and previously,<sup>6</sup> are presented in Table III. The values of  $(G_i)_{\text{hyd}}$  for  $[\text{C}_2\text{mim}]^+$ ,  $\text{HPO}_4^{2-}$  and  $[\text{EtSO}_4]^-$  at 298.15 K – to the best of our knowledge not available in the literature – were calculated using the related ionic radii and applying the calculation procedure set by Marcus.<sup>29</sup> The radii for  $[\text{C}_2\text{mim}]^+$  (0.303 nm)<sup>30</sup> and  $\text{HPO}_4^{2-}$  (0.238 nm)<sup>31</sup> were taken from the literature. However, no reported values for the radius of  $[\text{EtSO}_4]^-$  could be found. Thus, the radius was calculated either *i*) using the radius for  $\text{SO}_4^{2-}$  (0.230 nm)<sup>31</sup> and the contributions for the  $\text{CH}_3-$  and  $\text{CH}_2-$  groups given by Bondi<sup>32</sup> or *ii*) by applying the procedure based on the McGowan volumes,<sup>33</sup> given by Zhao *et al.*<sup>34</sup> – see the Supplementary Material to this paper for details. Both approaches gave very similar values of the anion radius: *i*) 0.280 and *ii*) 0.282 nm.

TABLE III. Molar Gibbs energies of hydration at 298.15 K and 0.1 MPa,  $(g_i)_{\text{hyd}}$ , of the ion species present in the studied salts (this work and from the literature<sup>6</sup>)

Ion	$(G_i)_{\text{hyd}} / \text{kJ mol}^{-1}$	Ion	$(G_i)_{\text{hyd}} / \text{kJ mol}^{-1}$
$\text{Na}^+$	-385	$\text{Cl}^-$	-270
$\text{K}^+$	-305	$\text{NO}_3^-$	-275
$[\text{C}_2\text{mim}]^+$	-53.2	$\text{SO}_4^{2-}$	-1145
$[\text{EtSO}_4]^+$	-139.7	$\text{PO}_4^{3-}$	-2835
$\text{OH}^-$	-345	$\text{HPO}_4^{2-}$	-1125.3

For the other ions in Table III, the experimental values of the molar Gibbs energies of hydration at 298.15 K and 0.1 MPa taken from the literature<sup>29</sup> were included.

In Table IV, for all these hitherto studied solutions, the cloud-point temperatures,  $T_{\text{cp}}$ , are given as a function of the effective Gibbs energies of hydration,  $(\Delta G_{\text{eff}})_{\text{hyd}}$ , of the salts and ionic strength increase of the solutions,  $\Delta I$ . The last two properties were calculated as follows:

$$(\Delta G_{\text{eff}})_{\text{hyd}} = \frac{1}{n_T} \sum_i n_i (G_i)_{\text{hyd}} \quad (5)$$

$$\Delta I = \sum_i m_i z_i^2 \quad (6)$$

In the equations above,  $n_i$ ,  $n_T$ ,  $m_i$  and  $z_i$  are number of moles of each ion, total number of moles in the ternary solution, molal concentration of every present ion and its formal charge, respectively.  $(G_i)_{\text{hyd}}$  is molar Gibbs energy of hydration of each ion  $i$  as explained above with the values given in Table III.

TABLE IV. Cloud-point temperatures ( $T_{\text{cp}}$ ), at a pressure of 0.1 MPa, as a function of the effective Gibbs energies of hydration  $(\Delta G_{\text{eff}})_{\text{hyd}}$  of the studied salts and of ionic strength of the respective solutions

$(\Delta G_{\text{eff}})_{\text{hyd}} / \text{kJ mol}^{-1}$	$\Delta I / \text{mol kg}^{-1} \text{a.c.u.}^2$	$T_{\text{cp}} / \text{K}$
Salt: NaCl		
0.000	0.000	335.0 <sup>a</sup>
1.954	0.212	329.3 <sup>a</sup>
2.861	0.311	326.3 <sup>a</sup>
4.232	0.461	323.2 <sup>a</sup>
5.768	0.630	318.5 <sup>a</sup>
9.822	1.079	309.5 <sup>a</sup>
10.939	1.204	306.3 <sup>a</sup>
12.764	1.409	301.1 <sup>a</sup>
Salt: Na <sub>2</sub> SO <sub>4</sub>		
0.000	0.000	335.0 <sup>b</sup>
1.430	0.168	328.2 <sup>b</sup>
2.439	0.287	323.1 <sup>b</sup>
3.398	0.400	318.4 <sup>b</sup>
4.155	0.489	314.7 <sup>b</sup>
4.845	0.571	311.3 <sup>b</sup>
Salt: KNO <sub>3</sub>		
0.000	0.000	335.0 <sup>b</sup>
5.168	0.621	326.3 <sup>b</sup>
7.776	0.939	322.2 <sup>b</sup>
10.763	1.306	317.0 <sup>b</sup>
14.707	1.797	310.6 <sup>b</sup>
17.019	2.087	306.3 <sup>b</sup>
Salt: Na <sub>3</sub> PO <sub>4</sub>		
0.000	0.000	335.0 <sup>a</sup>
0.633	0.062	330.4 <sup>a</sup>
1.416	0.152	327.4 <sup>a</sup>

TABLE IV. Continued

$(\Delta G_{\text{eff}})_{\text{hyd}} / \text{kJ mol}^{-1}$	$\Delta I / \text{mol kg}^{-1} \text{a.c.u.}^2$	$T_{\text{cp}} / \text{K}$
Salt: $\text{Na}_3\text{PO}_4$		
2.019	0.217	323.7 <sup>a</sup>
2.757	0.297	320.1 <sup>a</sup>
2.912	0.314	319.4 <sup>a</sup>
Salt: $[\text{C}_2\text{mim}][\text{EtSO}_4]$		
0.0000	0.000	335.0 <sup>a</sup>
1.513	0.583	339.8 <sup>a</sup>
5.692	2.246	343.3 <sup>a</sup>
7.453	2.970	340.3 <sup>a</sup>
10.159	4.111	334.6 <sup>a</sup>
12.276	5.028	329.7 <sup>a</sup>
14.775	6.141	321.6 <sup>a</sup>
15.953	6.676	318.2 <sup>a</sup>
19.255	8.218	305.8 <sup>a</sup>
22.051	9.572	296.2 <sup>a</sup>

<sup>a</sup>Cloud-point taken from the literature;<sup>6</sup> <sup>b</sup>cloud-point obtained within this work

It is known that the inorganic salts  $\text{NaCl}$ ,  $\text{KNO}_3$  and  $\text{Na}_2\text{SO}_4$  are practically completely dissociated in their aqueous solutions and the same is postulated for ECOENG212®.<sup>35</sup> However, in order to confirm experimentally that these expectations stand in the presence of nicotine, the pH values of the studied (nicotine+water+salt) solutions were measured at distinct salt compositions. The changes in pH upon addition of the aforementioned salts to (nicotine+water) solutions confirmed their complete dissociation. Namely, the percentages of the change in pH were, on average, 1.24 ( $\text{NaCl}$ ), 0.19 ( $\text{KNO}_3$ ), 2.01 ( $\text{Na}_2\text{SO}_4$ ) and 2.5 % (ECOENG212®). Thus, the values of  $n_i$  and  $m_i$  of the actual ions needed in Eqs. (5) and (6) were calculated using the respective stoichiometry. However, the large increase of pH observed when  $\text{Na}_3\text{PO}_4$  was included (17.47 %) imposes that the equilibrium:



has to be taken into account. The equilibrium constant for hydrolysis is  $K_b = 2.24 \times 10^{-2}$ , while the other two dissociation reactions can be neglected. Therefore,  $\text{PO}_4^{3-}$ ,  $\text{HPO}_4^{2-}$  and  $\text{OH}^-$  exist in the solutions and their molal concentrations were calculated using the aforementioned value of  $K_b$ .

A low molar entropy of hydration<sup>36,37</sup> imposes a weak temperature dependence of the molar Gibbs energies of hydration – this was true for all the ions of the studied inorganic salts and could be reasonably assumed for those of ECOENG212®. Therefore, the values of  $(G_i)_{\text{hyd}}$  at 298.15 K were used for the calculations of the effective Gibbs energies of hydration at the other temperatures presented in Table IV.

Figure 1 compares the liquid phase demixing data from Table II and from a previous study,<sup>6</sup> whereas Figs. 2 and 3 give cloud-point temperature as a function of the ionic strength increase in different salts and in ECOENG212<sup>®</sup>, all along with the fittings.

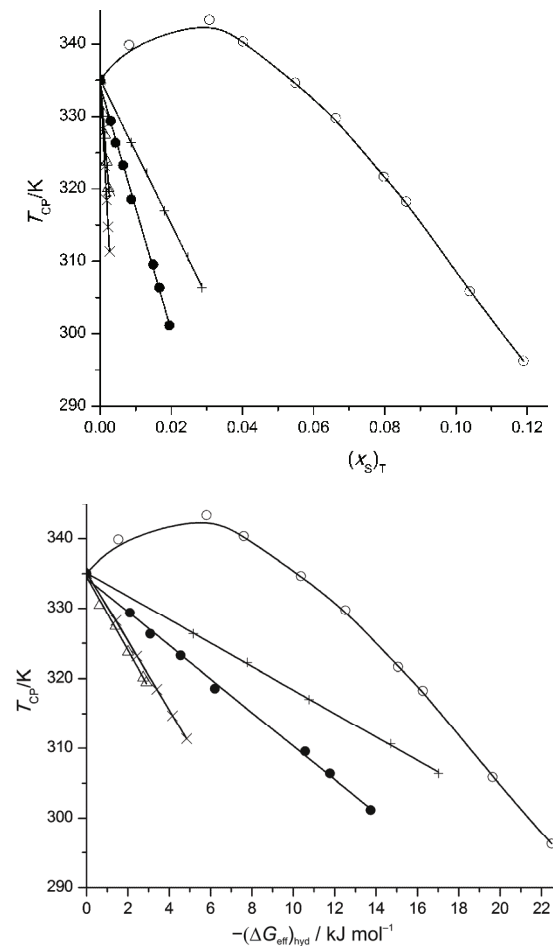


Fig. 1. Cloud-point temperatures ( $T_{cp}$ ) as a function of the composition of different salts in the ternary (nicotine+water+salt) solution ( $(x_S)_T$ ):  $\Delta$  –  $\text{Na}_3\text{PO}_4$  (literature data<sup>6</sup>),  $\times$  –  $\text{Na}_2\text{SO}_4$  (data from this work),  $\bullet$  –  $\text{NaCl}$  (literature data<sup>6</sup>),  $+$  –  $\text{KNO}_3$  (data from this work) and  $\circ$  – ECOENG212<sup>®</sup> (literature data<sup>6</sup>). The salts were added to the initial binary (nicotine+water) solution of near-critical nicotine concentration ( $(x_S)_T = 0$  and  $x_{\text{Nic}} = 0.0708$ ). The lines represent the fittings of the experimental data.

Fig. 2. Cloud-point temperatures ( $T_{cp}$ ) as a function of the effective Gibbs energy of hydration ( $(\Delta G_{eff})_{hyd}$ ):  $\Delta$  –  $\text{Na}_3\text{PO}_4$ ,  $\times$  –  $\text{Na}_2\text{SO}_4$ ,  $\bullet$  –  $\text{NaCl}$ ,  $+$  –  $\text{KNO}_3$  and  $\circ$  – ECOENG212<sup>®</sup>. The salts were added to the initial binary (nicotine+water) solution of near-critical nicotine concentration ( $(x_S)_T = 0$  and  $x_{\text{Nic}} = 0.0708$ ). The lines represent the fittings of the experimental data.

Table V presents the effective Gibbs energies of hydration calculated for ternary (nicotine+water+salt) solutions of a given composition ( $(x_S)_T = 0.0006$ ,  $(x_{\text{Nic}})_T = 0.07075$ , Eq. (5)) and the related negative cloud-point shifts ( $\Delta T_{cp}$ ) obtained from the linear fits of the data from Table II and from the previous study.<sup>6</sup> Thus, the obtained  $\Delta T_{cp}$  vs.  $(\Delta G_{eff})_{hyd}$  data are shown in Fig. 4. In respect to ECOENG212<sup>®</sup>, both procedures of the radius calculation (see above) gave also very similar values of  $(\Delta G_{eff})_{hyd}$  ( $-0.7507$  kJ mol<sup>-1</sup>) in the first case and

-0.7408 kJ mol<sup>-1</sup> in the second) and, for practical reasons, only the first point is included in Fig. 4.

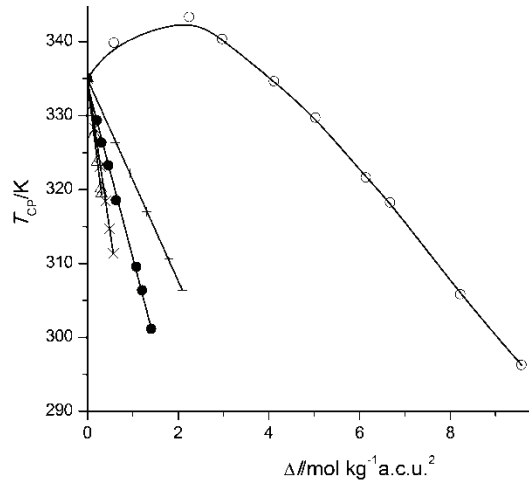


Fig. 3. Cloud-point temperatures ( $T_{\text{cp}}$ ) as a function of the ionic strength increase ( $\Delta I$ ):  $\Delta$  –  $\text{Na}_3\text{PO}_4$ ,  $\times$  –  $\text{Na}_2\text{SO}_4$ ,  $\bullet$  –  $\text{NaCl}$ ,  $+$  –  $\text{KNO}_3$  and  $\circ$  – ECOENG212®. The salts were added to the initial binary (nicotine+water) solution of near-critical nicotine concentration ( $(x_S)_T = 0$  and  $x_{\text{Nic}} = 0.0708$ ). The lines represent the fittings of the experimental data.

TABLE V. Effective Gibbs energies of hydration,  $(\Delta G_{\text{eff}})_{\text{hyd}}$ , and the related negative cloud-point shifts,  $\Delta T_{\text{cp}}$ , for the studied salts in (nicotine+water+salt) solutions of the given composition (ternary salt mole fraction was  $(x_S)_T = 0.0006$  and that of nicotine  $(x_{\text{Nic}})_T = 0.07075$ )

Salt	$-(\Delta G_{\text{eff}})_{\text{hyd}} / \text{kJ mol}^{-1}$	$\Delta T_{\text{cp}} / \text{K}$
$\text{Na}_3\text{PO}_4$	1.849	-10.1
$\text{Na}_2\text{SO}_4$	1.086	-5.3
$\text{NaCl}$	0.423	-1.0
$\text{KNO}_3$	0.357	-0.6
ECOENG212®	0.112	1.5

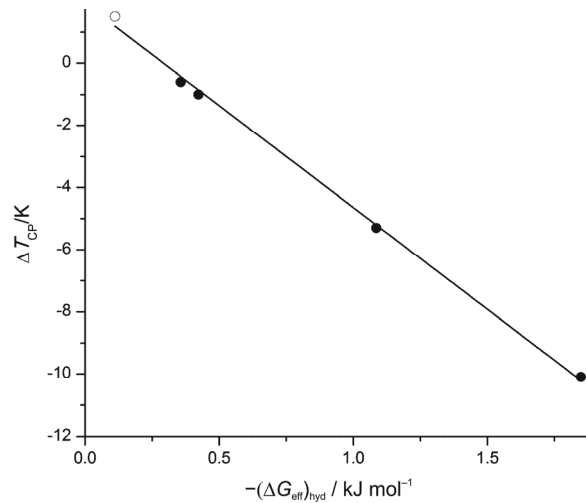


Fig. 4. Generalized graph: cloud-point shifts ( $\Delta T_{\text{cp}}$ ) as a function of the effective Gibbs energy of hydration ( $(\Delta G_{\text{eff}})_{\text{hyd}}$ ) (for the (nicotine+water+salt) solution of a given composition ( $(x_S)_T = 0.004$ ,  $(x_{\text{Nic}})_T = 0.07051$ ):  $\bullet$  – the points related to the four inorganic salts studied herein and  $\circ$  – the point related to ECOENG212®. The latter was excluded from the linear regression given in the graph.

## DISCUSSION

It is well-known and described in the literature that nicotine can exist in three forms in its aqueous solutions: as a free base (unprotonated, neutral molecule Nic<sup>0</sup>), singly protonated (monocation Nic<sup>+</sup>) and doubly protonated (dication Nic<sup>2+</sup>).<sup>12,27,38–40</sup> The first protonation ( $pK_b = 5.99$  or  $pK_a = 8.01$ ) occurs on the nitrogen atom (Nsp<sup>3</sup>) of the nicotine *N*-methylpyrrolidine ring, while the second one occurs on the nitrogen (Nsp<sup>2</sup>) in the pyridine ring ( $pK_b = 10.59$  or  $pK_a = 3.41$ ).<sup>28</sup> In other words, the much higher basicity of the pyrrolidine nitrogen compared to that of the pyridine one implies that the presence of the monocation, created by the protonation of the pyridine nitrogen, can be neglected.<sup>39</sup> However, it was also emphasized that the percentage of protonated nicotine is dependent on the pH of the solution.<sup>38,40</sup> Thus, Table I shows that the pH values of the (nicotine+water) solutions allowed that the major part of the nicotine remained as the free base. As the nicotine concentration was increased, the pH first increased, then exhibited a maximum and finally decreased, see Fig. 1. Both experimental<sup>41</sup> and simulation studies<sup>42</sup> imply that the network of hydrogen bonds between nicotine and water is a complex dynamic structure that depends on the protonation of nicotine that mainly occurs at the pyrrolidine nitrogen.<sup>38,40</sup> Briefly, it appears that this protonation – as an overall effect – even reinforces the hydrogen bond network by introducing one more (a two-fold) binding site and stabilizing the structure of the bonds *via* the specific interactions between water and the charged pyrrolidine ring.<sup>42</sup> Although any extrapolation to higher nicotine mole fractions is as yet uncertain, Table I shows a behavior that agrees with the aforementioned findings. Namely, in aqueous nicotine solutions with a nicotine content over  $\approx 36$  mol %, generally homogeneous at any temperature (see the nicotine+water temperature–composition “closed loop” phase diagram reported in literature<sup>3</sup>), protonation is increasingly present. The percentage of protonated nicotine follows an abrupt, practically linear increase with increasing nicotine composition, which commenced when the near-critical concentration of nicotine (0.0708 mole fraction) was surpassed. From the interaction point of view only, this analysis certainly concurs with a very good solubility of nicotine in water, depicted in the large areas of complete miscibility in its phase diagram.

Figure 1 showed that KNO<sub>3</sub> was the inorganic salt that provoked the worst salting-out effect, reasonably poorer than that of NaCl, determined previously,<sup>6</sup> probably due to the lower hydration abilities of the constituting ions. On the contrary, the achievement of Na<sub>2</sub>SO<sub>4</sub> was exceptionally good and very similar, although slightly inferior, to that of Na<sub>3</sub>PO<sub>4</sub>. This occurrence could have been expected since salts of doubly- and triply-charged anions are excellent water-structuring (kosmotropic) salts, having highly negative effective Gibbs energies of hydration.<sup>36,43</sup>

The effective Gibbs energies of hydration or ionic strengths necessary for each salting-out effect (cloud-point shift) of each salt added to the aforementioned initial binary (nicotine+water) solution are depicted in Figs. 2 and 3, respectively. These figures indicate that a change in ionic strength strongly affected the liquid phase demixing behavior.

On the other hand, as reported and discussed previously,<sup>6</sup> ECOENG212<sup>®</sup> changes its behavior from salting-in, at lower concentrations (chaotropic behavior prevails, provided by the non-polar alkyl side chains), to salting-out at higher concentrations, (kosmotropic behavior becomes dominant, due to the polar part of the ions). Thus, it has to be added in larger quantities in order to afford Gibbs energies of hydration and/or ionic strengths able to provoke a significant cloud-point decrease. Nevertheless, the fact that ECOENG212<sup>®</sup> is a molten salt (wide liquid range), completely soluble in water and that it is a relatively low-priced ionic liquid speak in favor of its use for the present purposes.

Figure 4, in relation to Table V, shows which effective Gibbs energy of hydration is required in order to achieve a certain temperature shift in nicotine aqueous solution after adding an exact quantity (0.06 mole fraction in the ternary solution) of salt in general. For the four studied inorganic salts, the linear regression was very good ( $R^2 = 0.999975$ ), which could have been expected from the linear form in the mole fractions of Eq. (5) and generally the very good linear fits of  $T_{cp}$  by ternary composition  $((x_S)_T)$  of the added inorganic salts, see Fig. 1. Actually, the results of this work and a previous study,<sup>6</sup> as well as the salting-out effects studied in the other aqueous solutions such as those of ionic liquids<sup>36</sup> and poly(ethylene glycol)<sup>44</sup> indicate, although still with caution, that the linear dependence shown in Fig. 1 is not a sheer coincidence but something that might reasonably be expected, once the experiments were performed carefully. If this assumption is accepted, Fig. 4 could be considered as a general graph for (nicotine+water) solutions and, thus, shows two interesting features: *i*) which effective Gibbs energy of hydration is expected to provoke a null cloud-point shift and *ii*) what is the salting-in effect that could be anticipated applying a salt that would give a null effective Gibbs energy of hydration. – in principle, this could occur since there are some ions that possess null or positive molar Gibbs energy of hydration.<sup>29</sup>

However, the point related to ECOENG212<sup>®</sup>, which was included in Fig. 4 but not in the regression since the ionic (van der Waals) radius of its anion, necessary to obtain  $(\Delta G_{eff})_{hyd}$ , was calculated and not taken from literature, see the text above and the Supplementary Material to this paper. Moreover, the positive shift for the given composition in the case of ECOENG212<sup>®</sup> was not obtained by linear but polynomial fit of the related cloud-point–composition curve (see Fig. 1). These could be the reasons for the worse agreement to a linear regression compared to the other four points.

Thus, Figs. 1–4 demonstrate which solutions should be prepared in order to expect certain salting-out effects ( $T_{cp}$  shifts) and which effective Gibbs energies of hydration and/or ionic strength are required to achieve them.

The results show that small quantities of inorganic salts, actually extremely small in the case of the salts with polyvalent ions, provide effective Gibbs energies of hydration and ionic strengths sufficient to allow strong salting-out effects and abrupt decreases in the cloud-point.

#### CONCLUSIONS

The pH measurements of (nicotine+water) solutions showed that the bulk of nicotine molecules therein exist in the neutral, unprotonated form. This study also demonstrated that the presence of the protonated form rapidly increases as the critical concentration of nicotine in water is surpassed. Moreover, as stated above, in nicotine solutions with a nicotine content over  $\approx 36$  mol %, the percentage of the protonated form steadily increases.

Analyses in literature clearly show that the hydrogen bonded network of nicotine with water is very stable and strong in both neutral and protonated form of its molecule. In fact, the overall effect of the protonation of nicotine is the strengthening of this network, which is in agreement with the results obtained in the present study.

The inorganic salts studied herein appeared as very efficient salting-out media – added in very small quantities they provided effective Gibbs energies of hydration and ionic strengths sufficient to allow large negative cloud-point shifts.

The results of this work may be useful as a guide in future applications of the studied salts in treating aqueous nicotine solutions.

#### SUPPLEMENTARY MATERIAL

Calculation of the McGowan volumes and the Pauling ionic radius are available electronically from <http://www.shd.org.rs/JSCS/>, or from the corresponding author on request.

*Acknowledgements.* This work was financially supported by the Research Fund of Ministry of Education, Science and Technological Development of the Republic of Serbia (Project No. 172063) through the Faculty of Technology and Metallurgy, University of Belgrade, Serbia, by the Fundação para a Ciéncia e a Tecnologia (FC&T), Portugal, through the project PTDC/EQU-EPR/103505/2008 and by the project “Projecto Estratégico – PEst-OE/QUI/UI0100/2013”, Instituto Superior Técnico, Portugal. Moreover, the authors are grateful to Professor Michael Abraham, University College London, for fruitful help.

## И З В О Д

ВОДЕНИ РАСТВОРИ НИКОТИНА: pH МЕРЕЊА И „SALTING OUT“ ЕФЕКТИ – АНАЛИЗА  
ЕФЕКТИВНЕ ГИБСОВЕ ЕНЕРГИЈЕ ХИДРАТАЦИЈЕ И ЈОНСКЕ ЈАЧИНЕ РАСТВОРАНИКОЛА Д. ГРОЗДАНИЋ<sup>1</sup>, МАРТА С. САЛАДО<sup>2</sup>, МИРЈАНА Љ. КИЈЕВЧАНИЋ<sup>1</sup>, СЛОБОДАН П. ШЕРБАНОВИЋ<sup>1</sup>  
и ЗОРАН П. ВИШАК<sup>2</sup><sup>1</sup>Технолошко–међуалуршки факултет, Универзитет у Београду, Карађорђева 4, 11120 Београд и <sup>2</sup>Centro de Química Estrutural, Instituto Superior Técnico, Universidade Técnica de Lisboa, Av. Rovisco Pais 1, 1049-001 Lisboa, Portugal

Рад је наставак претходне студије о немешљивости фаза у воденим растворима никотина. pH мерења су дала кратку анализу интеракција постојећих водоничних веза. Одређивани су „salting out“ ефекти изазвани додавањем две неорганске соли, калијум-нитрата и натријум-сулфата, који нису разматрани раније. У овој као и претходној студији, анализирани су „salting out or in“ ефекти у воденим растворима никотина за четири неорганске соли: натријум-хлорид, калијум-нитрат, натријум-сулфат и натријум-фосфат као и за јонску течност 1-етил-3-метилимидазолијум етил-сулфат ( $[C_2mim][EtSO_4]$ ), комерцијални назив ECOENG212<sup>®</sup>). За разматране соли, резултати и добијени дијаграми у овом раду могу да се узму за предсказивање померања тачака замућења, на основу количине додатих соли, Гибсове енергије хидратације и јонске јачине.

(Примљено 17. августа, ревидирано 2. октобра, прихваћено 19. октобра 2013)

## REFERENCES

1. R. E. Gosselin, R. P. Smith, H. C. Hodge, *Clinical Toxicology of Commercial Products*, 6<sup>th</sup> ed., Williams & Wilkins, Baltimore, MD, 1988, p. 311
2. J. Timmermans, *The Physico-Chemical Constants of Binary Systems in Concentrated Solutions*, Interscience, New York, 1959
3. A. N. Campbell, E. M. Kartzmark, W. E. Falconer, *Can. J. Chem.* **36** (1958) 1475
4. T. E. Novotny, F. Zhao, *Tob. Control* **8** (1999) 75
5. D. T. Sponza, *Water air soil poll.* **134** (2002) 137
6. N. D. Grozdanic, V. Najdanovic-Visak, M. Lj. Kijevcanin, S. P. Serbanovic, M. Nunes da Ponte, Z. P. Visak, *Fluid Phase Equilibr.* **310** (2011) 198
7. M. Quik, *Trends Neurosci.* **27** (2004) 568
8. P. A. Newhouse, A. Potter, A. Singh, *Curr. Opin. Pharmacol.* **4** (2004) 36
9. E. D. Levin, F. J. McClernon, A. H. Rezvani, *Psychopharmacology* **184** (2006) 523
10. R. M. Maduro, M. Aznar, *Fluid Phase Equilibr.* **259** (2007) 83
11. M. A. Garcia, A. De Lucas, J. L. Valverde, J. F. Rodriguez, *J. Chem. Eng. Data* **45** (2000) 540
12. A. De Lucas, P. Cañizares, M. A. García, J. Gomez, J. F. Rodriguez, *Ind. Eng. Chem. Res.* **37** (1998) 4783
13. D. L. C. Millen, R. W. Murphy, *Ind. Eng. Chem. Res.* **33** (1994) 3238
14. D. L. C. Millen, R. W. Murphy, *Ind. Eng. Chem. Res.* **32** (1993) 3056
15. Z. P. Visak, S. L. Yague, J. N. Canongia Lopes, L. P. N. Rebelo, *J. Phys. Chem., B* **111** (2007) 7934
16. K. Seddon, A. Stark, M. Torres, *Pure Appl. Chem.* **72** (2000) 2275
17. L. E. Ficke, H. Rodriguez, J. F. Brennecke, *J. Chem. Eng. Data* **53** (2008) 2112
18. U. Domanska, *Fluid Phase Equilibr.* **26** (1986) 201
19. U. Domanska, A. Marciniak, *J. Phys. Chem., B* **108** (2004) 2376

20. U. Domanska, *Pure Appl. Chem.* **77** (2005) 543
21. U. Domanska, K. Paduszyński, *J. Phys. Chem., B* **112** (2008) 11054
22. C. A. S. Trindade, Z. P. Visak, R. Bogel-Lukasik, E. Bogel-Lukasik, M. Nunes da Ponte, *Ind. Eng. Chem. Res.* **49** (2010) 4850
23. M. S. Calado, Z. Petrovski, M. S. Manic, V. Najdanovic-Visak, E. A. Macedo, Z. P. Visak, *Fluid Phase Equilibr.* **337** (2013) 67
24. G. R. Ivanis, J. M. Vuksanovic, M. S. Calado, M. Lj. Kijevcanin, S. P. Serbanovic, Z. P. Visak, *Fluid Phase Equilibr.* **316** (2012) 74
25. M. S. Manic, V. Najdanovic-Visak, *J. Chem. Thermodyn.* **44** (2012) 102
26. *A Guide to pH measurement – the theory and practice of laboratory pH applications*, Alliance Technical Sales, Clarendon Hills, IL, [http://www.alliancets.com/site/files/408/29497/109873/159912/Guide\\_to\\_pH\\_Measurement.pdf](http://www.alliancets.com/site/files/408/29497/109873/159912/Guide_to_pH_Measurement.pdf) (accessed Jul, 2014)
27. A. Ault, *J. Chem. Educ.* **78** (2001) 500
28. R. T. Fowler, *J. Appl. Chem.* **4** (1954) 449
29. Y. Marcus, *J. Chem. Soc., Farad. Trans.* **87** (1991) 2995
30. H. Tokuda, K. Hayamizu, K. Ishii, Md. Abu Bin Hasan Susan, M. Watanabe, *J. Phys. Chem., B* **109** (2005) 6103
31. Y. Marcus, *J. Solution Chem.* **23** (1994) 831
32. A. Bondi, *J. Phys. Chem.* **68** (1964) 441
33. J. C. McGowan, *J. Appl. Chem. Biotechnol.* **28** (1978) 599
34. Y. H. Zhao, M. H. Abraham, A. M. Zissimos, *J. Chem. Inf. Model.* **43** (2003) 1848
35. M. Bešter-Rogač, J. Hunger, A. Stoppa, R. Buchner, *J. Chem. Eng. Data* **56** (2011) 1261
36. J. Trindade, Z. P. Visak, M. Blesic, I. M. Marrucho, J. A. P. Coutinho, J. N. Canongia Lopes, L. P. N. Rebelo, *J. Phys. Chem., B* **111** (2007) 4737
37. Y. Marcus, A. Loewenschuss, *Annu. Rep. Chem. Soc., C* **81** (1984) 81
38. J. Graton, M. Berthelot, J. F. Gal, S. Girard, C. Laurence, J. Lebreton, J. Y. Le Questel, P. C. Maria, P. Nauš, *J. Am. Chem. Soc.* **124** (2002) 10552
39. J. H. Summerfield, *J. Chem. Educ.* **76** (1999) 1397
40. J. Banyasz, *The Physical Chemistry of Nicotine*, in *Analytical Determination of Nicotine and Related Compounds and their Metabolites*, J. W. Gorrod, P. Jacob III, Eds., Elsevier, Amsterdam, 1999, p. 149
41. V. Arnaud, M. Berthelot, J. Y. Le Questel, *J. Phys. Chem., A* **109** (2005) 3767
42. J. Graton, T. van Mourik, S. L. Price, *J. Am. Chem. Soc.* **125** (2003) 5988
43. K. E. Gutowski, G. A. Broker, H. D. Willauer, J. G. Huddleston, R. P. Swatloski, J. D. Holbrey, R. D. Rogers, *J. Am. Chem. Soc.* **125** (2003) 6632
44. B. Y. Zaslawsky, *Aqueous two-phase partitioning – physical chemistry and biological applications*, Marcel Dekker, New York, USA, 1995.



SUPPLEMENTARY MATERIAL TO

**Aqueous nicotine solutions: pH-measurements and salting-out effects – Analysis of the effective Gibbs energies of hydration and ionic strengths of the solutions**

NIKOLA D. GROZDANIĆ<sup>1</sup>, MARTA S. CALADO<sup>2</sup>, MIRJANA LJ. KIJEVČANIN<sup>1</sup>,  
SLOBODAN P. ŠERBANOVIĆ<sup>1</sup> and ZORAN P. VIŠAK<sup>2\*</sup>

<sup>1</sup>Faculty of Technology and Metallurgy, University of Belgrade, Karnegijeva 4, 11120 Belgrade, Serbia and <sup>2</sup>Centro de Química Estrutural, Instituto Superior Técnico, Universidade de Lisboa, Av. Rovisco Pais 1, 1049-001 Lisboa, Portugal

J. Serb. Chem. Soc. 79 (7) (2014) 829–842

CALCULATION OF THE McGOWAN VOLUMES AND THE PAULING IONIC RADIUS

McGowan volumes,  $V_x$ , in Å<sup>3</sup> per molecule, were calculated applying the following equation:<sup>1</sup>

$$V = \frac{1}{0.602} \left[ \sum_i (AC)_i - \sum 6.56B \right] \quad (\text{S-1})$$

in which  $(AC)_i$  are the related atom contributions (McGowan volumes of atoms, listed in the literature<sup>33</sup>) and  $B$  signifies the number (sum) of the existing bonds, whether being single-, double- or triple-. This number is approximated by the equation:<sup>2</sup>

$$B = N - 1 + R_g \quad (\text{S-2})$$

In Eq. (S-2),  $N$  and  $R_g$  are the numbers of all atoms and ring structures, respectively; ( $R_g = 0$  in the present case).

The McGowan radius per mol,  $R_x$ , was obtained from Eq. (S-1) using the volume–radius relation for a sphere.

Finally, Pauling (ionic radius)  $R_p$  is calculated using the relation<sup>2</sup> between  $R_x$  and  $R_p$ :

$$R_x = 1.115R_p + 0.0623 \quad (\text{S-3})$$

REFERENCES

1. A. Bondi, *J. Phys. Chem.* **68** (1964) 441
2. J. C. McGowan, *J. Appl. Chem. Biotechnol.* **28** (1978) 599

\*Corresponding author. E-mail: zoran.visak@ist.utl.pt



## Structural, thermal and surface characterization of thermoplastic polyurethanes based on poly(dimethylsiloxane)

MARIJA V. PERGAL<sup>1\*</sup>, IVAN S. STEFANOVIĆ<sup>1</sup>, DEJAN GODEVAC<sup>1</sup>,  
VESNA V. ANTIĆ<sup>2</sup>, VESNA MILAČIĆ<sup>3</sup>, SANJA OSTOJIĆ<sup>4</sup>, JELENA ROGAN<sup>5#</sup>  
and JASNA DJONLAGIĆ<sup>5#</sup>

<sup>1</sup>Institute of Chemistry, Technology and Metallurgy, University of Belgrade, Njegoševa 12,  
Belgrade 11000, Serbia, <sup>2</sup>Faculty of Agriculture, University of Belgrade, Nemanjina 6,  
Belgrade 11000, Serbia, <sup>3</sup>North Campus Research Complex, B20, University of Michigan,  
Ann Arbor, MI 48109, USA, <sup>4</sup>Institute of General and Physical Chemistry, University of  
Belgrade, Studentski trg 12–16, Belgrade 11000, Serbia and <sup>5</sup>Faculty of Technology and  
Metallurgy, University of Belgrade, Karnegijeva 4, Belgrade 11000, Serbia

(Received 19 August, revised 19 October, accepted 22 October 2013)

**Abstract:** In this study, the synthesis, structure and physical properties of two series of thermoplastic polyurethanes based on hydroxypropyl-terminated poly-(dimethylsiloxane) (HP-PDMS) or hydroxyethoxypropyl-terminated poly-(dimethylsiloxane) (EO-PDMS) as soft segments, and 4,4'-methylenediphenyl diisocyanate and 1,4-butanediol as hard segments were investigated. The polyurethanes were synthesized by two-step polyaddition in solution. The effects of the type and content of PDMS segments on the structure, thermal and surface properties of copolymers were studied by <sup>1</sup>H-, <sup>13</sup>C-nuclear magnetic resonance (NMR) spectroscopy and two-dimensional NMR spectroscopies (heteronuclear multiple bond correlation (HMBC) and rotating-frame nuclear Overhauser effect (ROESY)), gel permeation chromatography (GPC), differential scanning calorimetry (DSC), thermogravimetric analysis (TGA), wide-angle X-ray scattering (WAXS), scanning electron microscopy (SEM) and water contact angle and water absorption measurements. Thermal properties investigated by DSC indicated that the presence of soft PDMS segments lowers the glass transition and melting temperatures of the hard phase as well as the degree of crystallinity. SEM analysis of the copolymers with a lower soft segment content confirmed the presence of spherulite superstructures, which arise from the crystallization of the hard segments. When compared with polyurethanes prepared from HP-PDMS, the copolymers synthesized from EO-PDMS with the same content of the soft segments had a higher degree of crystallinity, better thermal stability and a less hydrophobic surface. The obtained results showed that the synthesized polyurethanes had good thermal and surface

\* Corresponding author. E-mail: marijav@chem.bg.ac.rs

# Serbian Chemical Society member.

doi: 10.2298/JSC130819149P

properties, which could be further modified by changing the type or content of the soft segments.

**Keywords:** thermoplastic polyurethanes; poly(dimethylsiloxane); 2D NMR spectroscopy; thermal properties, surface properties.

## INTRODUCTION

Thermoplastic polyurethane elastomers (TPUs) represent a group of heterogeneous biomaterials that have found a wide range of biomedical applications owing to their excellent mechanical properties, ability to be easily processed and relatively good biocompatibility.<sup>1</sup> TPUs are multi-block copolymers composed of a high molecular weight macrodiol, called a soft segment (SS), and a hard segment (HS) composed of a diisocyanate and a low molecular weight diol. The thermodynamic incompatibility between the hard and the soft segments results in a microphase separation at room temperature. Micro-domains rich in hard segments resulted from intermolecular interactions (*e.g.*, crystallization, hydrogen bonds), form so-called physical crosslinks and guarantee good mechanical strength, while the soft amorphous phase improves the flexibility of the polymeric material. By varying the type and molecular weight of the macrodiol, the chemical structure and symmetry of the diisocyanate, the HS/SS ratio, the polymerization method, and the crystallizability of both hard and soft segments, the mechanical and physical properties of TPUs could be tuned to the targeted values for specific clinical applications.<sup>2–7</sup>

Poly(dimethylsiloxane)s (PDMSs) were used as soft segments in various TPUs because of their low-temperature flexibility, high thermal and oxidative stability, good biocompatibility, water repellency, low surface tension, ultraviolet resistance, and high permeability of many gases.<sup>8–11</sup> At the beginning, TPUs based on PDMS exhibited poor mechanical properties due to the large differences between the solubility parameters of PDMS and the comonomers, which led to phase separation during the polyaddition reaction. However, in numerous subsequent papers, the preparation of thermoplastic polyurethane and polyurea copolymers based on the end-functionalized PDMS macrodiols, such as hydroxyhexyl-, aminopropyl-, and methylaminopropyl-PDMS, with a high molecular weight and good mechanical properties, were reported.<sup>12–14</sup> In order to avoid or reduce phase separation during the synthesis of PDMS-containing TPUs, several concepts were reported in the literature.<sup>15–18</sup> These concepts included mixing PDMS with conventional polyether or polyester macrodiols, the introduction of polar functionality into the PDMS, and use of PDMS–polyether or PDMS–polyester copolymers. In order to enhance the biostability of TPUs derived from the ethoxypropyl–PDMS macrodiol, reduction of the second polyether or polyester comonomer in the soft segment mixture is desirable.<sup>19,20</sup> TPUs containing PDMS segments have been employed in various biomedical applications,

because they can significantly reduce nonspecific protein adsorption and thrombus formation.<sup>21</sup> In the past few years, a significant amount of research has been realized to understand the correlation between the microstructure and properties of TPUs because these factors are important for achieving the ideal properties for specific medical applications. According to the literature, the type of SS, chemical composition, surface hydrophilicity, degree of crystallinity, and surface topography have great effects on the biocompatibility of TPUs.<sup>22–26</sup>

Recently, an extensive study was published on the thermal, mechanical, surface, and biocompatibility properties of a series of TPUs based on poly( $\epsilon$ -caprolactone)-*b*-poly(dimethylsiloxane)-*b*-poly( $\epsilon$ -caprolactone) (PCL-PDMS-PCL) as soft segments with different hard segment contents.<sup>27</sup> The synthesized samples were double crystalline block-copolymers in which both hard and soft segments were crystallized. It was found that the degree of crystallinity, storage modulus, hardness, hydrophobicity, and the degree of microphase separation of copolymers all increased with increasing HS content. It was also found that the presence of the crystallizable PCL segments in the SS improved the biocompatibility of TPUs and that the copolymers, with a good microphase separation and having a non-toxic nature, might have potential application as implants in medicine. The combination of good elastomeric properties and biocompatibility of polyurethanes and PDMS makes these block copolymers excellent candidates for drug encapsulation and biomedical applications.

In the present study, two series of PDMS-based thermoplastic polyurethanes (TPUSs) with different ratios of hard to soft segments were synthesized by a two-step polyaddition reaction in solution. These two series differed in the type of functionality of the terminated PDMSs, which were incorporated into the polyurethane backbone as flexible segments. In the first series, a hydroxypropyl-terminated PDMS was employed for the synthesis of the novel TPUSs, while in the second series hydroxyethoxy propyl-terminated PDMS was used. The structures of the TPUSs were characterized by <sup>1</sup>H-, <sup>13</sup>C-nuclear magnetic resonance (NMR) spectroscopy and 2D-NMR, *i.e.*, COSY (correlation spectroscopy), HMBC (heteronuclear multiple bond correlation) and ROESY (rotating-frame nuclear Overhauser effect spectroscopy). The degree of crystallinity was determined by differential scanning calorimetry (DSC) and wide-angle X-ray scattering (WAXS) analysis, while the thermal properties were examined by DSC and thermogravimetric analysis (TGA). The surface properties were investigated by scanning electron microscopy (SEM), and water contact angle and water absorption measurements. The effects of the type and content of the soft segments on the structural, thermal, morphological and some physical properties of TPUSs are presented.

## EXPERIMENTAL

*Materials*

$\alpha,\omega$ -Bis(hydroxypropyl)poly(dimethylsiloxane) (HP-PDMS) and  $\alpha,\omega$ -bis[3-(2-hydroxyethoxy)propyl]poly(dimethylsiloxane) (EO-PDMS), supplied from ABCR, were dried over molecular sieves (0.4 nm) before use. The number average molecular weights,  $\bar{M}_n$ , of the HP-PDMS and EO-PDMS were calculated from  $^1\text{H-NMR}$  spectroscopy results. The  $\bar{M}_n$  of the prepolymer HP-PDMS was 960 g mol<sup>-1</sup>, and for the prepolymer EO-PDMS 1000 g mol<sup>-1</sup>. 4,4'-Methylenediphenyl diisocyanate (MDI) (from Aldrich) with an isocyanate content of 33.6 wt. % was used as received. 1,4-Butanediol (BD) (from Aldrich) was distilled and dried over molecular sieves before use. *N,N*-Dimethylacetamide (DMAc) (from Acros) was dried for 24 h over calcium hydride and distilled under reduced pressure before use. Tetrahydrofuran (THF) (from J. T. Baker) was dried over lithium aluminum hydride and distilled before use. Stannous octanoate ( $\text{Sn}(\text{Oct})_2$ ; from Aldrich), was used as a dilute solution in an anhydrous mixture of THF/DMAc (1:1, V/V).

*Synthesis of the TPUSs*

The TPUSs were synthesized by a catalyzed two-step polymerization in solution. The reactants were MDI, BD and  $\alpha,\omega$ -bis(3-hydroxypropyl)PDMS (TPUS1 series) or bis[3-(2-hydroxyethoxy)propyl]PDMS (TPUS2 series). Both series consisted of five samples prepared with different contents of soft segments. The last two numbers in the name of the TPUSs represent the weight percent of the hard segment. The molar ratio of the reacting -NCO groups (from MDI) and -OH groups (from the BD and PDMS prepolymer) was 1.05. The catalyst was stannous octanoate (0.15 mol %  $\text{Sn}(\text{Oct})_2$ /PDMS prepolymer), while a mixture of DMAc/THF (1/1, V/V) was employed as the solvent.

The polymerization reactions were performed in a four-neck, round-bottom, Pyrex reaction flask equipped with a mechanical stirrer, an inlet for dry argon, a reflux condenser and a dropping funnel. A typical reaction procedure was as follows: the desired amounts of PDMS prepolymer and MDI were dissolved in DMAc/THF in the flask at room temperature and then heated up to 80 °C (for the TPUS1 series) or 40 °C (for the TPUS2 series) under an argon atmosphere. The reaction was started by the introduction of a solution of catalyst in DMAc/THF. The reaction mixture was stirred for 20 min at 80 °C (for the TPUS1 series) or 30 min at 40 °C (for the TPUS2 series) to prepare the NCO-terminated prepolymer, *i.e.*, until the theoretical NCO content was attained. The change in the NCO content during the reaction was monitored using the standard dibutylamine back-titration method.<sup>28</sup> In the second stage of the reaction, a dilute solution of BD in DMAc/THF was added drop-wise to the NCO-terminated prepolymer and the reaction was continued at 80 °C for 24 h (TPUS1 series) or at 50 °C for 24 h (TPUS2 series). The final polymer concentration was 25 wt. % for the TPUS1 and 15 wt. % for the TPUS2 samples. The reaction mixture was cooled down to room temperature and the copolymers were precipitated into a methanol/water (1/1, V/V) mixture, then washed several times with methanol, filtered and dried to a constant weight in a vacuum oven at 40 °C for 2 days. The yields of copolymers after precipitation in methanol/water mixture were in the range of 78.4–92.1 % for the TPUS1 samples and 86.5–94.2 % for the TPUS2 samples (Table I).

*Preparation of TPUS films*

The films were prepared by pouring the TPUS solution in DMAc (10 wt. %) onto a Teflon® dish (diameter 5 cm) and drying at 40 °C in a force-draft oven for 48 h. The films (typically about 0.5 mm thick) were then dried under vacuum at 40 °C for 24 h and stored in a desiccator at room temperature before characterization.

### Characterization

The NMR experiments were performed on Bruker Avance 500 spectrometer equipped with 5 mm inverse detection *z*-gradient probe. The <sup>1</sup>H- and <sup>13</sup>C-NMR spectra (at 500.13 and 125.75 MHz, respectively) were measured at 25 °C using DMF-*d*<sub>7</sub> as the solvent. Chemical shifts are given on the  $\delta$  scale relative to the solvent DMF signal. The quantitative <sup>13</sup>C-NMR spectra were obtained using the inverse gated decoupling method under the following conditions: pulse delay time, 10 s; acquisition time 1.10 s; pulse width, 16.8  $\mu$ s; spectral width, 29.8 kHz and number of scans,  $\approx$ 10000. The 2D NMR experiments, such as COSY, HMBC and ROESY were performed with standard Bruker pulse sequences. COSY was collected with eight scans per 512 increments, while HMBC and ROESY were collected with 16 scans per 512 increments.

TABLE I. Composition of the reaction mixture and the copolymers, the average degree of polymerization of the hard segments and yields of the synthesized TPUSs

Polymer	Molar ratio <sup>a</sup>	SS, mol % (in feed) <sup>b</sup>	SS, mol % (NMR)	SS, mol % (in feed) <sup>b</sup>	SS, mol % (NMR)	$L_n$ (HS) (NMR) <sup>c</sup>	Yield, %
TPUS1-20	1:2:1	50.0	41.4	78.1	71.5	1.3	78.4
TPUS1-35	1:3:2	33.3	30.2	64.0	60.6	2.0	88.3
TPUS1-45	1:4:3	25.0	23.8	54.3	52.7	2.9	90.2
TPUS1-50	1:5:4	20.0	19.5	47.1	46.2	3.4	91.7
TPUS1-55	1:6:5	16.7	16.5	41.6	41.2	3.9	92.1
TPUS2-20	1:2:1	50.0	54.9	78.6	78.2	1.4	86.5
TPUS2-35	1:3:2	33.3	36.9	64.8	63.3	2.1	89.9
TPUS2-45	1:4:3	25.0	27.5	55.1	54.7	3.0	92.6
TPUS2-50	1:5:4	20.0	21.2	47.9	45.2	3.5	93.1
TPUS2-55	1:6:5	16.7	23.0	42.4	40.4	4.4	94.2

<sup>a</sup>PDMS:MDI:BD in the reaction mixture at a 1.05 molar ratio of NCO/OH groups; <sup>b</sup>predetermined by the composition of the reaction mixtures; <sup>c</sup>determined by quantitative <sup>13</sup>C-NMR spectroscopy

The intrinsic viscosities ( $[\eta]$ ) were measured in an Ubbelohde viscometer at 25 °C using DMAc as the solvent.

A Waters 1525 GPC system (Waters, Milford, MA), consisting of two Styragel columns (HR 1 and HR-5E columns, 4.6 mm  $\times$  300 mm each, Waters, Milford, MA) connected in series, a binary HPLC pump, a Waters 717 plus autosampler and a Waters 2414 refractive index detector, and BreezeTM software were used to compute molecular weight distribution of the TPUS1 samples. Sample solutions of the TPUS1 series in THF at a concentration of 10 mg mL<sup>-1</sup> were filtered through a 0.45  $\mu$ m hydrophobic fluoropore (PTFE) filter (Millipore Corporation, Bedford, USA) before injection into the GPC system and eluted with THF at 40 °C at a flow rate of 0.3 mL min<sup>-1</sup>. The system was calibrated with a number of polystyrene standards ranging from 3680 to 570000 g mol<sup>-1</sup>. It is important to note that due to the insolubility of the TPUS2 samples in THF, DMAc was used as the mobile phase. The GPC chromatograms of TPUS2 samples were obtained on a Waters 600E instrument equipped with a refractive index detector and three Supelco Pl-Gel columns under similar conditions.

The DSC measurements were conducted on a DSC Q1000V9.0 Build 275 thermal analyzer. The TPUSs were analyzed under a dynamic nitrogen atmosphere (flow rate: 50 mL min<sup>-1</sup>) in the temperature range from -90 to 230 °C at a heating and a cooling rate of 10 and 5 °C

$\text{min}^{-1}$ , respectively. The weight of the samples was approximately 5 mg. All details of the calculation of degree of crystallinity from DSC results, are described in the literature.<sup>17,27</sup>

TGA was performed using a TGA Q500 V6.3 Build 189 instrument under a dynamic nitrogen atmosphere (flow rate: 50 mL min $^{-1}$ ), in the temperature range from 25 to 700 °C at a heating rate of 10 °C min $^{-1}$ . The average weight of the samples was around 10 mg.

The WAXS measurements were realized using a Diffractometric System APD 2000 diffractometer with Cu K $\alpha$  radiation using a copper anode (tube: 40 kV, 30 mA,  $\lambda = 0.154178$  nm). The diffraction patterns were obtained in the Bragg angle range of 5–50°. The scan speed was 0.02 s per step for all measurements. The degree of crystallinity was calculated by peak deconvolution and subsequent determination of the relative areas under the amorphous halo and the crystalline peaks of the X-ray diffraction pattern. The ratio of the area under the crystalline peaks to the total (amorphous + crystalline) area gave the degree of crystallinity.

The scanning electron microscopy (SEM) microphotographs were obtained on JEOL JSM-6460LV instrument, at a working distance of *ca.* 14 mm and an accelerating voltage of 20 kV.

The water contact angles were determined on Krüss DSA100 using the sessile drop method. The measurements were performed at 22 °C, 30 s after deposition of single drops (20 µL) on the sample surface. The average value of five measurements was used.

Water absorption was investigated at room temperature by sample immersion in phosphate buffered saline (PBS, 1.5 mM KH<sub>2</sub>PO<sub>4</sub>, 6.5 mM Na<sub>2</sub>HPO<sub>4</sub>, 2.7 mM KCl, 0.14 M NaCl, pH 7.4, Acros Organics) at 37 °C, for 1, 2.5, 4, 6, 24, 28 and 48 h. At each time point, the samples were removed and blotted with filter paper to remove excess water and weighed. The average value of three measurements for each sample was used. The weight percent of the water absorption was calculated as follows:

$$\text{Water absorption} = 100 \frac{w_t - w_0}{w_0}$$

where  $w_t$  is the weight of the hydrated sample after time  $t$  and  $w_0$  is the weight of the dry sample.

## RESULTS AND DISCUSSION

Two series of thermoplastic polyurethane copolymers based on  $\alpha,\omega$ -bis(3-hydroxypropyl)PDMS or  $\alpha,\omega$ -bis[3-(2-hydroxyethoxy)propyl]PDMS as soft segments and MDI-BD as hard segments were synthesized by catalyzed two-step polyaddition in solution under optimized conditions. Each series was composed of five samples of different soft segment contents (40–80 wt. %). The molar ratio of the PDMS prepolymer, MDI and BD, predetermined by the composition of the reaction mixture, was varied from 1:2:1 to 1:6:5 (Table I). The chemical structures of the segmented TPUSs based on HP-PDMS and EO-PDMS are presented in Fig. 1. The content and the type of the soft segments were varied to investigate the influence of these variables on some properties of the synthesized TPUSs, which could be optimized and adjusted for a specific medical application of the copolymers.

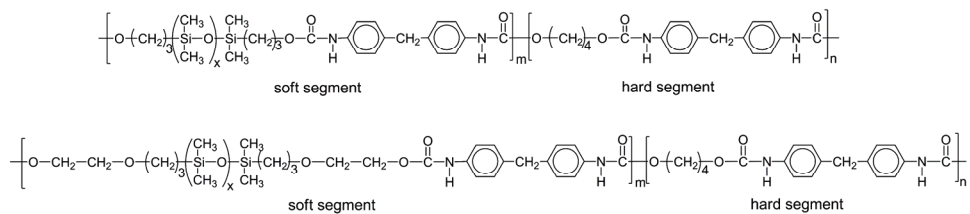


Fig. 1. Chemical structures of the polyurethane copolymers based on HP-PDMS or EO-PDMS soft segments.

Synthesis of TPUSs using an end-functionalized PDMS as a single soft segment is very difficult to realize, due to the extremely high immiscibility of polar urethane components with a non-polar PDMS prepolymer. In the synthesis of the second series samples, the terminal ethoxy units served as compatibilizers between the non-polar PDMS macrodiol and the polar comonomers, *i.e.*, MDI and BD. Optimization of the reaction conditions was performed at different times of the polyaddition reaction, at different reaction temperatures (40, 60 and 80 °C), and at different concentrations of reactants in the reaction mixture (15, 20 and 25 wt. %). The course of the first stage of the polyaddition was monitored using the standard dibutylamine back-titration method. Theoretically, the end of the first stage of the reaction was at 5.8 wt. % (TPUS1 samples) and at 5.6 wt. % (TPUS2 samples) of free NCO groups. According to the titration results, the reaction was very rapid and the values were attained after 20 and 30 min for TPUS1 and TPUS2 samples, respectively. Progress of the second stage of polyaddition reaction was assessed through the changes of intrinsic viscosities of the final copolymers. The optimal reaction temperatures to obtain the highest intrinsic viscosities were 80 °C for the TPUS1 and 40 °C for TPUS2 series. The optimal concentrations of reactants to obtain the highest intrinsic viscosity were 25 wt. % for the TPUS1 samples and 15 wt. % for the TPUS2 samples and the optimal time for the second stage of the reaction was 24 h for all the samples. These results indicate that the prepolymer EO-PDMS reacts more rapidly with MDI and BD than the HP-PDMS prepolymer, probably due to the presence of terminal ethoxy units. DMAc/THF (1/1, V/V) mixture was shown to be an excellent reaction medium for all the syntheses in this study.

*NMR analysis of the structure and composition of the TPUSs, the intrinsic viscosity measurements and GPC analysis*

In order to investigate the molecular structure of the synthesized TPUSs, <sup>1</sup>H-NMR, <sup>13</sup>C-NMR, and the two-dimensional NMR (COSY, HMBC and ROESY) analyses were performed. Representative <sup>1</sup>H-NMR spectra of the TPUSs with 45 wt. % HP-PDMS and 80 wt. % EO-PDMS soft segments are shown in Fig. 2.

In <sup>1</sup>H-NMR spectra, the signals of the SiCH<sub>3</sub> protons appeared in the region 0.2–0.3 ppm. The methylene protons attached to the silicon were at 0.62 ppm, and

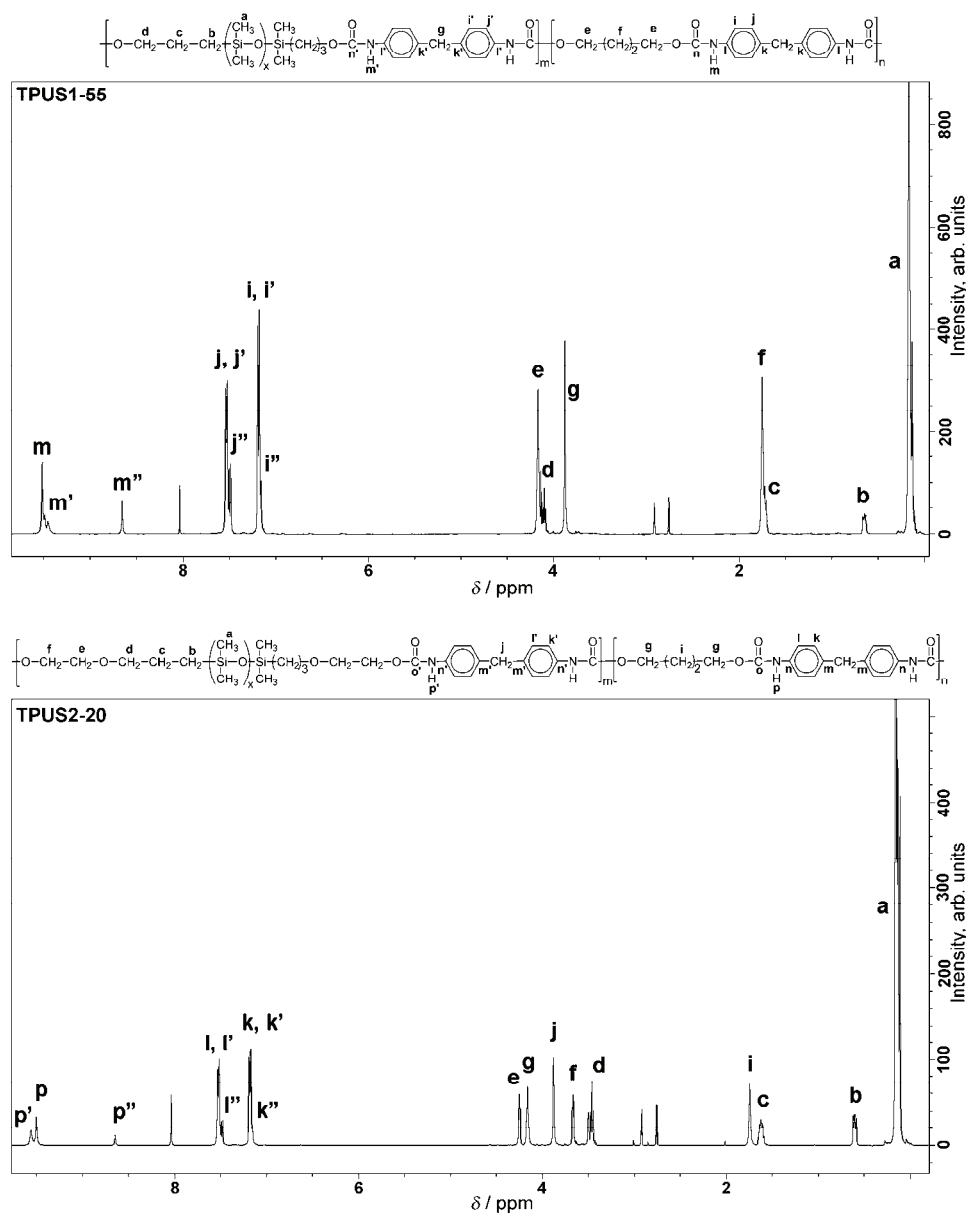


Fig. 2.  $^1\text{H}$ -NMR spectra of the TPUSs with 45 wt. % of HP-PDMS and with 80 wt. % of EO-PDMS soft segments.

the central methylene protons from PDMS propylene groups were at 1.60 ppm. The signals of the methylene protons from PDMS propylene groups connected to the oxygen atom appeared at 3.55 ppm. The proton resonances at 1.77 and 4.16

ppm originated from the central and terminal methylene groups from the BD residues. The signal of the methylene protons from the MDI residues appeared at 3.88 ppm. Proton resonances at 7.18 and 7.51 ppm from the aromatic protons, and at 8.64, 9.50 and 9.56 ppm from the urethane –NH protons in the soft and hard segments were observed. In  $^1\text{H}$ -NMR spectra of the samples from the TPUS2 series, the signals of the methylene protons from the ethylene oxide residue appeared at 3.67 and 4.25 ppm.

The composition of TPUSs was determined from the  $^1\text{H}$ -NMR spectra as the relative intensities of the Si-CH<sub>3</sub> protons signals and signals of the aromatic protons arising from the MDI moiety. The mole and weight fractions of the soft and hard segments were calculated using these formulas:

$$x_{\text{SS}} = \left[ \frac{\left( \frac{I(\text{SiCH}_3)}{6\bar{X}_x + 6} \right)}{\left( \frac{I(\text{Ar-H})}{8} \right)} \right]; x_{\text{HS}} = 1 - x_{\text{SS}}$$

$$w_{\text{SS}} = \frac{x_{\text{SS}} M_{\text{SS}}}{(x_{\text{SS}} M_{\text{SS}} + x_{\text{HS}} M_{\text{HS}})}; w_{\text{HS}} = 1 - w_{\text{SS}}$$

where:  $x_{\text{SS}}$  and  $x_{\text{HS}}$  are the mole fractions of the soft and hard segments, respectively;  $w_{\text{SS}}$  and  $w_{\text{HS}}$  are the weight fractions of the soft and hard segments, respectively;  $M_{\text{SS}}$ , 1210 or 1250 g mol<sup>-1</sup>, represents the molecular weights of the soft segments, *i.e.*, MDI-HP-PDMS and MDI-EO-PDMS segments, respectively;  $M_{\text{HS}}$ , 340 g mol<sup>-1</sup>, is the molecular weight of the MDI-BD unit;  $\bar{X}_x$ , 10.6 and 9.95, stands for the degrees of polymerization of the PDMS-block in the HP-PDMS and EO-PDMS prepolymers, respectively.

The values for the weight fraction of the soft segment ranged from 41.2 to 71.5 % for TPUS1 samples and from 40.4 to 78.2 % for TPUS2 samples, which is relatively in agreement with the values predetermined from the composition of the reaction mixtures (except for TPUS1-20 sample, Table I). However, the experimentally determined copolymer composition was in a slightly better agreement with the theoretical numbers calculated from the composition of the feed for TPUS2 series in comparison to TPUS1 series. It could be concluded that the EO-PDMS soft segments are efficiently incorporated into the polyurethane chains due to the presence of terminal ethoxy units in the soft segment.

The length of the hard segments, *i.e.*, the average degree of polymerization,  $L_n(\text{HS})$ , was calculated from the results of quantitative  $^{13}\text{C}$ -NMR spectroscopy, the results of which are given in Table I. The quantitative  $^{13}\text{H}$ -NMR spectra showed splitting from the non-protonated aromatic carbons of MDI in the *ipso* position relative to the urethane group and different signals at 134.9–135.5 and 137.1–137.7 ppm, resulting from the existence of MDI-BD and MDI-ethylene

oxide linkages. The average length of the hard segments was calculated as the ratio of the integral of aromatic carbon signal from MDI associated with BD and the sum of integrals of the two aromatic carbon signals from MDI associated with ethylene oxide: one from the original soft segment and one from the extended soft segment. Therefore, this calculation takes into account chain extension in the soft segment. The degree of polymerization of the MDI–BD segments in the macromolecular chain increased with decreasing soft segment content from 1.3 to 3.9 for samples in the TPUS1 series and from 1.4 to 4.4 for samples in the TPUS2 series. The experimental values of  $L_n$  were in relatively good agreement with  $L_n(\text{HS})$  values determined by the composition of the reaction mixture ( $L_n$  in the range 1–5), except for the TPUS1-55 and TPUS2-55 samples.

The chemical shifts observed in the  $^{13}\text{C}$ -NMR spectra of the copolymers at 0.8 and 1.8 ppm were from carbon atoms from the  $\text{SiCH}_3$  groups. The central methylene carbon atoms and methylene carbon atoms attached to the silicon from the PDMS propyl groups appeared at 14.9 and 22.0 ppm. The terminal methylene carbon atoms from the PDMS propyl groups appeared at 62.1 ppm. The signals of the central and terminal methylene carbon atoms from the BD residue appeared at 26.7 and 65.0 ppm, respectively. The carbon atom from the methylene group from MDI residue appeared at 41.2 ppm. The signals from the carbonyl atoms at 154.1 and 155.0 ppm originated from the urethane groups. The signals from the aromatic carbons appeared at 119.5, 130.1, 136.9 and 139.0 ppm. The carbon atoms of methylene groups from the ethylene oxide residues appeared at 69.8 and 74.5 ppm only for samples in the TPUS2 series.

To the best of our knowledge, no studies have been published in which the structures of these particular TPUS copolymers were investigated in detail by 2D NMR spectroscopy. The assignments of the proton and carbon resonances within the structures of the samples from both series, which belong to the aromatic protons and carbons, the carbonyl carbons and urethane –NH protons, were resolved in HMBC and ROESY experiments.

The HMBC and ROESY spectra of TPUS1-55 are shown in Figs. 3 and 4, respectively. The resonances for the  $\text{Hc}$  and  $\text{Hd}$  signals that were overlapped with  $\text{Hf}$  and  $\text{He}$  signals were identified from COSY (spectrum is not presented) based on  $\text{Hc}-\text{Hb}$  and  $\text{Hc}-\text{Hd}$  correlations, respectively. The aromatic carbons in the hard and soft segments were deduced from HMBC based on the correlations  $\text{Hj}-\text{Cj}$ ,  $\text{Hj}'-\text{Cj}'$ ,  $\text{Hj}''-\text{Ck}''$ ,  $\text{Hi}-\text{Cl}$ ,  $\text{Hi}'-\text{Cl}'$  and  $\text{Hi}''-\text{Cl}''$ . The position of the urethane carbonyl from the soft segment at 153.9 ppm was confirmed by HMBC correlation between  $\text{Hm}''-\text{Hn}''$ . The urethane –NH protons from the hard and soft segments were identified by HMBC based on  $\text{Hm}-\text{Cl}$  and  $\text{Hm}''-\text{Cl}''$  correlations. Furthermore, the urethane –NH protons from the hard and soft segments were assigned by ROESY correlations through space between  $\text{Hm}-\text{Hf}$ ,  $\text{Hm}-\text{He}$ ,  $\text{Hm}'-\text{Hc}$  and  $\text{Hm}''-\text{Hj}''$ . These results suggest that chain extension in the first phase of reaction

occurred to some extent (these signals are labeled with ", which refers to extension of soft segments) and consequently two types of –NH urethane signals in the soft segments appeared.

The HMBC and ROESY spectra of TPUS2-20 are shown in Figs. 3 and 4, respectively. The position of the urethane –NH protons in the hard segment at 9.50 ppm was confirmed by ROESY correlations between Hp–Hg and Hp–Hi, while the position of the urethane –NH protons in the soft segment at 8.64 and 9.56 ppm was confirmed by ROESY correlations between Hp"–Hi", Hp'–Hd, Hp'–Hf, Hp'–He, and Hp'–Hi'. The urethane –NH protons, aromatic and carbonyl signals from the soft and hard segments were identified by HMBC based on the correlations Hp"–Cn", Hp"–Co", Hp"–Cl', Hp–Cn and Hp–Cl, respectively. The NMR results confirmed that MDI moieties were incorporated into the polymer chains, both in the hard and soft segments. The presence of two types of –NH urethane signals, aromatic and carbonyl signals in the soft segments for both TPUS2 and TPUS1 samples suggest that the chain extension reaction occurred after the first phase of the polyaddition. The extent of the chain extension in soft segments ranged from 18.4 to 22.1 % for the TPUS1 samples and from 7.3 to 14.4 %

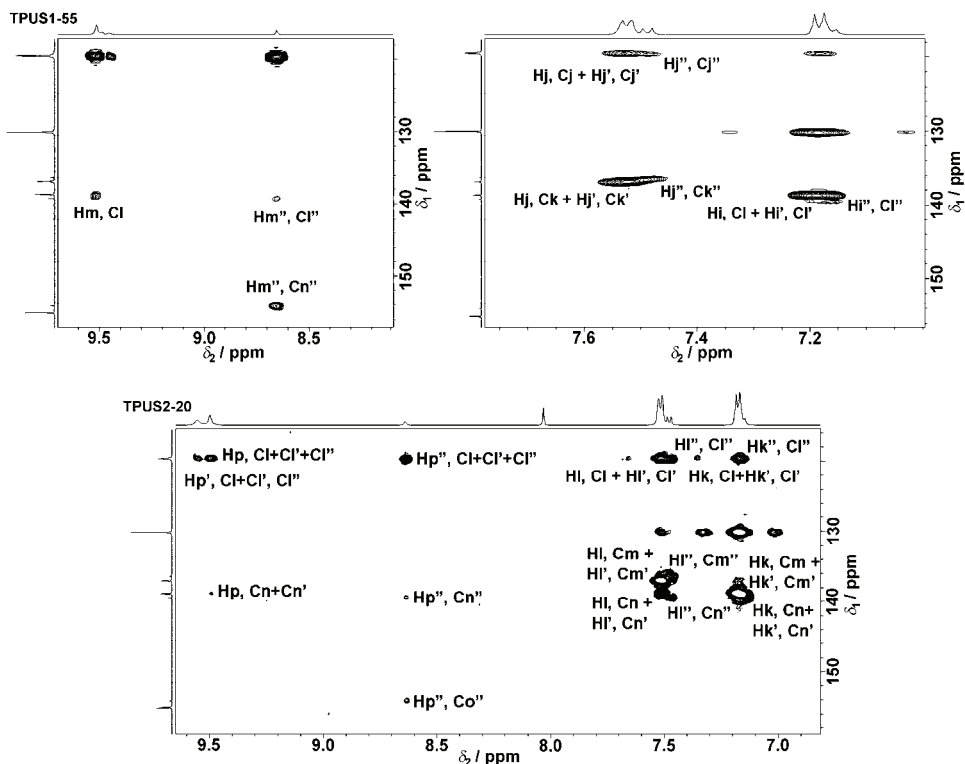


Fig. 3. HMBC spectra of the TPUSs with 45 wt. % of HP-PDMS and with 80 wt. % of EO-PDMS soft segments.

for the TPUS2 samples. These results were obtained from the  $^1\text{H}$ -NMR spectra based on the relative intensities of the –NH urethane proton signal arising from the chain extension in the soft segments and all the –NH urethane protons signals from the hard and soft segments and are in agreement with literature data.<sup>27</sup> It was previously found that the polydispersity of the NCO-terminated prepolymer after the first stage of the reaction mainly affects the increase of randomness in polyurethane chains and therefore increased polydispersity of the HS length.<sup>27</sup> Thus, chain extension after the first phase of the polyaddition has a significant influence on the structure and composition of the final copolymers.

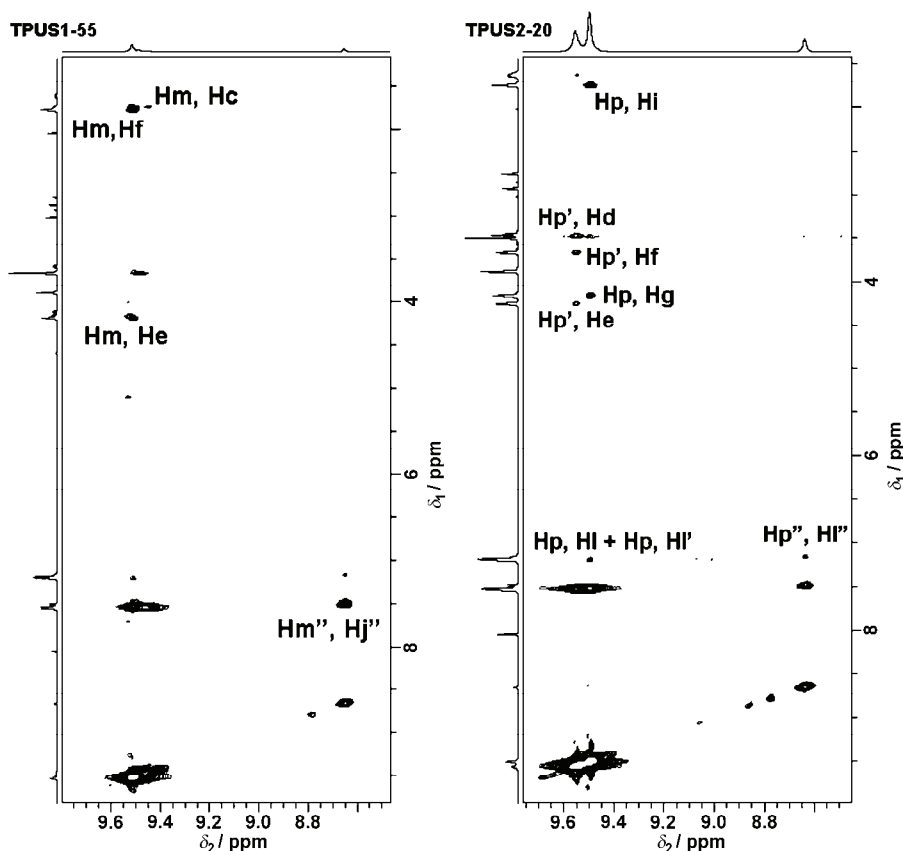


Fig. 4. ROESY spectra of the TPUss with 45 wt. % of HP-PDMS and with 80 wt. % of EO-PDMS soft segments.

The results of the intrinsic viscosity measurements and GPC analysis of the TPUss are listed in Table II. The intrinsic viscosities of the TPUss ranged from 0.42 to 0.56 dL g<sup>-1</sup> in the first series and from 0.59 to 0.69 dL g<sup>-1</sup> in the second series. It seems that the intrinsic viscosity increases with decreasing content of

PDMS segments. The number average molecular weights ( $\bar{M}_n$ ) of the TPUS1 samples, determined by GPC, ranged from 20050 to 30650 g mol<sup>-1</sup>, with a polydispersity index between 2.3 and 3.0. The  $\bar{M}_n$  values of the TPUS2 samples ranged from 22630 to 37760 g mol<sup>-1</sup> with a polydispersity of 1.9–2.7. The GPC chromatograms of the copolymers exhibited only one peak with a shape that corresponded to a typical high molecular weight product of a step-growth polymerization. The intrinsic viscosity and  $\bar{M}_n$  values were slightly higher for the TPUS2 series samples in comparison to those in the TPUS1 series.

TABLE II. Results of GPC analysis and intrinsic viscosities of the synthesized TPUSs

Polymer	$\bar{M}_n$ / g mol <sup>-1</sup>	$\bar{M}_w$ / g mol <sup>-1</sup>	$\bar{M}_w/\bar{M}_n$	[ $\eta$ ] / dL g <sup>-1</sup>
TPUS1-20	30650	70580	2.3	0.42
TPUS1-35	21690	52060	2.4	0.45
TPUS1-45	23940	58570	2.5	0.52
TPUS1-50	20050	60750	3.0	0.53
TPUS1-55	20650	54640	2.7	0.56
TPUS2-20	26080	61380	2.3	0.59
TPUS2-35	22630	44460	1.9	0.62
TPUS2-45	32290	83470	2.6	0.63
TPUS2-50	37510	103510	2.7	0.65
TPUS2-55	37760	92930	2.4	0.69

#### Thermal analysis

The TPUSs were semi-crystalline polymers, the melting, crystallization and glass transition temperatures of which were measured by DSC. The obtained DSC thermograms of selected TPUSs recorded during the second heating run are shown in Fig. 5 and the results are summarized in Table III.

TABLE III. Thermal properties and degree of crystallinity, determined by DSC and WAXS analyses, of selected TPUSs

Polymer	$T_{gHS}$ °C	$T_{mHS}$ °C	$\Delta H_m$ J g <sup>-1</sup>	$T_{cHS}$ °C	$\Delta H_c$ J g <sup>-1</sup>	$X_c$ %	$X_c^{HS}$ %	$X_c^{WAXS}$ %
TPUS1-20	25	155	0.80	40	4.5	0.88	3.39	6.2
TPUS1-45	65	203	17.0	160	18.6	18.9	36.5	18.1
TPUS1-55	71	205	24.8	164	32.5	27.2	45.5	26.4
TPUS2-20	32	157	3.9	84	5.1	4.3	19.5	6.5
TPUS2-45	37	186	17.5	93	5.8	19.6	42.3	18.5
TPUS2-55	48	191	26.0	94	8.7	28.5	47.8	27.7

The DSC curves show high-temperature transitions corresponding to the melting and crystallization temperatures of the hard MDI-BD segments. The melting and crystallization temperatures of the hard segments depend on the type of soft segments and on the average sequence length of the crystallizable units (Table III). Simultaneously, it seems that the melting and crystallization tempera-

tures of the HP-PDMS-based TPUSs were slightly higher than those of the polyurethanes in the EO-PDMS series, as shown in Fig. 5. As the soft segment content decreased, the melting and crystallization temperatures were shifted to the higher value, which indicates better ordering of the hard domains.

These results show that the enthalpy of melting ( $\Delta H_m$ ) and enthalpy of crystallization ( $\Delta H_c$ ) increased with decreasing weight fraction of the soft segments.

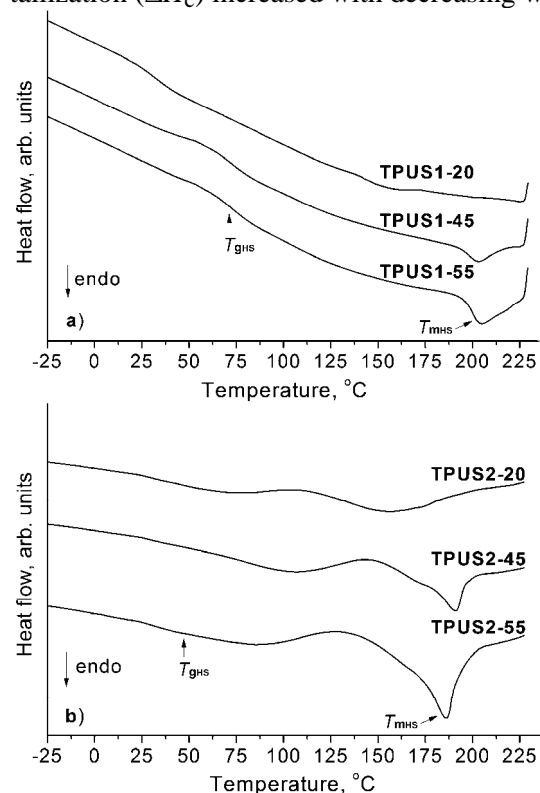


Fig. 5. DSC thermograms recorded during the second heating run of selected TPUSs.

The total degree of crystallinity ( $X_c$ ) ranged from 0.9 to 27.2 % for TPUS1 samples and from 4.3 to 28.5 % for TPUS2 samples, depending on the soft segment content and  $\Delta H_m$ . The degree of crystallinity ( $X_c^{HS}$ ), which was calculated based on the weight fraction of the hard segments in the TPUSs ranged from 3.39 to 45.5 % for the TPUS1 and from 19.5 to 47.8 % for the TPUS2 samples. These results indicate that the hard segments in the copolymers could not crystallize completely and that some short hard segments were incorporated into the amorphous phase. The  $X_c$  and  $X_c^{HS}$  values are higher for the samples in TPUS2 series in comparison with TPUS1 samples, probably due to the lower extent of the chain extension reaction after the first stage of the polyaddition for the TPUS2 samples. It was found that the side reaction led to further decrease in the length

of the hard segments for the TPUS1 samples (Table I) and, therefore, to a lower degree of crystallinity. These results are in agreement with previous reports<sup>27,29</sup> that the occurrence of the side reaction could degrade the thermoplastic properties of the hard phase by decreasing the degree of crystallinity and phase separation.

The DSC results show that even hard segments with only one MDI-BD unit can form a crystalline structure. According to the literature, hard segments with more than three MDI-BD units could form stable crystals.<sup>18,27,30</sup> Altogether, these data suggest that HS with an average length of 1 to 5 MDI-BD units can crystallize (Table III).

The glass transition temperatures of the hard segments ( $T_{gHS}$ ) ranged from 25 to 71 °C for samples in the TPUS1 series and from 32 to 48 °C for samples in the TPUS2 series. Similar results were reported for other MDI-BD-based polyurethanes.<sup>20,31–33</sup> The  $T_g$  of the high molecular weight MDI-BD homopolymer is 110 °C, and since the mean hard segment sequences for TPUSs are relatively short (Table I), the hard domain  $T_g$  would be expected to be lower than 110 °C.<sup>33</sup> As shown in Table III, the values of  $T_{gHS}$  increase with decreasing PDMS content. This is attributed to an increase in the physical cross-links that restricts the molecular motion of the polymer chains and leads to an increase in  $T_{gHS}$ . The  $T_g$  values of the hard segments were lower for the samples of the TPUS2 series, which indicates mixing of the amorphous hard segments with the terminal ethoxy units of the soft segment.

The thermal stability of the synthesized TPUSs was investigated by thermogravimetric analysis under a dynamic nitrogen atmosphere. The obtained TG and thermogram derivative (DTG) curves for the copolymers are presented in Fig. 6, and characteristic temperatures of thermal degradation, residual weight at 650 °C and temperatures at which maximum degradation occurred are listed in Table IV. Under the given experimental conditions, thermal degradation of these samples was expected to begin between 269 and 289 °C (temperatures at 5 % weight loss). According to the obtained results, thermal degradation mechanism of the synthesized TPUSs is quite complex and both thermal stability and thermal degradation mechanism are influenced by the type and content of the SS. Thermal stabilities of the samples in the TPUS2 series were higher than those of the samples in the TPUS1 series. Furthermore, the results obtained by TG analysis showed that on increasing the soft segment content, the thermal stability of the investigated samples increased. Thermal stabilities of the synthesized TPUSs based on EO-PDMS were similar to those of other polyurethanes derived from the PDMS macrodiol<sup>34</sup> and slightly higher than those of some poly(urethane–urea)s based on PDMS.<sup>35</sup>

Three peaks corresponding to the temperatures of a maximum rate of weight loss were evident in the DTG curves (Fig. 6, Table IV), indicating that the thermal

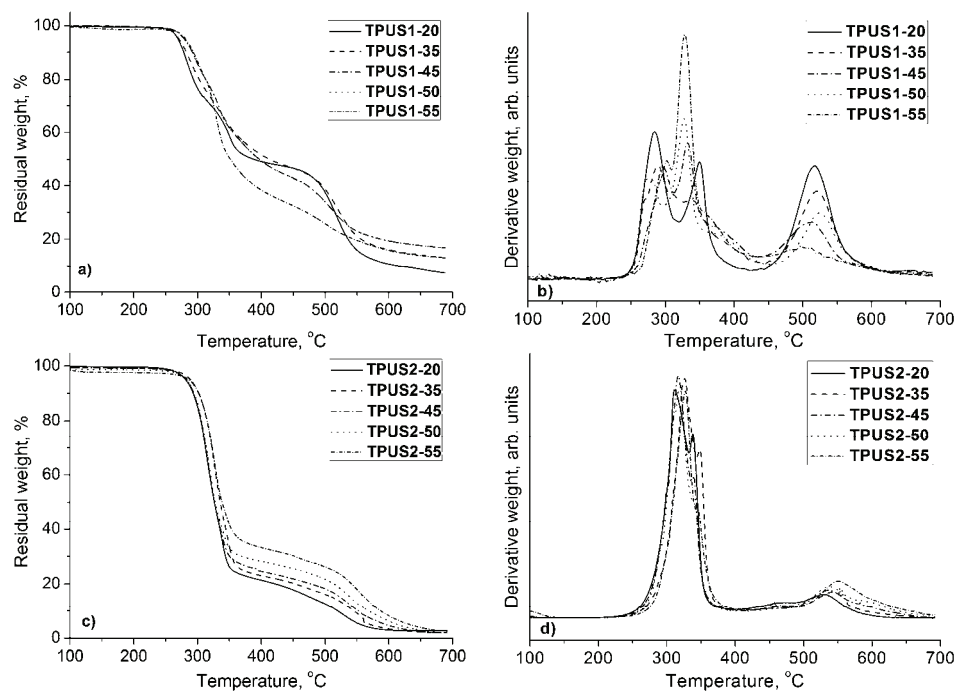


Fig. 6. TG and DTG curves for the TPUSs recorded at a heating rate of  $10\text{ }^{\circ}\text{C min}^{-1}$  under a dynamic nitrogen atmosphere.

degradation of these TPUSs is, at least, a three-step process under nitrogen. The first step of thermal degradation occurred in the hard segment by decomposition of the urethane bonds (the thermally weakest link in TPUSs), resulting in dissociation to the original macrodiol and isocyanate and to the formation of a primary or secondary amine, an alkene and carbon dioxide.<sup>36–38</sup> According to the results presented in Table IV, the temperatures corresponding to the maximum rate of thermal degradation in the first step are in the  $275\text{--}298\text{ }^{\circ}\text{C}$  range for the TPUS1 samples and in the  $313\text{--}325\text{ }^{\circ}\text{C}$  range for the TPUS2 samples. In the second step of thermal degradation, the PDMS components decomposed ( $324\text{--}351\text{ }^{\circ}\text{C}$  for the TPUS1 samples and  $338\text{--}345\text{ }^{\circ}\text{C}$  for the TPUS2 samples), while the decomposition of the aromatic compounds occurred in the temperature region between  $500$  and  $600\text{ }^{\circ}\text{C}$  ( $494\text{--}524\text{ }^{\circ}\text{C}$  for the TPUS1 samples and  $530\text{--}549\text{ }^{\circ}\text{C}$  for the TPUS2 samples).

The residual weights at  $650\text{ }^{\circ}\text{C}$  of the samples in TPUS1 series ranged from 8.6 to 17.6 %, whereas the residual weights at  $650\text{ }^{\circ}\text{C}$  of the samples in the TPUS2 series ranged from 0.05 to 3.7 % (Table IV). The values of the residual weight at  $650\text{ }^{\circ}\text{C}$  suggest that TPUSs with the higher SS content generally have a smaller residue. The residual weight under nitrogen originated mainly from the MDI-BD fraction, which could be explained by the degradation mechanism of

PDMS chains under a nitrogen atmosphere that occurs after disruption of the urethane bonds. The degradation occurs through depolymerization with the formation of cyclosiloxanes, which are thermally more stable than linear poly(dimethylsiloxane)s.<sup>39</sup>

TABLE IV. Results of thermogravimetric analysis under a dynamic nitrogen atmosphere

Polymer	$T_{5\%}$ / °C	$T_{10\%}$ / °C	$T_{50\%}$ / °C	$T_{85\%}$ / °C	$DTG_{\max}$ / °C	Residual weight at 650 °C, %
TPUS1-20	269	279	385	555	284 / 351 / 517	8.6
TPUS1-35	271	277	413	622	284 / 333 / 517	14.1
TPUS1-45	275	288	388	684	293 / 330 / 510	17.6
TPUS1-50	279	277	396	685	275 / 324 / 524	17.6
TPUS1-55	281	290	390	617	298 / 324 / 494	13.8
TPUS2-20	281	293	327	478	313 / 338 / 530	0.05
TPUS2-35	289	302	331	507	322 / 343 / 535	2.2
TPUS2-45	282	294	330	530	322 / 345 / 537	2.5
TPUS2-50	282	295	331	544	325 / 344 / 539	3.1
TPUS2-55	286	302	335	560	325 / 345 / 549	3.7

#### WAXS analysis

The synthesized polyurethanes were characterized by WAXS analysis and the degrees of crystallinity,  $X_c$ <sub>WAXS</sub>, determined by deconvolution of the signals belonging to the crystalline and amorphous parts, are presented in Table III. The X-ray diffractograms obtained for selected TPUSs are shown in Fig. 7. The diffraction profiles of TPUSs exhibited weak peaks at  $2\theta$  values of 19° and 24°, which correspond to the crystallinity of the hard MDI–BD segment.<sup>40–42</sup> Figure 7 clearly shows that the relative intensity of polyurethanes increased with the decreasing SS content in TPUSs. Shifts in the peak's positions were observed for every copolymer, which could be attributed to deformations of the unit cell due to constraints imposed by the segmented structure and strong hydrogen bonds. Based on combined X-ray and electron diffraction data, the unit cell of poly(MDI–BD) is triclinic with dimensions  $a = 5.33$  Å,  $b = 5.26$  Å,  $c = 38.68$  Å,  $\alpha = 113.6^\circ$ ,  $\beta = 116.0^\circ$ ,  $\gamma = 94.4^\circ$ .<sup>43</sup> For copolymers, two amorphous halos were also observed at  $2\theta \approx 12^\circ$  arising from the phase-separated PDMS segments and at  $2\theta \approx 20^\circ$  arising from non-PDMS segments. The crystallinity of the copolymers was clearly facilitated by the strong segregation of the PDMS and MDI–BD segments. The degree of crystallinity ranged from 6.2 to 26.4 % for the TPUS1 samples and from 6.5 to 27.7 % for the TPUS2 samples. The WAXS degrees of crystallinity decreased with the increasing weight fraction of soft segments, similarly to the degrees of crystallinity determined by DSC. The obtained results showed that degree of crystallinity did not significantly change by varying the type of soft segments. Based on the degree of crystallinity values, the total degree

of crystallinity in the TPUSs almost exclusively depended on the weight fraction of the SS content.

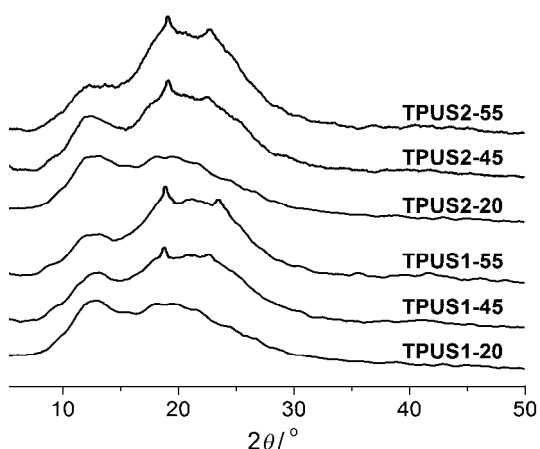


Fig. 7. X-ray diffraction patterns of selected TPUSs.

#### *Water contact angle and water absorption*

The wettability of TPUSs was investigated by static contact angle measurements. The water contact angle is indicative of the hydrophobicity of a surface, whereby a water contact angle of  $90^\circ$  or more indicates a non-wetting surface. The water contact angles were found to increase with increasing PDMS content in both series (Fig. 8). This may be attributed to the hydrophobic character of PDMS and its surface activity.<sup>34,44</sup> Thus, PDMS can migrate to the surface of samples due to its lower surface energy in comparison to the surface energy of a polyurethane. The observation of surface segregation of a low surface energy segment, such as PDMS, was reported for PDMS-containing polyurethane copolymers.<sup>8,34,44</sup> The TPUSs with a higher content of soft PDMS segments have a more hydrophobic surface and better water resistance. The higher water contact angles obtained for the HP-PDMS containing TPUSs indicate the presence of a larger hydrophobic surface compared to the EO-PDMS-based TPUSs.

The bulk hydrophobicity of the prepared copolymers was quantified by measuring the amount of absorbed water at  $37^\circ\text{C}$ . As shown in Fig. 9, the water absorption increased slightly at longer immersion times with the maximum water uptake value being attained after 24 h. The values of water uptake of the TPUSs after 24 h ranged from 0.5 to 1.47 % for the TPUS1 series and from 0.74 to 1.61 % for the TPUS2 series. The TPUSs based on HP-PDMS exhibited lower water uptakes compared with the samples based on EO-PDMS. The water uptake of the TPUSs decreased with increasing content of PDMS, which formed a hydrophobic surface that caused the reduction in the water uptake values of the copolymers. In comparison with polyurethanes prepared from the more hydrophilic

macrodiols reported by other group,<sup>45</sup> the synthesized TPUSs were considered rather hydrophobic due to the hydrophobic character of the PDMS. Therefore, thermoplastic polyurethanes based on PDMS with good waterproof properties show great promise for use as medical implants.<sup>11</sup>

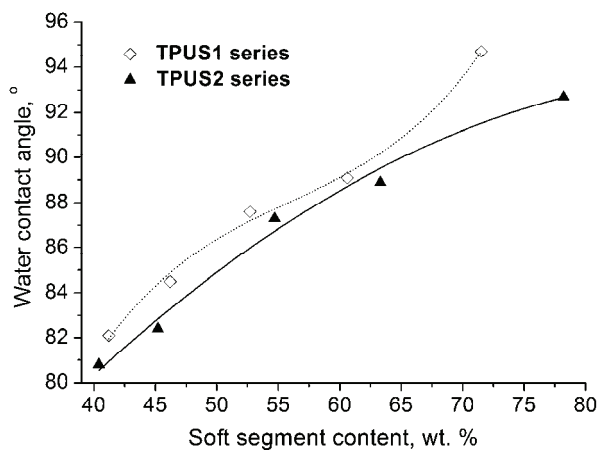


Fig. 8. Water contact angle of the TPUSs *vs.* soft segment content determined by  $^1\text{H-NMR}$  spectroscopy.

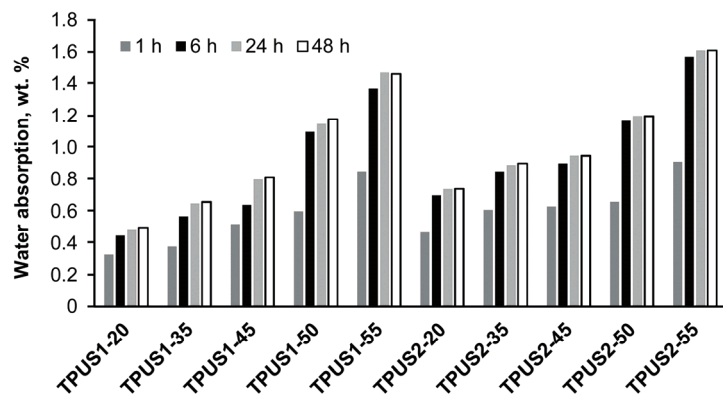


Fig. 9. Water absorption by TPUSs as a function of immersion time.

#### SEM analysis

The surface morphology of the synthesized TPUSs was examined by SEM (Fig. 10). SEM microphotographs of samples with 45 and 55 wt. % of the soft segment revealed a rather uniform surface with microphase separation. These TPUSs showed a spherulite-like structure that is believed to arise from the crystallization of the hard segments, which was also suggested by the DSC and WAXS results. The lack of crystalline fibrillar growth in these structures might be

due to the non-uniformity of the lengths of the hard segments in the mentioned samples, thereby impeding longer range ordering, but this is only a supposition.<sup>46</sup> The main size of these crystalline superstructures in TPUSs varied between 2 and 8  $\mu\text{m}$ . With decreasing SS content, an enhancement in the crystallinity of the hard domains was evidenced, but still the highest value of the main spherulite size was observed for samples TPUS1-55 and TPUS2-55. Samples TPUS1-20 and TPUS2-20 displayed phase mixing morphology and these samples showed increased homogeneity and surface smoothness. From these results and the water contact angle measurements, it could be concluded that the surface of the TPUSs with higher PDMS contents is more hydrophobic, because of the low surface tension of the PDMS segments and their ability to migrate to the surface.

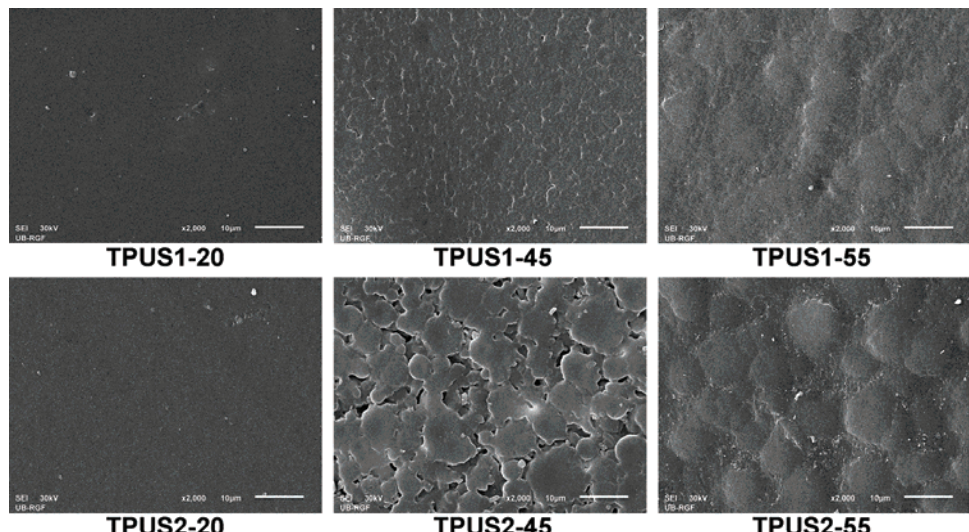


Fig. 10. SEM microphotographs of films prepared from TPUS copolymers.

The results indicate that TPUSs have good microphase separation, as well as surface and thermal properties, which could be tailored to the requirements for biomedical application, such as biomedical devices for short- and long-term uses, by changing the type of soft segments and the PDMS content. It was found that all the TPUSs were sufficiently stable to be melt processed, for example, by injection molding and extrusion. Furthermore, TPUSs based on EO-PDMS are less hydrophobic and have higher crystallinity, which would promote better cell attachment and growth on the polymer surface.<sup>27</sup> Therefore, TPUSs based on EO-PDMS soft segments could be expected to improve the adhesion of endothelial cells on the surface of the copolymers and consequently their biocompatibility due to the presence of ethylene oxide terminal units in the soft segments. The synthesized TPUSs based on the HP-PDMS and EO-PDMS thus combine

various chemical, surface and thermal properties that could be used for different biomedical applications, such as biomedical devices for short- and long-term uses, respectively.

#### CONCLUSIONS

The synthesis and the structural, thermal and surface characterization of polyurethane copolymers prepared from different types of soft PDMS segments and with varying PDMS contents were presented herein. Two series of medium molecular weight copolymers based on hydroxypropyl-terminated PDMS or hydroxyethoxypropyl-terminated PDMS as the soft segments were synthesized by a two-step polyaddition in solution. The multiblock structure of the synthesized TPUSs was confirmed by  $^1\text{H}$ -,  $^{13}\text{C}$ - and 2D-NMR spectroscopy. Based on the results of  $^1\text{H}$ -NMR spectroscopy, the composition of the copolymers was found to be close to the composition of the feed, with a slightly better efficiency of EO-PDMS segment introduction into the polymer chains. Quantitative  $^{13}\text{C}$ -NMR analysis confirmed that the chain extension occurred after the first stage of polyaddition reaction, with a higher degree of chain extension in the soft segment found in the copolymers based on HP-PDMS compared to those based on EO-PDMS. The TPUSs were semi-crystalline polymers, in which the hard segment, with an average length of crystallization from 1 to 5 MDI-BD units, crystallized. The melting temperature, glass transition temperature and the degree of crystallinity of the copolymers decreased with increasing content of soft PDMS segments. The X-ray diffraction patterns indicated that the hard MDI-BD segments in the TPUSs crystallized in a triclinic crystal lattice, similarly to the MDI-BD homopolymer. The synthesized TPUSs with a lower soft segment content showed a spherulite-like structure that is believed to arise from the crystallization of the hard segments. SEM analysis and water contact angle experiments showed that, due to hydrophobic character of PDMS and its low surface tension, samples with the higher PDMS contents had more hydrophobic surfaces. Compared to the HP-PDMS-containing TPUSs, the samples prepared from EO-PDMS have a higher degree of crystallinity, better thermal stability and less hydrophobic surfaces. It could be concluded that the inclusion of the PDMS prepolymer with a terminal ethoxy units resulted in slightly improved miscibility of the reaction mixture and therefore to better thermal and surface properties. In addition, the structural, thermal and surface properties of the synthesized TPUSs could be tailored by changing the type or content of the soft segment and adjusted to the requirements for biomedical applications. The impact of different types of soft PDMS segments on the microstructure-mechanical property relation and biocompatibility behavior of TPUSs will be discussed in further publications.

*Acknowledgment.* This work was financially supported by the Ministry of Education, Science and Technological Development of the Republic of Serbia (Project No. 172062).

## И З В О Д

СТРУКТУРНА, ТЕРМИЧКА И ПОВРШИНСКА КАРАКТЕРИЗАЦИЈА  
ТЕРМОПЛАСТИЧНИХ ПОЛИУРЕТАНА НА БАЗИ ПОЛИ(ДИМЕТИЛСИЛОКСАНА)

МАРИЈА В. ПЕРГАЛ<sup>1</sup>, ИВАН С. СТЕФАНОВИЋ<sup>1</sup>, ДЕЈАН ГОЂЕВАЦ<sup>1</sup>, ВЕСНА В. АНТИЋ<sup>2</sup>, ВЕСНА МИЛАЧИЋ<sup>3</sup>,  
САЊА ОСТОЈИЋ<sup>4</sup>, ЈЕЛЕНА РОГАН<sup>5</sup> И ЈАСНА ЂОНЛАГИЋ<sup>5</sup>

<sup>1</sup>Институт за хемију, технолоџију и међулртву, Универзитет у Београду, Његошева 12, 11000  
Београд, <sup>2</sup>Пољопривредни факултет, Универзитет у Београду, Немањина 6, 11000 Београд, <sup>3</sup>North

Campus Research Complex, B20, University of Michigan, Ann Arbor, MI 48109, USA, <sup>4</sup>Институт за  
оштаву и физичку хемију, Универзитет у Београду, Студентски трг 12–16, 11000 Београд и

<sup>5</sup>Технолошко-међулртски факултет, Универзитет у Београду, Карнејијева 4, 11000 Београд

У овом раду су испитивани синтеза, структура и физичка својства две серије термо-пластичних полиуретана са меким сегментима на бази хидроксипропил терминираног поли(диметилсилоксана) (HP-PDMS) и хидрокситетоксипропил терминираног поли(диметилсилоксана) (EO-PDMS), и тврдим сегментима на бази 4,4'-метилендиенил-диизоцијаната и 1,4-бутандиола. Свака серија се састојала од узорака који имају различит садржај меког сегмента. Полиуретани су синтетисани двостепеним поступком полиадиције у раствору. Утицај врсте и садржаја PDMS сегмената на структуру, термичка и површинска својства кополимера је испитан помоћу <sup>1</sup>H-NMR, <sup>13</sup>C-NMR, дводимензионалне NMR (HMBC и ROESY) спектроскопије, GPC, DSC, TGA, WAXS, SEM и одређивањем контактних углова са водом и мерењима апсорпције воде. Термичка својства испитана DSC методом указују да присуство меких PDMS сегмената снижава температуру остакљивања и топљења тврде фазе, као и степен кристалиничности. SEM анализа кополимера са ниским садржајем меког сегмента потврђује постојање сферулитне морфологије, која потиче од кристализације тврдих сегмената. У поређењу са полиуретанима на бази HP-PDMS, синтетисани кополимери на бази EO-PDMS имају већи степен кристалиничности, бољу термичку стабилност и мање хидрофобну површину. Добијени резултати су показали да синтетисани полиуретани имају добра термичка и површинска својства, што се може даље модификовати променом врсте или садржаја меког сегмента.

(Примљено 19. августа, ревидирано 19. октобра, прихваћено 22. октобра 2013)

## REFERENCES

1. S. Gogolewski, *Colloid Polym. Sci.* **267** (1989) 757
2. S. L. Cooper, J. C. West, R. W. Seymour, in *Plastics, Resins, Rubbers, Fibers*, H. Mark, N. M. Bikales, Eds., Wiley, New York, 1976, p. 521
3. D. K. Chattopadhyay, K. V. S. N. Raju, *Prog. Polym. Sci.* **32** (2007) 352
4. A. Saralegi, L. Rueda, B. Fernández-d'Arlas, I. Mondragon, A. Eceiza, M. A. Corcuer, *Polym. Int.* **62** (2013) 106
5. L. F. Wang, Q. Ji, T. E. Glass, T. C. Ward, J. E. McGrath, M. Muggli, G. Burns, U. Sorathia, *Polymer* **41** (2000) 5083
6. M. S. Sánchez-Adsuar, E. Papon, J. J. Villenave, *J. Appl. Polym. Sci.* **76** (2000) 1590
7. M. Špírková, R. Poręba, J. Pavličević, L. Kobera, J. Baldrian, M. Pekárek, *J. Appl. Polym. Sci.* **126** (2012) 1016
8. İ. Yilgör, J. McGrath, *Adv. Polym. Sci.* **86** (1988) 1
9. D. J. Martin, L. A. Poole Warren, P. A. Gunatillake, S. J. McCarthy, G. F. Meijis, K. Schindhelm, *Biomaterials* **21** (2000) 1021
10. A. Simmons, J. Hyvarinen, L. Poole-Warren, *Biomaterials* **27** (2006) 4484

11. N. Roohpour, J. Wasikiewicz, D. Paul, P. Vadgama, I. Rehman, *J. Mater. Sci.: Mater. Med.* **20** (2009) 1803
12. R. W. Hergenrother, Y. Xue-Hai, S. L. Cooper, *Biomaterials* **15** (1994) 635
13. J. P. Sheth, A. Aneja, G. L. Wilkes, E. Yilgor, G. E. Atilla, I. Yilgor, F. L. Beyer, *Polymer* **45** (2004) 6919
14. I. Yilgor, T. Eynur, E. Yilgor, G. L. Wilkes, *Polymer* **50** (2009) 4432
15. J. P. Sheth, E. Yilgor, B. Erenturk, H. Ozhalici, I. Yilgor, G. L. Wilkes, *Polymer* **46** (2005) 8185
16. R. Hernandez, J. Weksler, A. Padsalgikar, T. Choi, E. Angelo, J. S. Lin, L.-C. Xu, C. A. Siedlecki, J. Runt, *Macromolecules* **41** (2008) 9767
17. M. V. Pergal, V. V. Antić, M. N. Govedarica, D. Godevac, S. Ostojić, J. Djonlagić, *J. Appl. Polym. Sci.* **122** (2011) 2715
18. M. V. Pergal, V. V. Antić, S. Ostojić, M. Marinović-Cincović, J. Djonlagić, *J. Serb. Chem. Soc.* **76** (2011) 1703
19. R. Hernandez, J. Weksler, A. Padsalgikar, J. Runt, *J. Biomed. Mater. Res. Part A* **87** (2008) 546
20. T. Choi, J. Weksler, A. Padsalgikar, J. Runt, *Polymer* **51** (2010) 4375
21. Y. Marois, R. Guidoin, in *Biomedical Applications of Polyurethanes*, R. Vermette, H. J. Griesser, G. Laroche, R. Guidoin, Eds., Landes Bioscience, Texas, 2001
22. M. Bil, J. Ryszkowska, P. Woźniak, K. J. Kurzydłowski, M. Lewandowska-Szumiel, *Acta Biomater.* **6** (2010) 2501
23. F. Burel, L. Poussard, M. Tabrizian, Y. Merhi, C. Bunel, *J. Biomater. Sci., Polym. Ed.* **19** (2008) 525
24. Y.-X. Wang, J. Robertson, W. Spillman, Jr., R. Claus, *Pharm. Res.* **21** (2004) 1362
25. G. Balasundaram, M. Sato, T. J. Webster, *Biomaterials* **27** (2006) 2798
26. S.-H. Hsu, C.-M. Tang, C.-C. Lin, *Biomaterials* **25** (2004) 5593
27. M. V. Pergal, V. V. Antic, G. Tovilovic, J. Nestorov, D. Vasiljevic-Radovic, J. Djonlagic, *J. Biomater. Sci., Polym. Ed.* **23** (2012) 1629
28. A. Marand, J. Dahlin, D. Karlsson, G. Skarping, M. Dalene, *J. Environ. Monit.* **6** (2004) 606
29. R. Saint-Loup, T. Jeanmaire, J.-J. Robin, B. Boutevin, *Polymer* **44** (2003) 3437
30. G. Wang, B. Fang, Z. Zhang, *Polymer* **35** (1994) 3178
31. T. Choi, J. Weksler, A. Padsalgikar, J. Runt, *Polymer* **50** (2009) 2320
32. R. Adhikari, P. A. Gunatillake, S. J. McCarthy, G. F. Meijs, *J. Appl. Polym. Sci.* **78** (2000) 1071
33. T. Choi, K. A. Masser, E. Moore, J. Weksler, A. Padsalgikar, J. Runt, *J. Polym. Sci., B* **49** (2011) 865
34. H.-D. Hwang, H.-J. Kim, *Reac. Funct. Polym.* **71** (2011) 655
35. M. Balaban, V. Antic, M. Pergal, I. Francolini, A. Martinelli, J. Djonlagic, *J. Serb. Chem. Soc.* **77** (2012) 1457
36. D. K. Chattopadhyay, D. C. Webster, *Prog. Polym. Sci.* **34** (2009) 1068
37. F. S. Chuang, W. C. Tsen, Y. C. Shu, *Polym. Degrad. Stab.* **84** (2004) 69
38. T. Hentschel, H. Münstedt, *Polymer* **42** (2001) 3195
39. P. R. Dvornic, R. W. Lenz, *High Temperature Siloxane Elastomers*, Hüthing & Wepf, Heidelberg, New York, 1990
40. D. J. Martin, G. F. Meijs, P. A. Gunatillake, S. P. Yozghatlian, G. M. Renwick, *J. Appl. Polym. Sci.* **71** (1999) 937
41. J. T. Koberstein, A. F. Galambos, *Macromolecules* **25** (1992) 5618

42. J. Blackwell, M. R. Nagarajan, T. B. Hoitink, *Polymer* **23** (1982) 950
43. J. R. Quay, Z. Sun, J. Blackwell, R. M. Briber, E. L. Thomas, *Polymer* **31** (1990) 1003
44. M. A. Childs, D. D. Matlock, J. R. Dorgan, T. R. Ohno, *Biomacromolecules* **2** (2001) 526
45. J. Guan, W. R. Wagner, *Biomacromolecules* **6** (2005) 2833
46. Y. Xu, Z. Petrovic, S. Das, G. L. Wilkes, *Polymer* **49** (2008) 4248.



## Electrospinning of the laser dye rhodamine B-doped poly(methyl methacrylate) nanofibers

RAMDAN M. DUKALI<sup>1</sup>, IVANA M. RADOVIĆ<sup>1</sup>, DUŠICA B. STOJANOVIĆ<sup>1</sup>,  
DRAGUTIN M. ŠEVIĆ<sup>2</sup>, VESNA J. RADOJEVIĆ<sup>1\*</sup>, DRAGAN M. JOCIĆ<sup>1</sup>  
and RADOSLAV R. ALEKSIĆ<sup>1</sup>

<sup>1</sup>University of Belgrade, Faculty of Technology and Metallurgy, Belgrade and <sup>2</sup>University of Belgrade, Institute of Physics, Belgrade, Serbia

(Received 24 October 2013, revised 27 January, accepted 30 January 2014)

**Abstract:** The electrospinning of rhodamine B (RhB)-doped poly(methyl methacrylate) (PMMA) is presented as a promising technique for processing photoluminescent nanofibers. Nanofibers with concentrations of RhB in PMMA between 0.05 and 2.0 wt. % were studied. The FTIR spectrum, fiber morphology, thermal properties and optical properties of the nanofibers were investigated. Smooth, bead-free and nonporous nanofibers were obtained. Differential scanning calorimetry (DSC) results revealed that the glass transition temperature of the PMMA ( $T_g$ ) increased with the increasing of RhB content up to 0.5 wt. % and thereafter decreased. The laser induced fluorescence (LIF) technique was used to study the fluorescence properties of the nanofibers. The maximum fluorescence emission was observed at a concentration of RhB of 0.2 wt. %.

**Keywords:** electrospinning; nanofibers; dye-doped PMMA; fluorescence.

### INTRODUCTION

Polymer nanofibers offer a great opportunity for applications beyond nanoelectronics,<sup>1,2</sup> such as, for membrane materials,<sup>3</sup> tissue scaffolding and other biomedical applications,<sup>4</sup> sensing<sup>5</sup> and as reinforcements in composite materials.<sup>6,7</sup> Moreover, the properties of these nanoscale polymeric structures make them interesting candidates for the next generation of photonic devices.<sup>8,9</sup> For example, fibrous dielectric nanostructures could be used as single-mode light waveguides,<sup>10</sup> sensors<sup>5</sup> or building blocks of photonic band-gap materials.<sup>11</sup> Polymer nanofibers could be fabricated by diverse methods, including polymerization in nanoporous templates<sup>12</sup> dip-pen lithography<sup>13</sup> self-assembly,<sup>14</sup> direct drawing from polymer solutions<sup>15</sup> and molding,<sup>16</sup> although only electrospin-

\*Corresponding author. E-mail: vesnar@tmf.bg.ac.rs  
doi: 10.2298/JSC131014011D

ning<sup>17–22</sup> assures a low cost and high throughput production. Electrospinning is a versatile technique that has recently undergone significant development in the production of nanofibers. The polymer fibers are formed from a solution between two electrodes bearing electrical charges of opposite polarity. One of the electrodes is placed into the solution and the other onto a collector. Once ejected out of a metal needle, the charged solution of the jets evaporates to become fibers, which are collected on the collector. The structure and the morphology of electrospun polymer materials, be it fibers or particles, are determined by the synergistic effects of solution parameters (polymer concentration, solution viscosity and flow rate) and electrostatic forces (applied voltage and distance between the needle and collector).

A major advantage of electrospinning is the possibility to produce hybrid, functional photonic materials by incorporating, *e.g.*, light emitters into the fibers.<sup>23–25</sup> The polymer, the light emitter and the characteristic dimension (diameter of the fibers) can be varied independently, therefore allowing for a wide range of applications. Both organic dye molecules and inorganic materials can be embedded into the fibers. Organic dye-doped polymers have been widely investigated as gain media in solid-state dye lasers.<sup>26–29</sup> Dye molecules, which have large absorption and induced emission cross sections due to allowed  $\pi$ – $\pi$  transitions, are ideal active dopants for the generation and amplification of intense light pulses. Thus, many research groups have synthesized and tested numerous chemical substances that were proved good laser dyes. The dye has, however, to be embedded in a suitable matrix or host. The incorporation of a dye in liquid media adversely affects many thermodynamic and spectroscopic properties of the dye (kinetics of energy up-conversion). The adding of dye in polymer solution changes the viscosity of the solution and hence, influences the process of electrospinning.

Thermoplastic PMMA is considered as one of the most efficient dye matrices with excellent optical, thermal, photochemical and dimensional stability. As such, it has been widely used for laser and non-linear optical materials. The incorporation of rhodamine B (RhB) in the host polymer would obviously induce structural and morphological changes.<sup>30,31</sup>

Critical factors determining the optical response of dyes are related to the extent to which their physical and chemical properties are maintained. Thermal and optical properties of dye-doped polymers are important for the identification of suitable laser media. RhB is of great interest as it processes the highest photostability,  $\approx 9,000$  GJ mol<sup>-1</sup>.<sup>32</sup>

In this work, the electrospinning of PMMA–RhB nanofibers was performed, and the structure, morphology, and the linear and nonlinear optical properties of the resulting fibers were investigated.

## EXPERIMENTAL

Commercially available PMMA Acryrex® CM205 (Chi Mei Corp.) ( $\bar{M}_w \approx 90400 \text{ g mol}^{-1}$ ) pellets were used as the matrix for preparing the samples. Dimethylformamide (DMF, anhydrous, 99.8 %, Sigma–Aldrich) was chosen as the solvent and the laser dye RhB (Sigma–Aldrich,  $M = 479.01 \text{ g mol}^{-1}$ ) was chosen for incorporation into the polymer matrix. The aim of starting experiments was to establish the conditions for PMMA fiber electrospinning. Homogenous solutions of the polymer were obtained by magnetically stirring for 48 h at room temperature. The concentrations of PMMA in the DMF solutions were 6 and 22 wt. %, according to literature data.<sup>24</sup> The electrospinning was performed on an Electrospinner CH-01, Linari Engineering, Italy. A plastic syringe (20 mL) with a metallic needle of 1 mm inner diameter was set vertically on the syringe pump (R-100E, RAZEL Scientific Instruments) and the high-voltage power supply (Spellman High Voltage Electronics Corporation, model: PCM50P120) was set to a voltage of 28 kV. The distance of the needle tip from the collector was 15 cm and different flow rates were employed (5, 1 and 0.5 mL h<sup>-1</sup>). Electrospun fibers were dried for 8 h at 50 °C in a vacuum drying oven. The morphology of nanofibers was obtained using a field emission scanning electron microscope (FESEM, TESCAN MIRA 3) with the fracture surfaces sputtered with gold. SEM analysis revealed that the best results were achieved with a 22 wt. % solution of PMMA in DMF at a flow rate of 0.5 mL h<sup>-1</sup>. For this reason, it was decided to use this set of parameters for the fabrication of RhB-doped PMMA fibers.

The procedure for preparing the solutions for the production of RhB-doped PMMA fibers was similar to that employed for the fabrication of pure PMMA fibers. Homogenous solutions of polymer were obtained by magnetically stirring for 48 h at room temperature and after dissolution of the polymer, the dye was directly added into the solution and the stirring was continued for a further 10 min. The contents of RhB in the PMMA were 0.05, 0.1, 0.2, 0.5, 1.0 and 2.0 wt. % after evaporation of the solvent. The rheological behavior of the PMMA dye solutions was analyzed using a Discovery hybrid rheometer HR2 (TA instruments) with parallel plate (diameter 25 mm; gap 500 µm) geometry at 25 °C. The flow characteristics (steady-shear measurements) of the samples were measured by varying the shear rate from 1 to 2000 s<sup>-1</sup>.

The electrospinning process was setup as in the previously performed experiments: the applied voltage was 28 kV, the flow rate of polymer solution was constant at 0.5 ml h<sup>-1</sup> and the distance of the needle tip from the collector was 15 cm. All samples were obtained at 20 °C and 30 % air humidity. The obtained nanofibers were dried in a vacuum oven for 20 h at 80 °C.

The infrared (IR) spectra of samples in KBr discs were obtained by transmission Fourier transform infrared (FTIR) spectroscopy (Hartmann & Braun, MB-series). The FTIR spectra were recorded between 4000 and 400 cm<sup>-1</sup> with a resolution of 4 cm<sup>-1</sup>.

The diameter of the electrospun nanofibers was measured by Image Pro Plus 4.0 (100 measurements per photo). Differential scanning calorimetry (DSC) measurements were conducted using a TA Instruments, TA DSC Q10 instrument calibrated with indium standards. The samples mass was 0.5 mg. The measurements were performed under a dynamic nitrogen flow of 50 mL min<sup>-1</sup> in the temperature range from 30 to 155 °C. The samples were heated up to 155 °C at a rate of 10 °C min<sup>-1</sup>, kept at 155 °C for 5 min to erase thermal history and then cooled to 30 °C at the same rate. A second heating was performed on each sample. The glass transition temperature was determined at the midpoint of the initial slope change.

The basic setup of the time-resolved laser-induced fluorescence measurement system consisted of an Nd–YAG Vibrant OPO laser system and a Hamamatsu streak camera. The

output of the OPO could be continuously tuned over a spectral range from 320 to 475 nm. After analysis of the preliminary results, for measurements presented herein, the second harmonic of the Nd-YAG laser, 532 nm, was used as an excitation source of the samples. The wavelength of 532 nm is closer to the absorption peak of RhB than the OPO output. The emission spectra were recorded using a streak scope (Hamamatsu model C4334-01) with an integrated video streak camera. The fluorescence emission was collected at 90° to the excitation and dispersed by a 0.3 m focal length triple grating imaging spectrograph (SpectraPro-2300i). A grating of 50 g mm<sup>-1</sup> was used to cover the 330 nm spectral range.

## RESULTS AND DISCUSSIONS

In the initial experiments of electrospinning the PMMA solutions, nanofibers with three kinds of morphologies were obtained, *i.e.*, ring-like particles, bead-like

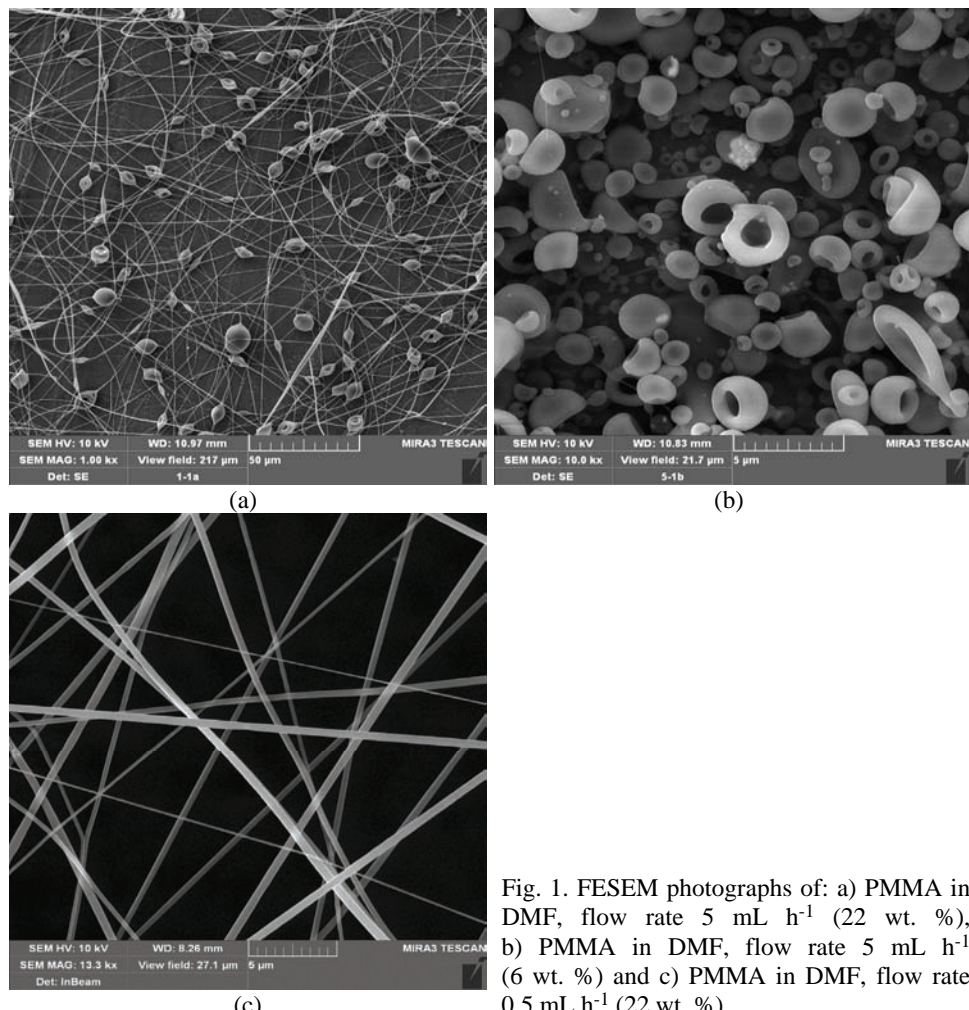


Fig. 1. FESEM photographs of: a) PMMA in DMF, flow rate 5 mL h<sup>-1</sup> (22 wt. %), b) PMMA in DMF, flow rate 5 mL h<sup>-1</sup> (6 wt. %) and c) PMMA in DMF, flow rate 0.5 mL h<sup>-1</sup> (22 wt. %).

nanofibers and ultrafine nanofibers. As shown in Fig. 1a, bead-like nanofibers were fabricated from the 22 wt. % PMMA in DMF solution at a flow rate of 5 mL h<sup>-1</sup>. The ring-like morphology (Fig. 1b) was obtained from the 6 wt. % PMMA in DMF at a flow rate of 1 mL h<sup>-1</sup>. Electrospinning at relatively low polymer concentrations resulted in particles rather than fibers.<sup>33</sup> It is obvious that the jet of polymer solution from the tip of the capillary began to break up into droplets at the lower polymer concentration. The solution viscosity should be above a minimum for fiber formation, *i.e.*, if the viscosity was too low, the process resulted in electrospraying to yield vesicles under the influence of an electric field. Smooth, bead-free nanofibers were produced with a combination of higher concentration and lower rate (22 wt. % solution of PMMA in DMF at a flow rate of 0.5 mL h<sup>-1</sup>). For this reason, it was decided to use this set of parameters to continue with the experiments in which PMMA fibers doped with RhB were fabricated.

The viscosities of solutions (measurements at shear rate 100 s<sup>-1</sup>) containing various concentrations of RhB are listed in Table I. FESEM photographs of the PMMA–RhB nanofibers are presented in Fig. 2a. Image analysis revealed that the nanofibers were beads-free and with a smooth surface. These fibers presented regular surface morphologies.

TABLE I. Viscosity of solutions and diameter of electrospun nanofibers from image analysis

Concentration of RhB, wt. %	Viscosity, Pa s	Mean diameter of fibers, nm
0	2.23	1395±262
0.05	1.75	1068±306
0.1	1.72	967±258
0.2	1.80	650±90
0.5	1.90	743±98
1.0	1.72	598±115
2.0	1.82	623±112

During the electrospinning process, a polymer solution is drawn from the nozzle of the spinneret and the electrical properties, viscosity and surface tension of the solution determine the extent of stretching of the solution under electrostatic forces. The smaller diameter of the nanofibers from the lower viscosity solution is the result of the solution being stretched easily during electrospinning. The larger nanofiber diameters are attributed to the viscosity of the solution being high enough to lower the bending instability of the jet. The solution becomes resistant to stretching by the electrical charges on the electrospinning jet. From Table I, it is obvious that the fiber diameter decreased as the viscosity of solution decreased from that of pure PMMA to that of the 0.05 wt. % RhB doped PMMA. Subsequently, the value the change in viscosity was in the range of 10 %, but the diameter of the nanofibers continually decreased. The explanation for such beha-

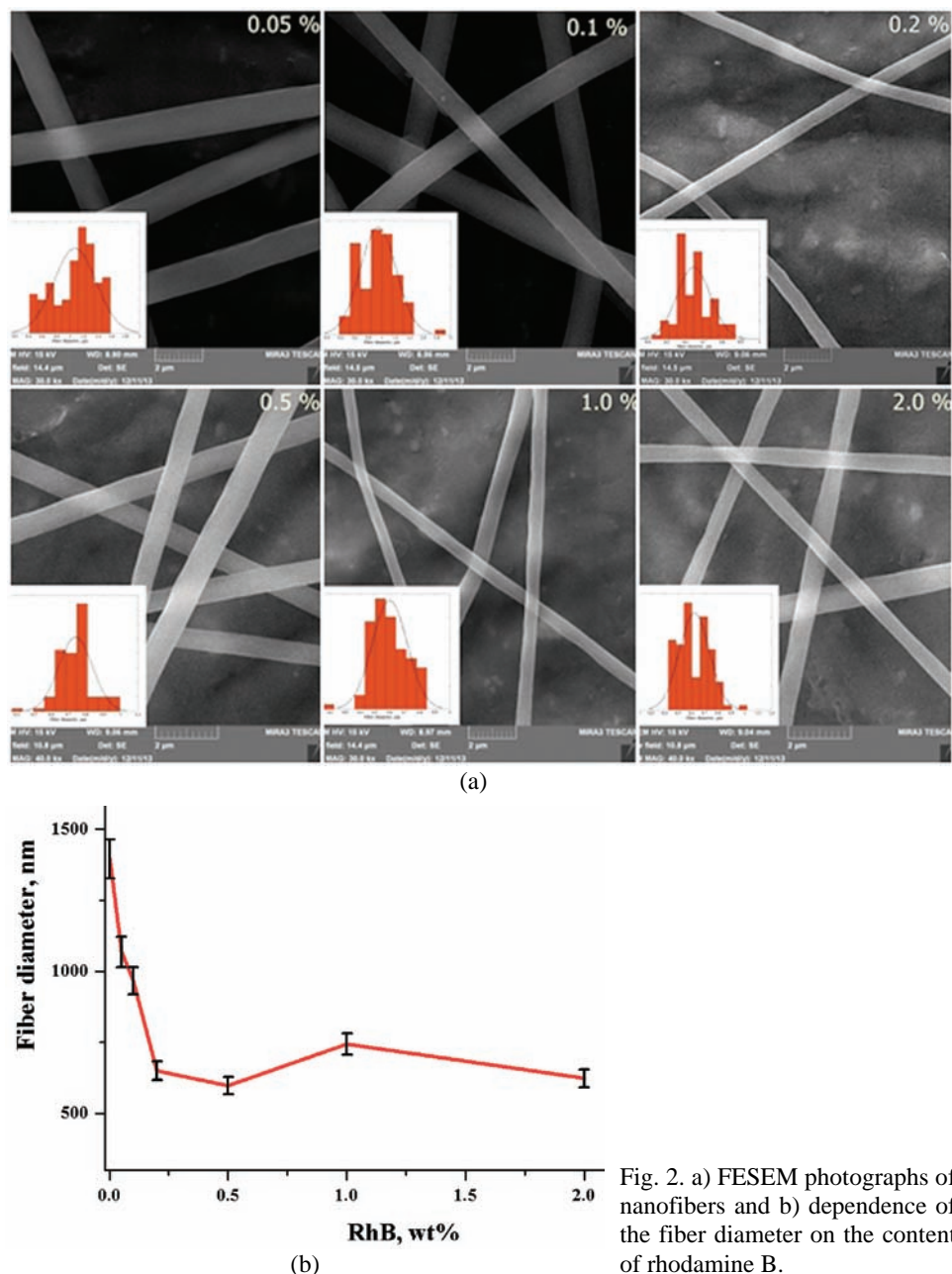


Fig. 2. a) FESEM photographs of nanofibers and b) dependence of the fiber diameter on the content of rhodamine B.

viour could be the change in the solution conductivity. RhB as a polar dye belongs to the xanthine family and it is easily dissolved in polar solvents, such as DMF. Depending on the pH of the solution, RhB can exists in a number of possible

molecular forms, such as cationic, zwitterionic, quinonic and lactonic.<sup>32</sup> Since ionic charges are in direct relation with the electrical conductivity of the solution, increasing the charge density on the surface of the ejected jet leads to an increase in the electric charges carried by the jet. When the conductivity of the solution is increased, more charges can be carried by the jet. An increase in the conductivity means that electrostatic forces can now overcome the surface tension more easily.<sup>34,35</sup> As a result, when the charge density increases in the jet, more stretching and elongation of the jet occurs during electrospinning, thereby causing a reduction in fiber diameter.

The fiber diameter decreased from  $1395 \pm 262$  nm for pure PMMA to  $598 \pm 115$  nm for PMMA doped with 1.0 wt. % RhB. The distribution of the fiber diameters followed the same trend, the standard deviation decreased from 362 nm for pure PMMA to 98 nm, and subsequently the concentration rose. These results indicated that for concentrations of RhB in the range 0.5–1.0 wt. %, the behavior of the solutions changed.

The FTIR spectra of pure poly (methyl methacrylate) (PMMA) fibers (spectrum a) and RhB (spectrum b) are presented in Fig. 3.

Fig. 3. FTIR spectra of a) poly(methyl methacrylate) fibers and b) RhB, and corresponding structural formulas of PMMA and RhB.

Available on line at [www.shd.org.rs/JSCS/](http://www.shd.org.rs/JSCS/)

(CC) 2014 SCS. All rights reserved.

Spectrum a exhibits vibrational bands typical for PMMA, *i.e.*, vibrational bands at 987 and 1453 cm<sup>-1</sup> that belong to O–CH<sub>3</sub> bending and stretching deformation of PMMA, respectively, bands at 1730 and 1250 cm<sup>-1</sup> that are assigned to stretching of C=O groups, a band at 1065 cm<sup>-1</sup> that could be ascribed to the C–O stretching vibration and a band at 1197 cm<sup>-1</sup> that belongs to the skeletal chain vibration. The other bands appearing in the 3000–2800 cm<sup>-1</sup>, 1490–1275 cm<sup>-1</sup> and 900–750 cm<sup>-1</sup> spectral regions correspond to different CH<sub>3</sub> and CH<sub>2</sub> vibrational modes.<sup>36,37</sup>

In spectrum b, vibrational bands corresponding to RhB can be seen. Namely, the broad intensity band at 3433 cm<sup>-1</sup> is associated with the O–H stretching vibration of hydroxyl groups. Its appearance is attributed to the absorption of water by the material. A weak intensity band at 3085 cm<sup>-1</sup> belongs to aromatic C–H vibrations, which also appear at 1130 cm<sup>-1</sup> (plane bending), 820 cm<sup>-1</sup> (out of plane bending) and at 685 cm<sup>-1</sup> (wagging vibrations). In addition, the band at 1710 cm<sup>-1</sup> belongs to the C=N stretching vibration, while the band at 1695 cm<sup>-1</sup> is associated with C=O stretching. A sharp absorption band appearing at 1590 cm<sup>-1</sup> was assigned to the asymmetric stretching vibration of the COO<sup>-</sup> group, the presence of which was further confirmed by the occurrence of a band at 1465 cm<sup>-1</sup>, ascribed to symmetric stretching of the group. The aromatic skeletal C–C stretch and C–O stretch could be observed at 1345 and 1250 cm<sup>-1</sup>, respectively.<sup>37,38</sup>

The FTIR spectra of PMMA fibers doped with different concentrations of the RhB, *i.e.*, 0.5, 1 and 2 wt. %, are presented in Fig. 4. The overall analysis of the spectra revealed that after the introduction of RhB into the PMMA fibers, the vibrational bands became more intense and their shape sharpened compared to

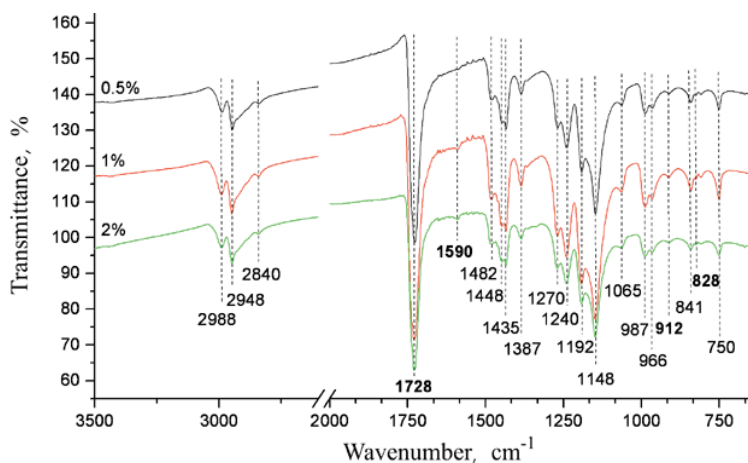


Fig. 4. FTIR spectra of poly(methyl methacrylate) fibers doped with different concentrations of RhB.

the corresponding bands of the pure PMMA fibers. Moreover, due to the presence of the RhB, the vibrational bands in the 3000–2800 cm<sup>-1</sup> and the 1750–1400 cm<sup>-1</sup> spectral regions were slightly shifted towards lower wavenumbers. Namely, these changes were the most visible in the case of the vibrational band at 1730, characteristic for the stretching of the C=O of PMMA fibers, which was strongly increased and insignificantly blue-shifted to the wavenumber 1728 cm<sup>-1</sup> after doping of the PMMA fibers with RhB. Since the band at 1695 cm<sup>-1</sup> associated with C=O stretching of the pure RhB (Fig. 3, spectrum b) does not appear in the spectra of PMMA doped with RhB (Fig. 4), the existence of such a strong band at 1728 cm<sup>-1</sup> could be attributed to the mutual vibrations of the C=O groups in the structure of PMMA fibers doped with RhB. In addition, the vibration of C=N groups of the RhB, found at 1710 cm<sup>-1</sup>, could also produce a slight shift in the band from 1730 to 1728 cm<sup>-1</sup>.

Detailed inspection of the IR spectra of PMMA fibers doped with RhB also revealed the formation of new vibrational bands of rather weak intensities, appearing at 1590, 912 and 828 cm<sup>-1</sup>. While the latter two could be attributed to the C–H vibration of the aromatic ring of RhB,<sup>35</sup> the appearance of the band at 1590 cm<sup>-1</sup>, characteristic for the COO<sup>-</sup> vibrations, confirms that RhB did not react with the functional groups of PMMA. By appearance of these peaks, the presence of RhB molecules within the PMMA matrix was confirmed, implying that the RhB was not chemically bonded but rather physically embedded within the PMMA matrix.<sup>18</sup>

The results of DSC analysis are given in the Fig. 5. The analyses were realized for pure powder PMMA, PMMA nanofibers and PMMA–RhB nanofibers of different compositions. The values of  $T_g$  and  $\Delta c_p/\Delta T$  are marked. The PMMA powder shows a  $T_g$  at 113.53 °C. It can be affirmed that the PMMA–solvent interaction was stronger, because the PMMA nanofibers electrospun from DMF solution had a  $T_g$  at 114.71 °C. The introduction of RhB into the polymer shifted the  $T_g$  to higher values up to a concentration of 0.5 wt. % (117.14 °C), but showed decreases at higher concentration. This is correlated to the viscosity/polarity-dependent behavior of RhB molecules in the solvent.<sup>39–41</sup> This is also in accord with the determined viscosity of the solutions with different concentrations of RhB. Having smaller dye–dye molecular distances, RhB in DMF permitted the formation of aggregates that were responsible for the reduction of the  $T_g$  of the fibers with higher contents of RhB.

A typical streak image of the fluorescence response of the fibers is shown in Fig. 6. The streak images acquired in gray scale are presented in pseudo-color, where different intensities are coded as different colors. The images were acquired in the photon counting mode operation; thus, the intensity corresponds to the number of counted photons. Wavelength scale (horizontal) is in the range between the 465 and 795 nm. Timescale (vertical) is about 50 ns. Laser excitation at 532

nm was also visible on the image. After deconvolution of the laser profile from the fluorescence response profile (green curve), an RhB fluorescence lifetime of about 3 ns was obtained, which is in agreement with published values.<sup>42,43</sup>

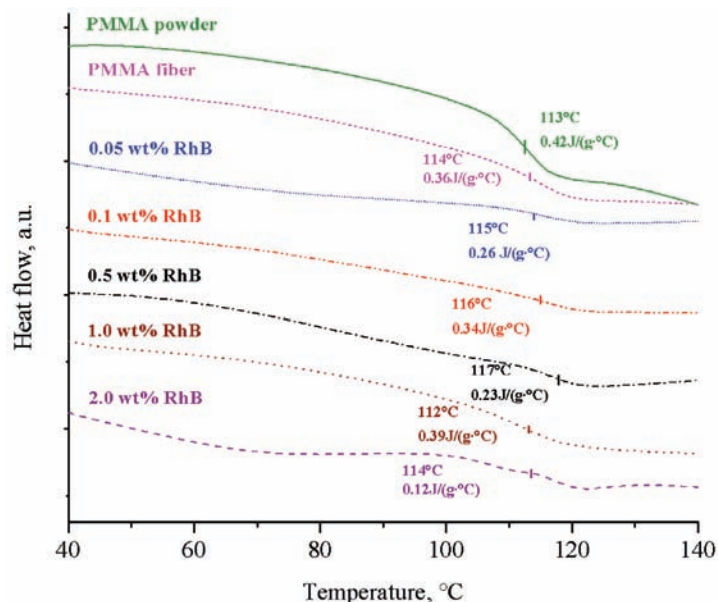


Fig. 5. DSC analysis of PMMA powder, PMMA nanofibers and PMMA-RhB nanofibers with different compositions.

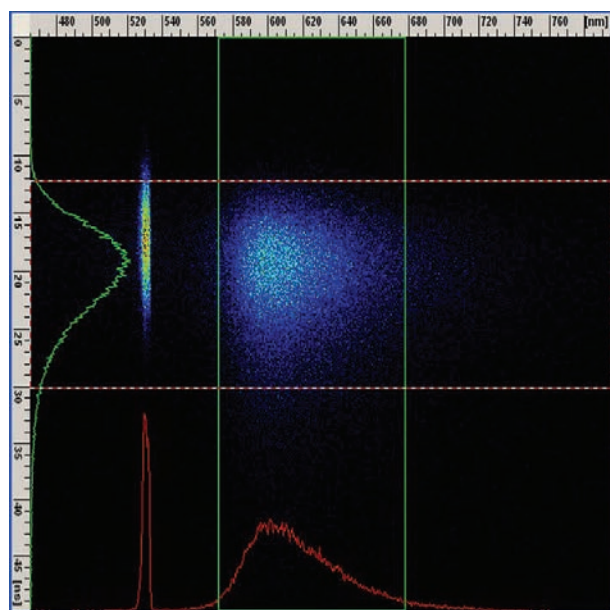


Fig. 6. A streak image of the fluorescence response of the PMMA-0.5 wt. % RhB fibers.

The fluorescence emission spectrum of the fibers is shown in Fig. 7. A shift of the fluorescence peak towards higher wavelengths could be noticed with increasing concentration of RhB. Increasing the concentration of the dye resulted in a red shift in the fluorescence wavelength as can be seen in Fig. 8, which shows the dependence of the wavelength of maximum emission on the concentration of RhB in PMMA. These results are in agreement with the literature.<sup>32,44</sup> It could also be noticed that a plateau was not reached.<sup>43</sup> When a plateau is reached, at high concentrations, aggregation formation restricts the peak shift.

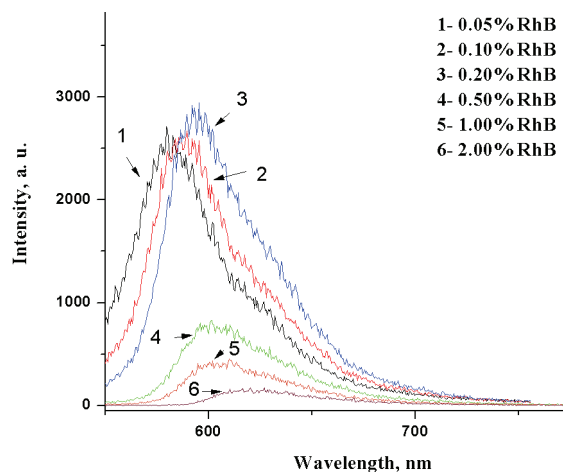


Fig. 7. Emission fluorescent spectrum of nanofibers with different contents of rhodamine B.

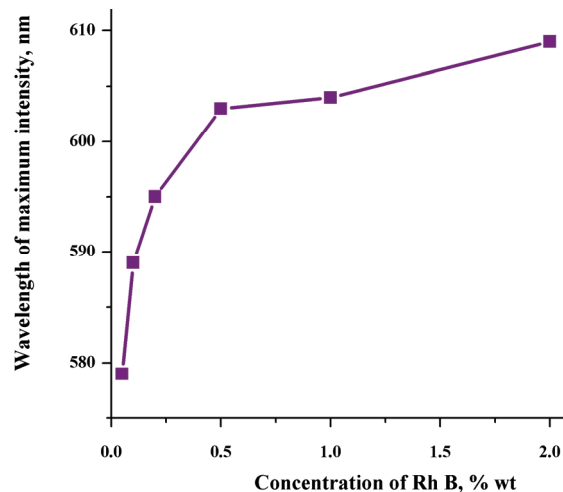


Fig. 8. Dependence of the wavelength of the maximum emission intensity on the content of rhodamine B.

The intensity of the fluorescence emission peak increased with concentration of RhB until 0.2 wt. % and then, at higher concentrations, it decreased and became broader, which is in agreement with published results for RhB in solution

and PMMA films.<sup>32,43</sup> This is correlated to the viscosity/polarity-dependent non-radioactive deactivation processes in RhB.

#### CONCLUSIONS

The electrospinning of PMMA doped with different contents of RhB was performed. Examination of the morphology of the formed fibers revealed bead-free nanofibers with a smooth surface and the mean diameter of the nanofibers decreased with increasing content of RhB in the PMMA. After addition of RhB into the PMMA, the  $T_g$  of the polymer increased with RhB content up to a concentration of 0.5 wt. %. The fluorescence response of fibers after laser excitation indicated that the emission peak increased with increasing concentration of RhB until 0.2 wt. %. The fluorescence emission intensity of RhB became broader and shifted to higher wavelength with increasing RhB concentration in the nanofibers. The values of the solution viscosity,  $T_g$  and fluorescence emission peak indicated that there was a significant and critical concentration of RhB (0.2–0.5 wt. %), and beyond these values the changes were in accord with their viscosity/polarity behavior.

*Acknowledgement.* This work was supported by the Ministry of Education, Science and Technology Development of the Republic of Serbia, Project Nos. TR 34011, III 45019 and 171020.

#### И З В О Д

#### ЕЛЕКТРОПРЕДЕЊЕ НАНОВЛАКАНА ПОЛИ(МЕТИЛМЕТАКРИЛАТА) ДОПИРАНОГ ЛАСЕРСКОМ БОЛОМ РОДАМИН Б

РАМДАН М. ДУКАЛИ<sup>1</sup>, ИВАНА М. РАДОВИЋ<sup>1</sup>, ДУШИЦА Б. СТОЈАНОВИЋ<sup>1</sup>, ДРАГУТИН М. ШЕВИЋ<sup>2</sup>,  
ВЕСНА Ј. РАДОЈЕВИЋ<sup>1</sup>, ДРАГАН М. ЈОЦИЋ<sup>1</sup> и РАДОСЛАВ Р. АЛЕКСИЋ<sup>1</sup>

<sup>1</sup>Универзитет у Београду, Технолошко-мештаришки факултет и <sup>2</sup>Универзитет у Београду,  
Институт за физику

У оквиру овог рада приказано је електропредење поли(метилметакрилат) допираниог родамина Б, које је веома перспективна техника за добијање фотолуминисцентних нановлакана. Изведен је процес електропредења нановлакана са различитим садржајем родамина Б од 0,05 до 2,0 мас. %. Интеракција полимерне матрице влакана и боје анализирана је применом методе Фуријеове трансформације инфрацрвеног спектра. Морфологија влакана као и величина и њихова расподела испитивана је помоћу SEM. Диференцијалном скенирајућом калориметријом анализирана су термичка својства, а оптичка својства техником ласерски индуковане флуоресценције (LIF). Добијена су влакна глатке површине и без мехурива. Анализа диференцијалном скенирајућом калориметријом је показала да  $T_g$  расте са порастом садржаја родамина Б у поли(метилметакрилату) до концентрације од 0,5 мас. %, а затим опада. При испитивању емисионог флуоресцентног спектра нановлакана, максимална флуоресцентна емисија је остварена при садржају родамина Б од 0,2 мас. %.

(Примљено 24. октобра 2013, ревидирано 27. јануара, прихваћено 30 јануара 2014)

## REFERENCES

1. Y. Xia, P. Yang, Y. Sun, Y. Wu, B. Mayers, B. Gates, Y. Yin, F. Kim, H. Yan, *Adv. Mater.* **5** (2003) 353
2. C. M. Lieber, *MRS Bull.* **287** (2003) 486
3. C. H. Wang, Y. Q. Dong, K. Sengothi, K. L. Tan, E. T. Kang, *Synth. Met.* **1021–1023** (1999) 1313
4. W. J. Li, C. T. Laurencin, E. J. Caterson, R. S. Tuan, F. K. Ko, *J. Biomed. Mater. Res.* **604** (2002) 613
5. X. Y. Wang, C. Drew, S. H. Lee, K. J. Senecal, J. Kumar, L. A. Samuelson, *Nano Lett.* **2** (2002) 1273
6. J. S. Kim, D. H. Reneker, *Polym. Compos.* **201** (1999) 124
7. S. Jiang, G. Duan, H. Hou, A. Greiner, S. Agarwal, *ACS Appl. Mater. Interfaces* **4** (2012) 4366
8. N. Tomczak, S. Gu, M. Han, N. F. van Hulst, G. J. Vancso, *Eur. Polym. J.* **42** (2006) 2205
9. Y. Shen, P. N. Prasad, *Appl. Phys., B* **74** (2002) 641
10. H. Q. Yu, B. J. Li, *Sci. Rep.* **3** (2013) 1674
11. R. Dersch, M. Steinhart, U. Boudriot, A. Greiner, J. H. Wendorff, *Polym. Adv. Technol.* **16** (2005) 276
12. K. J. Lee, J. H. Ho, Y. Kim, J. Jang, *Adv. Mater.* **18** (2006) 2216
13. A. Noy, A. E. Miller, J. E. Klare, B. L. Weeks, B. W. Woods, J. J. De Yoreo, *Nano Lett.* **2** (2002) 109
14. F. Quochi, F. Cordella, A. Mura, G. Dongiovanni, F. Balzer, H.-G. Rubahn, *Appl. Phys. Lett.* **88** (2006) 041106
15. H. Yu, Baojun Li, *Sci. Rep.* **3** (2013) 1674
16. D. Pisignano, G. Maruccio, E. Mele, L. Persano, F. Di Benedetto, R. Cingolani, *Appl. Phys. Lett.* **87** (2005) 123109
17. A. Formhals, US Patent 2,116,942 (1938)
18. C. Y. Hsu, Y. L. Liu, *J. Colloid Interface Sci.* **350** (2010) 75
19. A. G. Kanani, S. H. Bahrami, *Trends Biomater. Artif. Organs* **24** (2010) 93
20. D. H. Reneker, I. Chun, *Nanotechnology* **7** (1996) 216
21. R. Jaeger, H. Schonherr, G. J. Vancso, *Macromolecules* **29** (1996) 7634
22. M. Bognitzki, W. Czado, T. Frese, A. Schaper, M. Hellwig, M. Steinhart, *Adv. Mater.* **13** (2001) 70
23. S. Schlecht, S. Tan, M. Yosef, R. Dersch, J. H. Wendorff, Z. Jia, A. Schaper, *Chem. Mater.* **17** (2005) 809
24. X. Wang, S.-H. Lee, B.-C. Ku, L. A. Samuelson, J. Kumar, *J. Macromol. Sci., A* **39** (2002) 1241
25. J. L. Davis, K. Guzan, K. Mills, L. Han, in *Proceedings of NSTI-Nanotech 2010*, Nanotechnology Anaheim, CA, USA, 2010, p. 769
26. A. Tagaya, Y. Koike, T. Kinoshita, E. Nihei, T. Yamamoto, K. Sasaki, *Appl. Phys. Lett.* **63** (1993) 883
27. G. Somasundaran, A. Ramalingam, *Opt. Laser Technol.* **31** (1999) 351
28. H. Liang, Z. Zheng, Z. Li, J. Xu, B. Chen, H. Zhao, Q. Zhang, H. Ming, *J. Appl. Polym. Sci.* **93** (2004) 681
29. K. Geetha, M. Rajesh, V. P. N. Nampoori, C. P. G. Vallabhan, P. Radhakrishnan, *J. Opt., A* **6** (2004) 379
30. P. Kumar, D. R. Bajpai, M. Keller, *Microsyst. Technol.* **14** (2008) 1165

31. G. Sreekumar, P. G. Louie Fobel, S. Sreeja, S. R. Suresh, S. Mayadevi, C. I. Muneera, C. S. Suchand Sandeep, R. Philip, C. Mukharjee, *Chem. Phys. Lett.* **506** (2011) 61
32. M. Fikry, M. M. Omar, L. Z. Ismail, *J. Fluoresc.* **19** (2009) 741
33. H. Wang, Q. Liu, Q. Yang, Y. Li, W. Wang, L. Sun, C. Zhang, Y. Li, *J. Mater. Sci.* **45** (2010) 1032
34. C. Hsu, S. Shivkumar, *Macromol. Mater. Eng.* **289** (2004) 334
35. T. Jarusuwannapoom, W. Hongrojjanawiwat, S. Jitjaicham, L. Wannatong, M. Nithitanakul, C. Pattamaprom, P. Koombhongse, R. Rangkupan, P. Supaphol, *Eur. Polym. J.* **41** (2005) 409
36. I. S. Elashmawi, N. A. Hakeem, *Polym. Eng. Sci.* **48** (2008) 895
37. G. Socrates, *Infrared and Raman Characteristic Group Frequencies*, Wiley, New York, 2001, p. 347
38. A. A. M. Farag, I. S. Yahia, *Opt. Commun.* **283** (2010) 4310
39. A. V. Deshpande, E. B. Namdas, *J. Lumin.* **91** (2000) 25
40. N. Patra, A. C. Barone, M. Salerno, *Adv. Polym. Tech.* **30** (2011) 12
41. S. S. Musbah, V. Radojević, I. Radović, P. S. Uskoković, D. B. Stojanović, M. Dramićanin, R. Aleksić, *J. Min. Metall., B* **48** (2012) 309
42. T. W. J. Gadella, Jr., T. M. Jovin, R. M. Clegg, *Biophys. Chem.* **48** (1993) 2219
43. T. Robinson, Y. Schaerli, R. Wootton, F. Hollfelder, C. Dunsby, G. Baldwin, M. Neil, P. French, A. de Mello, *Lab Chip* **9** (2009) 3437
44. M. F. Al-Kadhemy, I. F. Alsharuee, A. D. Al-Zuky, *J. Phys. Sci.* **22** (2011) 77.



## An experimental and computational investigation of the effects of temperature on soot formation mechanisms

XIAOJIE BI<sup>1,2</sup>, MAOYU XIAO<sup>1</sup>, XINQI QIAO<sup>1</sup>, CHIA-FON F. LEE<sup>2,3</sup> and YU LIU<sup>4\*</sup>

<sup>1</sup>Key Laboratory for Power Machinery and Engineering of the Ministry of Education, Shanghai Jiao Tong University, Shanghai, 200240, China, <sup>2</sup>Department of Mechanical Science and Engineering, University of Illinois at Urbana-Champaign, IL, 61801, USA, <sup>3</sup>Center for Combustion Energy and State Key Laboratory of Automotive Safety and Energy, Tsinghua University, Beijing 100084, China and <sup>4</sup>Key Laboratory of Automobile Dynamic Simulation, Jilin University, Changchun, Jilin, 130012, China

(Received 14 June, revised 2 November, accepted 4 November 2013)

**Abstract:** Effects of the initial ambient temperature on combustion and soot emission characteristics of diesel fuel were investigated through experiments conducted in an optical constant volume chamber and simulation using a phenomenological soot model. Four different initial ambient temperatures were adopted in this research: 1000, 900, 800 and 700 K. In order to obtain a better prediction of soot behavior, the phenomenological soot model was revised to take into account the feedback of soot oxidation on the soot number density and good agreement was observed in the comparison of soot measurement and prediction. The results indicated that the ignition delay was prolonged with decreasing initial ambient temperature. The heat release rate demonstrated the transition from mixing controlled combustion at high ambient temperatures to the premixed combustion mode at low ambient temperatures. At lower ambient temperatures, soot formation and the oxidation mechanism were both suppressed. However, the soot mass concentration was finally reduced with decreasing initial ambient temperature. Although the drop in ambient temperature did not cool the mean in-cylinder temperature during the combustion, it did shrink the total area of local high equivalence ratios, in which soot usually is rapidly generated. At an initial ambient temperature of 700 K, soot emissions were almost negligible, which indicates that sootless combustion might be achieved under super low initial temperature operation conditions.

**Keywords:** soot emission; constant volume chamber; phenomenological soot model; multi-dimensional simulation.

\*Corresponding author. E-mail: xiaojie2163@hotmail.com  
doi: 10.2298/JSC130614125B

## INTRODUCTION

Soot, a major component of particulate matter (PM), is one of the key air pollutants emitted by diesel engines.<sup>1</sup> Previous research proved that soot nuclei with a radius between 0.1 and 0.5 μm are able to deposit directly in the lung and result in serious health issues.<sup>2</sup> Therefore, there is a global trend to enforce more stringent regulations for this air pollutant. In addition to the emissions challenge, soot formation in diesel engines can also influence the engine performance and have feedback effects on in-cylinder combustion and emission characteristics. Soot, once present within a flame, plays an important role in radiative heat transfer;<sup>3,4</sup> soot produces broadband incandescent radiation, which typically dominates over narrow-band radiation from intermolecular processes. Therefore, soot appearance within a flame would enhance the flame emissivity and hence increase radiative heat loss. The combustion efficiency then tends to decrease. In addition, a lower flame temperature, owing to the larger radiative heat transfer through soot nuclei, will in turn suppress NO<sub>x</sub> formation.<sup>5</sup>

Although it is essential to clarify soot formation and oxidation mechanisms, the understanding about the factors affecting soot particles is still limited. Most research was conducted under near-atmospheric conditions.<sup>6–9</sup> However, combustion and soot formation in diesel fuel jets under a high-temperature and high-pressure environment is far removed from atmospheric conditions. Laser diagnostics measurements conducted in high-temperature, high-pressure combustion vessels<sup>10–14</sup> are typical tools capable of yielding detailed measurements of soot processes under diesel-like operation conditions. Overall, soot in diesel fuel jets begins to be generated shortly after auto-ignition and lasts throughout all the transient premixed phase and the ensuing mixing-controlled phase of combustion.<sup>15–17</sup>

There is a wide range of parameters, such as temperature, pressure, equivalence ratio, fuel composition and structure, as well as engine design and operation parameters, that are involved in soot evolution, among which temperature plays the most important role.<sup>1</sup> Soot and temperature have an inherent coupled dependence: temperature depends on soot concentration due to heat transfer through radiation and soot depends on temperature due to the chemical and physical processes controlled by temperature. Therefore, a detailed understanding of soot must depend on an in-depth analysis of temperature. In a constant volume chamber, an increase in soot generation with increasing temperature was observed by Pickett and Siebers,<sup>18</sup> due to increasing rates of the soot formation reaction. In shock-tube measurements, Graham *et al.*<sup>19</sup> found that soot volume fraction exhibited a bell-shaped behavior as a function of temperature in the pyrolysis of aromatics. This behavior was also reported by Frenklach *et al.*<sup>20</sup> within the flame of non-aromatic fuels, when the soot volume fraction initially increased and then decreased with increasing temperature. The temperature under which the soot

yield reaches its peak was found to vary widely over various configurations.<sup>21,22</sup> Additionally, multi-dimensional simulation is essential for the interpretation of experimental discoveries in order to obtain an in-depth understanding about soot evolution. For decades, many contributions have been made to explore suitable models to describe soot formation and oxidation in a turbulent non-premixed flame. Moss *et al.*<sup>23</sup> developed a two-step soot model using vapor-phase diesel fuel as the soot precursor. The first step is a soot mass fraction equation, including surface growth and nucleation and the second is an equation of soot number density, using nucleation and coagulation as the source and sink terms. Tesner *et al.*<sup>24</sup> introduced a general precursor species and linked the precursor species with soot particles through a coagulation process. Sequentially, Surovikin *et al.*<sup>25</sup> improved the Tesner model<sup>24</sup> and adopted surface growth to be the conversion pathway from the soot precursor to soot nuclei, once the diameter of precursor species was larger than a critical diameter. Based on the previous work, Leung *et al.*<sup>26</sup> adopted acetylene as the precursor species and further considered surface growth reactions between soot and acetylene. Subsequently, Fusco *et al.*<sup>27</sup> developed an eight-step phenomenological soot model by introducing oxidative reactions of acetylene and precursor species to avoid an overestimation of their concentrations. Tao *et al.*<sup>22</sup> improved the Fusco model<sup>27</sup> by including the involvement OH radicals in a soot oxidation mechanism through the Neoh OH-related oxidation model<sup>28</sup> in a newly revised phenomenological soot model.<sup>22</sup>

Some may argue that this phenomenological soot model is too simplified to describe soot evolution in a turbulent non-premixed flame since it is a rather complex process, involving the interaction of chemical kinetics, heat and mass transfer as well as fluid flow and a description of pre-particle chemistry. However, the soot formation and oxidation process under diesel-like conditions were elusive, especially gas-phase kinetics from diesel fuel to soot nuclei were then uncertain subjects.<sup>29</sup> At present, a detailed chemistry soot model is well accepted as the most accurate model for the prediction of soot behavior because all known reactions and species relevant to soot formation and oxidation were taken into account.<sup>30–33</sup> However, a detailed representation of soot chemical reactions needs the interactions between the detailed chemistry and turbulent mixing on a sub-grid level to be solved. By doing this, the model is super demanding in terms of computational time and rather impractical. Additionally, accurate predictions of soot evolution are extremely sensitive not only to the soot model itself, but also to the other models that are applied to describe the complex processes of spray and combustion processes, such as the turbulence model, the spray model and the evaporation model. These existing uncertainties in these models could essentially eliminate the advantages of using a detailed kinetic treatment of soot formation. Therefore, the choice of a simplified phenomenological soot model is the combination result of computation efficiency and acceptable accuracy.

The objective of the current study was to explore the temperature effects on soot formation and oxidation of diesel fuel under diesel-like operation conditions. Detailed analysis of the in-cylinder pressure, heat release rate and time related soot behavior was provided to expand the understanding of the coupled dependence of temperature and soot nuclei. In order to interpret the new experimental findings, a phenomenological soot model was revised and applied to predicted soot behavior under the same operational conditions. Time related traces and spatial distributions of soot relevant species, such as acetylene, soot precursor species, OH radicals and soot number density were predicted as well.

## EXPERIMENTAL

### *Experimental apparatus*

The experiments were conducted in an optical-accessible constant volume chamber with a bore of 110 mm and a height of 65 mm. The chamber was designed to imitate spray and combustion processes in compressed ignition engines with a maximum operating pressure of 18 MPa. The chamber together with a liquid spray scattering, combustion flame and soot formation measurement setup is shown schematically in Fig. 1. In order to pass laser beams and take photographs, a fused silica (Dynasil 1100) end window, 130 mm in diameter, 60 mm thick and with high UV transmittance down to 190 nm, was installed opposite to the injector.

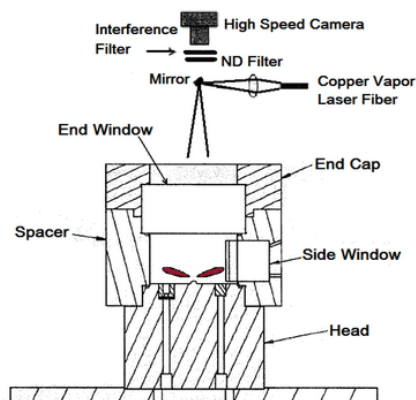


Fig. 1. A schematic presentation of the constant volume chamber.

Details of the apparatus are given in the Supplementary material to this paper.

### *Experimental methods*

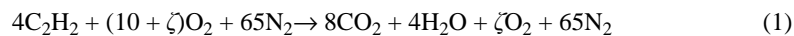
In these experiments, the forward illumination light extinction (FILE) method developed by Xu and Lee<sup>34</sup> was used as the soot diagnostic technology. This method was able to provide two dimensional time-resolved quantitative soot measurements. As shown in Fig. 1, in the FILE method, the light source and the camera are placed on the same side of the flame through the same window. By doing this, only one window with a light diffuser is required in the forward-illumination setup, as shown in Fig. S-1 of the Supplementary material. Compared to the back illumination light-extinction method, in which two aligned windows are

required, the FILE technique was easier to operate. The light diffuser set behind the flame was to ensure sufficient reflected light that could be collected by the camera.

Details of the extinction measurements and the subsequent calculations are given in the Supplementary material.

#### *Experimental procedure*

Initially, a premixed, combustible-gas mixture of acetylene ( $C_2H_2$ ), air and nitrogen was filled into the test chamber. After the mixture had been ignited by spark plugs, a high-temperature, high-pressure environment modeling typical diesel in a cylinder environment with the piston at TDC was created in the test chamber. Due to its flammability and low window contamination, acetylene, with unity C/H ratio, was adopted here as the pilot combustion gas. Thus, the density of the filling mixture can be determined by the chemical reaction as:



where  $\zeta$  denotes the amount of excess oxygen, which was used to simulate the ambient oxygen concentration for diesel compressed ignition combustion. After the acetylene had been completely consumed, the ambient air contained 21 % oxygen, 66.7 % nitrogen, 8.2 % carbon dioxide and 4.1 % water vapor by volume. The density of the mixture for post-combustion was  $14.8 \text{ kg m}^{-3}$ , which mimics the operation conditions without the EGR rate of realistic diesel engines. In addition, the vessel pressure slowly decreases due to heat transfer through the vessel walls. When the desired pressure was achieved the injection signal triggered the HEUI injector and the high-speed camera simultaneously, and diesel fuel was injected into the cylinder and the camera began to record the whole injection, auto-ignition and combustion processes.

In this study, four different ambient temperatures were investigated: 700, 800, 900 and 1000 K, covering both low-temperature and conventional high-temperature combustion modes in diesel engines, *i.e.*, initial temperatures of 700 to 800 K present low temperature low load combustion while an initial temperature of 1000 K presents typical high temperature higher load combustion. The test fuel in these experiments was European low sulfur diesel fuel.

#### *Simulation models*

In order to obtain insight into the formation and oxidation mechanisms of soot particles, a phenomenological soot model was adopted and revised to simulate compressed ignition combustion and soot emission behavior at initial ambient temperatures of 700 to 1000 K. The soot model in the present paper restrained the main feature of the phenomenological soot model developed by Tao *et al.*,<sup>22</sup> but improved the governing differential equation of soot number density by taking into account the effects of soot oxidation. A schematic presentation of the revised phenomenological soot model is shown in Fig. 2, from which it can be seen that the Phenomenological soot model has nine main steps.

Complete descriptions of the models considered in this study are given in the Supplementary material.

## RESULTS AND DISCUSSION

#### *Analysis of the combustion characteristics*

The measured in-cylinder pressure and heat release rate under ambient temperatures of 700, 800, 900 and 1000 K are presented in Fig. 3. Since the chamber volume is constant, the in-cylinder pressure is directly proportional to temperature and the higher the initial temperature, the higher is the initial pressure. In

order to avoid the influence of the initial in-cylinder pressure, all initial pressures were set to zero and hence the pressures shown in the Fig. 3 are relative pressures, which are actually the increase of pressure caused by heat released from the diffusion-dominated combustion.

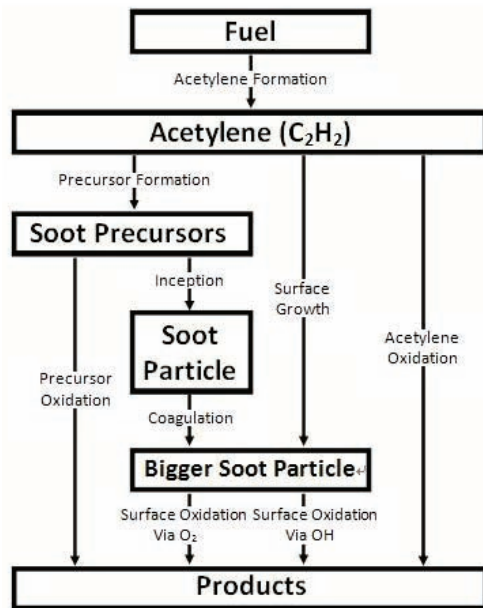


Fig. 2. Structure of the nine-step phenomenological soot model.

As shown in Fig. 3, the ignition delay became longer with decreasing initial temperature from 1000 to 700 K. The threshold of combustion here is defined as the time when a sudden increase in the heat release rate first appeared. Based on the theory of chemical kinetics, the ambient temperature is the most essential parameter in the determination of chemical reaction rates. With decreasing ambient temperature, the effective coagulation frequency between reactants tends to

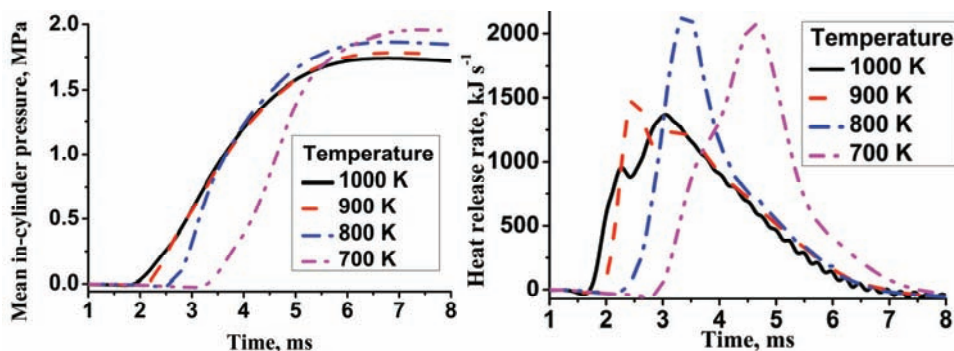


Fig. 3. In-cylinder pressure and heat release rate determined using the phenomenological soot model.

decrease and the reaction rates of all chemical reactions are retarded. Therefore, a milder and slower heat release rate could be expected for pre-flame reactions. More time was required to achieve self-ignition and the ignition delay was longer.

On the other hand, premixed combustion becomes a more and more important part of the whole combustion process with decreasing initial ambient temperature. When the ambient temperature was as high as 1000 K, there were two peaks in the rate of heat release trace, indicating premixed and diffusion combustion, respectively. On dropping the ambient temperature to 900 K, a higher premixed combustion peak as well as a lower diffusion combustion peak than at 1000 K initial ambient temperature were found in Fig. 3. When the initial ambient temperature was further decreased to 800 K, only one peak was observed in heat release rate trace, which illustrated that premixed combustion was the absolutely dominant combustion mode under this operation condition and the combustion pressure was even higher than that under 900 K initial ambient temperature. At 700 K initial ambient temperature, the heat release rate retained a one-peak characteristic and the highest combustion pressure was found, Fig. 3, evidencing the highest combustion efficiency. As discussed above, the ignition delay became longer with decreasing initial ambient temperature. A longer ignition delay gives more time for the fuel and fresh air to mix, resulting in the formation of a larger premixed charge before self-ignition and hence a stronger premixed combustion would occur on ignition of the diesel. Hence, the peak of the premixed combustion was higher at the lower initial ambient temperature. The speed of premixed flames is dependent on the chemical reaction rates, while the speed of diffusion flames is determined by the diffusion speed. Since chemical reaction rates are much faster than diffusion speed, the combustion duration was much shorter for premixed dominated combustion for initial ambient temperature of 800 and 700 K than that occurring with initial ambient temperatures of 900 and 1000 K. The heat loss was decreased due to the shorter combustion duration at lower initial ambient temperatures. In the experiments, the total fuel mass was kept constant, which indicated a constant energy input for all operation conditions. With a lower heat loss, the combustion efficiency was higher with decreasing initial ambient temperature and became the highest at 700 K initial ambient temperature; thus, the highest-pressure peak was observed at 700 K initial ambient temperature, as shown in Fig. 3.

#### *Soot behavior analysis*

The time related total soot mass concentrations at initial ambient temperatures of 700 to 1000 K are shown in Fig. 4. In order to avoid the effects of the amount of fuel injected on the soot generation, the unit  $\mu\text{g g}_{\text{fuel}}^{-1}$  was adopted here, which was defined as the total mass of soot in the chamber over the total mass of injected diesel fuel. In Fig. 4, the soot mass exhibited “bell-shaped”

characteristics regardless of the initial temperature, *i.e.*, the amount of soot initially increased rapidly to achieve maxima values and then decreased to zero thereafter. Similar results were also reported in previous studies.<sup>21,22,27</sup> The threshold of soot mass formation was gradually delayed on decreasing the initial ambient temperature from 1000 to 700 K and the duration of the delay became longer in the order 900 to 1000 K, 800 to 900 K and finally 700 to 800 K. As discussed above, the auto ignition delay was longer at lower initial ambient temperatures. Since soot particles are the incomplete products of compressed ignition combustion, they followed the same characteristics of combustion and their appearance occurred later with decreasing initial temperature from 1000 to 700 K.

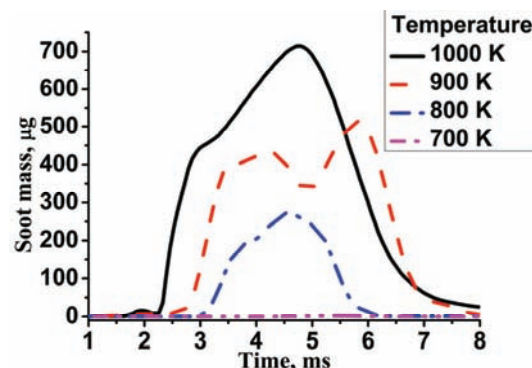


Fig. 4. Soot mass generated by 1 g of fuel for initial temperatures of 700, 800, 900 and 1000 K.

The later appearance of soot also demonstrates the reduced tendency of sooting of diesel fuel at lower initial ambient temperatures. Therefore, the total soot mass increased with increasing ambient temperature, which emphasized the importance of intake temperature cooling and its beneficial effects on mitigating soot formation. The soot emissions here were the combined results of soot formation and soot oxidation. Under conditions of higher ambient temperatures, weaker premixed combustion was observed, Fig. 3, so less entrainment of ambient air would result in higher fuel richness within the diesel fuel jet, higher soot formation rates at the early stage of combustion and finally higher soot mass concentration, as shown in Fig. 4.

#### *Validation of phenomenological soot model*

Comparisons between the measured and predicted soot behavior using the revised phenomenological soot model for initial temperatures of 700, 800, 900 and 1000 K are illustrated in Fig. 5, which shows that the overall soot traces predicted by revised phenomenological soot model were in good agreement with the measurements. Therefore, it is reasonable to believe that phenomenological soot model is able to reproduce successfully the soot formation and oxidation

processes of diesel fuel and its prediction for relevant intermediate species, such as acetylene, soot precursor species and OH radicals.

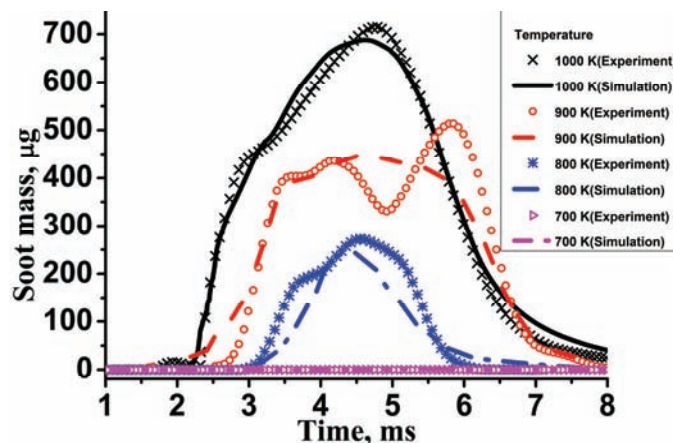


Fig. 5 Comparison of the measured and predicted soot mass generated by 1 g of fuel for initial temperatures of 700, 800, 900 and 1000 K.

#### *Predicted traces of soot relevant species*

The temporal mass concentrations of  $C_2H_2$ , soot precursors, OH radicals and soot number predicted by the revised phenomenological soot model for initial ambient temperatures of 700 to 1000 K are shown in Fig. 6, from which it can be seen that all traces shared the same “bell-shaped” characteristics as the soot mass concentration. Comparing Fig. 6 to Fig. 5, it is evident that there were no significant differences between the soot mass and the amount of soot, which indicated that the initial temperature had negligible effects on the mean particle diameter of the soot in the constant volume chamber.

As shown in Fig. 6, the thresholds for soot relevant species were also retarded with decreasing initial ambient temperature from 1000 to 700 K. Acetylene and soot precursor species are typical intermediate species involved in diesel compressed ignition combustion. The initial temperature is the most essential parameter determining the rates of pre-flame reactions. In Fig. 4, the longest ignition delay was observed at the lowest initial temperature, when the lowest reaction rates for the pre-flame reactions were also observed. As a result, lower formation rates of acetylene and soot precursor species could be expected in the early stages of combustion and delayed appearances of acetylene and soot precursor species were found at the lowest initial temperature, as shown in Fig. 6.

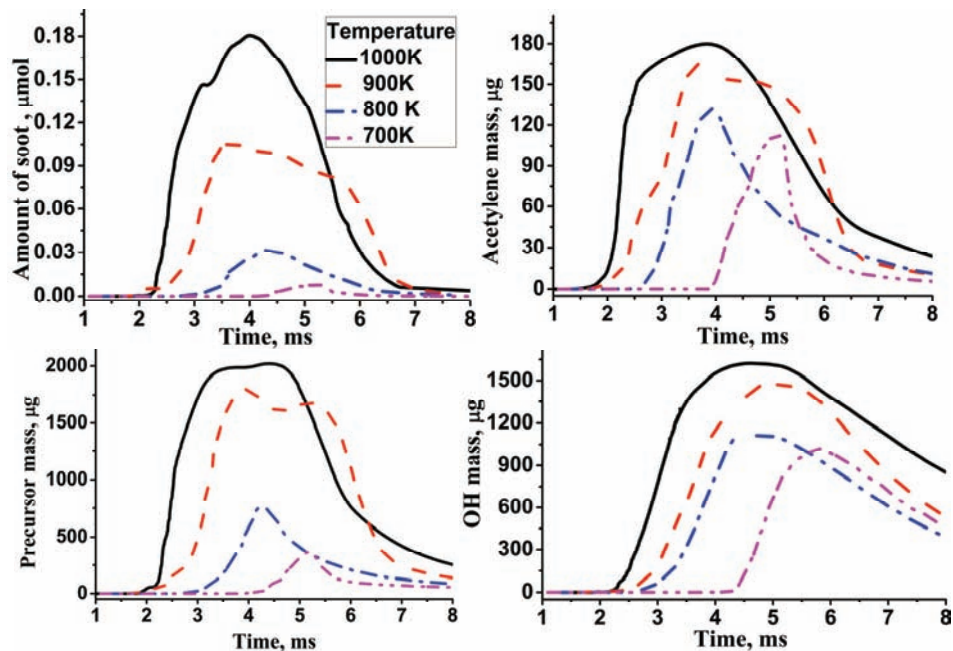


Fig. 6. Soot mass, amount of soot, mass of  $\text{C}_2\text{H}_2$ , soot precursor and OH generated by 1 g of fuel for initial temperatures from 700 to 1000 K.

In Fig. 6, the continuous decrease in the maximum mass concentrations of species relevant for soot formation and oxidation mechanisms, such as acetylene, soot precursor species and OH radicals, indicated that both soot formation and oxidation reactions were strongly suppressed by the reduced initial ambient temperature. However, a lower total soot mass concentration with the decreasing ambient temperatures was previously proved. Therefore, it is reasonable to believe that the soot formation mechanism played a leading role in dominating the behaviors of soot when the initial ambient temperature was decreased.

Below an initial ambient temperature of 800 K, a suddenly sharp drop appeared in the mass concentration of soot precursor species. In the new proposed model, there are one formation pathway and mainly two consumption pathways directly linked to the mass concentration of the soot precursor species: generation from an acetylene-rich pool, condensation to form soot nuclei and directly oxidation to  $\text{CO}_2$  and  $\text{H}_2\text{O}$ . As shown in Fig. 6, the mass concentration of OH radicals continued to decrease with decreasing initial ambient temperature, which led to a lower oxidation rate of the soot precursor species. At the same time, a lower rate of soot formation from soot precursor species was also proved previously at lower initial ambient temperatures. Therefore, the reason for the lower peak of the precursor mass concentration at lower initial ambient temperatures should only be the lower formation rate of soot precursor species from

acetylene. The decrease of initial temperature not only suppressed the formation rate of soot particles but also restrained the formation mechanism of the intermediate species. When the initial temperature was 700 K, the mass concentration of soot precursor species was almost zero and a super low level of soot emissions (near zero), as presented in Fig. 5. Since soot emissions exhibited a continuous decrease with decreasing initial ambient temperature, smokeless combustion might be achieved after a further reduction in the initial ambient temperature.

#### *Predicted spatial distributions of soot emissions and relevant species*

The spatial distributions of the mean in-cylinder temperature, equivalence ratio, amount and mass of soot nuclei, acetylene, soot precursor species as well as OH radicals are presented in Fig. S-2, Supplementary material, for initial ambient temperatures from 700 to 1000 K at 4.5 ms, when the mass concentrations of soot emissions achieved their peaks under 800, 900 and 1000 K initial ambient temperatures.

Under the constant initial ambient temperature, the diesel fuel, acetylene, precursor species, soot particles and OH radicals were all detected within the high temperature area, which determined that there should be a switch temperature above which soot formation and oxidation reactions could be reactivated. Compared to the distributions of acetylene and the soot precursor species, the distributions of the OH radical, which is the representative reactant involved in soot oxidation reactions, had shapes more similar to those of the temperature distributions. Thus, the oxidation mechanisms of soot particles were highly dependent on the ambient temperature.

For initial temperatures from 1000 to 700 K, the local highest mean in-cylinder temperature did not show an obvious decrease under the operation condition with the lower initial ambient temperatures, as shown in Fig. S-2. Furthermore, the overall temperature was even higher at an initial ambient temperature 800 K than that at initial ambient temperatures of 900 and 1000 K. At 700 K ambient temperature, the region of high combustion temperatures started to shrink. Since a continuous drop in the peaks of the total mass concentrations of soot were observed in Fig. 5, the decrease in initial ambient temperature was not the direct reason for the reduction of soot emissions.

The equivalence ratio is defined as the local fuel/oxidizer mass ratio divided by the stoichiometric fuel/oxidizer mass ratio. When the initial temperature dropped from 1000 to 800 K, the maximum equivalence ratio value of local fuel-rich reaction zone did not decrease very much. However, the area of local fuel-rich zone did decrease gradually. Similar results were also observed in the mass concentration distributions of acetylene and the soot precursor species for ambient temperatures from 800 to 1000 K, the maximum mass density of acetylene and the soot precursor species at the lowest initial temperature maintained the

same level as those at the higher initial ambient temperatures, which was evidenced by the almost same red color in Fig. S-2. However, the area of the local rich reaction zone of acetylene and the soot precursor species shrank a lot at lower initial ambient temperatures, especially at an initial ambient temperature of 800 K. Therefore, the suppressed soot formation mechanism at the lower initial temperature conditions should be directly caused by the reduced area of the local diesel-rich reaction zones.

Comparing spatial distributions in Fig. S-2, it is clearly noticeable that the soot mass distributions did not duplicate the distributions of the equivalence ratios. However, it looked more like the distributions of soot precursor species. This result revealed that soot precursors were the species to determine the locations where soot particles existed. The soot mass density was the result of combining both the effects of acetylene and the soot precursor species.

When initial temperature dropped to as low as 700 K, the highest local equivalence ratio should be below 2, since all the red and yellow color in equivalence ratio distribution faded away. As shown in Fig. 5, the soot mass concentration was negligible under this condition. Furthermore, it is very clear that the mass concentration became larger in the order of soot particles, soot precursor species and acetylene, which means gas-phase species, including acetylene and soot precursor species, had a wider region of equivalence ratio for their formation. Similar conclusions were also reached in an investigation of Kitamura *et al.*,<sup>35</sup> who modeled the equivalence ratio and temperature dependence of soot formation for paraffinic hydrocarbons, aromatic hydrocarbons and oxygenated hydrocarbons using a detailed soot kinetic model. In their research, the critical equivalence ratio of *n*-heptane was around 2, indicating that soot is not formed at equivalence ratios below 2, regardless of the temperature. Moreover, they found that the acetylene formation region was distributed over a wider equivalence ratio region than the sooting region. These results were consistent with the present observations. Since soot mass concentration decreased with decreasing initial temperature, sootless combustion could be expected when the initial temperature is below 700 K.

## CONCLUSIONS

Experiments were conducted in an optical constant volume chamber to explore combustion and soot emission characteristics under different initial ambient temperatures, 700, 800, 900 and 1000 K. To aid interpretation of the experimental results, a phenomenological soot model was revised and the revision applied to predict soot behavior under the same operation conditions as in the experiments. Qualitatively, a comparison of soot measurements and the predictions from the phenomenological soot model were given to validate the revised soot model. Detailed analysis about soot relevant species, such as acetylene, pre-

cursor species and OH radicals was also presented to reveal the responsible factor that contributed to the reduction of soot emissions with decreasing initial ambient temperature. The main conclusions are as follows:

The heat release rates demonstrate the transition from mixing controlled combustion at 1000 and 900 K to premixed combustion dominant at 800 and 700 K. A longer ignition delay was also observed at lower initial ambient temperature conditions. The in-cylinder pressure traces proved that the combustion efficiency became higher when initial ambient temperature was decreased from 1000 to 700 K.

Similar to the combustion characteristics, a delayed appearance of soot emissions was found at lower initial ambient temperatures. Moreover, the total soot mass increased with increasing ambient temperatures. At an initial ambient temperature of 700 K, the soot emissions were almost negligible, which indicates that sootless combustion might be achieved under low initial temperature conditions.

All species relevant to soot formation and the oxidation mechanism presented a delayed threshold of increase in soot formation as the initial ambient temperature decreased from 1000 to 700 K. The mass concentrations of acetylene, soot precursor species and OH radicals decreased with decreasing temperature. The slower formation and oxidation reaction rates at lower initial temperature indicated that the soot formation mechanism dominated the soot behavior under various initial ambient temperatures.

The effects of the initial ambient temperature on the mean in-cylinder temperature were unperceivable. However, variation in the initial ambient temperature could strongly affect the distribution of the equivalence ratio within the whole test chamber. The total area of local high equivalence ratio shrunk at lower initial ambient temperature revealed a reduced sooting tendency; hence, lower soot emissions were detected with decreasing initial ambient temperature. At an initial ambient temperature of 700 K, the equivalence ratio was under the value of 2. Soot was not formed at equivalence ratios below 2, regardless of temperature.

#### SUPPLEMENTARY MATERIAL

Details of the apparatus, information on the measurement and subsequent calculation of extinction values, model description, a list of employed symbols and figures of spatial in-cylinder phenomena are available electronically at <http://www.shd.org.rs/JSCS/>, or from the corresponding author on request.

## ИЗВОД

## ЕКСПЕРИМЕНТАЛНО И РАЧУНАРСКО ИСПИТИВАЊЕ УТИЦАЈА ТЕМПЕРАТУРЕ НА МЕХАНИЗМЕ СТВАРАЊА ЧАЋИ

XIAOJIE BI<sup>1,2</sup>, MAOYU XIAO<sup>1</sup>, XINQI QIAO<sup>1</sup>, CHIA-FON F. LEE<sup>2,3</sup> и YU LIU<sup>4</sup>

<sup>1</sup>Key Laboratory for power machinery and Engineering of Ministry of Education, Shanghai Jiao Tong University, Shanghai, 200240, China, <sup>2</sup>Department of Mechanical Science and Engineering, University of Illinois at Urbana-Champaign, IL, 61801, United States, <sup>3</sup>Center for Combustion Energy and State Key Laboratory of Automotive Safety and Energy, Tsinghua University, Beijing 100084, China и <sup>4</sup>Key Laboratory of automobile dynamic simulation, Jilin University, Changchun, Jilin, 130012, China

Испитани су утицаји почетних температура средине на карактеристике сагревања дизел горива и емисије чаћи применом експеримента спроведених у оптичкој комори сталне запремине и помоћу симулације која користи феноменошки модел чаћи. У истраживањима су разматране четири почетне температуре средине: 1000, 900, 800 и 700 К. Како би се добило боље предвиђање понашања чаћи ревидиран је феноменошки модел чаћи како би се узео у обзир повратни утицај оксидације чаћи на густину расподеле чаћи, при чему је добијено добро слагање између мерења и предвиђања. Резултати су показали да је одлагање паљења везано са смањењем почетне температуре средине. Интезитет ослобађања топлоте демонстрира прелаз од дифузионог сагревања на високој температури до предмешаног сагревања на ниској температури. На нижој температури су потиснути процеси оксидације и формирања чаћи. Ипак, на крају је масена концентрација чаћи смањена са смањењем почетне температуре средине. Иако пад у температури средине није охладио главни улазни вод за време сагревања, он није смањио високе вредности локалног еквивалентног односа гориво/ваздух, у којој се чаћ по правилу брзо стварала. На почетној температури средине од 700 К, емисије чаћи су биле скоро занемарљиве, што указује на то да сагревање без чаћи може бити остварено у условима изузетно ниских почетних радних температура.

(Примљено 14. јуна, ревидирано 2. новембра, прихваћено 4 новембра 2013)

## REFERENCES

1. D. R. Tree, K. I. Svensson, *Prog. Energ. Combust. Sci.* **33** (2007) 272
2. V. Lépicier, M. Chiron, R. Joumard, *Environ. Impact Assess. Rev.* **38** (2013) 35
3. K. Boulouchos, M. K. Eberle, B. Ineichen, C. Klukowski, *Heat Transfer in Diesel Engines*, SAE Technical Paper 890573, 1989, doi:10.4271/890573
4. P. Flynn, M. Mizusawa, O. A. Uyehara, P. S. Myers, *SAE Trans.* **81** (1972) 95
5. B. J. Alder, L. K. Tseng, N. M. Laurendeau, J. P. Gore, *Combust. Sci. Technol.* **152** (2000) 167
6. F. Douce, N. Djebaili-Chaumeix, C. E. Paillard, C. Clinard, J. N. Rouzaud, *Proc. Combust. Inst.* **28** (2000) 2523
7. A. V. Eremin, *Prog. Energ. Combust. Sci.* **38** (2012) 1
8. O. Mathieu, N. Djebaili-Chaumeix, C. E. Paillard, F. Douce, *Combust. Flame* **156** (2009) 1576
9. N. Ohashi, K. Ishii, A. Teraji, M. Kubo, *Nihon Kikai Gakkai Ronbunshu, B. Hen, Trans. Jpn. Soc. Mech. Eng., B* **75** (2009) 2520
10. Á. Díez, H. Zhao, T. Carrozzo, A. E. Catania, E. Spessa, *P. I. Mech. Eng., D – J. Aut. Eng.* **226** (2012) 684
11. Y. Wu, R. Huang, C. F. Lee, C. Huang, *P. I. Mech. Eng., D – J. Aut. Eng.* **226** (2012) 372
12. H. Liu, X. Bi, M. Huo, C. F. F. Lee, M. Yao, *Energy Fuels* **26** (2012) 1900

13. H. Liu, C. F. Lee, M. Huo, M. Yao, *Energy Fuels* **25** (2011) 1837
14. H. Liu, C. F. F. Lee, M. Huo, M. Yao, *Energy Fuels* **25** (2011) 3192
15. D. H. Qi, H. Chen, L. M. Geng, Y. Z. Bian, *Energy Convers. Manage.* **51** (2010) 2985
16. D. H. Qi, H. Chen, L. M. Geng, Y. Z. Bian, X. C. Ren, *Appl. Energy* **87** (2010) 1679
17. D. H. Qi, L. M. Geng, H. Chen, Y. Z. Bian, J. Liu, X. C. Ren, *Renew. Energy* **34** (2009) 2706
18. L. Pickett, J. López, *Jet-Wall Interaction Effects on Diesel Combustion and Soot Formation*, SAE Technical Paper 2005-01-0921, 2005, doi: 10.4271/2005-01-0921
19. S. Graham, J. Homer, J. Rosenfeld, *Proc. Roy. Soc. London* **344** (1975) 259
20. M. Frenklach, S. Taki, M. B. Durgaprasad, R. A. Matula, *Combust. Flame* **54** (1983) 81
21. F. Tao, D. E. Foster, R. D. Reitz, *Proc. Combust. Inst.* **31** (2007) 2991
22. F. Tao, R. D. Reitz, D. E. Foster, Y. Liu, *Int. J. Therm. Sci.* **48** (2009) 1223
23. J. B. Moss, C. D. Stewart, K. J. Syed, *Proc. Combust. Inst.* **22** (1989) 413
24. P. A. Tesner, T. D. Smegiriova, V. G. Knorre, *Combust. Flame* **17** (1971) 253
25. V. F. Surovkin, *Solid Fuel Chem.* **10** (1976) 92
26. K. M. Leung, R. P. Lindstedt, W. P. Jones, *Combust. Flame* **87** (1991) 289
27. A. Fusco, A. L. Knox-Kelecy, D. E. Foster, in *Proceedings of the 3rd International Symposium on Diagnostics and Modeling of Combustion in Internal Combustion Engines*, COMODIA 94, Yokohama, Japan, 1994, p. 571
28. K. G. Neoh, J. B. Howard, A. F. Sarofim, *Proc. Combust. Inst.* **20** (1985) 951
29. A. E. Karataş, O. L. Gülder, *Prog. Energ. Combust. Sci.* **38** (2012) 818
30. F. Tao, V. I. Golovitchev, J. Chomiak, *Combust. Flame* **136** (2004) 270
31. Y. Ren, X. G. Li, *P. I. Mech. Eng., D – J. Aut. Eng.* **225** (2011) 531
32. M. Yao, Z. Zheng, *P. I. Mech. Eng., D – J. Aut. Eng.* **220** (2006) 991
33. H. Zhao, Z. Peng, N. Ladommatos, *P. I. Mech. Eng., D – J. Aut. Eng.* **215** (2001) 1297
34. Y. Xu, C. F. Lee, *Appl. Optics* **45** (2006) 2046
35. T. Kitamura, T. Ito, J. Senda, H. Fujimoto, *Int. J. Engine Res.* **3** (2002) 223.





SUPPLEMENTARY MATERIAL TO  
**An experimental and computational investigation of the effects  
of temperature on soot formation mechanisms**

XIAOJIE BI<sup>1,2</sup>, MAOYU XIAO<sup>1</sup>, XINQI QIAO<sup>1</sup>, CHIA-FON F. LEE<sup>2,3</sup> and YU LIU<sup>4\*</sup>

<sup>1</sup>Key Laboratory for Power Machinery and Engineering of the Ministry of Education,  
Shanghai Jiao Tong University, Shanghai, 200240, China, <sup>2</sup>Department of Mechanical  
Science and Engineering, University of Illinois at Urbana-Champaign, IL, 61801, USA,

<sup>3</sup>Center for Combustion Energy and State Key Laboratory of Automotive Safety and Energy,  
Tsinghua University, Beijing 100084, China and <sup>4</sup>Key Laboratory of Automobile Dynamic  
Simulation, Jilin University, Changchun, Jilin, 130012, China

J. Serb. Chem. Soc. 79 (7) (2014) 881–895

DETAILS OF THE APPARATUS

At the center of the chamber head, a hydraulic-actuated electronic-controlled unit injector (HEUI, Caterpillar) was mounted, the relevant configurations of which are given in Table S-I. In order to mimic realistic diesel engine operation conditions, the cylinder wall was heated to 380 K by eight heaters made of Watlow Firerod and the temperature of the oil line and fuel line inside the chamber head were kept at 350 K. The in-cylinder pressure was measured by a quartz pressure transducer (Kistler 6121) embedded in the chamber wall in conjunction with a charge amplifier.

TABLE S-I. Configuration of the HEUI 300A injector and the fuel injection conditions

Parameter	Value
Nozzle style	Valve covered orifice
Number of nozzle holes	6
Spray angle	140°
Orifice diameter	0.145 mm
Injection pressure	134 MPa
Injection duration	3.5 ms
Fuel volume	120 mm <sup>3</sup>
Fuel temperature	350 K

As shown in Fig. 1, images were obtained using a high-speed digital camera (Phantom V7.1) above the optical chamber and a light source was provided by a copper vapor laser (Oxford Lasers LS20-50). Two-wavelength output at 511 and 578 nm with a power ratio of 2:1 was provided by a copper-vapor laser. The high-speed camera and the copper-vapor laser were set

\*Corresponding author. E-mail: xiaojie2163@hotmail.com

to be synchronized up to 15037 frames per second to provide time related records at a resolution of 256×256 pixels. Only one of the six spray jets was examined in the experiment. A 105 mm focal length lens made by Nikkor with a maximum aperture of *f* 4.5 was adopted for the images taking. To suppress flame emission, two interference filters at 510 and 515 nm with 10 nm full width at half maximum (FWHM) were adopted to filter out the light at 578 nm. A FWHM of 5 nm could be achieved when these two filters were aligned together. Before laser light entrance into the test constant volume chamber, it was focused by a condenser through a 6 mm diameter reflecting mirror in front of the condenser lens to a point source. The high-speed camera was triggered by injection signal and was set to record the whole combustion process of diesel fuel.

#### MEASUREMENTS AND SUBSEQUENT CALCULATION OF THE EXTINCTIONS

As shown in Fig. S-1, the laser beam passed through the soot cloud twice in the forward illumination technique. Therefore, the light intensity should be adjusted by the extinction due to light diffuser and soot absorption.

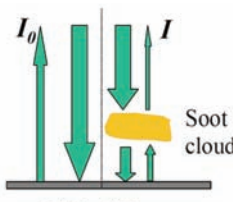


Fig. S-1. Light extinction by the soot cloud.

A variation in the reflected light intensity was caused only by the presence of soot, following the Lambert–Beer Law:

$$I = I_0 \exp(-\int_0^{2L} K_{\text{ext}} dx) \quad (\text{S-1})$$

where  $I$  is the reflected light intensity with or without the presence of a soot cloud,  $I_0$  is the reflected light intensity without the presence of a soot cloud,  $K_{\text{ext}}$  is the extinction coefficient and  $L$  is the path length through the soot cloud. Unlike the traditional back illumination method, the light extinction in the FILE method is proportional to  $2L$  rather than  $L$  due to the light passing twice through the soot cloud.

The extinction coefficient of the soot cloud is dependent on the particle number density, and on the particle diameter and optical properties. Based on the Rayleigh approximation, the soot volume fraction could be expressed as:

$$C_v = \frac{\lambda}{(2L)K_a} \ln\left(\frac{I_0}{I}\right) \quad (\text{S-2})$$

where  $\lambda$  is the wavelength of mono-wavelength light,  $K_a$  is the dimensionless absorption constant determined by soot refractive index  $m$ . A value of 5.47 was adopted here with  $m = 1.62 + i0.66$ . The soot volume fraction could be calculated using Eq. (S-2) by analysis of the images with and without soot clouds, pixel by pixel. However, for a non-axisymmetric diesel flame, the thickness of the soot cloud cannot be measured and the only the line-of-sight,

expressed as  $C_v L$ , can be detected. If the area of each pixel is represented by a dimension of  $\Delta r$  and a mean mass density of soot particles  $2.0 \text{ g cm}^{-3}$  is adopted,<sup>1</sup> then the soot mass at each pixel could be calculated as:

$$m_i = \rho_s C_v L \Delta r \quad (\text{S-3})$$

Equation (S-3) indicates that each pixel value represented the local soot mass in each column vertical to the image plane, and the total soot mass at this time could be obtained by summing all the pixel values. A detailed introduction about FILE methods in detecting a spray, combustion flame and soot emissions can be found in previous reports.<sup>2-4,5</sup>

#### DESCRIPTIONS OF THE MODELS

The phenomenological soot model, Fig. 2, has nine main steps: 1) acetylene formed through a fuel pyrolysis process, 2) precursor species formed merely from acetylene pools, 3) soot inception reaction, 4) surface growth of soot nuclei, 5) coagulation of small soot particles to form bigger ones, 6) soot surface oxidation *via* oxygen attachment, 7) soot surface oxidation *via* OH radicals, 8) acetylene oxidized by O<sub>2</sub> and 9) precursor radicals oxidized by OH radicals. All of the reaction formulas, reaction rates and relevant reaction constants are listed in Table S-II. The concentration of OH radical was estimated based on a H<sub>2</sub>-O<sub>2</sub>-CO<sub>2</sub> system, and a detailed description can be found in a previous study.<sup>6</sup> The precursor species were assumed to be general gaseous soot precursors, such as fullerene, based on the observation of heavier PAHs in hydrocarbon diffusion combustion.<sup>7,8</sup>

TABLE S-II. Reaction mechanism of the phenomenological soot model

No.	Reaction	Reaction rate	$k = A \exp\left(\frac{-E_a}{RT}\right)$	
			A	$E_a / \text{kJ mol}^{-1}$
1	Fuel $\rightarrow$ C <sub>2</sub> H <sub>2</sub>	$\omega_1 = k_1[\text{Fuel}]$	$1.0 \times 10^{10}$	207.85
2	C <sub>2</sub> H <sub>2</sub> $\rightarrow$ P <sub>c</sub>	$\omega_2 = k_2[\text{C}_2\text{H}_2]$	$1.0 \times 10^{11}$	166.28
3	P <sub>c</sub> $\rightarrow$ S <sub>c</sub>	$\omega_3 = k_3[\text{P}_c]$	$5.0 \times 10^7$	209.51
4	S <sub>c</sub> + S <sub>c</sub> $\rightarrow$ S <sub>c</sub>	$\omega_4 = k_4 N^2$	Collision frequency constant <sup>6</sup>	
5	S <sub>c</sub> + C <sub>2</sub> H <sub>2</sub> $\rightarrow$ S <sub>c+2</sub> + H <sub>2</sub>	$\omega_5 = k_5[\text{C}_2\text{H}_2] A_s^{\frac{1}{2}}$	$1.05 \times 10^4$	25.77
6	S <sub>c</sub> + O <sub>2</sub> $\rightarrow$ S <sub>c-2</sub> + 2CO	$\omega_6 = \frac{6[\text{S}_c]MW_c}{\rho_s d_s} k_{\text{NSC}}$	NSC Oxygen oxidation model <sup>9</sup>	
7	S <sub>c</sub> + OH $\rightarrow$ S <sub>c-1</sub> + CO + $\frac{1}{2}$ H <sub>2</sub>	$\omega_7 = \gamma_7 \frac{3[\text{OH}]}{N_A} \left( \frac{8RT}{\pi M_{\text{OH}}} \right)^{\frac{1}{2}}$	The OH oxidation model of Neoh <i>et al.</i> <sup>10</sup>	
8	C <sub>2</sub> H <sub>2</sub> + O <sub>2</sub> $\rightarrow$ 2CO + H <sub>2</sub>	$\omega_8 = k_8[\text{C}_2\text{H}_2][\text{O}_2]$	$6.0 \times 10^{12}$	209.51
9	P <sub>c</sub> + OH $\rightarrow$ CO	$\omega_9 = k_9[\text{P}_c][\text{OH}]$	$1.0 \times 10^9$	166.28

In the Tao model,<sup>6</sup> the original principal governing equations for solving the soot mole density and the soot mass density were listed as:

$$\frac{d[S_c]}{dt} = \omega_3 - \omega_4 \quad (\text{S-4})$$

$$\frac{dm_s}{dt} = MW_s \omega_3 + MW_s (\omega_5 - \omega_6 - \omega_7) \quad (\text{S-5})$$

where  $\omega$  indicates the reaction rate, the subscript number is the number of the reaction listed in Table S-II,  $MW_s$  is the molecular weight of the soot particles. Since the flame speed of diffusion combustion is determined by the speed of turbulent mixing, all reaction rates in these equations were modified by the Turbulence-Chemistry interaction model.<sup>11</sup>

*Model modification.* As can be seen in Eq. (S-4), only inception and coagulation were taken into account for the determination of the soot number density. However, previous results<sup>12</sup> proved that surface oxidation is also possible, which would lead to a reduction in the soot number density. During the early stage of diffusion combustion, the soot formation mechanism dominates the soot evolution and a large number of soot particles in the form of a ball core are newly generated within the chamber. Compressed ignition combustion is a kind of diffusion-controlled combustion, in which the distribution of fuel and oxidants is extremely heterogeneous. Since these young soot particles contain very few carbon atoms, they could be quickly consumed in a locally rich-oxidant environment and finally result in a reduction in soot number density. At a later stage of diffusion combustion, the oxidation mechanism takes the place of the formation mechanism and becomes dominant in soot evolution. Although the mature soot is cluster-like or chain-like hydrocarbon aggregates composed of tens to hundreds of spherical particles, it was still possible for them to be eliminated completely by strong surface oxidation, which would finally lead to a decrease in the soot number quantity. The soot number density is significant for the calculation of the soot mean diameter and the total surface area, which could sequentially affect the final soot mass concentration. Therefore, it is essential to introduce surface oxidation feedback into the calculation of the soot number density.

The effects of surface oxidation on the soot number density were taken into account for both incipient and mature soot particles. For small incipient soot particles, once the surface oxidation wins the competition with surface growth, which means that more carbon atoms were depleted than accumulated on the active surface area, the soot number density began to decrease. For mature soot particles formed after coagulation and surface growth, surface oxidation was required to deplete the shell-shaped surface carbon atoms first before contributing to number density reduction. In order to detect the turning point when surface oxidation began to affect the number density of mature soot particles, a parameter termed as critical diameter,  $d_{\text{cri}}$ , was adopted to describe the diameter of an incipient particle and the mean diameter of the soot particle is expressed as:

$$d_s = \left( \frac{6m_s}{\pi N_s \rho_s} \right)^{1/3} \quad (\text{S-6})$$

where  $m_s$  is the soot mass density,  $N_s$  is soot number density and  $\rho_s$  is the density of the soot particles, which was assumed to be  $2 \text{ g cm}^{-3}$ .

When surface oxidation loses the competition with surface growth, surface oxidation does not affect the soot number density. The governing differential equation of soot number

density is the same as that in the Tao model.<sup>6</sup> When surface oxidation wins the competition with surface growth, but  $d_s$  is still larger than  $d_{\text{cri}}$ , the number density deduction only led to a number density reduction of the incipient soot particles and the adjusted mole density could be represented as:

$$\frac{d[S_c]}{dt} = \omega_3 - \omega_4 - \omega_{\text{inc}} \quad (\text{S-7})$$

$$\omega_{\text{inc}} = \frac{MW_c(\omega_5 - \omega_6 - \omega_7)\omega_3}{MW_s(i)[S_c] + \omega_3 MW_c} \quad (\text{S8})$$

where  $\omega_{\text{inc}}$  is the amount the number density of incipient soot particles is reduced because of oxidation effects. When surface oxidation wins the competition with the surface growth and simultaneously  $d_s$  is equal or less than  $d_{\text{cri}}$ , number density reduction occurs in both incipient and mature soot particles and the revised soot mole density can be represented as:

$$\frac{d[S_c]}{dt} = \omega_3 - \omega_4 + \frac{MW_c}{MW_s(i)}(\omega_5 - \omega_6 - \omega_7) \quad (\text{S-9})$$

where  $MW_s(i)$  is the mean molecular weight of soot particles of computational cells  $i$  ( $i$  denotes the cell number). As soot is a super complex aggregate, in the present study,  $MW_s(i)$  was not considered a constant as previously,<sup>6</sup> but was renewed after each computational time step.

*Numerical implementation.* In this study, KIVA-3V Release 2 code was the numerical solver to calculate the mass, momentum and energy conservation equations for soot and other gas-phase species involved in the diesel combustion system. Spray dynamics was simulated using the “blob” injection model.<sup>13</sup> Spray atomization and droplet breakup were modeled by the Rayleigh–Taylor model.<sup>14</sup> The RNG  $k-\varepsilon$  model<sup>15</sup> for turbulent flow was also included to interpret the average effects of turbulent motions on the main flow characteristics, such as mass, density, velocity, etc. The ignition was modeled using the Shell ignition model.<sup>16</sup>

## IN-CYLINDER SPATIAL PHENOMENA

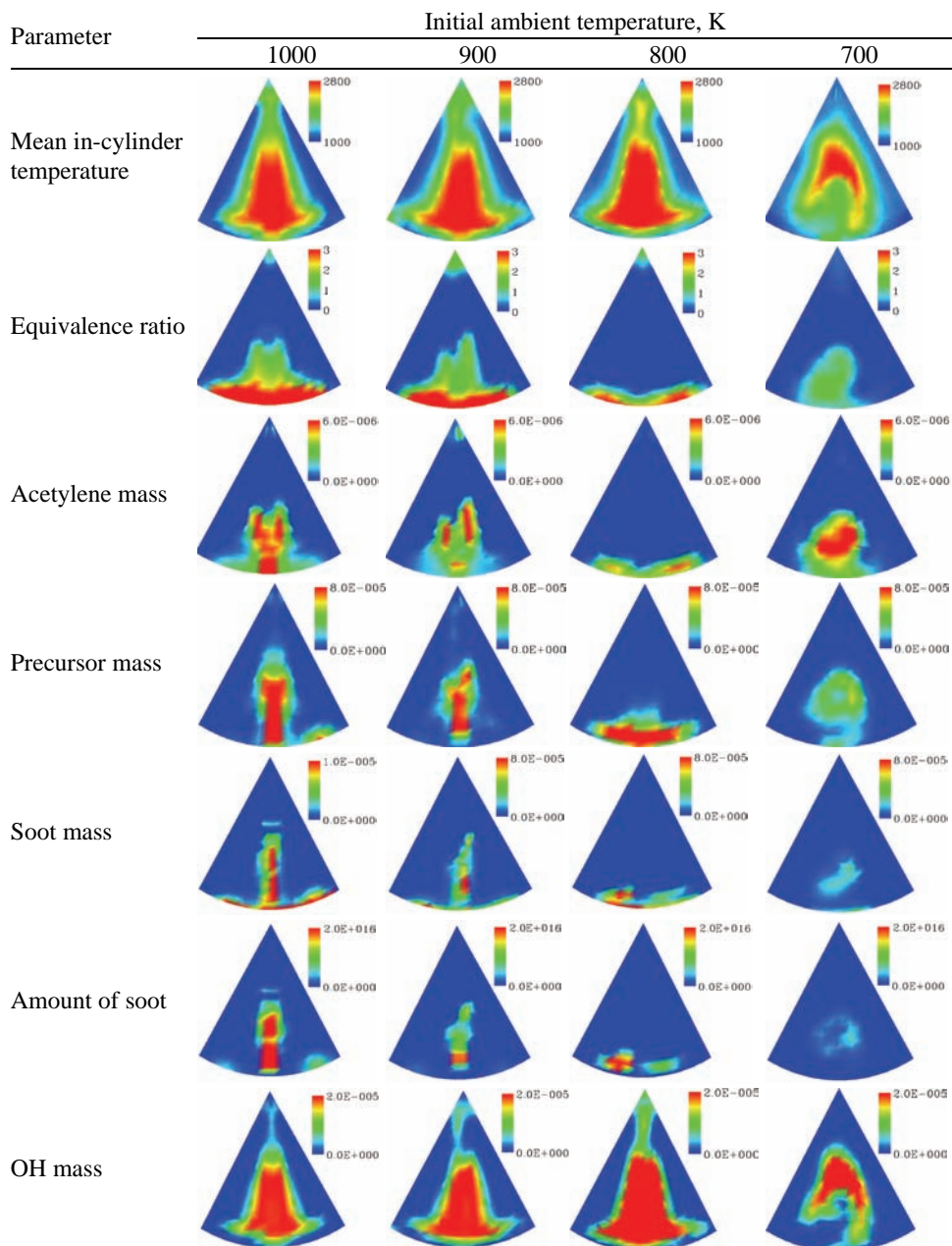


Fig. S-2. Spatial distributions of the in-cylinder temperature, mass of acetylene, precursor species, soot nuclei, OH radicals and amount of soot generated in 4.5 ms by 1 g fuel for ambient temperatures of 700, 800, 900 and 1000 K. The bars on the upper right corners present the upper and lower limits for each parameter.

## NOMENCLATURE

$A$	Exponential factor
$A_s$	Surface area of soot particle
$C_v$	soot volume fraction
$d_{cri}$	Critical diameter of incipient soot particles
$d_s$	Diameter of soot particle
$E_a$	Activation energy
FILE	Illumination light extinction
$i$	Cell number
$I$	Reflected light intensity
$I_0$	Reflected light intensity without the presence of a soot cloud
$K_a$	Dimensionless absorption constant
$K_{ext}$	Extinction coefficient
$L$	Path length through the soot cloud
$m$	Soot refractive index
$m_s$	Soot mass concentration
$MW_c$	Molar weight of carbon atom
$MW_s$	Molar weight of soot particle
$MW_{OH}$	Molar weight of OH radical
$N_s$	Number density of soot particle
$N_A$	Avogadro's number
NSC	Nagle–Stickland–Constable oxidation model
$p$	Mean pressure
[ $P_c$ ]	Mole concentration of soot precursor
$R$	Universal gas constant
$\Delta r$	Area of each pixel
[ $S_c$ ]	Mole concentration of soot particle
$T$	Mean temperature
$\lambda$	Wavelength of monochromic light
$\rho_s$	Soot particle density
$\omega$	Reaction rate
$\omega_{mc}$	Reduced incipient soot number density caused by the oxidation effects

## REFERENCES

1. A. Braun, F. E. Huggins, S. Seifert, J. Ilavsky, N. Shah, K. E. Kelly, A. Sarofim, G. P. Huffman, Combust. Flame 137 (2004) 63
2. H. Liu, X. Bi, M. Huo, C. F. F. Lee, M. Yao, Energy Fuels 26 (2012) 1900
3. H. Liu, C. F. Lee, M. Huo, M. Yao, Energy Fuels 25 (2011) 1837
4. H. Liu, C. F. F. Lee, M. Huo, M. Yao, Energy Fuels 25 (2011) 3192
5. Y. Xu, C. F. Lee, Appl. Optics 45 (2006) 2046
6. F. Tao, R. D. Reitz, D. E. Foster, Y. Liu, Int. J. Therm. Sci. 48 (2009) 1223
7. A. Keller, R. Kovacs, K. H. Homann, Phys. Chem. Chem. Phys. 2 (2000) 1667
8. O. Mathieu, G. Frache, N. Djebaili-Chaumeix, C. E. Paillard, G. Krier, J. F. Muller, F. Douce, P. Manuelli, Proc. Combust. Inst. 31 (2007) 511
9. H. Hiroyasu, T. Kadota, M. Arai, B. JSME 26(1983) 569.
10. K. G. Neoh, J. B. Howard, A. F. Sarofim, Proc. Combust. Inst. 20 (1985) 951
11. L. A. Vulis, T. P. Leontéva, Z. B. Sakipov, I. B. Palatnik, B. P. Ustimenko, Int. J. Heat Mass Tran. 4 (1961) 111

12. D. R. Tree, K. I. Svensson, Prog. Energ. Combust. Sci. 33 (2007) 272
13. R. D. Reitz, R. Diwakar, Structure of High-Pressure Fuel Sprays, SAE Technical Paper 870598, 1987, doi: 10.4271/870598
14. M. Patterson, S. Kong, G. Hampson, R. D. Reitz, Modeling the Effects of Fuel Injection Characteristics on Diesel Engine Soot and NO<sub>x</sub> Emissions, SAE Technical Paper 940523, 1994, doi: 10.4271/940523
15. Z. Han, R. D. Reitz, Combust. Sci. Technol. 31 (1995) 267
16. S. Kong, Z. Han, R. D. Reitz, The Development and Application of a Diesel Ignition and Combustion Model for Multidimensional Engine Simulation, SAE Technical Paper 950278, 1995, doi: 10.4271/950278.



## Bagasse wastewater treatment using biopolymer – A novel approach

KARICHAPPAN THIRUGNANASAMBANDHAM, VENKATACHALAM SIVAKUMAR\*  
and JEGANATHAN PRAKASH MARAN

Department of Food Technology, Kongu Engineering College, Perundurai,  
Erode-638052, TN, India

(Received 19 June, revised 9 December, accepted 13 December 2013)

**Abstract:** In this study, the removal of turbidity, biological oxygen demand (*BOD*) and chemical oxygen demand (*COD*) in the treatment of bagasse-based wastewater from the paper and pulp industry were investigated via response surface methodology (RSM) under different operating conditions, such as agitation time ( $X_1$ : 15–25 min), initial pH ( $X_2$ : 4–8), chitosan dose ( $X_3$ : 1.2–2.0 g L<sup>-1</sup>) and settling time ( $X_4$ : 40–80 min). The obtained experimental data were fitted to a second-order polynomial equation using multiple regression analysis and ANOVA (analysis of variance) was used to examine the significance of the developed mathematical models. The 3-D response surface plots were derived from the mathematical models in order to study the interactive effects of the process variables on the treatment efficiency. The Derringer desired function methodology was applied to determine the optimal conditions, which were found to be: an agitation time of 20 min, an initial pH of 6, a chitosan dose of 1.8 g L<sup>-1</sup> and settling time of 60 min. Under these conditions, the removal of turbidity, *BOD* and *COD* were found to be 84, 90 and 93 %, respectively.

**Keywords:** chitosan; coagulation; Bagasse wastewater; BBD design; model development.

### INTRODUCTION

The pulp and paper industry is one of the highest water consuming industries in which bagasse is a potential raw material.<sup>1</sup> Bagasse is a fibrous mass that is derived from the sugar industry after extraction of juice from sugarcane.<sup>2</sup> The wastewater generated from bagasse-based pulp and paper industry contains large amounts of organic and inorganic matter, resulting in high values of chemical oxygen demand (*COD*), biological oxygen demand (*BOD*) and turbidity, due to the processes involved in bagasse processing, such as storage, washing and bleaching with chemicals.<sup>3</sup> Discharge of this untreated bagasse wastewater into

\*Corresponding author. E-mail: drsivakumar@yahoo.com  
doi: 10.2298/JSC130619153T

the environment has negative impact on the ecological systems. An extensive literature survey showed that little information has been reported regarding the treatment of wastewater from the bagasse-based pulp and paper industry, *i.e.*, a UASB reactor treatment process and treatment with white route fungus. However, these treatment processes have drawbacks, such as long treatment time, start-up problems, difficulty in maintaining environmental conditions and low treatment efficiency. Therefore, there is a critical need to develop an efficient and economic treatment process for bagasse-based paper and pulp industry wastewater, before its discharge into natural resources.

One of the most commonly used wastewater treatment techniques involves the process of coagulation/adsorption, which is the physical adhesion of chemicals onto the surface of a solid. Widely available biopolymers are being used for coagulation mainly because they are a cheap resource or a freely available resource. Chitosan is a biopolymer that is extracted from crustacean shells or from fungal biomass.<sup>4</sup> Chitosan has the potential to reduce and solve some environmental pollution problems for the creation of a “greener environment”. Chitosan is a renewable polymer, which undergoes natural decomposition, is non-toxic to both the environment and humans and has no side effects or allergic effects if implanted in the body.<sup>5,6</sup> Chitosan has been used as a coagulant to treat various wastewaters, such as food processing industrial wastewaters, brewery wastewater, pulp and paper mill wastewater, olive oil wastewater and an effluent containing metal ions and phenol derivatives.<sup>7</sup> Moreover, the process parameters of chitosan-based treatment methods, such as initial pH, coagulant dose, settling time and agitation time are complex and their optimization will pave the way for effective treatment efficiency. Optimization and simulation studies of such treatment process variables are essential for industrial scale-up. To date, most studies on the optimization of wastewater treatment methods have focused on the traditional one-factor-at-a-time approach. However, this approach does not take into account cross effects from the factors considered and results in poor optimization results. Response surface methodology (RSM) is a powerful statistical-based technique for modeling complex systems, evaluating the simultaneous effects of several factors, and thus searching for the optimum conditions for desirable responses.<sup>8</sup> In addition to analyzing the effects of independent variables, RSM generates a mathematical model that could be used to predict the response of a system to any new conditions.<sup>9</sup>

However, until now, RSM has not been used as a modeling and optimization tool for the treatment of bagasse-based paper and pulp effluent using chitosan as the coagulant. Hence, the present study was planned to investigate the individual and interactive effects of the process variables, such as agitation time, initial pH, chitosan dose and settling time, on the percentage removal of turbidity, biological oxygen demand (*BOD*) and chemical oxygen demand (*COD*) from bagasse

wastewater using response surface methodology (RSM) coupled with the Box–Behnken experimental design (BBD).

## EXPERIMENTAL

### *Wastewater sample*

The wastewater used in this study was collected from the bagasse-based pulp and paper industry near Erode, Tamil Nadu, India. The characteristics of the wastewater, such as an initial pH of 5.08, a turbidity of 1768 NTU, a *BOD* of 2048 mg L<sup>-1</sup> and a *COD* of 6500 mg L<sup>-1</sup> indicates the presence of higher amounts of organic and inorganic matters in the bagasse wastewater. All the chemicals used in this study were of analytical grade. Chitosan powder was purchased from Sigma Chemicals, Mumbai, India.

### *Experimental procedure*

Conventional batch studies were performed under different operating conditions, such as agitation time (15–25 min), initial pH (4–8), chitosan dose (1.2–2.0 g L<sup>-1</sup>) and settling time (40–80 min) in 250 mL conical flask containing 100 mL of composite bagasse-based paper and pulp industry wastewater. The pH of the wastewater was adjusted by using either sulfuric acid (0.1 M) or sodium hydroxide solutions (0.1 M). The agitation was realized using incubator shaker equipment (SLM-INC-OS-250) with the desired dose of chitosan. Then the supernatant was filtered and used to determine its turbidity, *BOD* and *COD* values.

### *Analytical methods*

The initial pH, turbidity, *BOD* and *COD* determinations were performed according to the procedures described by the American Public Health Association (APHA). The percentage removal efficiency (*RE*) of turbidity, *BOD* and *COD* were calculated using the following equation:<sup>10</sup>

$$RE = \left( \frac{c_0 - c_e}{c_0} \right) \times 100 \quad (1)$$

where,  $c_0$  and  $c_e$  are the turbidity *BOD* and *COD* values before and after the process, respectively.

### *Experimental design*

Response surface optimization is more advantageous than the traditional single parameter optimization in that it saves time, space and raw materials.<sup>11</sup> Thus, in this study, a Box–Behnken response surface experimental design (BBD) with four factors at three levels was used to investigate the influence of the operating variables, *i.e.*, agitation time, initial pH, chitosan dose and settling time on the removal of turbidity, *BOD* and *COD* from the bagasse-based wastewater using chitosan as a coagulant. The process variables and their ranges are given in Table I. The experiments were established based on a BBD and the complete design consisted of 29 experiments, the total number of experiments being calculated from the following equation:<sup>12</sup>

$$N = 2K(K - 1) + C_0 \quad (2)$$

where,  $K$  is number of factors and  $C_0$  is the number of central points. The initial pH, chitosan dose, agitation speed and settling time were referred to by the uncoded variables  $X_1$ ,  $X_2$ ,  $X_3$  and  $X_4$ , respectively. The variables in uncoded form were converted to their coded form:  $x_1$ ,  $x_2$ ,  $x_3$  and  $x_4$  using the following equation:<sup>13</sup>

The general mathematical form of a second-order polynomial equation is given below:<sup>14</sup>

$$Y = \beta_0 + \sum_{j=1}^k \beta_j X_j + \sum_{j=1}^k \beta_{jj} X_j^2 + \sum_i \sum_{i < j=2}^k \beta_{ij} X_i X_j + e_i \quad (3)$$

where,  $Y$  is the response;  $X_i$  and  $X_j$  are variables ( $i$  and  $j$  range from 1 to  $k$ );  $\beta_0$  is the model intercept coefficient;  $\beta_j$ ,  $\beta_{jj}$  and  $\beta_{ij}$  are the interaction coefficients of the linear, quadratic and the second-order terms, respectively;  $k$  is the number of independent parameters ( $k = 4$  in this study); and  $e_i$  is the error. The experimental data was analyzed by multiple regression analysis (sequential sum of squares and model summary statistics) on the experimental data to evaluate the adequacy of various mathematical models, such as linear, interactive (2FI), quadratic and cubic.<sup>15</sup> Pareto analysis of variance (ANOVA) was used to study the statistical significance of mathematical model using student's  $F$ -test and the significance of the  $F$ -values at probability levels ( $p \leq 0.05$ ). All the statistical analyses were realized using the Stat ease Design Expert 8.0.7.1 statistical software package (Stat-Ease Inc., Minneapolis, MN, USA).

Then the mathematical models were used for the construction of three dimensional (3D) response surface plots to predict the relationships between the independent and dependent variables.<sup>16</sup> The adequacy of the model equation for predicting the response values were validated under the selected optimized conditions.<sup>17,18</sup> Triplicate verification experiments were performed under the optimized conditions and the average value of the experiments was compared with the predicted values of the developed model equations.

TABLE I. The process variables and their ranges

Variable	Level		
	-1	0	1
Agitation time, min	15	20	25
Initial pH	4	6	8
Chitosan dose, g L <sup>-1</sup>	1.2	1.6	2
Settling time, min	40	60	80

## RESULTS AND DISCUSSION

The percentage removal of turbidity, biological oxygen demand (*BOD*) and chemical oxygen demand (*COD*) were investigated under different operating conditions, *i.e.*, agitation time ( $X_1$ : 15–25 min), initial pH ( $X_2$ : 4–8), chitosan dose ( $X_3$ : 1.2–2 g L<sup>-1</sup>) and settling time ( $X_4$ : 40–80 min) using chitosan as a coagulant to treat bagasse-based paper and pulp industry wastewater *via* the response surface methodology (RSM). In this study, a four-factor three-level BBD was used to evaluate the effect and optimize the process variables on the responses. A total number of 29 batch experiments including three centre points were performed in triplicate using statistically designed experiments, the results of which are given in Table II.

### BBD analysis

The BBD experimental data were analyzed by multi regression analysis, namely the sequential model sum of squares (Table III) and model summary

statistics (Table IV), in order to select the best regression mathematical model among the various models, *i.e.*, linear, interactive, quadratic and cubic. From the results, it was found that the quadratic model shows the highest  $R^2$ , adjusted  $R^2$ , and predicted  $R^2$  values and also had the lowest  $p$ -values compared to the other models considered. Therefore, the quadratic model was chosen to describe the effects of the process variables on the removal efficiency of turbidity, *BOD* and *COD* from bagasse-based paper and pulp industry wastewater.<sup>19</sup>

TABLE II. BBD experimental design results

No.	Agitation time, min	Initial pH	Chitosan dose, g L <sup>-1</sup>	Settling time, min	Turbidity removal, %	<i>BOD</i> removal, %	<i>COD</i> removal, %
1	20	4	2.0	60	62.2	71.2	67.9
2	20	4	1.6	40	22.5	31.3	27.9
3	15	4	1.6	60	45.6	54.2	50.9
4	15	8	1.6	60	46.3	55.4	51.9
5	15	6	1.6	40	16.2	25.3	21.9
6	25	8	1.6	60	41.3	50.4	47.3
7	20	8	2.0	60	51.2	60.8	56.9
8	20	6	1.2	40	29.9	38.7	35.6
9	25	6	2.0	60	56.2	65.2	61.5
10	20	6	1.6	60	81.5	90.3	87.2
11	20	8	1.2	60	66.2	75.4	71.9
12	20	4	1.6	80	58.9	67.7	64.6
13	20	6	2.0	40	31.2	40.6	36.9
14	20	6	1.6	60	81.5	90.3	87.2
15	25	6	1.6	80	54.2	63.8	59.9
16	20	6	1.6	60	81.5	90.3	87.2
17	25	6	1.2	60	56.2	65.6	61.9
18	20	6	2.0	80	75.5	84.3	81.2
19	20	6	1.6	60	81.5	90.4	87.2
20	20	8	1.6	40	24.2	33.2	29.9
21	15	6	1.2	60	54.4	63.3	60.3
22	25	4	1.6	60	31.3	40.1	37.5
23	25	6	1.6	40	26.2	35.3	31.9
24	20	4	1.2	60	44.2	53.4	49.9
25	20	8	1.6	80	68.3	77.2	74.3
26	20	6	1.2	80	81.7	90.4	87.7
27	15	6	1.6	80	70.2	79.2	75.9
28	20	6	1.6	60	81.5	90.3	87.2
29	15	6	2.0	60	61.5	69.8	66.7

#### *Mathematical equation development*

An empirical relationship between the responses and independent variables was expressed by a second-order polynomial equation with interaction terms. Three empirical models were developed in order to understand the interactive correlation between the responses and the process variables. The final model

obtained in terms of coded factors is given below (Eqs. (5)–(7)). These equations will help to predict the removal efficiency of different sets of combinations of the four process variables on the responses.<sup>20</sup>

$$Y_1 = 81.50 - 2.40X_1 + 2.73X_2 + 0.43X_3 + 21.55X_4 + 2.32X_1X_2 - \\ -1.77X_1X_3 - 6.50X_1X_4 - 8.25X_3 + 1.92X_2X_4 - \quad (5)$$

$$-1.88X_3X_4 - 19.78X_1^2 - 19.46X_2^2 - 5.93X_3^2 - 19.86X_4^2$$

$$Y_2 = 90.32 - 2.23X_1 + 2.88X_2 + 0.42X_3 + 21.51X_4 + 2.27X_1X_2 - \\ -1.72X_1X_3 - 6.35X_1X_4 - 8.10X_2X_3 + 1.90X_2X_4 - \quad (6)$$

$$-2.00X_3X_4 - 19.70X_1^2 - 19.36X_2^2 - 5.81X_3^2 - 19.78X_4^2$$

$$Y_3 = 87.20 - 2.30X_1 + 2.79X_2 + 0.32X_3 + 21.62X_4 + 2.20X_1X_2 - \\ -1.70X_1X_3 - 6.50X_1X_4 - 8.25X_3 + 1.93X_2X_4 - \quad (7)$$

$$-1.95X_3X_4 - 19.83X_1^2 - 19.42X_2^2 - 5.98X_3^2 - 19.82X_4^2$$

where  $Y_1$ ,  $Y_2$ , and  $Y_3$  are turbidity, *BOD* and *COD* removal, respectively, and  $X_1$ ,  $X_2$ ,  $X_3$  and  $X_4$  are the agitation time, initial pH, chitosan dose and settling time, respectively.

TABLE III. Sequential model sum of squares results for the responses

Source	Sum of squares	Df	Mean square	F-value	Prob > F	Remarks
Sequential model sum of squares for turbidity removal						
Mean	86420.88	1.00	86420.88	—	—	—
Linear	5734.23	4.00	1433.56	5.61	0.0025	—
2FI	504.39	6.00	84.06	0.27	0.9444	—
Quadratic	5512.65	4.00	1378.16	167.02	< 0.0001	Suggested
Cubic	91.73	8.00	11.47	2.89	0.1064	Not fit
Sequential model sum of squares for <i>BOD</i> removal						
Mean	117176.67	1.00	117176.67	—	—	—
Linear	5717.16	4.00	1429.29	5.66	0.0024	—
2FI	486.80	6.00	81.13	0.26	0.9477	—
Quadratic	5467.70	4.00	1366.93	173.50	< 0.0001	Suggested
Cubic	87.25	8.00	10.91	2.84	0.1103	Not fit
Sequential model sum of squares for <i>COD</i> removal						
Mean	105398.38	1.00	105398.38	—	—	—
Linear	5770.26	4.00	1442.56	5.67	0.0023	—
2FI	502.24	6.00	83.71	0.27	0.9445	—
Quadratic	5504.32	4.00	1376.08	184.78	< 0.0001	Suggested
Cubic	83.53	8.00	10.44	3.02	0.0975	Not fit

TABLE IV. Model summary statistics for the responses

Source	S.D.	R <sup>2</sup>	Adjusted R <sup>2</sup>	Predicted R <sup>2</sup>	PRESS	Remarks
Model summary statistics for turbidity removal						
Linear	15.9851	0.4832	0.3971	0.3410	7820.13	
2FI	17.6826	0.5257	0.2622	0.1110	10549.06	
Quadratic	2.8725	0.9903	0.9805	0.9439	665.66	Suggested
Cubic	1.9914	0.9980	0.9906	0.7113	3426.22	Not fit
Model summary statistics for BOD removal						
Linear	15.8965	0.4852	0.3995	0.3435	7734.63	
2FI	17.6037	0.5266	0.2635	0.1108	10476.54	
Quadratic	2.8069	0.9906	0.9813	0.9461	635.61	Suggested
Cubic	1.9602	0.9980	0.9909	0.7183	3318.80	Not fit
Model summary statistics for COD removal						
Linear	15.9567	0.4857	0.3999	0.3447	7785.60	
2FI	17.6519	0.5279	0.2657	0.1178	10481.87	
Quadratic	2.7290	0.9912	0.9824	0.9494	600.78	Suggested
Cubic	1.8590	0.9983	0.9919	0.7487	2985.87	Not fit

#### Adequacy of developed mathematical models

It is very important that the developed mathematical models described the coagulation process effectively. Thus, the adequacy of the models was evaluated by constructing diagnostic plots, *i.e.*, predicted *versus* actual for the data predicted by models and the experimental data (Fig. 1A–C). From the figures, it could be observed that the data points on these plots lie very close to the diagonal lines, which indicates good agreement between the experimental data and the data predicted by the developed models.<sup>21</sup> This confirms the normal distribution of the observed data and the adequacy of the developed models.

#### Statistical significance of the quadratic model

Pareto analysis of variance (ANOVA) was used to analyze the significance of the developed model equations by using their corresponding *F* and *p*-values, which are listed in Table V. The higher model *F* values and lower *p*-values (*p* < 0.0001) of both the mathematical models demonstrated that the developed model was highly significant. The robustness of the model was analyzed by the determination of the coefficient (*R*<sup>2</sup>), the adjusted determination coefficient (*R*<sub>a</sub><sup>2</sup>), the predicted determination coefficient (*R*<sub>p</sub><sup>2</sup>), the coefficient of variance (CV) and the adequate precision (AP). The high *R*<sup>2</sup> value of the developed models showed that the relationship between the operating variables and the response is well correlated. The lower CV values and the higher AP values clearly confirm that the deviations between the experimental and predicted values were low and showed the reliability of the conducted experiments.<sup>22</sup>

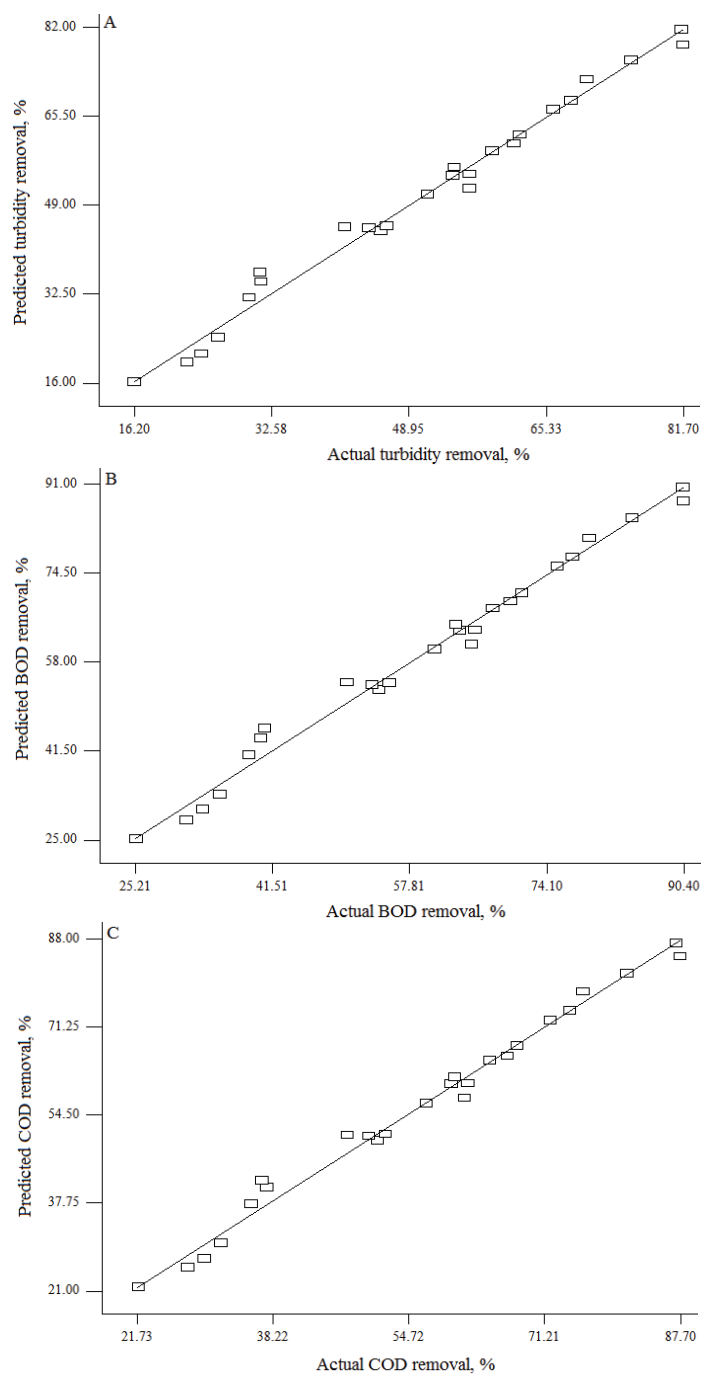


Fig. 1. Plots of the predicted *versus* the actual values for the responses. A – turbidity removal, B – BOD removal and C – COD removal.

TABLE V. ANOVA results for the responses

Response	Turbidity removal		<i>COD</i> removal		<i>BOD</i> removal	
	F-value	p-value	F-value	p-value	F-value	p-value
Model	101.73	<0.0001	112.96	<0.0001	105.82	<0.0001
$X_1$	8.38	0.0118	8.52	0.0112	7.60	0.0155
$X_2$	10.88	0.0053	12.57	0.0032	12.60	0.0032
$X_3$	0.27	0.6102	0.16	0.6946	0.27	0.6089
$X_4$	675.16	<0.0001	753.28	<0.0001	704.92	<0.0001
$X_1X_2$	2.62	0.1278	2.60	0.1292	2.63	0.1273
$X_1X_3$	1.53	0.2371	1.55	0.2335	1.51	0.2395
$X_1X_4$	20.49	0.0005	22.70	0.0003	20.48	0.0005
$X_2X_3$	32.99	<0.0001	36.56	<0.0001	33.31	<0.0001
$X_2X_4$	1.80	0.2015	1.99	0.1801	1.83	0.1973
$X_3X_4$	1.70	0.2128	2.04	0.1749	2.03	0.1761
$X_1^2$	307.61	<0.0001	342.41	<0.0001	319.51	<0.0001
$X_2^2$	297.64	<0.0001	328.37	<0.0001	308.71	<0.0001
$X_3^2$	27.67	0.0001	31.14	<0.0001	27.83	0.0001
$X_4^2$	310.01	<0.0001	342.04	<0.0001	322.01	<0.0001
CV	5.2		4.5		4.4	
AP	31.6		33.3		32.2	

#### *Effect of process variables*

Three dimensional (3D) response surface plots were plotted from the developed models in order to study the individual and interaction effects among the process variables on the responses and to determine the optimal conditions of each process variable for the maximum removal of turbidity, *BOD* and *COD* from bagasse wastewater using chitosan as the coagulant. The response surface plots are shown in Fig. 2A–F.

#### *Effect of agitation time*

In order to investigate the effect of agitation time on the treatment efficiency, experiments were performed for various agitation times (15–25 min). From the results, it was observed that the removal efficiencies increased linearly with increasing agitation time from 15–20 min (Figs. 2A–C). Increasing the agitation time up to 20 min increases the collision between the chitosan and the organic matters present in the bagasse-based paper and pulp industry wastewater, which enhanced the removal efficiencies of turbidity, *BOD* and *COD*. However, agitation times longer than 20 min resulted in lower removal efficiencies of turbidity, *BOD* and *COD*.

#### *Effect of initial pH*

Experiments were performed to study the effect of the initial pH (4, 6 and 8) on the removal efficiency of turbidity, *BOD* and *COD*. From the results, it was observed that the removal efficiencies increased linearly with increasing pH from

4 to 6 (Fig. 2A–C). Increasing the pH up to 6 increases the solubility of chitosan, which increases the protonation of the chitosan surface and enhances the removal efficiencies of turbidity, *BOD* and *COD*.<sup>23</sup> However, an initial pH higher than 6 resulted in lower removal efficiencies of turbidity, *BOD* and *COD*, due to the decrease in the solubility of chitosan.<sup>24</sup>

#### *Effect of chitosan dose*

The chitosan dose is one of the important process variables for the coagulation process and it is associated with the removal efficiency of turbidity, *BOD* and *COD*. As can be seen in Figs. 2D–F, the removal efficiencies increased rapidly with increasing the chitosan dose in the range of 1.2–1.8 g L<sup>-1</sup>. This phenomenon could be explained by the increased number of reactive site available for the coagulation process with increasing chitosan dose, which considerably increases the amounts of organic matter that can be adsorbed.<sup>25,26</sup> Increasing the chitosan dose above 1.8 g L<sup>-1</sup> had negligible effects on the removal efficiencies of turbidity, *BOD* and *COD*.

#### *Effect of settling time*

The settling time is also a primary factor influencing the coagulation process. To examine the effect of settling time on the treatment efficiency, experiments were performed in which various settling times were examined and the results are shown in Figs. 2D–F. From Figs. 2D–F, it was observed that, the removal efficiency was increased with increasing settling time from 40–60 min. This could be explained by the fact that increases in settling time would lead to the formation of more compact flocs *via* the bridging mechanism, which increases the removal efficiencies of turbidity, *BOD* and *COD*.<sup>27</sup> A settling time longer than 60 min allows for desorption of organic matter from the surface of the chitosan,<sup>28</sup> which decreases the removal efficiencies of turbidity, *BOD* and *COD*.

#### *Optimization*

The Derringer desired function methodology<sup>29,30</sup> was applied to determine the optimal conditions and they were found to be an agitation time of 20 min, an initial pH of 6, a chitosan dose of 1.8 g L<sup>-1</sup> and a settling time of 60 min. Under these conditions, the removal efficiencies of turbidity, *BOD* and *COD* were 83.6, 93.2 and 90.4 %, respectively, with a desirability value of 0.986 were predicted for the developed mathematical models. Under these conditions, the experimental removal efficiencies of turbidity, *BOD* and *COD* were 84, 93 and 90 %, respectively, which are in close agreement with the values predicted by the developed mathematical models. These results validate the optimized conditions.

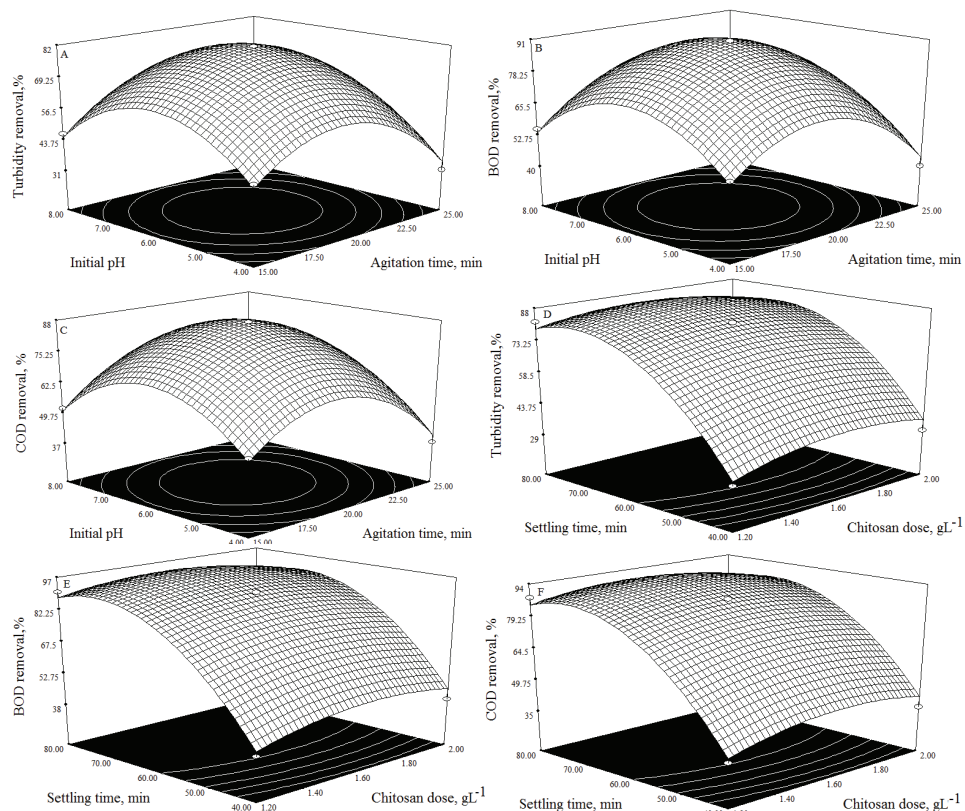


Fig. 3. Effect of the process parameters on the responses; A, B and C – effect of initial pH and agitation time on turbidity removal, *BOD* removal and *COD* removal, respectively; D, E and F – effect of initial settling time and chitosan dose on turbidity removal, *BOD* removal and *COD* removal, respectively.

#### CONCLUSIONS

In this study, BBD was employed to investigate and optimize the process variables, *i.e.*, agitation time, initial pH, chitosan dose and settling time, on the removal efficiencies of turbidity, *BOD* and *COD* to treat bagasse-based wastewater using chitosan as a coagulant. From the results, it was observed that the variables of the operating process have significant effects on the treatment efficiency. Quadratic models were developed from the experimental data and their adequacies were analyzed by the Pareto analysis of variance (ANOVA). 3D response surface plots were generated in order to study the interactive effect of the process variables on the treatment efficiency. The Derringer desired function methodology was applied to determine the optimal conditions, which were found to be: an agitation time of 20 min, an initial pH of 6, a chitosan dose of  $1.8 \text{ g L}^{-1}$  and a settling time of 60 min. Under these conditions, the removal efficiencies of

turbidity, *BOD* and *COD* were 84, 93 and 90 %, respectively. These results show the effectiveness of chitosan as a coagulant for the eco-friendly treatment of bagasse wastewater.

#### ИЗВОД

#### ПРЕРАДА ОТПАДНЕ ВОДЕ ОД ТРШЧАНОГ ОТПАДА КОРИШЋЕЊЕМ БИОПОЛИМЕРА – НОВИ ПРИСТУП

KARICHAPPAN THIRUGNANASAMBANDHAM<sup>1</sup>, VENKATACHALAM SIVAKUMAR<sup>2</sup> и JEGANATHAN PRAKASH MARAN<sup>3</sup>

<sup>1</sup>Department of Food Technology, Kongu Engineering College, Perundurai, Erode-638052, TN, India, E-mail: thirusambath5@gmail.com, <sup>2</sup>Department of Food Technology, Kongu Engineering College, Perundurai, Erode-638052, TN, India и <sup>3</sup>Department of Food Technology, Kongu Engineering College, Perundurai, Erode-638052, TN, India, E-mail: prakashmaran@gmail.com

У овом истраживању, уклањање замућености, биолошке потрошње кисеоника (*BOD*) и хемијске потрошње кисеоника (*COD*) испитани су под различитим радним условима, као што су време мешања ( $X_1$ : 15–25 min), почетна pH ( $X_2$ : 4–8), доза хитозана ( $X_3$ : 1,2–2,0 g L<sup>-1</sup>) и време таложења ( $X_4$ : 40–80 min) у преради отпадне воде тршчаног отпада индустрије хартије, методологијом анализе површине одговора. Експериментални подаци су апроксимирани полиномном једначином другог реда коришћењем мултипне регресионе анализе, а метода ANOVA (анализа варијансе) је употребљена за испитивање значајности развијеног математичког модела. Из математичких модела су добијени графици тродимензионалне површине одговора, како би се проучили утицаји интеракције процесних променљивих на ефикасност прераде. За одређивање оптималних услова примењена је методологија Дерингерове (Derringer) жељене функције и дала следеће резултате: време мешања 20 min, почетни pH 6, доза хитозана 1,8 g L<sup>-1</sup>, а време мировања 60 min. Под овим условима, нађено је да је замућеност 84 %, *BOD* 90 % и *COD* 93 %.

(Примљено 19. јуна, ревидирано 9. децембра, прихваћено 13. децембра 2013)

#### REFERENCES

1. A. G. Kulkarni, R. M. Mathur, S. Panwar, *Business meeting on energy recovery from pulp and paper mill effluent*, organized by the Indian Agro & Recycled Paper Mill Association, New Delhi, India, 2001
2. F. Shahidi, R. Abuzaytoun, *Adv. Food Nutr. Res.* **49** (2005) 93
3. F. H. Chi, W. P. Cheng, *J. Polym. Environ.* **14** (2006) 411
4. R. Divakaran, V. N. S. Pillai, *Water Res.* **36** (2002) 2414
5. M. Ashmore, J. Hearn, F. Karpowicz, *Langmuir* **17** (2001) 1069
6. P. S. Strand, K. M. Vårum, K. Østgaard, *Colloids Surfaces, B* **27** (2003) 71
7. E. Guibal, J. Roussy, *React. Funct. Polym.* **67** (2007) 33
8. K. Thirugnanasambandham, V. Sivakumar, J. Prakash Maran, *Carbohyd. Polym.* **112** (2014) 622
9. N. V. Ravi Kumar, *React. Funct. Polym.* **46** (2000) 1
10. B. Amit, S. Mika, *Adv. Colloid Interfac.* **152** (2009) 26
11. K. Thirugnanasambandham, V. Sivakumar, J. Prakash Maran, *J. Serb. Chem. Soc.* **78** (2013) 613
12. E. Ahmet, V. T. Nuket, T. Aydemir, S. Becerik, D. Ayse, *Chem. Eng. J.* **210** (2012) 590

13. J. Prakash Maran, S. Manikandan, K. Thirugnanasambandham, C. Vigna Nivetha, R. Dinesh, *Carbohyd. Polym.* **92** (2013) 604
14. M. S. Bhatti, A. S. Reddy, A. K. Thukral, *J. Hazard. Mater.* **172** (2009) 839
15. E. Ashtoukhy, N. K. Amin, *J. Hazard. Mater.* **179** (2010) 113
16. C. Escobar, C. Soto-Salazar, M. I. Toral, *J. Environ. Manage.* **81** (2006) 384
17. J. Prakash Maran, V. Sivakumar, R. Sridhar, V. Prince Immanuel, *Ind. Crop. Prod.* **42** (2013) 159
18. R. Sridhar, V. Sivakumar, V. Prince Immanuel, J. Prakash Maran, *Environ. Prog. Sustain. Energy* **31** (2012) 558
19. M. Helen Kalavathy, I. Regupathi, M. G. Pillai, L. R. Miranda, *Colloids Surfaces, B* **70** (2009) 35
20. R. Sridhar, V. Sivakumar, J. Prakash Maran, K. Thirugnanasambandham, *Int. J. Environ. Sci. Technol.* (2013), doi: 10.1007/s13762-013-0301-5
21. E. Gengec, M. Kobya, E. Demirbas, A. Akyol, K. Oktor, *Desalination* **286** (2012) 200
22. J. Prakash Maran, V. Sivakumar, K. Thirugnanasambandham, R. Sridhar, *Prep. Biochem. Biotech.* **44** (2014) 56
23. J. Prakash Maran, V. Mekala, S. Manikandan, *Carbohyd. Polym.* **92** (2013) 2018
24. K. Thirugnanasambandham, V. Sivakumar, J. Prakash Maran, S. Kandasamy, *Carbohyd. Polym.* **99** (2013) 593
25. T. Olmez, *J. Hazard. Mater.* **162** (2009) 1371
26. M. Kumar, F. Ponselvan, J. RamMalviya, V. Srivastava, I. Mall, *J. Hazard. Mater.* **165** (2009) 345
27. M. Y. Nordin, V. C. Venkatesh, S. Sharif, S. Elting, A. Abdullah, *J. Mater. Process. Technol.* **145** (2004) 46
28. K. Thirugnanasambandham, V. Sivakumar, J. Prakash Maran, *Carbohyd. Polym.* **97** (2013) 451
29. A. L. Ahmad, S. Sumathi, B. H. Hameed, *Water Res.* **39** (2005) 2483
30. K. Thirugnanasambandham, V. Sivakumar, J. Prakash Maran, *J. Serb. Chem. Soc.* **79** (2014) 743.